MOLDING BEHAVIOUR AND MICROSTRUCTURE OF INJECTION MOLDED SHORT GLASS FIBER REINFORCED POLYPROPYLENE COMPOSITES

© PETER SINGH

A Thesis Submitted to the Faculty of Graduate Studies and Research in Partial Fulfilment of the Requirement for the Degree of Doctor of Philosophy

Department of Chemical Engineering
McGill University
Montreal, Canada

April 1989

MICROSTRUCTURE OF INJECTION MOLDED POLYPROPYLENE COMPOSITES

ABSTRACT

Injection molded Short Glass Fiber Reinforced Thermoplastics (SFRTP) are widely used in industry because of advantages in material properties, availability, economics and ease of processing. The thermo-mechanical history experienced by the material during processing produces significantly anisotropic microstructural and consequently mechanical properties, varying not only spatially, but directionally.

This work attempts to examine quantitatively various aspects of microstructure and the effect of processing conditions in SFRTP. The matrix phase properties, such as crystallinity, morphology and molecular orientation distribution, as well as the fiber phase microstructure such as concentration, length and orientation distributions have been analyzed quantitatively, and explained. Experimental techniques, including optical and electron microscopy, differential scanning calorimetry, Fourier transform infrared spectroscopy, thermo-gravimetric analysis, etc have been used. The results indicate complex changes in microstructure from skin to core in the injection molded samples. Both matrix and fiber phase microstructures are affected by the basic thermal and flow processes that occur during the injection molding process. A first order model has been developed to predict fiber orientation distributions, which agree well with the experimental results.

RESUME

Le moulage par injection des thermoplastiques renforcés aux fibres de verre est un procédé largement utilisé dans l'industrie. Cette forte demande est surtout reliés aux avantages des propriétés de la résine, de la disponibilité, de l'économie ainsi que de la mise en oeuvre. L'histoire thermo-mécanique subie par la résine durant la transformation engendre une microstructure fortement anisotropique qui influence de la même manière les propriétés mecaniques qui varient non seulement dans l'espace mais aussi en direction.

Le but de cette thèse tente d'examiner quantitativement divers les aspects de la microstructure et les effects des conditions de transformation dans des systèmes thermoplastiques renforcés de fibres de verre courtes. Les propriétés de la matrice telles la crystallinité, la morphologie et la distribution de l'orientation moléculaire ainsi que la microstructure de la phase des fibres, telles la concentration, la distribution de la longueur et de l'orientation des fibres ont été analysées, quantitativement et expliquees. Les téchniques experimentales incluant la microscopie polarisante et électronique, l'analyse enthalpique différentielle, la spectroscopie infrarouge par transformation de Fourier, l'analyse thermogravimétrique, etc. on été utiliseés. Les résultats montrent des changements complexes dans la microstructure de la surface (couche en peau) au centre (couche en coeur) de l'épaisseur dans les pièces injectées. Les deux microstructures aussi bien de la matrice que de la phase des fibres sont influencées par l'histoire thermique et d'écoulement qui sont développees durant le moulage par injection. Un modéle mathématique de premier ordre a été développé afin d'obtenir les predictions de la distribution de l'orientation des fibres, qui ont montrées un bon recoupage avec les résultats éxperimentaux.

DEDICATED TO

Zamina

ACKNOWLEDGEMENTS

I would like to express my sincerest gratitude to the many people who have assisted me during the term of this work. In particular, I would like to express my deepest appreciation to:

- Dr. M. R. Kamal, my research supervisor, for his encouragement, guidance and helpful suggestions that he bestowed unto me.
- The staff of the Department of Chemical Engineering, for making my stay a pleasant one.
- My colleagues, O. Khennache, D. Abu Fara, M. Samara, T. Mutel, E. Chu, F. Mijangos and other members of the fifth floor for their helpful advice and discussions.
- Mr. A. Krish and the staff of the machine workshop for their assistance in construction and repair of research equipment.
- Mr. J. Dumont, Mr. L. Cusmitch and Mr. N. Habib for their help in supplying research materials.
- The Department of Chemical Engineering at McGill

University, the Natural Science and Engineering Research Council of Canada, and the Ministère de l'Education du Gouvernment du Quebec for their financial support.

TABLE OF CONTENTS

LIST OF FIGURES

LIST OF TABLES

NOMENCLATURE

a = radius of the sphere

A_n = absorption at the specific peak in cm^{-1}

$2b$ = thickness of sample

C = concentration of absorbing units = $1-X$

C = the Stress-Optical coefficient

c_L = the specific heat capacity of the melt

C_p = specific heat of material at constant pressure

C_p' = specific heat of sample without heat of fusion

d_{xx}, d_{xy}, d_{yy} = components of the rate of deformation tensor.

D = the measured dichroic ratio.

E = elastic modulus

E = electric field vector for incident infra-red radiation

f_c, f_{am} = orientation functions of the amorphous and crystalline phases respectively.

$(h-h^*)$ = the thickness of the frozen wall layer

H_c = heat of crystallization of the sample

ΔH = heat of crystallization of crystalline material

ΔH_{pc} = heat of fusion of the pure crystal

k = the thermal conductivity of the mixture

k_c = thermal conductivity of the continuous phase

k_d = thermal conductivity of the discrete phase

k_e = thermal conductivity of the two phase mixture

k_n, k_g = the thermal conductivities of the polymer and reinforcement, respectively

k_L = the thermal conductivity of the melt

k_s = the thermal conductivity the solid

K = absorption coefficient of the 1155 cm^{-1} band

$K_A(T)$ = parameter related to the Avrami isothermal crystallization rate constant Z(T)

L = Length of the mold

L = film thickness

n = Avrami index determined in the isothermal experiments

Δn_{ij} = the birefringence

N = the doubled ratio of the absorption coefficient of these two bands E_{841}/E_{809} (N = 5.80, obtained from the spectra of isotropic films)

p = the pressure

P_x, P_y, P_z = orientation parameters which represent apparent fractions of polymer chain segments (in crystalline or amorphous phase) aligned parallel to the corresponding axes. Thus $P_x + P_y + P_z = 1$

Q = volume flux per unit width

Q = the volumetric flow rate

R = radius of curvature

R = radius of the sphere

R = heat transfer coefficient

t = time

T = the injection time

T = temperature of the polymer

T_s = ambient temperature

u = thickness of removed layer

$\bar{V}$ = velocity

W = Width of the mold

x_f = melt front position in the mold

X = crystallinity

y = the distance parallel to the thickness of the mold cavity; $y = \pm h$ being the walls

y=y1 = new layer formed after each removal

z0-z1 = half of sample thickness

Greek Symbols

$\sigma_x(y1)$ = longitudinal stress

υ = Poisson ratio

σ_1 = residual stress at position z1 from the centre of sample

$\rho(x1)$ = curvature when (z0-z1) has been removed

ρ_x, ρ_z = measured curvature in the x and z directions.

$\sigma_{1y}(z)$ = residual stresses prior to layer removal

$\sigma_{1x}(z)$ = residual stresses prior to layer removal

$\sigma'_{1y}(z)$ = residual stresses after layer removal

$\sigma'_{1x}(z)$ = residual stresses after layer removal

γ = strain

σ = the Stress Tensor

$\vec{\Omega}$ = angular velocity of the rigid bead

σ = density of the fluid

ν = the ambient velocity field.

ϕ = volume concentration of particle

ψ_1 = the primary normal stress coefficient

$|\tilde{y}|$ = surface of fiber accumulation

η = dynamic viscosity

α = negative ratio of secondary to primary normal stress difference.

$\dot{\phi}$ = the material time derivative of the orientation angle.

ψ = vorticity

ϕ_n, ϕ_g = the volume fractions of resin and reinforcement respectively.

ϕ = volume fraction of the discrete phase

χ = degree of crystallinity.

$\chi(\infty)$ = the maximum achievable degree of crystallinity at the isothermal crystallization temperature

τ^* = induction time

$\chi(t)$ = the degree of crystallinity at time t

$\chi(\infty)$ = the limiting crystallinity level which is dependent on the temperature ; $\chi(\infty) < 1$

$\epsilon_1, ..\epsilon_n$ = the errors in the variables $x_1 ... x_n$.

$<\nu>$ = the mean velocity of the fluid

μ = the melt viscosity is described by a power law relationship

ρ_L = Density of the melt

Λ = latent heat of fusion of polymer

β = fraction crystallinity

μ_a, μ_b, μ_c = transition moment unit vectors

<u>Subscript</u>

c = crystalline phase.

am = amorphous phase.

// = parallel polarized spectra

$\perp$ = perpendicular polarized spectra

$^\circ$ = nonpolarized spectra

x = axis of stretching direction

y = perpendicular to the stretching direction in the plane of the polymer film

z = axis perpendicular to the stretching direction and to the film plane

CHAPTER 1

1 INTRODUCTION

The greatest potential market for plastics lies in the metal replacement area. An important way of achieving this is to incorporate fillers and reinforcements. Reinforced plastic parts are now replacing metals in many industries, the most prominent being in land, marine and aerospace transportation. The world consumption of reinforced plastics was 2.2 million metric tons in 1985, with an estimated annual growth rate of 8 to 12% for the next decade [1]. The majority of composites are based on unsaturated polyesters, while about 15% are based on thermoplastics. The use of thermoplastics, especially engineering thermoplastics is expected to increase dramatically in the balance of the century.

Thermoplastics are widely used in many applications because of their numerous advantages. These include raw material availability, ease of processing, mechanical properties and low cost. The incorporation of reinforcing fillers enhances these advantages by making the material stronger, stiffer and tougher at higher temperatures.

Short Glass Fiber Reinforced Thermoplastics (SFRTP) are an important class of materials in the field of composites. They usually contain up to 30% by weight of short glass fibers of average length up to 6 mm. There are often other components such as coupling agents, lubricants and miscellaneous additives. The most commonly used thermoplastic matrices include polypropylene and nylon 6,6.

When compared to unreinforced material, SFRTP have the following advantages:

(i) lower cost/performance ratio;
(ii) lower polymer utilization;
(iii) better mechanical properties - higher modulus, higher strength, higher impact resistance;
(iv) better heat resistance;
(v) better creep resistance;
(vi) reduced thermal expansion;
(vii) reduced shrinkage.

SFRTP are usually processed by injection molding, which is also widely used for unreinforced materials. The ease of injection molding as well as cost effectiveness in high volume parts have contributed to the growth of industrial applications of SFRTP [2].

The use of the polymeric material in making a finished product does not guarantee the attainment of desired material properties. The physical properties of the product are markedly affected by the properties of the components, the mold geometry, the machine design and processing conditions. These factors interact to produce the thermo-mechanical history, (i.e. the temperature, pressure, velocity, stress field distributions) that is experienced by the polymer during the molding cycle.

A manufacturer's main concern is to minimize cycle time and costs. This can be achieved by using processing variables such as low melt and mold temperatures and high injection speeds. However, the limits on such variables are determined by intrinsic properties such as melting temperature, heat of fusion, temperature and shear rate dependence of viscosity and processing stability. The processing conditions have a profound influence on the microstructural properties. Severe anisotropies in microstructure are produced, with differences in morphology not only in the plane of the molded part, but also in the thickness direction. This is reflected in anisotropy of mechanical properties not only at different positions but also in different directions.

Quantitative analysis of polymer behaviour during the injection molding cycle can be achieved by formulating and solving the equations that describe the process. This involves the general conservation equations of mass, momentum and energy and the constitutive equations which describe the properties of the processed material. The equations must be solved subject to the initial and boundary conditions which usually describe the geometry of the system and the forces acting at the boundaries. Often, other simplifying assumptions are needed to facilitate solution of the equations. Such mathematical formulations are not possible to solve analytically and, as a result, require numerical solution with the aid of a computer. The mathematical model usually predicts velocity, temperature, pressure and stress distributions in the material, which in turn can be utilized to predict microstructural properties.

A full understanding and control of the final properties of composite materials can only be gained by understanding the relationships between processing variables and the microstructure and the relationships between microstructure and the final properties. The present study attempts to contribute to this area through experimental and theoretical analysis. It involves a detailed experimental study of the matrix phase properties, such as crystallinity, morphology and molecular orientation distribution, and the fiber phase microstructure, including concentration and length and orientation distributions. Experimental techniques used include optical and electron microscopy, differential scanning calorimetry, Fourier transform infrared spectroscopy, thermo-gravimetric analysis, etc. A theoretical analysis of the development of fiber orientation during the injection molding cycle has been carried out, employing a first order mathematical model. Fiber orientation predictions are compared with the experimental observations.

CHAPTER 2

2 SCOPE AND PROJECT OBJECTIVES

This project is part of a comprehensive program at McGill University for studying processing-microstructure-property relationships in injection molded thermoplastics. Earlier work [3-5] in this program have dealt with the microstructure of injection molded pure polymers. The present work represents the first effort to extend the analysis of microstructure to injection molded short glass fiber reinforced composites.

The general objective of this research has been to characterize the microstructure of injection molded composites and to evaluate the relationships between microstructure distributions in injection molded samples and processing conditions.

2.1 Specific Project Objectives

The specific aims and objectives of this research project are summarized as follows:

(1) to select a suitable composite material (short glass fiber reinforced polypropylene) to be used in the experimental study. A full characterization of the material is then to be carried out;

(2) to produce injection molded plaques of short glass

fiber reinforced polypropylene at various molding conditions, and to record processing variables, such as pressure, temperature and velocity profiles during each cycle, in order to evaluate the processability of the material and to obtain some insight into the thermo-mechanical history experienced by the material;

(3) to develop methods for characterization of the microstructure of the injection molded composite plaques. This would involve measuring such properties as fiber orientation, crystallinity, crystalline and amorphous orientation distributions, etc;

(4) to characterize the microstructure of the injection molded plaques. Measurements would be carried out to quantify variations most importantly in the z-direction (ie. in the thickness direction from skin to core.), and in the x-direction (ie. from gate to the end of the mold in the direction of flow);

(5) to employ first order models to predict fiber orientation distribution;

(6) to compare the predictions of fiber orientation distribution with experimental results.

This study involved extensive experimental measurements, with the aim of integrating all the microstructural characterization results. The availability of complete microstructural characteristics and processing variables history for a given set of injection molded samples will be of immense value to future injection molding modelling studies. The experimental work, being on a micro scale, was painstaking, laborious and time-consuming, and it involved taking measurements on a large number of samples. The results presented are explained in terms of the processes occurring during the injection molding of the material. It should be pointed out that these explanation are only of first order, originating from experimental observations, and elementary models. Accurate quantitative explanations can only be obtained from detailed mathematical models.

The thesis is organized into seven chapters. Chapter 1 is a brief introduction to the scope of this study. The objectives are presented in Chapter 2. Chapter 3 is a short review of theoretical and experimental literature relating to the microstructure of molded parts, especially SFRTP. The materials and experimental techniques utilized in this study are presented in Chapter 4. Chapter 5 summarizes the experimental results on microstructural analysis of the molded samples. The analytical treatment of frozen layer development and fiber orientation distribution are presented in Chapter 6. Important conclusions of the study are given in Chapter 7.

CHAPTER 3

3 BACKGROUND

In this chapter, an introduction to the injection molding process and a discussion and review of experimental and theoretical studies relating to the microstructure of injection molded articles, especially SFRTP, are presented. The discussion on microstructural aspects is divided into three main sections: morphology, matrix phase microstructure and fiber phase microstructure.

3.1 Injection Molding

Polymer processing involves the transformation of the raw polymer resin, usually in the form of beads, powder, granules or liquid, into a useful product with specified geometry and physical properties. Among the many polymer processing techniques for the production of solid articles, injection molding is the most widely used. It offers the economy of operation with fast cycles and high part quality in appearance and performance. The majority of injection molding machines utilizes a reciprocating screw plunger.

In the injection molding of thermoplastics, the solid polymer or composite is heated until it melts. The melt is then injected under pressure into a hollow mold cavity, which is cooled to allow the material to solidify into a shape that conforms with the shape and dimensions of the cavity.

The injection molding machine consists of two basic components: the injection unit and the clamping unit, as shown in Figure 3.1. The injection unit serves to melt the polymeric material and inject it under pressure into the mold, which is held by the clamping unit. The clamping unit serves to keep the mold closed during injection when the melt is under pressure. It opens the mold and ejects the molded part when it has solidified. The polymer resin or the composite in the form of pellets are placed into a hopper and fed by gravity to the barrel which contains a rotating screw. The material is conveyed forward in the barrel where the combination of external heaters and mechanical heating by the screw rotation causes the polymer to melt. The melt accumulates in front of the screw behind the nozzle and the screw starts to retract to the back position of its travel. After sufficient melt is produced for the next part, screw rotation stops. At this point, the cycle of the previous part ends and the mold is opened for part ejection. Subsequently, the mold closes and the whole barrel assembly moves forward until the nozzle touches the injection port of the mold. At this point, the screw moves forward like a ram and fills the mold with melt.

After the initial filling stage, an additional amount of material is packed into the mold to compensate for shrinkage due to cooling and to enhance the surface finish of the

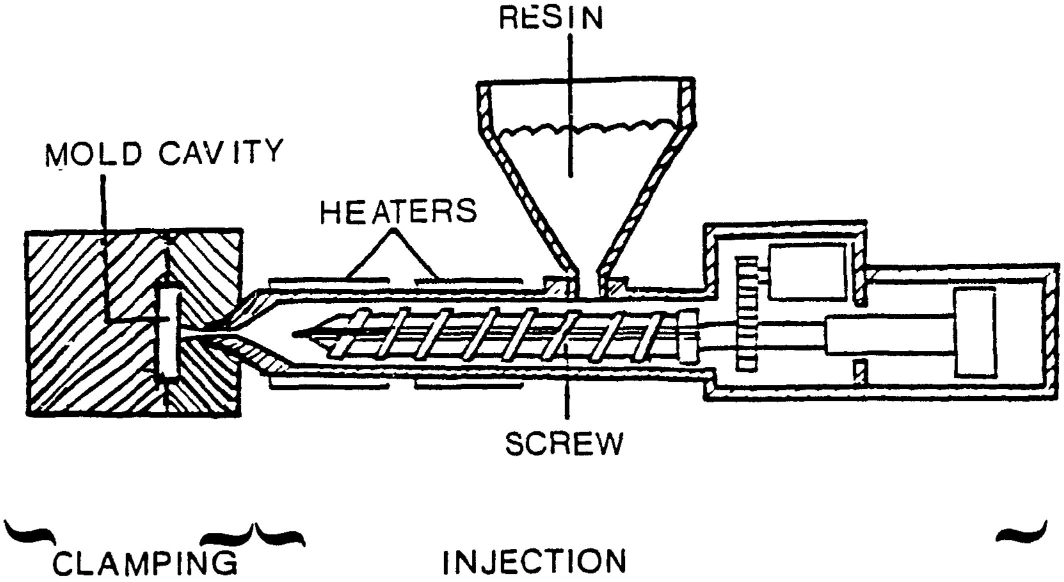

Figure 3.1 Schematic diagram of injection and clamping units of an injection molding machine.

product. Packing causes the pressure in the mold cavity to rise drastically. After the packing stage, the injected melt is held under pressure during what is called the holding stage. A no-return valve at the end of the screw prevents the material from flowing back into the barrel. During the hold stage, additional melt is also injected, offsetting contractions due to cooling and solidification. As soon as the melt enters the cold mold, it starts to cool and solidifies when it reaches the solidification temperature. The gate which is the narrow entrance to the mold, freezes, thus isolating the mold from the injection unit. After gate freezing, screw rotation begins to accumulate melt in front of the screw for the next cycle. When the part becomes rigid, the mold is opened and ejected with the aid of ejection pins.

The injection molding process is an unsteady but continuous cyclic process. Each cycle can be divided into three stages:

(1) filling;
(2) packing and holding;
(3) cooling.

The three stages are apparent in the cavity pressure profile as shown in Figure 3.2. The cavity pressure rises steadily as the material flows into the mold. When the mold is filled, the cavity pressure increases sharply to a plateau, which is the holding pressure. As the melt slowly cools, the part solidifies, with a resulting steady decrease in cavity

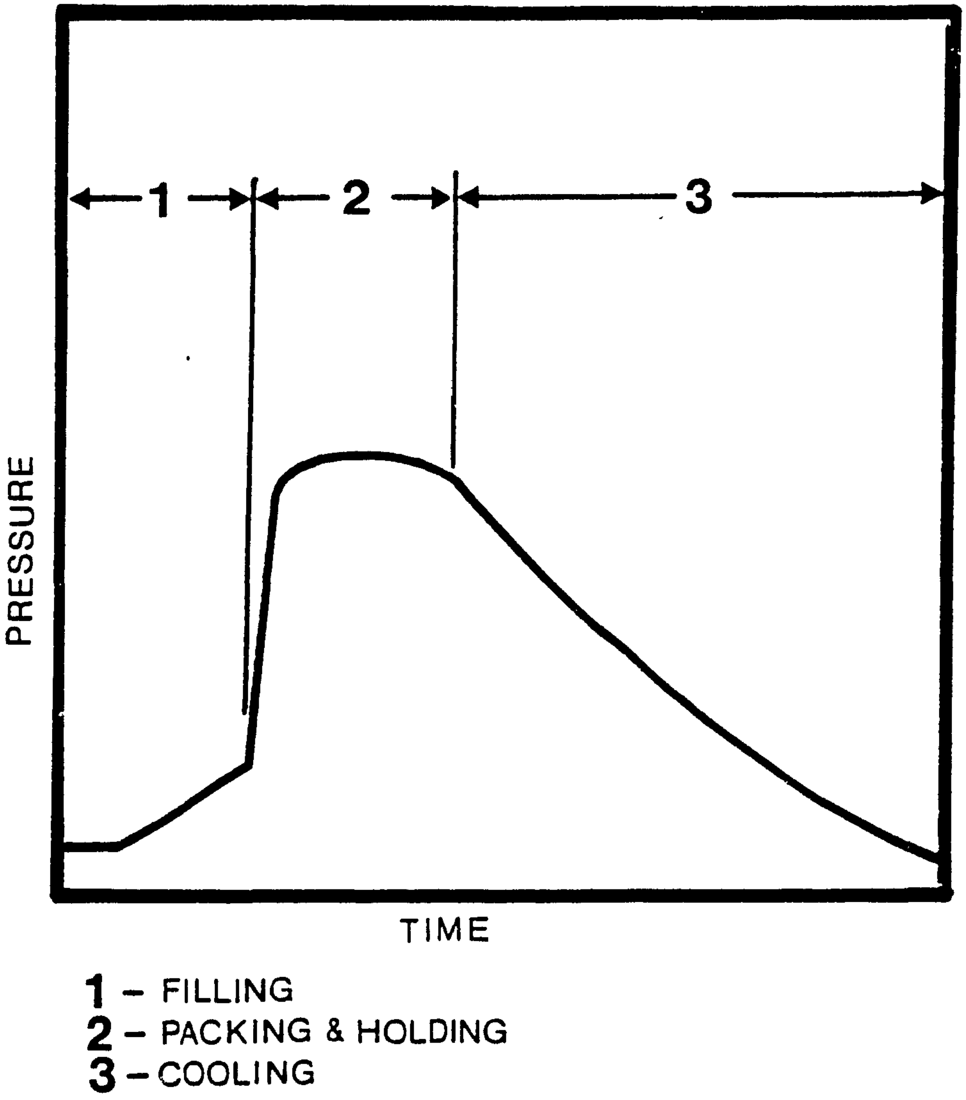

Figure 3.2 Schematic diagram of cavity pressure profile illustrating the stages in the injection molding cycle.

pressure.

The filling stage is visualized as the unsteady state flow of a hot non-Newtonian melt into an empty cavity, which is held at a temperature below the solidification point of the polymer. The actual filling is quite complex. It involves spreading radial flow where the melt emerges from the gate and spreads to the outer boundaries of the cavity. In the front region of the flow, the melt at the centre of the thickness direction, which moves with high velocity, spills out or fountains out to the mold wall and to the surface of the molded article at that point. This is illustrated in Figure 3.3a. Fountain flow was the term used by Rose [6] to describe this type of phenomenon. The role of fountain flow in influencing the microstructure of molded parts has been recognized in many studies [7-9]. The fountain flow phenomenon is illustrated in Figure 3.3b [7].

When the gate faces a mold wall that is far away, and when the filling rate is very high, the phenomenon of jetting is observed. The melt emerges from the gate in the form of a jet that advances until it hits the opposite mold face. Two modes of jetting, melt fractured and smooth melt jets have been observed. In the melt fractured mode, jetting continues after the jet tip has touched the opposite mold wall. The jet folds over many times starting from the opposite mold wall and continuing towards the gate. When the cavity is almost full, regular forward filling begins. In the smooth jet filling

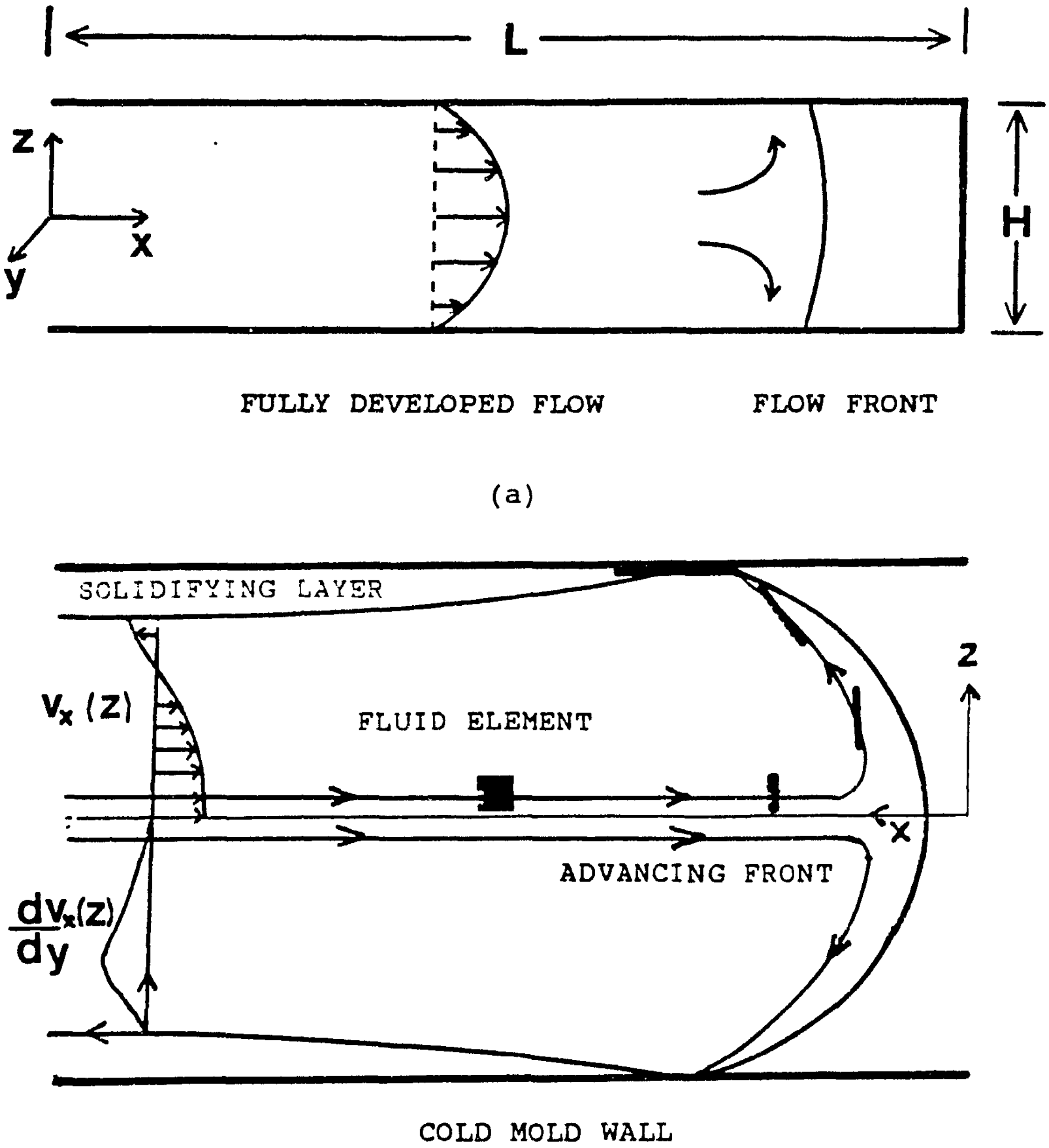

BLACK RECTANGLES DENOTE THE STRETCHING AND ORIENTATION OF A FLUID PARTICLE APPROACHING THE FRONT IN THE CENTRAL REGION OF THE FRONT. THE CURVED SHAPE OF THE FRONT CAUSES FLUID PARTICLES INITIALLY ORIENTED IN THE Z-DIRECTION TO END UP ON THE WALL, ORIENTED IN THE X-DIRECTION. THE VELOCITY PROFILE UPSTREAM THE FRONT IS IN THE X-DIRECTION. THE VELOCITY PROFILE UPSTREAM THE FRONT IS VIEWED FROM A COORDINATE SYSTEM LOCATED ON THE FRONT.

(b)

Figure 3.3 Fountain flow in injection mold filling [7].

mode, jetting stops after impingement of the jet on the opposite mold wall and regular filling begins immediately. Jetting occurs whenever the dimensions of the fluid stream are smaller than the dimensions of the plane perpendicular to the flow [10]. It is thus related to the gate size, mold dimensions and the degree of extrudate swelling of the melt. Reinforced polymers exhibit low degrees of extrudate swell and thus could jet at lower fill rates.

In the packing stage, the cavity pressure increases to a set pressure which is then maintained during the holding stage. This is achieved by compressing more material into the mold to compensate for shrinkage during cooling. In the cooling stage, a continuous decrease of cavity pressure is observed. No flow takes place in this stage. Thermal parameters such as melt temperature, mold temperature and cooling rate play an important role in determining the temperature profile in the molded part during the molding cycle. The temperature distribution pattern governs the development of such microstructural properties as crystallinity, which in turn affect the final properties of the molded article.

3.2 Morphology

A review of studies regarding the microstructure of injection molded semi-crystalline polymers is given by Katti and Schultz [11]. Clark, Boehme and Kantz [12,13-18] observed three morphological zones in the thickness direction, in their studies of injection molded polypropylene. The three layers can be identified as follows:

(i) a non-spherulitic skin possessing a high degree of chain orientation parallel to the injection direction; this layer displays high birefringence;

(ii) a spherulitic, row nucleated intermediate layer; this layer contains small spherulites along thin negatively birefringent rows;

(iii) a spherulitic, randomly nucleated core. The core contains large but randomly sized spherulites.

The following interpretations of this morphology are given by the authors. The skin is the portion that is crystallized during the filling stage. Under the high stress of quasi-extensional flow, a large number of fibrillar nuclei are formed, and lamellar overgrowths have a planar habit. The shear zone is due to the portion that is crystallized during the packing stage. With a few fibrils present, the lateral extent of the lamella may be greater under high stress. The ribbons can branch and fill space with some loss of orientation as in the case of spherulitic growth. These structures can appear as oblate spherulites with their short axes parallel to the injection direction [19].

Menges, et al. [20] and Fitchum and Mencik [21,22] found a four layer, skin and core morphology. Zone I has a fine grain structure; Zone IIa has fine spherulites; Zone IIb texture exhibits preferred orientation, while Zone IIc contains fibrous trans-crystalline material. Zone III, which is the core, has random orientation with two types of spherulites. Zone I through IIb can be described in terms of a spherulitic texture, although the spherulites in Zone II are elongated in the flow direction. The material nearest to the wall is thought to be crystallized rapidly under a rheological condition approaching perfect lubrication under the circumstances of little or no extensional or shear strain. In this case, a large undercooling would result in a high spherulitic nucleation rate and a high nucleation density. Because of this build-up of a solid layer, the melt inside is forced into a larger degree of shearing flow over the solid to which it is molecularly connected. Thus, the inner melt will reach crystallization conditions under higher degrees of shear and in turn molecular orientation. In this case, fibrillar nucleation and growth should be expected.

Kamal and Tan [23] carried out similar studies on polyethylene and found a four layer morphology, as shown in Figure 3.4. Zone I has a non-spherulitic structure. It exhibits tiny slots of vertical bright lines arranged in rows

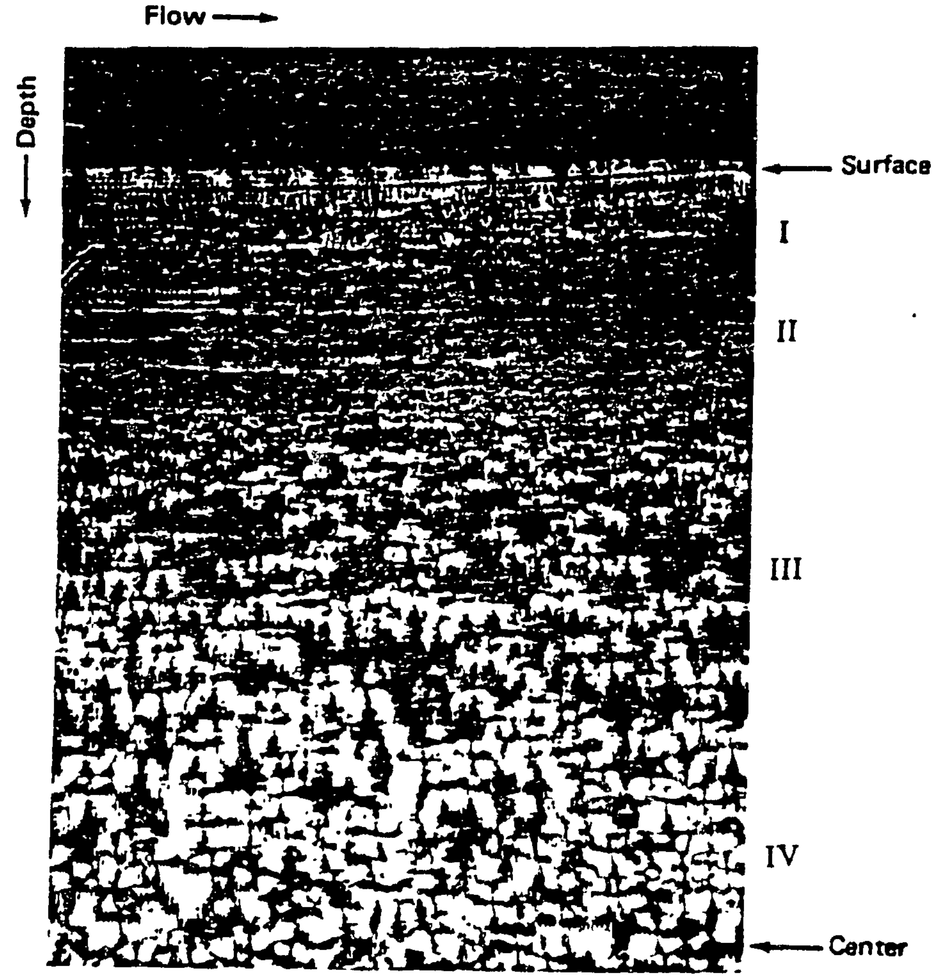

Figure 3.4 Morphological layers in injection molded samples of High Density Polyethylene as seen by cross-polarized light microscopy [23].

and running parallel to the surface of the molding. This row structure can be interpreted to be stacks of lamellae with the chain axis oriented in the flow direction and growing in the depth direction. Zone II contains very fine asymmetric spherulites of almost uniform size which are formed under large thermal gradients. The size of the spherulites is limited by the fast nucleation rates. Zone III has asymmetric oblate spherulites with their axis of symmetry in the depth direction where a thermal gradient exists. These spherulites have a greater growth potential. Zone IV contains randomly nucleated spherulites that grow in all directions until impingement halts their growth. The authors suggested that Zones I and II are formed during the filling stage, while the other two Zones are formed during the packing, holding and cooling stages.

3.2.1 Effect of Process Variables on Morphology

The increase in mold wall temperature results in a decrease of the thickness of the skin and shear zone, due to the smaller fraction of polymer solidified during the filling and packing stages [19,23]. A lower mold wall temperature produces a greater depth of oriented structures, because more melt is frozen during the filling and packing stages.

An increase in melt temperature reduces the portion of the polymer crystallized during the first two stages but increases the content of spherulitic material [13,21,23,24]. These results suggest that molding at or close to the melting point would lead to the incorporation of a highly oriented morphology in the sample. Screw speed or the fiber concentration did not show any effects on the matrix crystallinity [25].

Injection pressure could affect the microstructure, depending on the sensitivity of the solidification temperature to pressure. Clark [14] found that, as the injection pressure increased, the surface layer of preferred orientation became thicker. Kantz, et al. [13] found that injection pressure had no effect on the area of the skin, but it had some effect on decreasing the area fraction of the shear zone. Bowman, et al. [24] reported that an increase in the injection pressure resulted in a small change in the volume of oriented material.

3.2.2 Microstructure-Property-Processing Relationships

In studies on injection molded unreinforced thermoplastics, the thermo-mechanical history experienced by the material during injection molding significantly influences the microstructure, and in turn, the mechanical properties of the polymer. The microstructure is not uniform throughout the product but varies at each position, depending on the thermal and deformation history of the material at that point [11,26].

Fleissner [27] investigated mechanical properties of injection molded polyethylene. He found a high yield stress and a low ultimate strain in the surface layers and higher ductility and lower yield stress in the core. This behaviour is typical of an oriented material at the surface and a random spherulitic core. Kantz, et al. [13] and Clark [19] showed that the tensile yield strength along the flow axis increased with increased combined area fraction of shear and skin zones.

Shrinkage distribution in injection molded amorphous polystyrene has been shown to be anisotropic as well as inhomogeneous [28]. Shrinkage is highest in the highly oriented surface layers and lowest in the interior. Small shrinkage is observed normal to the injection direction, compared to the large shrinkage observed in the flow direction, upon heat treatment above the glass transition temperature or near the melting point.

The situation is more complex in composites, since the microstructure involves the properties of both the matrix and fiber phases as shown in Figure 3.5. Few studies have been reported regarding matrix microstructure in composites. Patel and Bogue [29] studied the effect of molecular orientation on the properties of fiber filled polystyrene. They found that orientation resulted in increasing ductility which allowed for stress transfer between fibers. This resulted in improvements in properties.

A number of studies have been reported regarding the relationships between molding conditions and mechanical

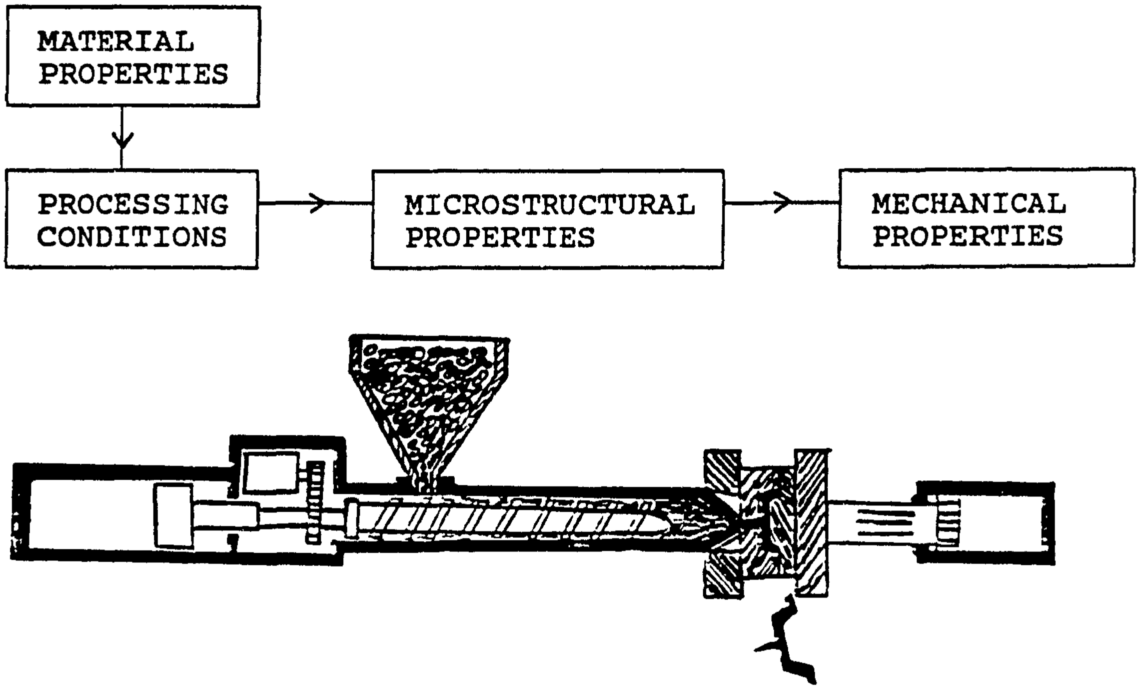

RESIN PROPERTIES	PROCESSING CONDITIONS	MICROSTRUCTURE	PRODUCT PROPERTIES
Thermodynamic	Injection pressure	Matrix properties	Tensile properties
- PVT	Melt temperature	- Morphology	Impact "
- T_m, T_g	Mold temperature	- Crystallinity	Dynamic "
- C_p, ΔH	Packing pressure	- Orientation	Shrinkage
Transport	Holding time	- Frozen stresses	Appearance
- Rheology	Screw speed	Fiber properties	
- Thermal		- Concentration	- - -
Kinetics	- - -	- Length	
- Crystallization		- Orientation	
		Interphase properties	
- - -			
		- - -	

Figure 3.5 A Schematic of Processing-Microstructure-Properties relationships.

properties and between microstructure and mechanical properties [13,30-34]. Some of the typical findings are reported below. Flexural strength and tensile strength increase with frozen orientation which increases with packing time. Tensile and impact strengths rise with increasing birefringence in the flow direction, but decrease in the transverse direction. The birefringence is a measure of the flow direction orientation. The increasing flow direction orientation results in less material being oriented in other directions. It has been suggested that the modulus is dependent on variables other than orientation [31]. Tensile and impact properties vary in both the flow and transverse directions, depending on molding conditions [13,32-34]. Yield strength increases as the fraction of skin and intermediate layers increases. The tensile strength decreases with increasing melt temperature but increases with increasing mold temperature [34].

3.3 Matrix Phase Microstructure

The matrix phase can be either a semi-crystalline or an amorphous thermoplastic. The semi-crystalline matrix response to external forces reflects the combined behaviour of the crystalline and amorphous phases. The properties of one phase may dominate the response of the material in some environments, while the properties of the other phase may control in others [35].

The matrix phase may be characterized by defining the following microstructural parameters [36-38]:

(i) degree of crystallization;

(ii) morphology of the crystalline phase, i.e. size and shape of the crystallites, and their participation in the superstructure;

(iii) orientation of polymer chains in the crystalline phase;

(iv) orientation of polymer chains in the amorphous phase;

(v) connectivity of the crystalline regions by the amorphous chains.

3.3.1 Crystallization

Matrix crystallization is controlled by deformation and thermal history [39-51]. Deformation could enhance crystallization by virtue of orientation of the polymer chains in the stress direction. The modulus of the material is greatest in the chain direction. The cooling rate and the degree of undercooling ($T-T_m$), influence crystal nucleation and growth. High cooling rates generally give rise to low crystallinity with a large number of small spherulites. Low cooling rates produce high crystallinity with a smaller number of larger spherulites.

Commercial polypropylene consists of an isotactic phase contaminated with a small amount of an atactic phase. The isotactic phase represents the crystallizable portion, while the atactic phase does not crystallize because of its irregular molecular conformation. Isotactic polypropylene is polymorphic because it can exist in at least three crystalline forms, with either a monoclinic or hexagonal unit cell [42]. The α form is the most stable form. It involves a monoclinic unit cell with a three fold helix conformation. The cell parameters are a = 6.65, b = 20.96, c = 6.50, and β = 99° 26' [43]. It has a theoretical density of 0.936 g/cm. This is the form most commonly obtained by primary nucleation. It is also found in single crystals grown from solution. The β form exists in single spherulites, mixed with α form spherulites. It occurs at levels of only a few percent, except under special conditions, e.g. when certain heterogenous nuclei are present, upon crystallization in a temperature gradient [44,45], or crystallization in a shear field [46]. The β form has a higher growth velocity than the α form [47]. The γ form develops from low molecular weight fractions by slow cooling, and from normal commercial polypropylene by crystallizing under pressure [48].

During crystallization from the melt, polypropylene forms spherulites. Spherulites are formed as assemblages of crystals starting usually from heterogenous nuclei and spreading out in a spherical manner. They consist of radial fibrils of lamellae, which are of the same order of thickness as single crystals. The polymer chains are folded regularly and are oriented perpendicular to the fibrils and tangential to the spherulite [49,50].

Melt crystallized polypropylene assumes a monoclinic as well as a hexagonal crystalline form, with amorphous regions in between the spherulites. The crystallographic a-axis lies along the spherulite radius.

3.3.2 Molecular Orientation

In the crystalline state, polymer chains are aligned parallel to each other. The bonds along the chain are covalent, while Van der Waals or hydrogen bonds, which are much weaker, govern interactions among different chains. The moduli along the chain axis are, therefore, generally greater than those in the transverse direction. In describing the orientation of polymer chains in the material, it is necessary to specify the amount of orientation associated with chains having different types of entanglement junctions [52].

Molecular orientation is greatly affected by flow history in the injection molding process [7,23,26,28]. Both elongational and shear flow fields are present and have pronounced effects on local orientation. For a cavity with a rectangular cross-section, the flow front advances in the cavity as shown in Figure 3.6 [8,9,12,53-58]. In stage I, the melt experiences biaxial orientation. The flow pattern is similar to that in a centre-gated circular cavity. In stage II, both elongation and transverse orientation are present, with transverse orientation occurring at the edges and longitudinal orientation dominating in the centre regions. The flow in stage III is quite complex because of back-mixing.

Menges and Wubken [28] suggested that molecular orientation at the surface originated from the fountain flow effect at the advancing melt front during the filling process. The orientation in the rest of the part was due to shear flow after the front had passed. Tadmor [7] used flow and heat transfer analyses in the mold, combined with a macromolecular model, to obtain a semi-quantitative orientation model. The results indicated that the magnitude of residual flow orientation was controlled by the relaxation time, which would be dependent on such factors as temperature and the rate of elongation.

In injection molding, the polymer melt flows into a mold

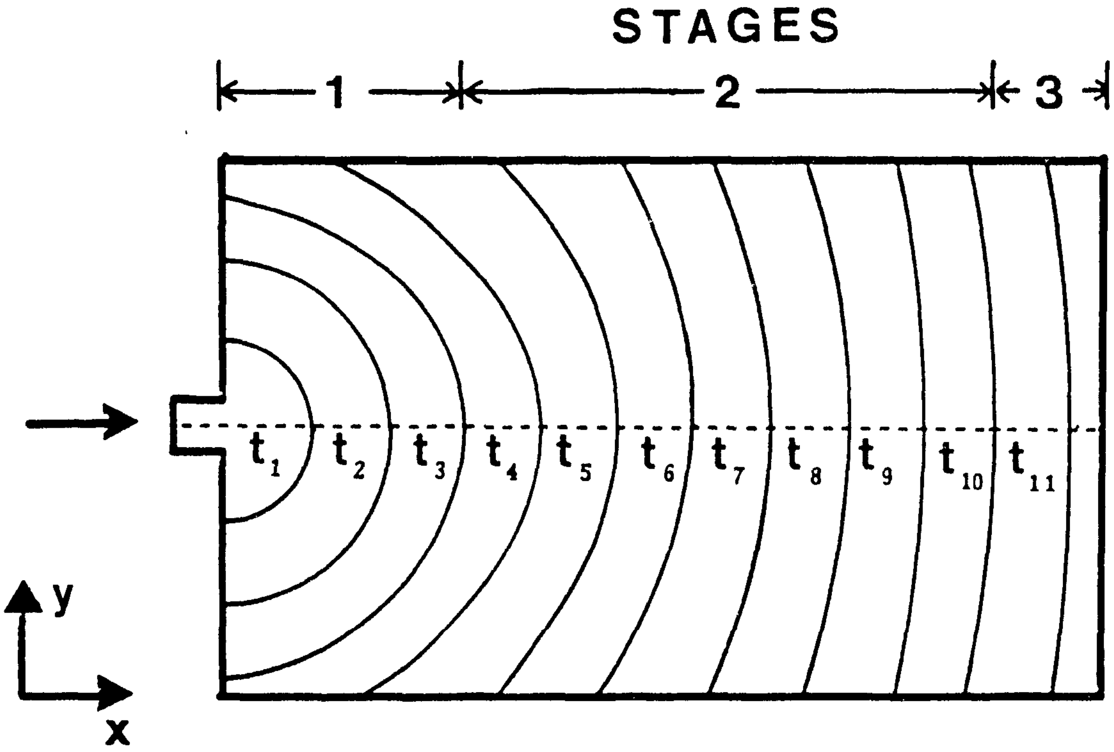

STAGE I	-	SEMICIRCULAR FLOW FRONT
STAGE II	-	FLOW FRONT IS SHAPED AS AN ARC OF A CIRCLE. THE ANGLE OF THE ARC DECREASES AS TIME INCREASES
STAGE III	-	THE FLOW FRONT IS COMPLEX AS THE CORNERS ARE FILLED

Figure 3.6 Progression of flow front profile in a rectangular cavity as a function of fill time $t_1 < t < t_{11}$

held at a constant temperature below the solidification temperature of the polymer. The polymer is subjected to both elongation and shear flow fields, and these have pronounced effects on local orientation, leading to the build up of flow induced shear and normal stresses. Such molecular orientation becomes frozen in when the material is cooled rapidly. The stresses do not have time to relax, thus producing frozen in stresses. Residual stresses are due to flow stresses and thermal stresses. Frozen flow and thermal stresses have a significant influence on the optical and mechanical properties of the molded parts, e.g. birefringence and tensile modulus [31].

3.3.2.1 Residual Stresses

Residual stresses are affected by both thermal and flow effects and their influences are difficult to separate [59,60]. The first arises from the deformation process. When a material is cooled, the orientation is frozen in along with the internal stresses which led to the deformation. The second involves the cooling process. When a material is cooled rapidly to below its T_g, there is non-equilibrium shrinkage, because it is cooled from its surface inward.

The cooling process is inhomogeneous and results in the development of thermal stresses and orientation due to non-equilibrium density changes and temperature dependence of the elastic properties of the material [59]. Inhomogeneous cooling can be considered to consist of two steps. Initially the temperature of the specimen is uniform and greater than the solidification temperature, T_s. At a given time, the outer layer solidifies and is at a temperature below T_s. In this first stage, no appreciable stresses are built up. The outside layer contracts, but the molten core does not counteract, since the modulus is about one thousand times smaller. In the second stage, the core will contract and the outer shell, being rigid, will counteract the contraction. Consequently, a compression stress is created in the shell, and a tensile stress is created in the core. If the elastic properties were not a function of temperature, then a zero stress profile would be the result.

The residual stresses have been shown to be influenced by processing conditions such as [59-61]:

(i) cooling rate distribution;
(ii) injection rate;
(iii) holding pressure;
(iv) holding time or time at which the gate freezes.

The total residual stresses, resulting from the combined effects of flow and thermal phenomena, can be measured using a layer removal technique developed by Treuting and Read [62]. Thin layers of a rectangular sample are removed from one surface of the sample. The sample will then warp towards that surface in order to re-establish a stress equilibrium. The sample is clamped on ends and stuck on the machine table top by double sided adhesive tape. A specified layer is removed by high speed milling. The machined surface can be checked for mechanical or heat damage by use of a scanning electron microscope. Usually, the interior of the material is in tension while the surface is in compression. The curvature of the sample may be measured in many ways, one of which involves an elaborate system of lasers and mirrors [63]. Residual stresses can be calculated from the resultant curvature, using the general biaxial stress relationship:

$$\sigma_x(y1) = \frac{-E}{\sigma(1-\upsilon^2)} \left\{ (b+y1)^2 \left[\frac{d\rho_x(y1)}{dy1} + \frac{\upsilon d\rho_z(y1)}{dy1} \right] + 4(b+y1) + 4(b+y1) \left[\rho_x(y1) + \upsilon\rho_z(y1) - 2\int_{y1}^{b} \{\rho_x(y) + \upsilon\rho_z(y)\}dy \right] \right\} \quad (3.1)$$

where:

$\sigma_x(y1)$ = longitudinal stress

2b = thickness of sample

y=y1 = new layer formed after each removal

E = elastic modulus

υ = Poisson ratio

ρ_x, ρ_z = measured curvature in the x and z directions.

An expression for the transverse stress can be obtained by exchanging the subscripts x and z. In injection molded samples, the total stress components in the x and z directions will not be zero. Uniaxial formulation for internal stress distribution is:

$$\sigma_i(z1) = \frac{-E}{(1-\upsilon^2)}\left\{(z0+z1)^2\frac{d\rho(z1)}{dz1} + 4(z0+z1)\rho(z1) - 2\int_{z1}^{z0}\rho(z1)dz1\right\} \quad (3.2)$$

where:

σ_i = residual stress at position z1 from the centre of sample

z0-z1 = half of sample thickness

ρ(x1) = curvature when (z0-z1) has been removed

Equations 3.1 and 3.2 are good for uniaxial residual stress. They also assume that the tensile modulus is uniform throughout the sample.

Coxon and White [63] used the layer removal technique to study injection molded polypropylene. They showed that stresses near the surface were compressive and those in the interior were tensile in contradiction to Kubat and Rigdahl [64]. White [65] also computed the residual stress for polymer moldings with depth varying Young's modulus. The equations obtained were:

$$\sigma'_{ix}(z) = \left\{ \frac{E_x(z)\{\gamma_x + (z+u/2)/R_x\}}{(1-\nu_{xy}\nu_{yx})} + \sigma_{ix}(z) + \frac{\nu_{yx}E_x(z)\{\gamma_y + (z+u/2)/R_y\}}{(1-\nu_{xy}\nu_{yx})} \right\} \tag{3.3}$$

$$\sigma'_{iy}(z) = \left\{ \frac{E_y(z)\{\gamma_y + (z+u/2)/R_y\}}{(1-\nu_{xy}\nu_{yx})} + \sigma_{iy}(z) + \frac{\nu_{zy}E_y(z)\{\gamma_x + (z+u/2)/R_x\}}{(1-\nu_{xy}\nu_{yx})} \right\} \tag{3.4}$$

where:

R = radius of curvature

$\sigma_{iy}(z)$ = residual stresses prior to layer removal

$\sigma_{ix}(z)$ = residual stresses prior to layer removal

u = thickness of removed layer

$\sigma'_{iy}(z)$ = residual stresses after layer removal

$\sigma'_{ix}(z)$ = residual stresses after layer removal

γ = strain

A relationship exists between the effective stress field at the instant of solidification and the frozen in birefringence. The concept is based on the hypothesis that the stress ellipsoid in the solid polymer at the time of solidification is coaxial with the refractive index ellipsoid, and that the principal birefringences are proportional to the principal stresses. This relationship is known as the Stress-Optical law [10].

$$\Delta n_{ij} = C\sigma_{ij} \tag{3.5}$$

C = the Stress-Optical coefficient

σ = the Stress Tensor

Δn_{ij} = the birefringence

This law provides a simple relationship for polymeric materials above the glass transition temperature. Equation 3.5 can be used in calculating the frozen-in stresses due to flow, from birefringence data. However, it should be pointed out that birefringence measurements in molded parts are due to contributions from both thermal and flow induced orientations [59]. White and Dietz [66] and Isayev and Hieber [67] have made attempts to theoretically predict birefringence distribution in molded parts in terms of flow induced orientation.

3.3.2.2 Thermal Stresses

In order to obtain a better understanding of thermal stresses, fast cooling processes have been studied by many researchers using both layer removal and birefringence techniques [59,63,68]. Quenching involves heating a polymer sample to a temperature above its glass transition temperature followed by immersion in a constant temperature bath to achieve rapid cooling.

Several authors obtained results showing negative birefringence near the core and positive birefringence near the surface [69-71]. The position of zero birefringence was seen to shift towards the surface as the initial temperature increased, causing unequal areas of positive and negative birefringence [69]. So and Broutman [69] used the layer removal technique in their studies. They found the stress profile to be basically parabolic. In some cases, the maximum tensile stress was not located at the centre of the specimen. The mid-plane tensile stresses seem to be only slightly affected by the thermal history of quenching.

3.3.2.3 Relaxation of Stresses

Isayev [70,71] studied the effect of time on frozen in birefringence. Relaxation takes place in the core region where positive birefringence occurs. Over a period of 207 days, birefringence decreased by 30 %. In the surface region, where negative birefringence occurs, no relaxation of birefringence was observed. The shape of the birefringence profiles remained essentially parabolic with little or no shift in the zero stress position.

3.3.2.4 Frozen Stresses in Injection Molding

In the injection molding process, thermal effects are compounded with flow induced effects. Thus measurements of birefringence and residual stresses reflect the combined effect. In injection molded polystyrene samples, the gap-wise birefringence passes through a maximum near the surface of the sample. The birefringence distribution in the thickness direction for an injection molded polystyrene part is illustrated in Figure 3.7 [72]. The position of this maximum does not change with the downstream distance unlike the value of the maximum, which decreases downstream. The highest value is observed at the entrance [59]. The average birefringence decays rapidly in the entrance region while a more gradual decrease occurs in the intermediate zone. Increase in the melt temperature decreases the average value of the birefringence [61]. The flow effects dominate in the entrance region whereas the thermal effects dominate at the far end of the cavity.

In a comparison of gap-wise birefringence and thermal birefringence due to quenching, the differences are nearly one order of magnitude near the surface but are comparable in the core [61]. This is evidence that the non-zero birefringence in the centre of an injection molded sample is most likely due to the effects of cooling. The difference in the value of birefringence throughout the sample suggests that the bulk of frozen-in stresses in injection molded samples are

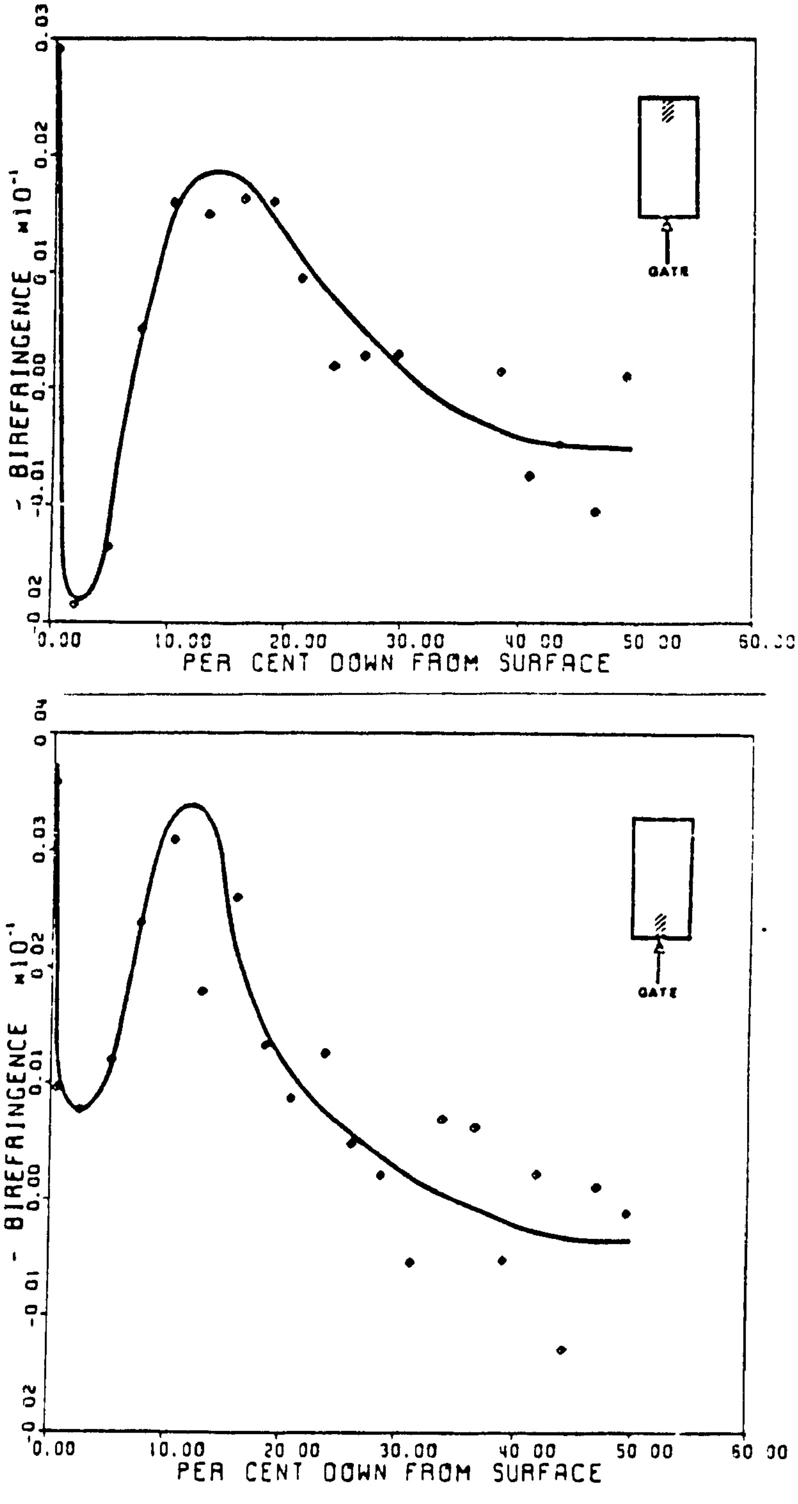

Figure 3.7 Birefringence distribution in injection molded sample [72].

basically due to flow rather than thermal effects [59].

Thermal stresses are known to be positive in the core and negative near the surface. Flow stresses are positive throughout the sample. Since both effects are present and of comparable magnitude, the residual stresses can be either positive or negative.

3.3.2.5 Effect of Processing Parameters

Isayev, et al. [59,67], employing layer removal analysis, found the effect of melt temperature on residual stresses in injection molded polystyrene to be quite substantial. The residual stress for the higher temperature shows maximum compressive stress at the surface while the lower temperature yields tensile stresses. This is explained in that there is competition between the compressive thermal stresses and the tensile flow stresses. At low temperatures, the tensile flow stresses dominate, giving rise to a resultant tensile stress at the surface. Thicker cavities give rise to larger compressive stresses near the entrance, probably due to the decreased effect of tensile flow stresses. Mold temperature had little effect on residual stresses; only above 60 °C, a decrease in residual stresses was noticed.

The effect of injection speeds, from 3 to 80 g/s, is quite complex and difficult to analyze. At high injection rates, the residual stress profile is similar to a typical quenching profile. At low speeds, a total reversal of the quenching profile is noticed, with compressive stresses at the centre and tensile stresses at the surface. At intermediate values, a maximum appears and shifts towards the centre of the profile as speed decreases. As holding pressure in increased, the residual stresses at the surface increase to a maximum. Further increase in holding pressure leads to a decrease in residual stresses until the stresses change sign and became tensile.

Residual stresses are highly dependent on process conditions. In order for a mathematical model to describe the residual stress distribution, the complete history of the melt must be known. This includes temperature,pressure and stress distributions in both time and space.

3.3.2.6 Effect on Mechanical Properties

Various authors have carried out studies to determine the effect of residual stresses on mechanical properties [68,69,73]. So and Broutman [69] showed that residual stresses increased the critical thickness in impact studies. The critical thickness is the thickness at which the transition from ductile to brittle failure occurs.

Broutman and Krishnakumar [73] showed that higher quenching temperatures led to lower compressive stresses at the surface, resulting in a decrease in impact strength. Fast cooling rates increased the impact strength.

Seigmann, et al. [68] have found that the tensile modulus varies from surface to core. Once the surface is removed, the sample behaves in a more ductile manner. The fracture initiation takes place at the position of maximum residual stress. The level of residual stress in the polymer sample governs the location of fracture initiation. Seigmann, et al. suggested that density and residual stresses affect mechanical behaviour, with residual stresses being responsible for the ultimate properties.

3.4 Fiber Phase Microstructure

Short fiber composites (SFRTP) provide improved properties relative to those of unfilled materials. In order to attribute the improvement of mechanical properties to the fiber phase in quantitative terms, the state of the fiber phase must be well defined. The following parameters must be known:

(i) fiber concentration distribution;
(ii) fiber length distribution;
(iii) fiber orientation distribution.

3.4.1 Fiber Concentration

Fiber concentration is usually specified as the mass fraction of the fibers in the composite. However, for the theoretical prediction of composite properties, it is more appropriate to represent fiber content by volume fraction V_f [27]. The volume fraction V_f can be easily obtained from the mass fraction of fibers M_f, by the equation:

$$V_f = \left\{ \frac{(M_f/\rho_f)}{(M_f/\rho_f + M_m/\rho_m)} \right\} \tag{3.6}$$

where ρ_f and ρ_m are the densities of the fiber and matrix, respectively, and M_m is the mass fraction of the matrix.

The addition of fibers to a polymer results in increased stiffness and strength. Increasing the fiber content increases the strength and stiffness, but only up to an optimum fiber volume fraction. A very high fiber content can result in insufficient continuity in the matrix material, resulting in poor bonding and poor stress transfer to the fibers. This results in a weaker material.

3.4.1.1 Fiber Migration

Migration effects have been reported where glass fibers migrate towards the flow axis, away from shear regions, leaving fiber-free regions where most of the shear takes place [27,74]. Migration of fibers to the flow front has also been reported [19,20]

Emerman [75] studied the filler redistribution in the processing of an initially homogeneous mixture. The final part may be inhomogeneous in the length or width direction as well as in the thickness direction. Particles migrate away from the walls during filling into a region of higher fluid velocity. The deficit of particles near the wall is accompanied by an excess of particles far from the gate.

Wu [76] studied fiber orientation and distribution during extrusion of fiber filled composites. There was a migration of fibers inward towards the axis and outward to the surface from position $r/R = 0.63$ (r is the radial position in the flow tube, and, R is the radius). Thus a depleted layer formed at position 0.63 r/R. After another transition point at 2000 s^{-1}, at higher wall shear rates (3470 - 6940 s^{-1}), many fibers migrated inward and not many were seen at the surface. The result was a depleted surface layer. The surface of the extruded pure matrix was smooth for the entire shear rate range. The shear rate transition points were found to be dependent on capillary radius but were independent of the fiber content or capillary length. The fiber migration process is affected by pseudo-plasticity (i.e. the parameter n in the power law; when n = 0, there is no migration; when n increases, then the migration is more pronounced).

Hegler and Mennig [77] studied filler distribution in injection molded glass fiber and bead filled thermoplastics. They found that redistribution effects occurred in both extrusion and injection molding (i.e. both continuous and cyclic processes). It occurred in both the fiber and bead composites. The migration occurred only in the thickness direction in extruded samples and in both the thickness and axial directions in injection molded parts. In a bar shaped mold, the concentration of glass beads was high at the far end and low at the gate. With lower injection time and higher barrel temperatures, the samples became more homogeneous. Their investigation showed that processing conditions used in practice generally lead to inhomogeneous filler concentration distribution in composites. The distributions were also affected by mold and filler geometry. The fiber composite had less inhomogeneity than when the beads were used.

Fiber and particle migration have been the subject of various theoretical studies [75,77,78]. Rubinow and Keller [78] calculated the lateral forces on a rigid, spherical bead moving in a Newtonian fluid:

$$\{\ \vec{F}_1 = \pi R^3 \sigma \vec{\Omega} x \vec{V}\ \} \tag{3.7}$$

where:

$\vec{\Omega}$ = angular velocity of the rigid bead

$\vec{V}$ = velocity of the bead

σ = density of the fluid

R = radius of the sphere

The velocity, $\vec{U}$, of a rigid, neutrally buoyant sphere freely suspended in an unbounded, creeping Newtonian flow is given by Faxen's law [75]:

$$\vec{U} = \vec{\nu}_0 + \left\{ \frac{a^2}{6} \nabla^2 \vec{\nu}_0 \right\} \tag{3.8}$$

where:

a = radius of the sphere

ν = the ambient velocity field.

Subscript "0" refers to values at the centre of the sphere.

Equation 3.8 indicates that spheres in a Couette or Poiseuille flow of a creeping Newtonian fluid do not undergo lateral migration. While in some mold geometries such as converging channels, lateral particle migration does occur, fluid particle redistribution does not.

The equation of conservation of particles is given by:

$$\left\{\frac{\partial\phi}{\partial t}\right\} + \left\{\nabla\ (\phi\bar{U})\right\} = 0 \qquad (3.9)$$

where:

ϕ = volume concentration of particle

t = time

A solution to this equation is ϕ = constant. In this case, an initially homogeneous distribution of rigid spheres remains homogeneous. Equations have been proposed for ellipsoidal particles. However, the analysis remains the same. The explanations for fluid-particle redistribution can only be understood in terms of Non-Newtonian properties.

Experiments by Gauthier [79] showed that particles migrate in the direction of increasing shear rate in a pseudoplastic fluid and decreasing shear rate in an elastico-viscous fluid. Particle redistribution can be explained in terms of shear thinning and normal stresses. Only spheres were dealt with since neither theoretical nor experimental work was done for lateral migration of fibers or rods.

For a power law fluid, where ($\tau = K\dot{\gamma}^n$), an empirical equation was derived to predict the migration behaviour in the fluid [75].

$$U = \frac{1}{50}(1-n)\frac{V}{h^2}\left(\frac{a}{h}\right)^n\left(\frac{y}{h}\right)^{2(n-1)} \qquad (3.10)$$

The equation predicts that:

(i) for $n = 1$ (Newtonian fluid) there is no radial migration;

(ii) for $n < 1$ (pseudo-plastic fluid) there is outward migration;

(iii) for $n > 1$ (dilatant fluid) there is inward migration.

The average migration rate is defined as :

$$\langle U_y \rangle = \frac{2}{h^2} \left\{ \int_0^h y U_y \, dy \right\} \tag{3.11}$$

$$U_y = \frac{2^{3n}}{50} (1-n) \frac{Q}{h} \left\{ \frac{a}{h} \right\}^n \left\{ \frac{y}{h} \right\}^{2n-1} \tag{3.12}$$

where:

y = the distance parallel to the thickness of the mold cavity; $y = \pm h$ being the walls.

Q = volume flux per unit width.

Equation 3.11 and 3.12 give the lateral migration rate in the y-direction of a spherical filler particle during injection molding due to the shear thinning of the polymer melt. The equation for the prediction of polymer filler redistribution is given by:

$$\left\{ \frac{|\tilde{y}|}{h/2} \right\} = \frac{2}{h} \left\{ \frac{2^{3n}(1-n)\eta}{964 \; Q\psi_1} \left\{ 1 + \frac{259\alpha}{241} \right\}^{-1} \right\}^{\frac{1}{2(1-n)}} \left\{ \frac{a}{h^3} \right\}^{\frac{n-2}{2(1-n)}} \tag{3.13}$$

where:

ψ_1 = the primary normal stress coefficient

$|\tilde{y}|$ = surface of fiber accumulation

η = dynamic viscosity

α = negative ratio of secondary to primary normal stress difference.

This equation is meaningful only if lateral migration rates are sufficiently high so that significant polymer-filler redistribution can occur within the injection time. Two dimensionless numbers λ_{ns} and λ_{st} are defined for the effects of normal stresses and shear thinning. The relative values of these two numbers refer to the importance of each effect on the polymer-filler redistribution process.

$$\lambda_{ns} = \left\{ \frac{<U_y>_{ns}T}{(h/2)} \right\} \tag{3.14}$$

$$\lambda_{st} = \left\{ \frac{<U_y>_{st}T}{(h/2)} \right\} \tag{3.15}$$

where

T = the injection time

<f> is the average of the function f(y):

$$<f> = \frac{2}{h} \int_0^{h/2} f(y)dy \tag{3.16}$$

If at least one of the parameters, λ_{ns} or λ_{st}, is of the order of magnitude of 1, then the dimensionless surface of accumulation equation becomes meaningful. The analysis leads to the following conclusions:

(i) if $|\tilde{y}| > |y_{av}|$, then the average filler velocity in the x-direction is less than the average fluid velocity and the concentration of the filler decreases away from the gate.

(ii) if $|\tilde{y}| < |y_{av}|$, then the opposite is true

(iii) if $|\tilde{y}| = |y_{av}|$, then there is no filler redistribution.

Some of the conditions tested were injection time and barrel temperature [75]. The results show that with increasing injection time, $|\tilde{y}|$ becomes much smaller than $|y_{av}|$. Increasing the barrel temperature decreases the lengthwise concentration differences if $|\tilde{y}| < |y_{av}|$ and increases the difference if $|\tilde{y}| > |y_{av}|$ [75].

3.4.2 Fiber Length

Fiber length is not the usual measurement to define fiber dimensions. Rather, it is the aspect ratio, which is defined as the ratio of the major to the minor dimensions of a particle. In the case of fibers, it is the length to diameter ratio. This value is more appropriate for theoretical treatment than the length dimension. In general, the stiffness and the strength of SFRTP increases with aspect ratio, reaching a maximum for continuous fibers.

The fiber length distribution is an important factor for composites. Many properties are determined by this parameter [80-83]. Chiu and Shyu [25] studied the effect of various processing conditions on the fiber length. They showed that the fiber content decreased from the surface to the core of the sample. The average fiber length in the twice-through extruded material was shorter than the once-through material. The number average fiber length was 2.66 mm for the once-through material and 0.96 mm for the twice-through material. The original material was 6 mm chopped strands with diameters of 15 - 22 μm. As the fiber content increased, fiber contact also increased. This produced more friction and thus caused more fiber breakage. The average fiber length increased with a higher melt temperature.

During processing, fibers may undergo length reduction. Fiber length reduction lowers the efficiency of the reinforcement,thus affecting the final mechanical properties [81]. Fiber damage may be due to one or more of the following processes [22]:

(i) fiber-fiber interactions, surface abrasions and fiber overlap lead to stress concentration and bending stresses that produce fiber fracture;

(ii) fiber-machine surface interactions, screw action, abrasion at the runner and mold surfaces;

(iii) fiber-polymer interactions, viscous forces imparted by the polymer may cause fracture.

The final length of glass fibers in a reinforced thermoplastic matrix undergoing screw plastication is not significantly affected by fiber volume fraction or process variables, such as screw speed and barrel temperature. The observed fiber fracture can be accounted for by dilute suspension theory [22], which deals with a dilute suspension of thin rigid rods in shear flow. For concentrated suspensions, the theory is inadequate because of several factors:

(i) Fiber-Fiber interactions. The maximum packing volume fraction for randomly oriented fibers as a function of average fiber aspect ratio in a material is shown in Figure 3.8 [84]. Most commercial reinforced materials have fiber concentrations exceeding the maximum packing volume fraction. This indicates that fibers may be in aligned clumps, bent or broken.

(ii) Hydrodynamic interactions. Concentrated fiber suspensions exhibit plug flow profiles, as opposed to parabolic profiles.

(iii) Fiber concentration non-uniformity in the flow. This is due to fiber interactions with the mold surfaces or to flow effects. There is segregation away from the high shear rate areas near the moving surfaces.

Chiu and Shyu [25] removed the fibers from the polymer matrix by solvent extraction. The fibers were then dried and dispersed in an aqueous solution. In their study of the fiber

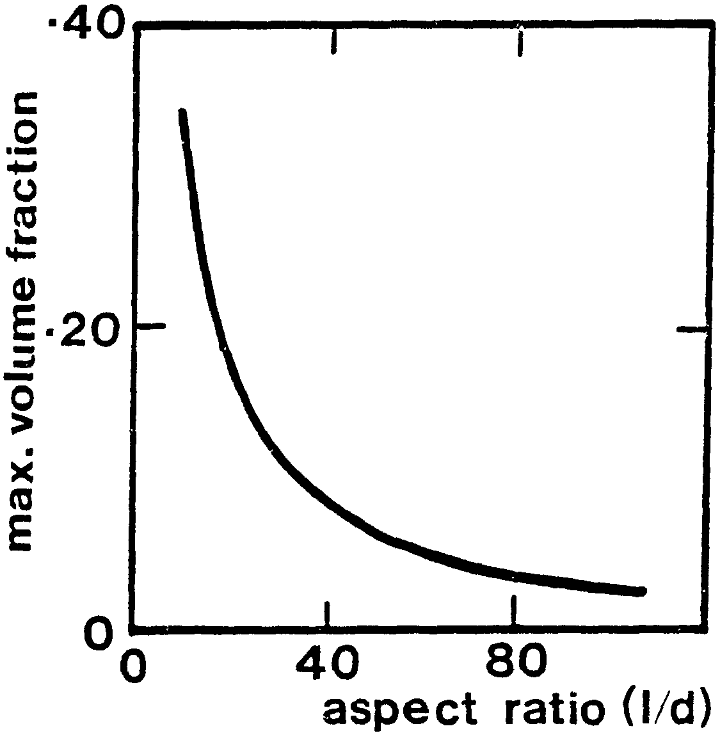

Figure 3.8 Maximum packing volume for randomly oriented fibers as a function of average fiber aspect ratio.

length distribution along the length of the barrel, they showed that :

(i) fiber bending due to solid walls and inter-fiber abrasion does not play a main role in fiber fracture;

(ii) during melting, there is a rapid reduction of fiber length due to viscous loading of the fiber by the polymer in shear flow.

Most of the reduction in fiber length occurred in the barrel, though some was observed in the runners and mold due to the high shear during molding. Increasing the melt temperature and decreasing the screw speed resulted in slightly longer fibers. The studies showed that the fiber breakage could be described by the dilute suspension theory.

During processing, there is considerable shear induced fiber breakage, especially in high viscosity materials. Biggs [85] showed that there was substantial fiber breakage during the compounding of carbon fiber composite. The fibers which were initially 3 mm long were reduced to between 100 and 200 μm in length. The highest reduction in fiber length was found in the composites with the highest melting matrix. In order to provide sufficient transferral of mechanical load from the matrix to the fiber phase, the fibers must exceed a certain critical aspect ratio. The critical fiber aspect ratio was in the range 16:1 to 25:1 for the polymer carbon composites.

3.4.3 Fiber Orientation

Particles having a high aspect ratio, such as fibers, can exhibit random orientation of the major and minor axes, where the probability of finding fibers oriented in any particular direction is the same, or they can be perfectly oriented where all the fibers are aligned in one particular direction. However, fibers in real short fiber composites usually exhibit preferential orientation, i.e. an intermediate distribution between random and perfectly aligned orientation. Fibers contribute strength and stiffness in the direction parallel to their major axis, so that composites with preferentially oriented fibers exhibit higher strengtn and stiffness in the direction of fiber orientation. On the other hand, random orientation in composites would contribute to products with balanced properties in all directions. Thus, the degree of orientation determines the amount of anisotropy in the composite properties.

When material is injected into the mold, the fibers assume complex orientation patterns which are retained in the product. The fiber orientation distribution has significant influence on the final mechanical properties of the product [15]. Anisotropy of physical properties will result when fibers show a preferred direction of orientation.

Most studies on fiber orientation have been experimental. Fiber orientation studies entail microscopic examination with either x-ray [86], contact micro-radiography [87,88] or optical methods [89], as described in chapter 4.

Various studies have attempted to elucidate the effect of flow on fiber orientation [16-21,90]. Both extensional and shear stresses affect orientation significantly. However, extensional strain has been shown to be more effective in aligning fibers [18]. Convergent flow results in high fiber alignment in the flow direction, while divergent flow results in fiber alignment perpendicular to the flow direction [90,91]. In shear flows, there is an increase in orientation parallel to the flow direction, and this effect becomes stronger at low flow rates [17].

The viscosity of the melt increases with both fiber length and concentration, but, at high shear rates, the effect of fibers on viscosity is not large [21] The flow profile is very blunt and the material flows as a plug.

The fiber orientation distribution is determined by the complex flow fields developed in the mold. Flow patterns are determined by such variables as:

(i) mold geometry: length to width to thickness dimensions, gate size relative to cavity, non-parallel wall sections, curved channels, etc.;

(ii) material characteristics: viscosity, fiber concentration, aspect ratio, etc.;

(iii) pressure, flow rate, inertial and visco-elastic effects;

(iv) temperature of both the mold and the material.

The fibers are located in the plane of the molded part and can be divided into individual layers of different orientations. Some authors have found at least four layers from the surface to the centre [87,92,93], while others have shown a three layered structure [74,94]. Figure 3.9 illustrates the typical fiber orientation distribution in a cross-section of a molded part [74].

Fibers are oriented perpendicular to the flow direction in the core and nearly parallel in the skin. Bright and Darlington [92] used molds of varying geometry: a rectangular bar, a corner gated square mold and a centre gated disc mold. They also varied injection speed, mold temperature and melt temperature. The general fiber orientation profile did not change with molding conditions. They found glass fiber orientation in the skin layer to be parallel for polyamide and random for polypropylene samples. Diverging flows gave rise to transverse orientation in the core, while orientation in the surface layer was dependent on the polymer and the flow geometry.

The outer layer contained fibers preferably oriented in the flow direction while the core had highly transverse orientation. In some moldings, the outer layer had a random orientation, while an intermediate layer had highly oriented fibers in the flow direction. The core region occupied approximately 10 - 15% of the thickness. Changes in injection

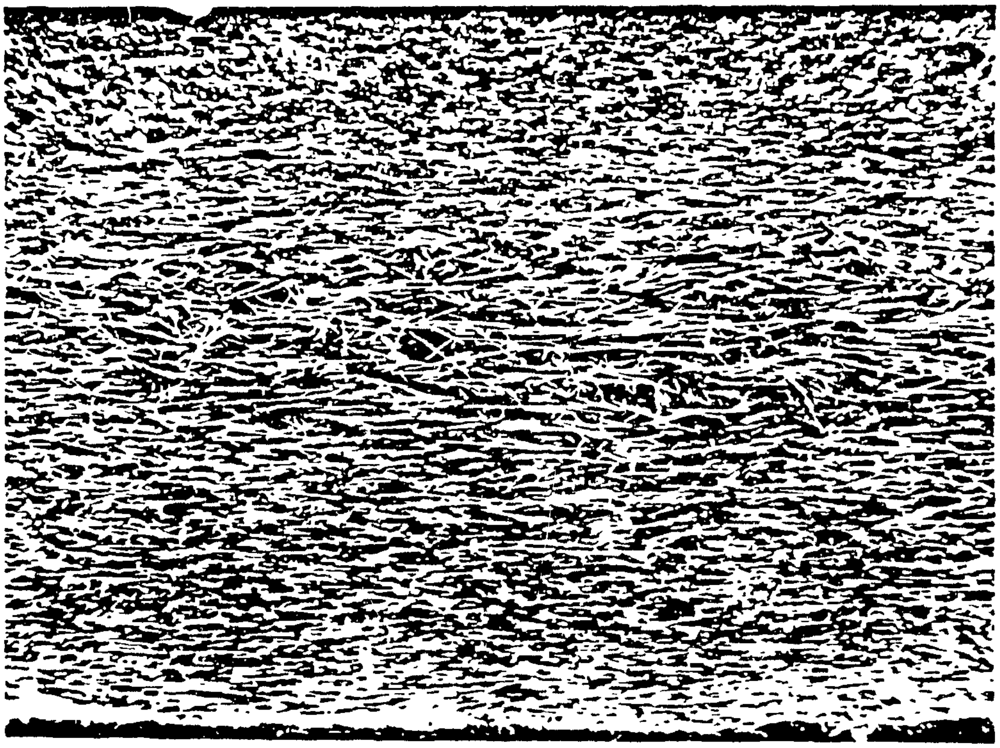

Figure 3.9 Contact MicroRadiography of transverse slices of injection molded composite part [75].

speed led to changes in core thickness or in the number of oriented layers, depending on the polymer. The layer thicknesses were predicted from calculations of the frozen skin thickness and velocity profile in the melt, using a simplified heat conduction model. The velocity profile was calculated assuming an isothermal melt.

3.4.3.1 Mold Geometry

Mold geometry appears to be the most significant variable [15,23,24]. Gate designs which are fan shaped produce diverging flow fields leading to fiber orientation transverse to flow. Converging flow fields lead to fiber orientation parallel to the flow direction.

In the molding process, the material is forced into a converging channel prior to entry in the mold. It is already strongly aligned in the flow direction. As the material enters the mold, diverging flow occurs because of the increase in cross-section from gate to the cavity. This produces a deceleration which is accompanied by compressive forces. Fibers inclined slightly away from the axis are rotated to a transverse orientation. Streamlines radiate from the cavity in all directions in the mold. The fibers become oriented perpendicular to the streamlines. This gives rise to transverse orientation in the centre and longitudinal orientation near the wall which is enhanced by shear near the walls. In the thickness direction, there is a transversely oriented core surrounded by longitudinally oriented skin. At the vent of the mold, the material is folded back onto itself during compaction. Because shear stresses are small, strong transverse orientation occurs.

The effect of gate design is primarily dependent on the amount of extensional strain imposed on the material. A smaller mold to gate cross-sectional area ratio produces more longitudinal orientation [24]. This reduces pressure and velocity gradients near the mold surface and leads to smaller boundary layers of fibers aligned near the surface [23]. The effects of fan gates depend strongly on fill rates, and more transverse orientation is produced than is the case of edge gates [15].

Overall, mold geometry plays a critical role in determining fiber orientation. Other variables play a smaller role, except in their influence on fiber orientation near the surface. The important variable in this regard is the material viscosity [23]. There is need to investigate the roles of other parameters of mold geometry, such as width-to-length-to-thickness ratios, non-parallel wall sections etc.

3.4.3.2 Melt Viscosity

The viscosity of the material, and, therefore, the variables that determine viscosity influence fiber orientation [21]. Low viscosity produces a high degree of longitudinal fiber orientation. High concentrations of fibers lead to plug-like flow. At high flow rates, the material is strongly pseudo-plastic, and thus, the velocity profile for tube flow is very blunt. At shear rates above 10,000 s^{-1}, glass fibers have little effect on the shear viscosity. In tube flow, most of the shearing takes place in the regions close to the wall and the material in the central region moves along without shearing; thus, in the central region, no fiber-fiber collisions occur. In the region near the wall, where all the shearing occurs, the majority of fibers are longitudinally oriented. The probability of fiber-fiber collisions is much less and thus the viscosity is not increased with increasing fiber content. Also, fibers may migrate away from the surface to leave a fiber-free layer. The velocity profile for high shear rates is very blunt, and, thus all the shearing could take place in this layer [17]. The effect of fiber aspect ratio on viscosity is not clear. The effect of fiber content on viscosity is more important [21].

3.4.3.3 Injection Speed

Investigations on the effect of injection speed have shown that it can significantly affect fiber orientation distribution [15,17]. With fast injection speeds and a small gate, a high degree of longitudinal orientation is produced.

Using edge gates and fast injection speeds, mainly transversely oriented fiber orientation is obtained in the core region. At the surfaces, longitudinal orientation is obtained. The fiber orientation changes drastically within the gate area but much slowly along the rest of the length of the sample. A squirting effect or jetting may occur during fast fills through a small gate.

Using slow injection speeds through a large gate, the longitudinal fiber orientation may be kept intact. In normal edge gates, the fibers in the core region exhibit significant longitudinal orientation. The core region is also of greater thickness than that obtained with fast injection speeds. The skin layer contains fibers of fairly random orientation in the plane of the molding [15].

Injection speed affects the surface finish of the sample. With fast injection speeds, the surface is glossy, with no fibers protruding. At low injection speeds, a matt surface is produced. Fibers covered with the matrix protrude. Pressure must be applied to press the material to the mold wall before it solidifies. This effect is readily achieved in the case of high injection speeds. High melt and mold temperatures lead to a lower material viscosity, and, thus, have the same surface effects as high injection speed [17].

Wu [76] observed that fiber orientation undergoes order-disorder transitions at certain wall shear rates. At low wall shear rates (10 - 42 s^{-1}), fibers appeared to be oriented parallel to the flow direction with many exposed but few protruding out of the plane. The distribution of fibers was uniform. A transition point occurred at 100 s^{-1}. At medium wall shear rates (416 - 694 s^{-1}), many fiber were disoriented and stuck out at the surface.

Bright, et al. [87] showed that the fiber orientation in the core was strongly affected by injection speed. At high injection speeds, the normal layer structure was observed. However, at very low speeds, the fiber orientation is parallel to the flow direction throughout the thickness of the mold. They related this to the shape of the velocity profile and the thickness of the frozen layer.

Vincent and Agassant [89] showed that fibers were slightly oriented in the flow direction in the skin, highly oriented under the skin and highly transverse in the core. An increase in flow rate led to less orientation in the skin and core but the profile maintained the same shape. Low melt temperatures led to similar results in the skin. The thickness of the skin layer decreased with a high mold temperature. The different fiber orientation near to the wall was attributed to the combined effect of the fountain flow and the frozen skin phenomena. Fibers flow from the core to the skin and can be perpendicular to the flow. At the skin, the layer of molten polymer solidifies, and, thus, shear flow is inhibited; Accordingly, fiber orientation in the flow direction is limited.

Goettler [95] showed that the shearing effect of flow is essentially limited to the regions close to the wall, while the central core flows as a plug. The fiber orientation in the core is affected substantially by the extensional flow field.

3.4.3.4 Theoretical Studies on Fiber Orientation

Predictions of fiber orientation are based on the flow kinematics. The earliest work on suspended particle motion was reported by Jeffrey [96]. He solved a linearized Newtonian equation of motion for a single ellipsoidal particle immersed in a viscous fluid, under the following simplifying assumptions:

(i) the particle is spheroidal;

(ii) the particle assumes the translational velocity of the adjacent fluid which displaces it;

(iii) the fluid has a steady motion away from the disturbed motion in the immediate neighbourhood of the particle;

(iv) any interactions between the particles and between the particles and the boundary are neglected;

(v) the fluid is Newtonian.

Mason et al. [79,97] made many experimental and theoretical studies on orientation of rods and disks in a variety of flow fields. They considered other effects on particle orientations that were neglected by Jeffrey.

These are:

(i) fluid inertia;
(ii) non-uniform shear field;
(iii) non-uniform particle size distribution;
(iv) particle interactions;
(v) particle Brownian motion.

They showed that if these effects were considered, then a steady state orientation would exist instead of the periodic solution predicted by Jeffrey. Leal and Hinch [98], and Cohen et al. [99] considered the effect of Brownian motion, while Folger and Tucker [100] analyzed particle-particle interactions in concentrated fiber solutions to derive steady state orientation solutions. Fiber orientation predictions have been presented based on a macroscopic flow field [101].

Gillespie et al. [102] and Givler et al. [103] attempted numerical simulation of fiber orientation of flows in complex geometries. Fiber orientation was calculated from numerical integration of Jeffrey's orientation equation [96] along the streamline. Jeffrey's equation in the form used is shown below.

$$\dot{\phi} = \psi + B\left\{ d_{xy}\cos 2\phi - \frac{1}{2}(d_{xx}-d_{yy})\sin 2\phi \right\} \qquad (3.17a)$$

$$\text{where } B = \left\{ \frac{r_p^2-1}{r_p^2+1} \right\} \qquad (3.17b)$$

and

$\dot{\phi}$ = the material time derivative of the orientation angle.

d_{yx}, d_{xy}, d_{yy} = components of the rate of deformation tensor.

ψ = vorticity

A steady state finite element solution was used to calculate streamlines and fiber orientation based on creeping flow and incompressible fluid assumptions. The calculations were restricted to steady state planar flow. The results were comparable to experimental results. Givler *et al.* [103] predicted fiber orientation in both expansive flow at the gate and in fountain flow.

Kenig [93] analyzed the filling stage of filled thermoplastics, and identified mechanisms that governed the formation of the layered fiber orientation structure. Jeffrey's equation, which was limited to dilute fiber suspensions, was extended to treat concentrated fiber-polymer compounds by defining an orientability parameter. The orientability parameter accounted for such factors as fiber interactions.

3.5 Fiber-Matrix Interactions

In view of the need for improved fiber-matrix bonding, a variety of fiber finishes have been developed. These include sizing agents, such as a thick coating of polyvinyl acetate to protect the fiber surface from abrasion caused by handling and fiber-fiber contact. Lubricants are added to permit easy processing of the fibers. Most importantly, coupling agents protect the fibers and promote fiber matrix bonding.

Organo-silanes are the most widely used coupling agents for glass. They have the general structure X_3S-R, where the X group is usually methoxy, ethoxy or chloro, and the R group is selected to form covalent bonds with the matrix. The advantages of silane coupling agents are:

(i) Protection against fracture, and healing of micro-flaws in the fibers.

(ii) Strengthening the boundary layer of the interface by forming an interpenetrating polymer network.

(iii) Improving meltability of the composite and dispersability of the fibers. This aids in the displacement of air and micro-voids.

(iv) The hydrophobic side groups can improve water resistance of the composite.

The interface region consists of three layers. The first is an extensively cross-linked three-dimensional structure. The second consists of oligomers which are only connected by a few bonds, while the third layer consists of physio-sorbed oligomers. The third layer can be extracted with water at room temperature, while the second can be removed with boiling water. The first layer cannot be removed [104]. It has been observed that the removal of the physico-sorbed layer leads to better composite properties while the loosely chemi-sorbed layer may be beneficial for the fibers [105].

The fiber-matrix interface plays a critical role in determining properties of composite systems. Therefore, significant effort has been made to understand, control and modify the interface [106-108].

A number of models have been proposed for predicting the mechanical behaviour of composites [109]. These models generally consider the fiber-matrix interface as a perfect mathematical surface with continuity of stress and displacement. However, the real situation is quite different. Stress transfer from fibers to matrix occurs by adhesion as well as by friction [110]. Stress concentration occurs at the interface, because of the following reasons:

(i) The surface of a real fiber is rough, leading to stress concentration near corners. The contact area between the matrix and fiber is generally larger than the assumed value.

(ii) There are differences in the thermal expansion coefficients of the fiber and matrix.

(iii) Crystallization of the matrix often occurs. The interface serves as a nucleation site.

3.6 **Summmary**

The microstructure of injection molded materials is controlled by the thermo-mechanical history that the material experiences during processing. The thermo-mechanical history is characterized by the temperature, pressure, stress fields, etc., that are present during processing, and is affected by material properties, processing conditions and other machine related properties.

Many studies have been carried out with regard to the microstructure of unreinforced thermoplastics, resulting in a general understanding of some of the phenomena involved. However, the introduction of a two-phase raw material, such as in short glass fiber reinforced composites, complicates the process and introduces new phenomena. Many studies have been performed on separate aspects of injection molded composite microstructure. However, very little has been done on the integration of microstructural characteristics. Thus, there is need for more detailed and integrated fundamental understanding of the behaviour and characteristics of injection molded composites. It is hoped that the present work will represent a significant step in this direction.

CHAPTER 4

4 EXPERIMENTAL

The materials used in the study are described and the relevant physical properties are presented and discussed. A description of each of the experimental techniques used for processing samples and for measuring microstructural properties is presented.

4.1 Materials

The matrix material used in this study was a commercial injection molding grade isotactic polypropylene (PRO-FAX 6501) which was supplied by Hercules Canada Limiteé. The polymer was compounded with glass fibers which were treated with a proprietary silane coupling agent. The average fiber diameter was 10 μm with an average length of approximately 560 μm. The average fiber content in the pellets was measured by Thermo-Gravimetric Analysis to be 29.55 weight percent, which is in reasonable agreement with the nominal value of 30 weight percent.

The composite material chosen was ideal because of:

(i) its availability in the Department of Chemical Engineering at McGill University;

(ii) the availability of substantial information on the rheological properties from another study being carried out in the Department [111];

(iii) its widespread use in industry which would make this work a valuable and meaningful contribution to the plastics processing industry.

Short glass fiber reinforced polypropylene is one of the most important composite material used in the injection molded process. Its high temperature performance, excellent physical properties and low cost have propelled its extensive use in the automotive industry. Injection molded polypropylene composites are used for under-the-hood parts such as fan shrouds, heater and air conditioner ducts, lamp housings and fender liners, in addition to uses such as bases and housings for appliances [2].

Some of the important physical properties of the polypropylene resin are presented in Table 4.1.

4.2 Material Characterization

4.2.1 Rheological Properties

All previous rheological characterization of the pure polypropylene and the polypropylene composite material has been carried out by Mutel [111] in his Ph.D study. This included the measurement of viscosity as a function of shear rate and temperature for both materials. Figure 4.1 shows the

TABLE 4.1

4.1 Physical properties of the material used.

Physical Properties	Polypropylene PRO-FAX 6501)	Source
M_w ave (g/mole)	3.71×10^5	1
M_n ave	6.64×10^4	1
M_w/M_n ave	5.59	1
Z ave	1.22×10^6	1
Melt Index (g/10 min) (230°C and 2.16 kg force)	1.8	1
Density (g/cm^3) (23°C and 1 atm.)	0.905	2
Melting range (°C)	120 - 170	2
Specific heat		2
C_p solid (23°C, J/g/°C)	1.4	
C_p melt (170-270°C, J/g/°C)	2.0 - 3.4	
Thermal Conductivity		2
k_s solid (23°C, J/m.s.°C)	0.22	
k_m melt(170-270°C, J/m.s.°C)	0.26 - 0.28	

Source : (1) Hercules Canada Limiteé
(2) Results from this study.

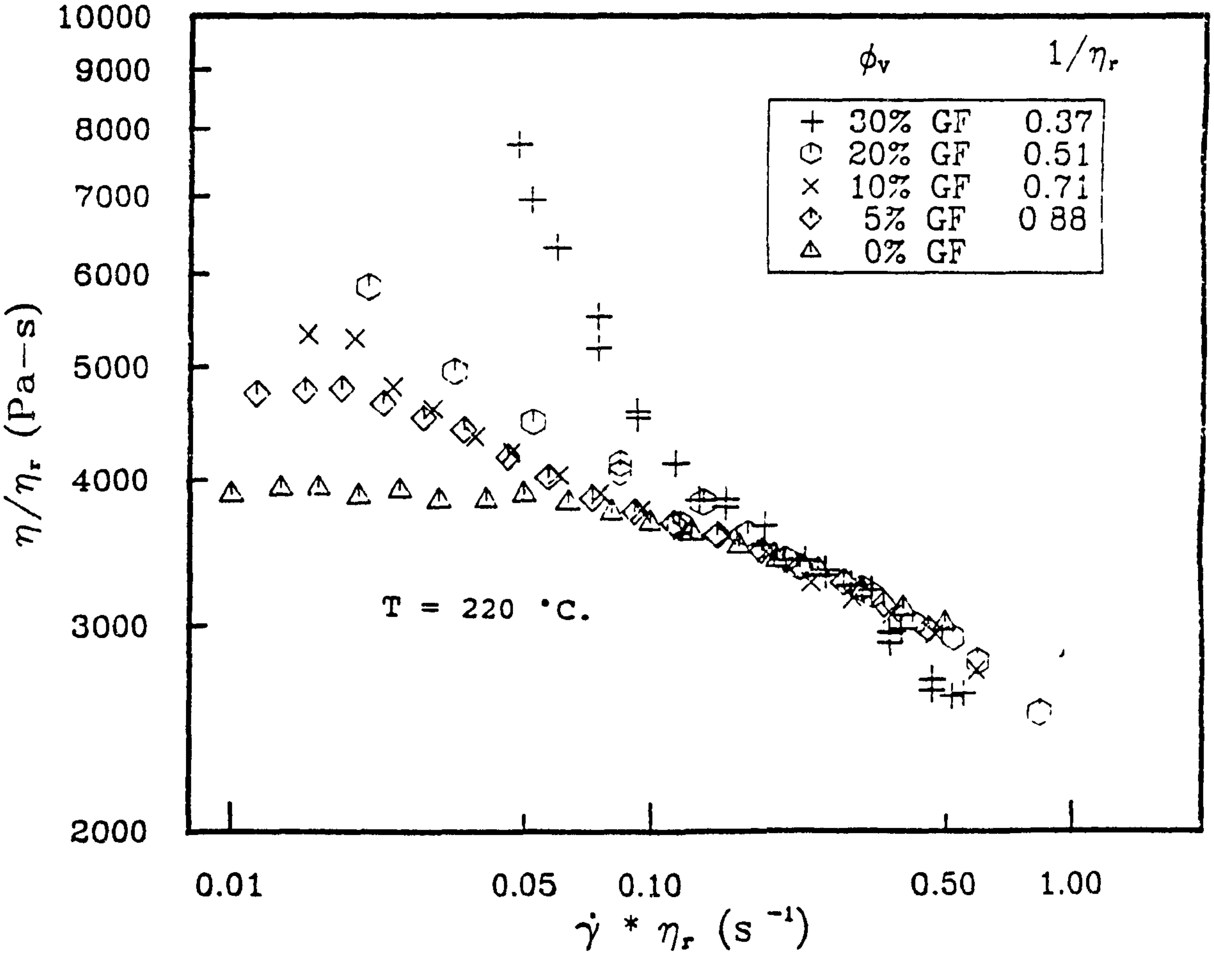

Figure 4.1 Steady shear viscosity for polypropylene and 30% glass fiber filled polypropylene melts [111].

relationship between viscosity and shear rate for the materials. The rheological behaviour of the composite melt is determined not only by the base polymer rheological properties but also by the state of fiber orientation. Although extensive research has been carried out on the rheology of fiber filled polymer melts, there are no precise relations between the rheological properties and fiber orientation.

The effect of increasing fiber content is generally observed as an increase in the steady shear viscosity of the melt [112]. This effect on the steady shear viscosity increase at low shear rates for all fiber concentration. The steady shear viscosities for the unreinforced and reinforced polypropylene increased with decreasing shear rate at low shear rates. The unfilled melt develops a shear rate independent plateau at the lower shear rates.

The relative shear viscosity (defined as the ratio of the viscosities of the filled and unfilled melt at the same bulk shear stress) decreases with increasing shear rate, approaching an asymptotic plateau at high shear rates [112]. At the higher shear rates, the fibers are almost totally oriented within the shear planes, and any further increase in shear rate has no significant effect on the fiber orientation.

4.2.2 Thermal Conductivity

The measurements were carried out using an apparatus developed in this laboratory [113,114]. It consists of an environmental chamber controlled at a preset temperature and a sample holder with two cavities holding identical samples on both sides of a circular heater. At steady state, the temperature difference across the thickness of each sample is measured. The thermal conductivity, k, can then be calculated from the known thermal flux, area, thickness and the temperature difference. Data on the thermal conductivity of polymeric materials are scant, and available data have accuracies of not better than ±10%.

The thermal conductivity of both reinforced and unreinforced polypropylene was measured in the thickness direction as a function of temperature. The data are presented in Figure 4.2. The thermal conductivity of pure polymer was measured to be approximately 0.20 J/sec.m.°C at room temperature. This value lies within the range of 0.12 to 0.24 J/sec.m.°C that is reported in literature [49]. The thermal conductivity of pure polypropylene is lower than that of the polypropylene composite. This result is expected because of the higher thermal conductivity of the glass fibers. The thermal conductivities of both materials show an increase with temperature, with a transition region at the melt temperature in the vicinity of 168 °C.

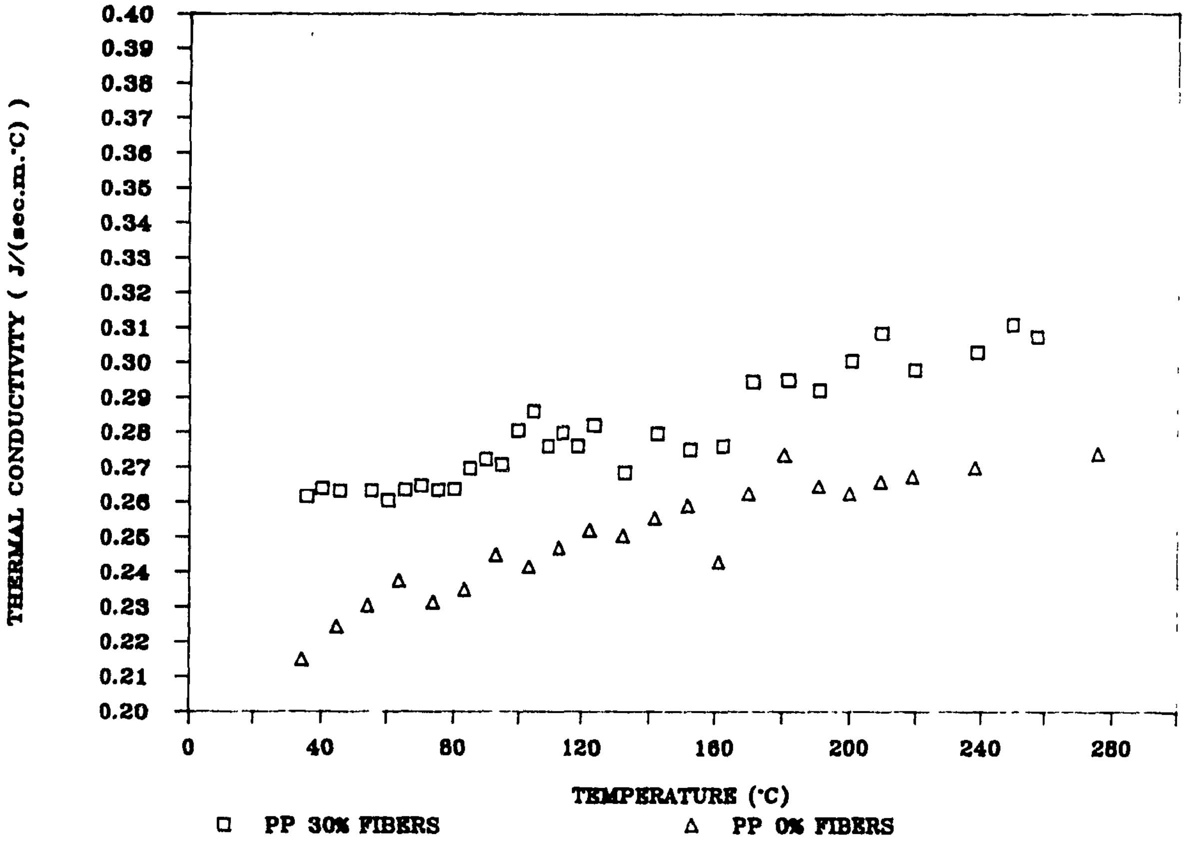

Figure 4.2 Thermal conductivity versus temperature for reinforced and unreinforced polypropylene.

The thermal conductivity of amorphous polymers increases with increasing temperature below T_g (the glass transition temperature). This is because of the increasing segmental mobility of the polymeric chains. Above the T_g, the conductivity decreases because of the volumetric expansion that counteracts the effect of the increasing segment mobility. The T_g of polypropylene has been reported to be in the range of -30 to 20 °C [49]. The thermal conductivity of semi-crystalline polymers is affected by morphology. The crystallite size, density and orientation have been shown to affect k [115]. The crystalline phase conducts energy much better than the amorphous phase because of the ordered lattice structure of the polymer chains. Energy is transmitted more efficiently along the chain axis. Increasing the temperature leads to breakup of the crystalline regions. This decrease in k of the crystalline phase counteracts the increase of k of the amorphous phase due to segmental mobility. Fuller, et al. [116] have shown that polypropylene exhibits only a slight increase of k with increasing temperature in the range 150 to 250 °C. In general, polymer melts show either a linear increase of k with temperature or weak dependence of k on temperature.

The material in this study showed an increase in thermal conductivity with temperature. It appears that the effect of increased segmental mobility on the thermal conductivity is much greater than that of volume expansion, as suggested by

Fuller, et al. [116].

Thermal conduction in reinforced composites is a complex phenomenon. It is affected by a variety of factors such as filler shape, orientation, etc., and as a result, it is quite difficult to predict. A review of estimation methods is given by Progelof, et al. [117]. One of the simplest methods employs an addition rule comparable to that used for the addition of electrical resistances in parallel, with known values of the thermal conductivity of both the polymer and the reinforcement [117]:

$$\left(\frac{1}{k}\right) = \left\{\frac{\phi_n}{k_n} + \frac{\phi_g}{k_g}\right\} \tag{4.1}$$

where:

k = the thermal conductivity of the mixture,

k_n, k_g = the thermal conductivities of the polymer and reinforcement, respectively

ϕ_n, ϕ_g = the volume fractions of resin and reinforcement respectively.

The formula does not take into consideration any dimensional variation in the thermal conductivity of glass fiber reinforcement. Measurements of the thermal conductivity of glass fibers have only been carried out in the length direction [118]. A value of 1.08 J/m.sec.°C at room temperature has been reported.

Cheng and Vachon [119] obtained a solution to Tsao's equation [120] relating mixture conductivity to the conductivity of the individual components and two other parameters.

$$\left(\frac{1}{k_e} \right) = \left\{ \frac{1-B}{k_c} + \frac{1}{\{C(k_d-k_c)[k_c + B(k_d-k_c)]\}^{1/2}} \text{ x } \ln \frac{[k_c + B(k_d-k_c)]^{1/2} + B/2[C(k_d-k_c)]^{1/2}}{[k_c + B(k_d-k_c)]^{1/2} - B/2[C(k_d-k_c)]^{1/2}} \right\} \tag{4.2}$$

where:

$$B = \left\{ \frac{3\phi}{2} \right\}^{1/2} \tag{4.2a}$$

$$C = -4 \left\{ \frac{2}{3\phi} \right\}^{1/2} \tag{4.2b}$$

k_c = thermal conductivity of the continuous phase

k_d = thermal conductivity of the discrete phase

k_e = thermal conductivity of the two phase mixture

ϕ = volume fraction of the discrete phase

Although equation 4.2 was derived for spherical glass particles, it has been used with short fiber composites. The particle shape has negligible effects on the conductivity for k_d/k_c ratio of less than 100 [121,122].

Halpin-Tsai [123] also put forward an equation for thermal conductivity of composites. Lewis and Nielsen [124] modified the equation to account for particle shape and orientation.

$$k_e = k_c \left\{ \frac{1+AB\phi}{1-B\phi\psi} \right\} \tag{4.3}$$

where:

$$A = k_{en} - 1 \tag{4.3a}$$

$$B = \left\{ \frac{k_d/k_c - 1}{k_d/k_c + A} \right\} \tag{4.3b}$$

$$\psi = \left\{ 1 + \frac{(1-\phi_m)\phi}{\phi_{m2}} \right\} \tag{4.3c}$$

The equations are used to obtain thermal conductivity predictions for the composite samples at 35 °C and these are compared to the experimental measurements in Table 4.2. The prediction using the parallel resistance type model is lower, while the Cheng-Vachon and the Lewis-Neilsen models over-predicts the thermal conductivity for the composite polypropylene.

4.2.3 Specific Heat

The specific heat of both unreinforced and reinforced polypropylene was measured as a function of temperature. The measurements were carried out using a Perkin Elmer DSC-7. A heating rate of 10 °C/min was used. High heating rates could introduce error when the instrument response time does not permit it to respond to and control fast temperature changes. On the other hand, low heating rates could produce material changes during the measurement. A heating rate of 10 °C/min was assessed to be the optimum. Indium and sapphire were used

TABLE 4.2

4.2 Thermal Conductivity Predictions of Composite samples.

PREDICTIONS	THERMAL CONDUCTIVITY J/sec.m.°C
Parallel	0.241
Cheng and Vachon	0.278
Lewis and Neilsen	0.283
EXPERIMENTAL	0.260
Data	
Polypropylene	
k_p J/sec.m.°C	0.215
ρ_p g/cm^3	0.905
ϕ_p	0.87
Glass	
k_g J/sec.m.°C	1.082
ρ_g g/cm^3	2.54
ϕ_g	0.13

for calibration. The data are shown in Figure 4.3. Only the linear part of the curve was used to obtain a linear correlation between heat capacity and temperature. The nonlinear portion (with the peak) is due to the melting of the crystalline portion of the samples. The latent heat of fusion can be included in the specific heat equation, assuming that the specific heats of the melt and the solid are independent of the cooling process within the range of solidification [125].

$$C_p = C_p' + \left(\frac{dH_c}{dT} \right) = C_p' + \Delta H_{pc} \left(\frac{d\chi}{dT} \right) \qquad (4.4)$$

where:

C_p = specific heat of the sample

C_p' = specific heat of sample without heat of fusion

H_c = heat of crystallization of the sample

ΔH_{pc} = heat of fusion of the pure crystal

χ = degree of crystallinity.

The reported values for the heat of fusion of 100% isotactic polypropylene range from 63 to 260 J/g [126]. A value of 153 J/g [127] appears to be reasonable, since it appears to give realistic crystallinity values for the material used in this study.

In Figure 4.3a, it can be seen that the specific heat of the materials increases linearly with increasing temperature above and below the melting temperature range. The chains

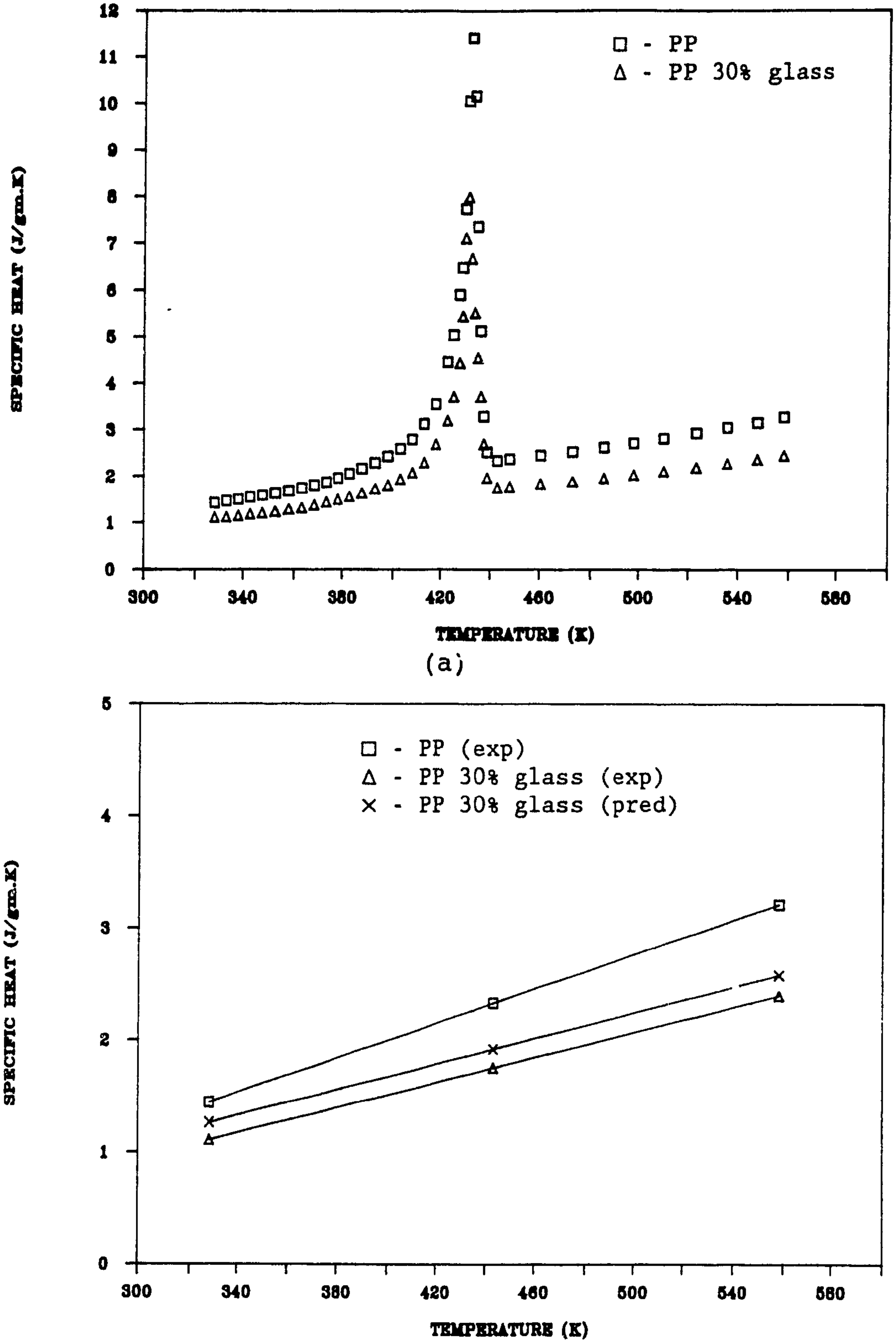

(a)

(b)

Figure 4.3 (a) Experimental and (b) Correlations of Specific heat versus temperature for the polypropylene and composite.

become more mobile and absorb more energy in the process. The correlations for the linear portions of the data curves are presented below and plotted in Figure 4.3b:

Experimental measurements:

PP - C_p (J/g.K) = 1.02 + 0.008T (T in °C)
GLASS - C_p (J/g.K) = 0.78 + 0.001T (T in °C)
PP 30% GLASS - C_p (J/g.K) = 0.80 + 0.006T (T in °C)

Temperature range 55 - 100 °C and 180 - 285 °C

Value reported in the literature [128]:

PP - C_p (J/g.K) = 1.53 + 0.010T (T in °C)

Predictions using the formula:

$$C_p(\text{PP 30\% GLASS}) = 0.70C_p(\text{PP}) + 0.30C_p(\text{GLASS}): \qquad (4.5)$$

PP 30% GLASS - C_p (J/g.K) = 0.95 + 0.006T (T in °C)

The specific heat data reported in the literature are significantly higher than those obtained experimentally in this study. This difference may be due to variation in the composition of the polypropylene. The specific heat for the composite sample was predicted using equation 4.5. The predicted correlation showed good agreement with the experimentally obtained result.

4.2.4 Crystallization Kinetics

The rate of crystallization during a cooling experiment, can be related to the temperature by using a heat balance equation:

$$\left\{\frac{d\chi}{dt}\right\} = \left[\frac{R(T-T_s)}{\Delta H}\right] + \left[\frac{C_p}{\Delta H}\right]\left[\frac{dT}{dt}\right] \qquad (4.6)$$

where:

$d\chi/dt$ = rate of crystallization

dT/dt = rate of cooling

T_s = ambient temperature

T = temperature of the polymer

ΔH = heat of crystallization of crystalline material

C_p = specific heat of material at constant pressure

R = heat transfer coefficient

The results of isothermal crystallization studies on polypropylene obey the Avrami equation, which is improved by making allowances for secondary crystallization [129,130]:

$$\chi(t) = \chi(\infty)\ \{1 - \exp(-Z_p t_f^n) \qquad (4.7)$$

$$\chi(c,t) = \chi(p,\infty)\{1 - \exp(-Z_p t_f^n)\} +$$

$$\chi(s,\infty) Z_s \left\{\int_0^{t_f} \{1 - \exp(-Z_p \theta^n)\}\{\exp(-Z_s (t_f-\theta))\}d\theta\right\} \qquad (4.8)$$

where:

$\chi(\infty)$ = the maximum achievable degree of crystallinity at the isothermal crystallization temperature

τ^* = induction time

t_f = $t-\tau^*$

p and s refer to primary and secondary processes, respectively.

Nakamura, et al. [131] proposed a model for non-isothermal crystallization based on the Avrami equation.

$$\chi(t) = \chi(\infty)\left[1 - \exp\left\{-\left(\int_0^t K_A[T(\tau)]d\tau\right)^n\right\}\right] \qquad (4.9)$$

where:

$\chi(t)$ = the degree of crystallinity at time t

n = Avrami index determined in the isothermal experiments

$K_A(T)$ = parameter related to the Avrami isothermal crystallization rate constant Z(T)

$\chi(\infty)$ = the limiting crystallinity level which is dependent on the temperature ; $\chi(\infty) < 1$

The crystallization kinetics were evaluated for the polypropylene composite, using isothermal crystallization experiments in the Perkin Elmer DSC-7. The crystallization data are presented in Figure 4.4. The calculated values of n lie close to 3. A value of 3, as reported in literature [49], signifies crystallization by spherical growth and heterogenous athermal nucleation. In the isothermal crystallization curves, there is no induction period, signifying that the nuclei begin to grow immediately and that there is no preceding nucleation process.

Crystallization in injection molded samples occurs non-isothermally at a rate dependent on the cooling conditions.

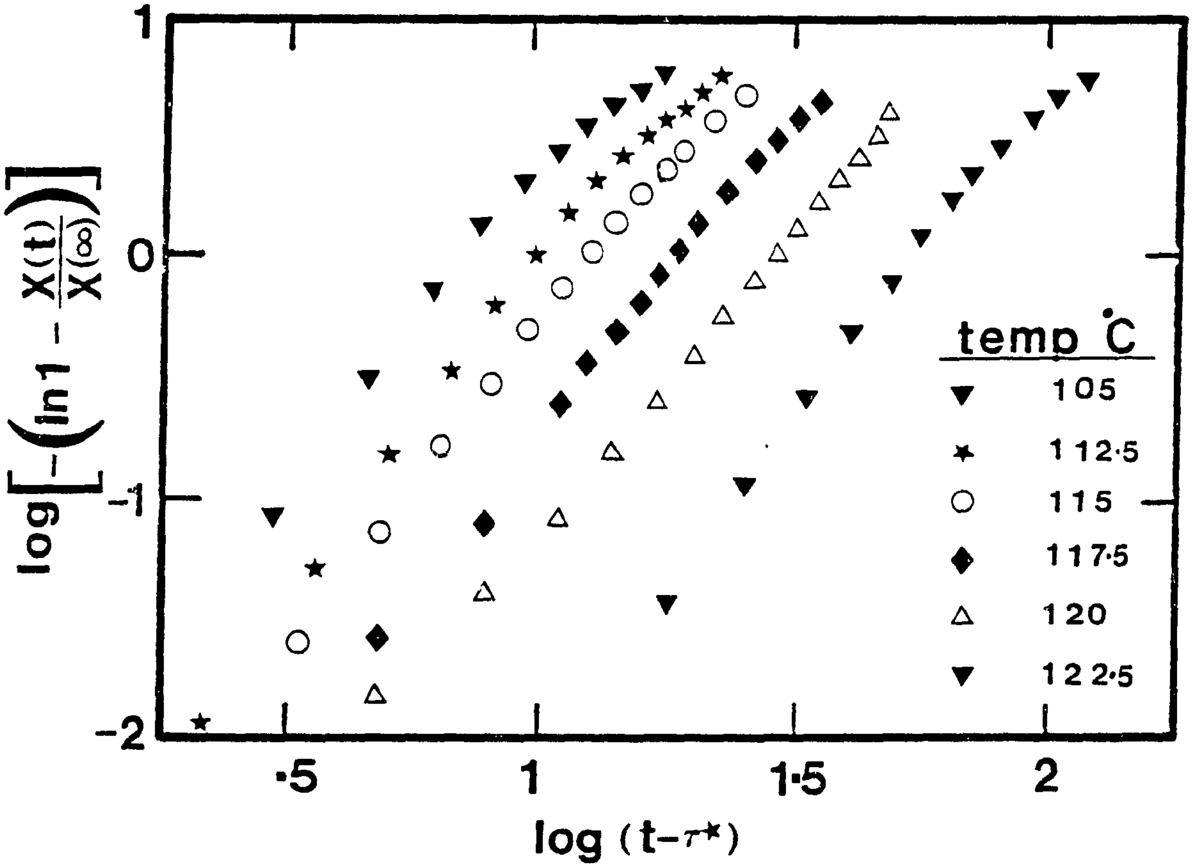

Figure 4.4 Isothermal Crystallization kinetics for the polypropylene composite.

Thus, the crystallization kinetics obtained by the isothermal process have to be adapted for the non-isothermal case. With composite materials, the crystallization process is further complicated because the fiber surface could provide nucleation sites for crystallization. The addition of nucleating agents has the same effect of increasing the concentration of nuclei and accelerating the overall rate of crystallization. This leads to smaller and more numerous spherulites.

4.2.5 Pressure-Volume-Temperature Data

The Pressure-Volume-Temperature (PVT) characteristics of the polypropylene resin were obtained using an Instron Capillary Rheometer. The capillary exit was blocked to form a cylindrical chamber which is controlled at a set temperature. A weighed amount of resin was introduced into the capillary and the plunger was depressed at a predetermined rate. The instantaneous pressure changes were recorded versus the plunger displacement. Thus, it was possible to calculate the volume of the melt. The P-V-T data for the resin are presented in Figure 4.5. It should be emphasized that this data reflect only an approximation of the P-V-T behaviour resin, in view of the apparatus and experimental technique employed.

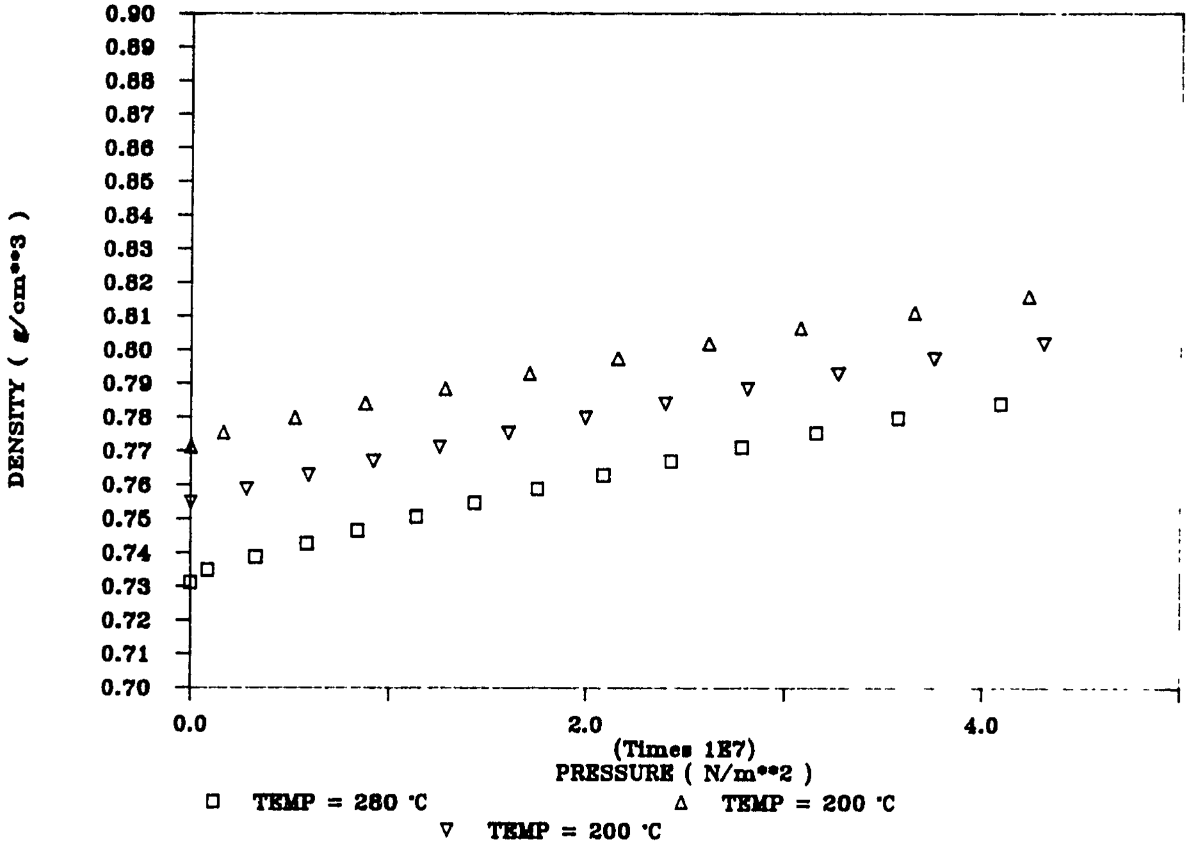

Figure 4.5 P-V-T data for polypropylene resin.

4.3 Injection Molding

Injection molding was carried out using a Danson Metalmec (Model 60-SR), 2 1/3 ounce, 68 ton, reciprocating screw injection molding machine, as shown in Figure 4.6.

A rectangular cavity, 10 cm x 6 cm x 3 mm, was used. This simple geometry was chosen in order to facilitate interpretation of data and to simplify analysis of the relevant phenomena. A semi-circular shaped gate, 7.8 mm diameter, was located at the centre of the smaller side of the rectangle. A schematic of the mold cavity is given in Figure 4.7. The mold was cooled by circulation of water, using a Sterlco heating-cooling unit, Model 7000. The temperature of the water was maintained at 30 ± 2 °C.

The injection molding machine was interfaced with a Cromenco microcomputer, for both data acquisition and process control. A schematic of the injection molding machine with the computer interface and instrumentation is shown in Figure 4.6. Data acquisitions could be accomplished at a rate of up to 100 times per second using assembly language programs. The mold cavity was equipped with four pressure transducers, P_1 to P_4, and four temperature sensors, T_1 to T_4, fitted flush to the inner surface of the cavity walls. However, only two of each were used in this study. The locations chosen were near the gate, P_1 and T_1, and at the centre of the cavity, P_3 and T_3. Pressure transducers were also installed at the barrel nozzle

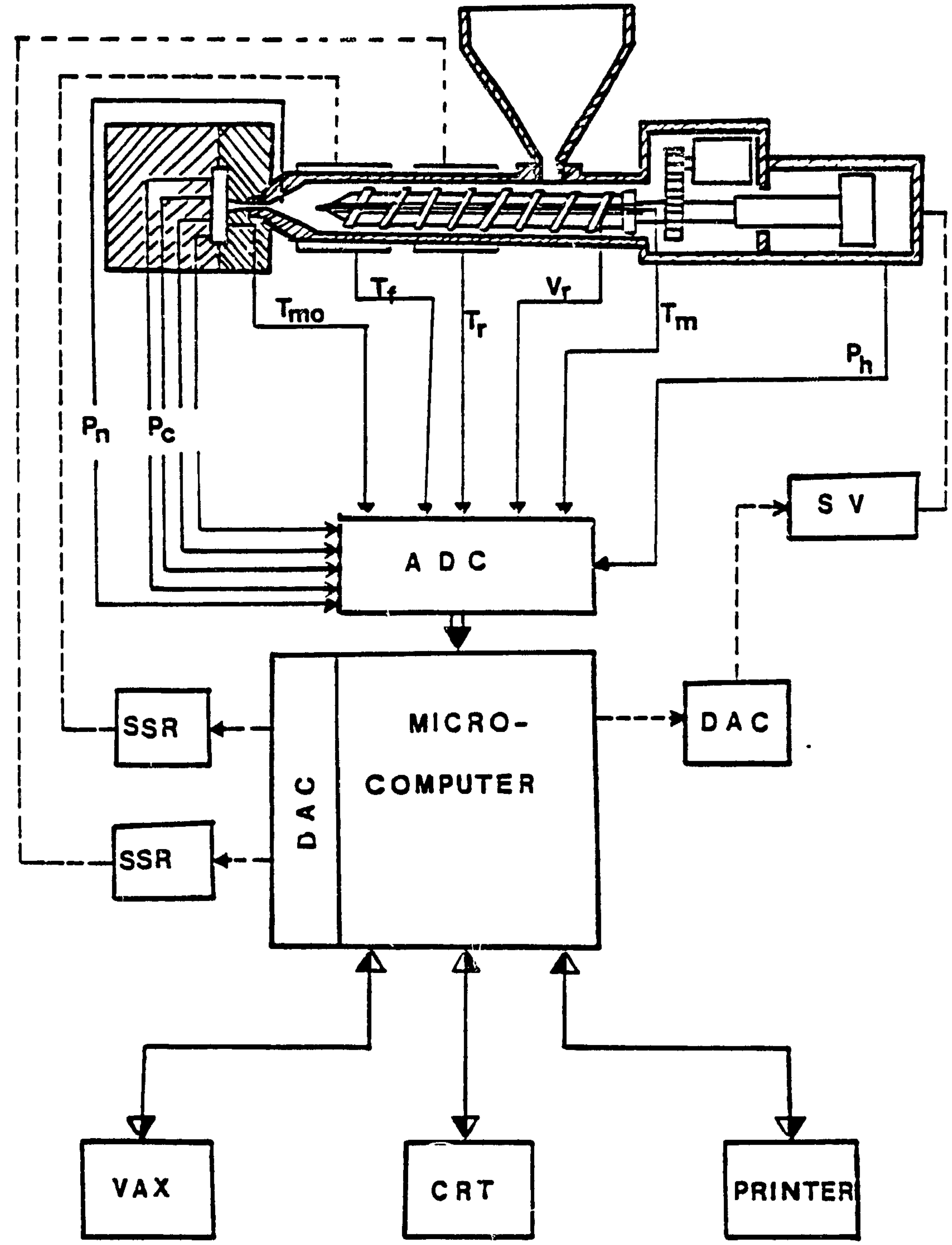

Figure 4.6 Schematic of the injection molding machine and computer interface.

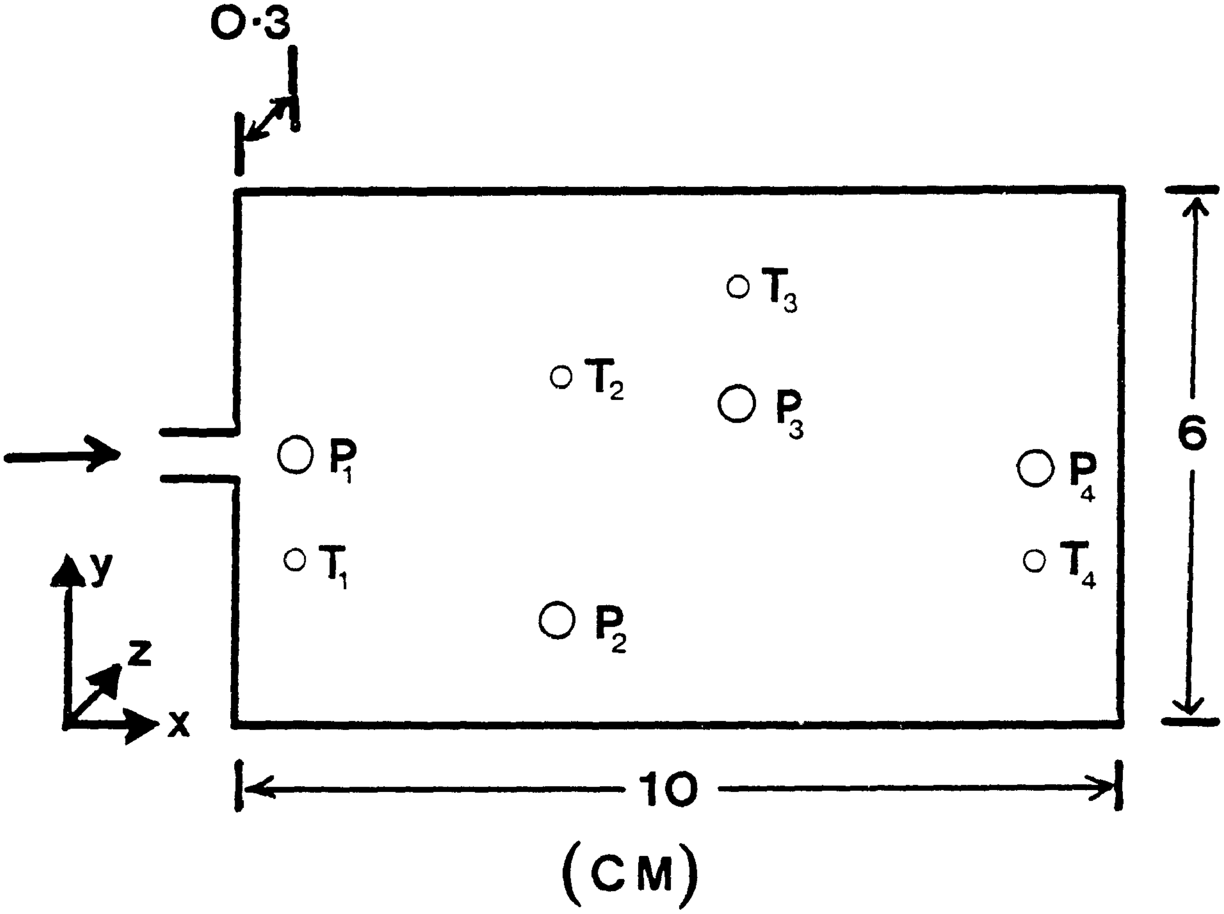

Figure 4.7 Schematic of the mold cavity and the location of pressure and temperature probes (P - pressure transducers, T - thermocouples).

and on the hydraulic line, in order to monitor the polymer pressure and the hydraulic oil pressure, respectively. A thermocouple was located at the tip of the screw to monitor polymer melt temperatures. A linear displacement transducer, as well as a velocity transducer, were attached on to the screw. Only linear displacement measurements were recorded in this study, since only eight channels could be monitored simultaneously.

All of the pressure transducers were calibrated using a special pressure calibration device. The millivolts readings were measured as functions of the pressure, and calibration equations were fitted. Calibration equations were fitted for the thermocouples from the known value of the e.m.f. for the specific type of thermocouple. The linear displacement transducer was calibrated by moving it and recording the position as well as the millivolt reading.

The injection molding variables, such as injection pressure, injection or filling time, hold pressure, hold time and cycle time could be manipulated by either machine or computer control. Machine control was employed in the present study, and the computer was used only for data acquisition. Computer control was not used in order to avoid fluctuations in process variables as a result of computer control strategies.

The injection molding conditions employed in the experimental design are shown in Table 4.3. When changing one

TABLE 4.3

4.3 Injection molding variables

PROCESSING VARIABLE	VALUES USED		
MATERIAL	POLYPROPYLENE		
REINFORCEMENT	30% WT. SHORT GLASS FIBERS		
MOLD TEMPERATURE (°C)		30	
COOLING TIME (sec)		30	
INJECTION TIME (sec)	1.0 (LIT) (a)	1.5	2.0 (HIT) (a)
MELT TEMPERATURE (°C)	200 (LMT) (a)	240	280 (HMT) (a)
HOLDING TIME (sec)	0.0 (LHT) (a)	1.0	2.0 (HHT) (a)
HOLDING PRESSURE ($N/m^2 x10^7$)	1.03 (LHP) (a)	1.72 (CEN) (a)	2.41 (HHP) (a)

REPLICATES WERE PROCESSED AT THE CENTRAL VALUES

ALL OTHER MACHINE VARIABLES WERE HELD CONSTANT.

(a) These letters give designation of experiments; Y and Z were used to indicate pure and reinforced polypropylene, respectively, e.g. ZLMT - indicates reinforced polypropylene processed at the low melt temperature condition.

of the variables, all other machine variables were held constant. For example, in the case of varying injection speed, only a servo-valve opening on the injection ram pressure line was changed; for varying melt temperature, the temperature setpoints of the barrel heaters were changed. Before collecting samples, the system was purged by injection into the air and then by molding a large amount of samples until a consistent steady state was achieved. At least 10 SFRTP moldings were collected for each set of processing conditions. The molded samples were stored in a constant temperature room at 23 °C, 1 atm. and 50% relative humidity. Measurements were carried out on sets of samples produced and kept at identical conditions, in order to eliminate variations due to aging.

4.4 Composite Characterization

4.4.1 Microstructure

In order to study the microstructure of the moldings, various locations in the molded plaques were selected as shown in Figure 4.8. Measurements were taken in the thickness direction only at the six points from the surface to the centre, because of the symmetry of the molded part which was established during preliminary experiments. A variety of techniques were employed to study the microstructure, both qualitatively and quantitatively, as described below.

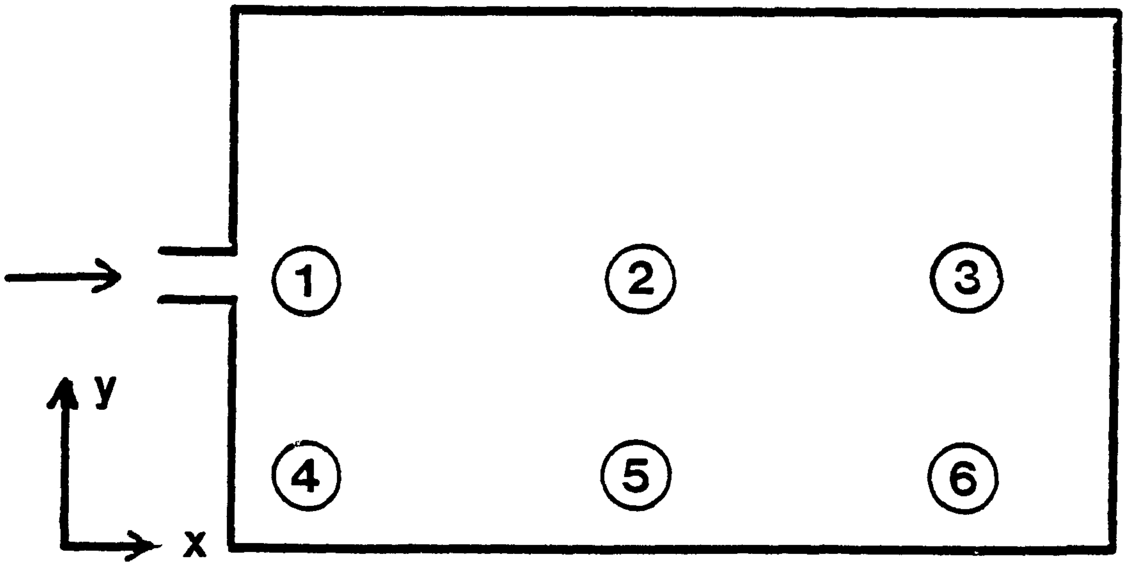

Figure 4.8 The locations of positions 1-6 for microstructural analysis.

4.4.1.1 Microtoming

Rectangular pieces were removed from the designated locations and mounted on Plexiglas sample holders, using Krazy glue, in order to facilitate microtoming. At each of the six positions, microtomed layers were removed in the x-y plane from the top surface towards the centre. Microtomed layers in the x-z plane were also used for analysis. One molding was used for obtaining microtomed samples for each of the measuring techniques used for evaluating microstructure. A sliding Reichert Microtome Model OME, with a steel knife, was used. The knife and the sample were mounted such that the cutting direction was at 90° to the plane of interest and the knife was inclined at 15°. Microtomed layers with thicknesses varying from 20 to 100 microns were used for the various experimental techniques. After cutting, the microtomed sections were gently pressed flat between microscope slides and temporarily stored before further testing. Preliminary experiments to evaluate microtoming samples frozen in liquid nitrogen and at room temperature revealed no significant differences.

4.4.1.2 Photomicrography

Optical micrography was carried out using a Reichert Zetopan-Pol polarization microscope. This was used for studying the matrix morphology as well as the fiber orientation and length. The optical properties of the matrix are dependent on the polarizability of symmetrical arrangements of the molecules. The morphology becomes evident when the samples are viewed under cross-polarized light, in which case spherulites show up in a characteristic Maltese cross pattern.

Microtomed sections of 20 micron thickness were mounted on glass slides, using immersion oil and a glass cover slip. The polarization stages were set at right angles to each other. The sample was then placed in the rotating stage and rotated until a position of maximum darkness was achieved. The sample was then rotated 45° to a position of maximum brightness, at which a photograph was taken. The films used were both in Polaroid and 35 mm format.

4.4.1.3 Scanning Electron Microscopy

Samples for Scanning Electron Microscopy (SEM) were obtained by breaking the samples under liquid nitrogen in both x-z and y-z planes (see Figure 4.6). In this way, the microstructure variation in the thickness direction could be viewed. The samples were mounted and then metallized by a Polaron sputtering apparatus with Au-Pd alloy. A JEOL JSM-T300 instrument was used to view the samples and take Polaroid photographs at varying magnifications.

4.4.1.4 Experimental Techniques for Measuring Fiber Phase Parameters

Techniques to measure fiber orientation include optical microscopy and contact micro-radiography. Vincent and Agassant [89] used optical microscopy for observation of fibers located in a polished plane. Burns and Pennington [132] measured fiber length distribution by a wire sieving method. This can also be done by using optical photomicrographs and by automatic image analysis systems. Automatic image analysis is rapid and effective, but the equipment and software costs make the process rather expensive. Also, it is not obvious that dependable systems are available for analysis of concentrated fiber composites. One alternative is to use less sophisticated semi-automatic methods. In such methods, the operator uses a magnetic pen to locate the end points of each fiber. This requires 10 to 20 minutes to digitize a 400 fiber slide. A computer program can then be used to calculate lengths and angles.

Fiber imaging may be achieved in two ways. Microtomed layers of the material can be placed under a polarized light microscope and subsequently photographed. The photographic images of the fibers appear much sharper, if the sample surface is covered with a liquid of refractive index close to that of the polymer. The sample can be heated for 5-10 seconds slightly above the softening point to eliminate knife traces.

Another way of obtaining fiber micrographs is by Contact Micro-Radiography (CMR) [87]. In this technique, thin samples (100-150 microns) are cut, using a slow speed diamond cutting blade. The section is laid onto a fine grain photographic plate and exposed to an uncollimated, unfiltered beam of X-rays. The resolution obtained depends on the grain size of the photographic plate and the width of the penumbra. The contrast depends on the difference between the X-ray absorption coefficients of the fibers and that of the matrix material. The fiber images are much clearer and sharper if the fibers are made of high lead content glass.

The variety of techniques were explored for the measurement of fiber phase properties.

(1) Optical microscopy and Contact Micro-Radiography (CMR) techniques were evaluated for obtaining fiber micrographs. Optical microscopy was found to be the optimum technique based on available resources and achievable photographic quality, and this technique was used.

(2) A fully automated fiber analysis program developed jointly with the Department of Electrical Engineering at McGill University [133] and a semi-automated system developed during this work were evaluated for measuring fiber length and orientation. The semi-automated system was found more suitable.

(3) Thermo-Gravimetric Analysis (TGA) was used to obtain measurements of fiber concentration.

4.4.1.4.1 Fiber Orientation and Length

Microtomed sections, approximately 50 μm in thickness, were obtained in the x-y plane, i.e. parallel to the surface. Precautions were taken to ensure that the orientation of the microtomed layers relative to the plaque as well as the position in the depth direction were recorded. Microtomed samples were mounted on microscope slides, using immersion oil. A Reichert Zetopan-Pol microscope was used to obtain photographs of the layers under transmitted light and at 100 times magnification.

Digitization of the fiber images was carried out using an Applicon CAD/CAM/CAE system interfaced with a VAX 11/780 computer. The process consisted of fixing the window size to correspond to the dimensions of the photograph placed on the digital pad. The operator then placed the pen cursor at the end point of each fiber in turn, thus reproducing the fibers on the screen. The coordinates were then processed by a FORTRAN program to generate the angle and length of each individual fiber. Subsequently, the distribution functions were calculated. Typical photographs of fibers alongside the reproduced digitized images are shown in Figure 4.9.

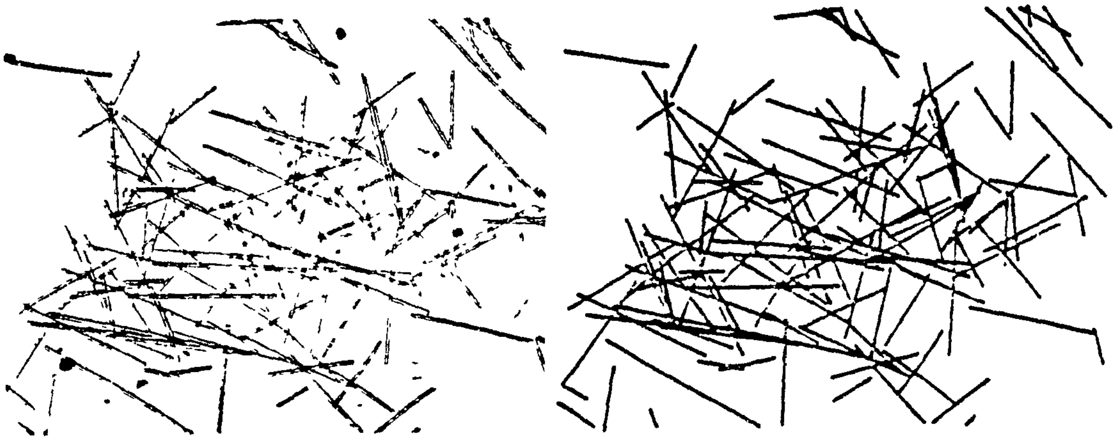

(a) Photomicrograph of Glass Fibers (matrix removed) (x45)

(b) Regenerated Image on Applicon CAD/CAM System

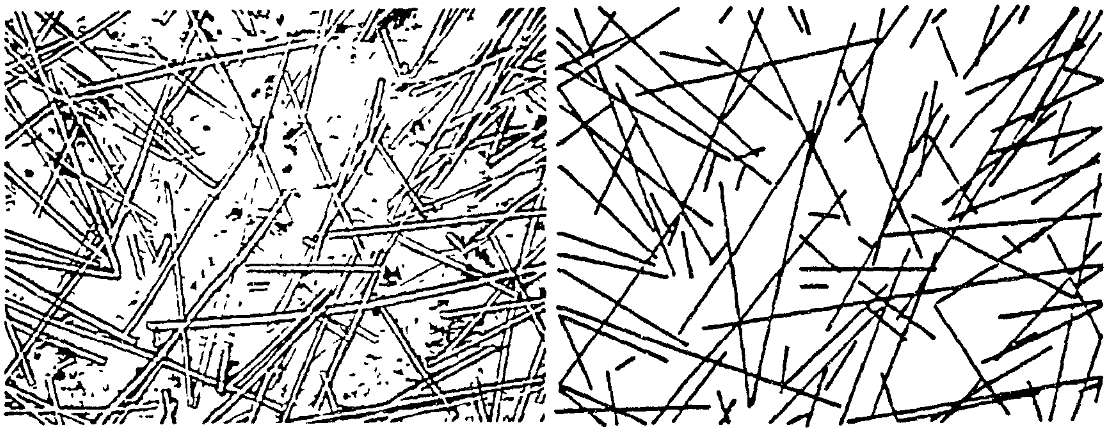

(c) Photomicrograph of Glass Fibers in Injection Molded Samples (x100)

(d) Regenerated Image on Applicon CAD/CAM System

Figure 4.9 Photographs and digitized images of fibers.

4.4.1.4.2 Thermo-Gravimetric Analysis

Fiber concentration was measured using a General V2.2A DuPont 9900 TGA system. The aim was to remove all of the matrix by burning, thus leaving behind the glass fibers. The sample was placed in a platinum pan and then introduced into the induction-heated chamber. The temperature and weight were allowed to stabilize and then the run was started. The temperature was increased at a rate of 20 °C/min to 575 °C. The temperature was kept at this value until the weight was stabilized. A nitrogen atmosphere was provided to prevent combustion with unwanted by-products. The initial and final steady state weights were used to calculate the fiber concentration.

The TGA was calibrated using standard weights. An initial run with a blank sample pan was carried out at the beginning and end of each set of experiments, in order to correct for any weight discrepancies due to the temperature. After each run, the sample holder was immersed in a Bunsen burner flame to free it of any volatile organic contaminants. At the beginning of each run, the weight of the empty sample pan was set to zero.

4.4.1.5 Experimental Techniques for Measuring Matrix Parameters

Some of the techniques that may be used for the characterization of matrix microstructure include Differential Scanning Calorimetry (DSC), density columns, sonic modulus, X-ray diffraction, birefringence, infra-red dichroism, small angle light scattering and electron microscopy. These techniques have been used quite effectively in studying pure polymers. However, some of them cannot be used for studying polymer matrices in SFRTP.

The glass fibers are a hindrance to some of the above techniques because they scatter light and radiation. The glass fibers can be removed by hydrofluoric acid. However, the resulting voids could interfere with some of the measurements. The following techniques were evaluated for microstructural characterization of the matrix in the present work.

(1) Differential Scanning Calorimetry (DSC) to obtain data regarding sample crystallinity, morphology, and thermal behaviour.

(2) Fourier Transform Infrared Spectroscopy (FTIR) to obtain data regarding molecular orientation in both the crystalline and amorphous phases;

(3) Wide Angle X-ray Diffraction (WAXD) to support DSC and FTIR results;

(4) Photomicrography, using cross polarized light to

study spherulites and crystallite distribution;

(5) Electron microscopy to view the microstructure and fiber matrix adhesion.

4.4.1.5.1 Fourier Transform Infrared Spectroscopy

Molecular orientation was measured for both the crystalline and amorphous phases using infra-red dichroism. Infra-red dichroism is a non-destructive technique that provides a quantitative measure of molecular orientation [35,134,135].

The method used was based on the work of Kissin, et al. [136] and is described in Appendix I. Samples were microtomed in the X-Y plane at the designated positions, proceeding from the skin to the core. The thickness of the samples was 50 microns. The sections were sufficiently thin to ensure good resolution of measurements, but thick enough to avoid surface damage by microtoming. The reference direction was taken to be the X-direction (ie. the direction of flow from the gate).

The FTIR study was carried out, using a Nicolet 7199 FTIR instrument. A gold wire grid polarizer (Perkin Elmer Part no. 186-0243) was used to polarize the infra-red radiation. A total of 128 scans were taken and averaged for each spectrum. Three spectra were taken for each layer: an unpolarized spectrum obtained without using the polarizer, a parallel polarized spectrum with the sample reference direction being parallel to the polarization direction, and a perpendicular polarized spectrum with the sample reference direction perpendicular to the polarization direction. The scans were in the frequency range 4000 cm^{-1} to 400 cm^{-1}.

4.4.1.5.2 Differential Scanning Calorimetry

Differential Scanning Calorimetry was carried out to measure crystallinity and specific heat as well as to give some qualitative insight regarding the crystalline structure. Experiments were carried out using a Perkin Elmer DSC-7.

Samples were microtomed, in the X-Y plane, with thicknesses of 100 microns and approximate weights of 1 - 3 mg. The microtomed samples were then cut in a circular shape and sealed in aluminum pans. The DSC was calibrated using the melting point of indium at 156.60 °C and with a heat of fusion of 28.45 J/gm. All samples were scanned by heating at a rate of 10 °C/minute from 50 °C to 240 °C. High heating rates introduces error when the instrument is ineffective in responding to and controlling fast temperature changes. On the other hand, low heating rates permit material changes during the measurement. A baseline was obtained by placing empty pans in both the sample and reference holders. Individual scans were made by placing the sample pan in the sample holder and an empty pan in the reference holder.

4.5 Reproducibility of Measurements

In many of the experimental techniques employed, the errors involved were difficult to estimate. In these cases, many experiments were performed to examine the reproducibility of the measurements. The data for each case are presented in the appropriate section in chapter 5. The measurements in which the error could be estimated are examined below.

The error estimate ϵ_y for a dependent variable y can be estimated from the equation below:

$$\epsilon_y = \left\{ \left[\frac{\partial y}{\partial x_1}\epsilon_1\right]^2 + \left[\frac{\partial y}{\partial x_2}\epsilon_2\right]^2 + \ldots \left[\frac{\partial y}{\partial x_n}\epsilon_n\right]^2 \right\}^{1/2} \qquad (4.10)$$

where

$\epsilon_1, ..\epsilon_n$ = the errors in the variables $x_1 \ldots x_n$.

The above equation is used in the calculation of the errors of some of the measurements presented below.

(1) Crystallinity

The equation that was used to calculate crystallinity, χ, is:

$$\chi = \frac{1}{\Delta H_{theor}} \left\{ \frac{\Delta H_{meas}}{W} \right\} \qquad (4.11)$$

where:

ΔH_{theor} = 153 J/gm.

W = weight of the sample

The errors in the measured and calculated quantities are estimated to be:

Variable	mean	error.
ΔH_{meas}	90.0 ± 0.25 mJ/mg	0.28%
W	10.0 ± 0.01 mg	0.1%
ϵ_x		0.6%

(2) Crystalline orientation

The equations that were used to calculate orientation in the crystalline phase are:

$$f = \frac{1}{2}\left\{(3P - 1)\right\} \tag{4.14}$$

where

$$(A_{841}/A_{809})_{//} = D = NP/(1-P) \qquad (N=5.8) \tag{4.15}$$

The errors in the measured and calculated quantities are estimated to be:

Variable	mean	error.
D	1 ± 0.05	5%
ϵ_p		0.6%
ϵ_f		0.9%

(3) Fiber Orientation

The equation for calculating the orientation function is:

$$f = \frac{1}{2}\left\{ 3\langle\cos^2\phi\rangle - 1)\right\} \tag{4.16}$$

The experimental errors are estimated to be:

Variable	mean	error
ϕ	45° ± 1.5°	3.3%
ϵ_f		5.0%

CHAPTER 5

5 RESULTS AND DISCUSSION

The injection molding cycle is a complex process involving simultaneous fluid flow of a visco-elastic fluid and heat transfer with phase change. In order to understand the process fully, it is necessary to study the relationships between processing variables and the microstructure. In this chapter, detailed experimental observation of the matrix phase properties such as crystallinity, morphology and molecular orientation distribution, and the fiber phase microstructure such as concentration, length and orientation distributions are presented. Fiber orientation is analyzed in more detail because of its importance in the determination of the final product properties.

5.1 Processing Characteristics

Figure 5.1 shows the injection molding data obtained for a typical single run. The cavity pressure profile can be divided into several parts. At the beginning of the cycle, the cavity pressure at the gate is zero. The melt is flowing through the runner system and has not yet reached the transducer location in the cavity. The lag time in the cavity pressure is the time needed for the melt to flow from the

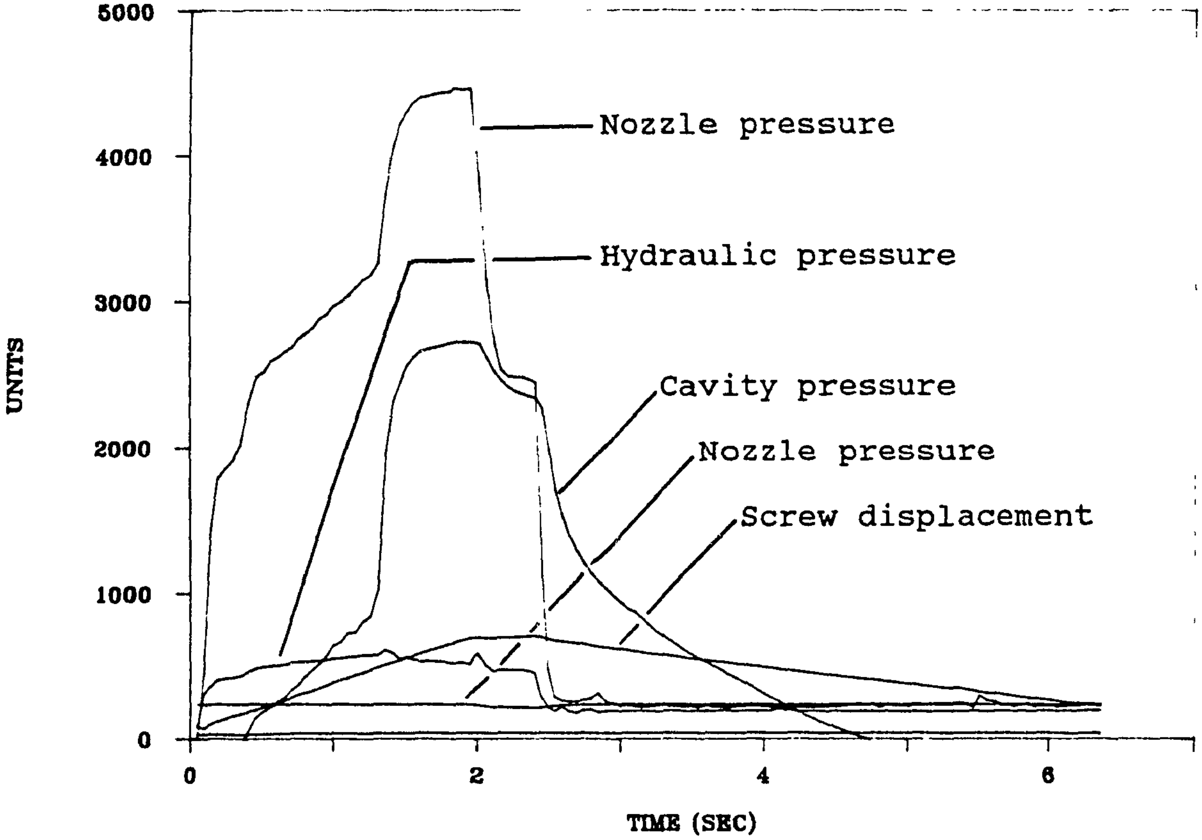

Figure 5.1 Typical injection molding processing data obtained during a single run (Condition ZCEN).

nozzle to the mold through the runner system. After the lag time, the cavity pressure begins to increase. The nozzle pressure increases more rapidly in order to force the melt through the runner system as well as into the cavity. The rate of pressure build-up is governed by hydrodynamic as well as heat transfer effects. When the mold is completely filled, the packing stage begins. The pressure in the cavity increases rapidly in this stage. During the holding stage, the cavity pressure is maintained or allowed to decrease slowly, depending on the holding pressure settings of the machine, as well as on the hydrodynamics, heat transfer and compressibility characteristics. Sometime during the holding stage, the gate solidifies. If the gate is not frozen, then the material flows back out of the mold into the nozzle during plastication. At the end of the holding stage, the pressure in the cavity drops off slowly to zero. This stage is the cooling stage in which the polymer solidifies until it may be ejected without damage. The duration of this stage is controlled by heat transfer and thermodynamic considerations. The pressure at the centre of the mold lags behind that at the gate. This is because the melt reaches the gate position first. Runs were recorded and samples were taken only after the process was operating smoothly without interruptions.
The repeatability of the data obtained is excellent as shown in Figure 5.2.

Figure 5.3 shows the cavity and nozzle pressure profiles

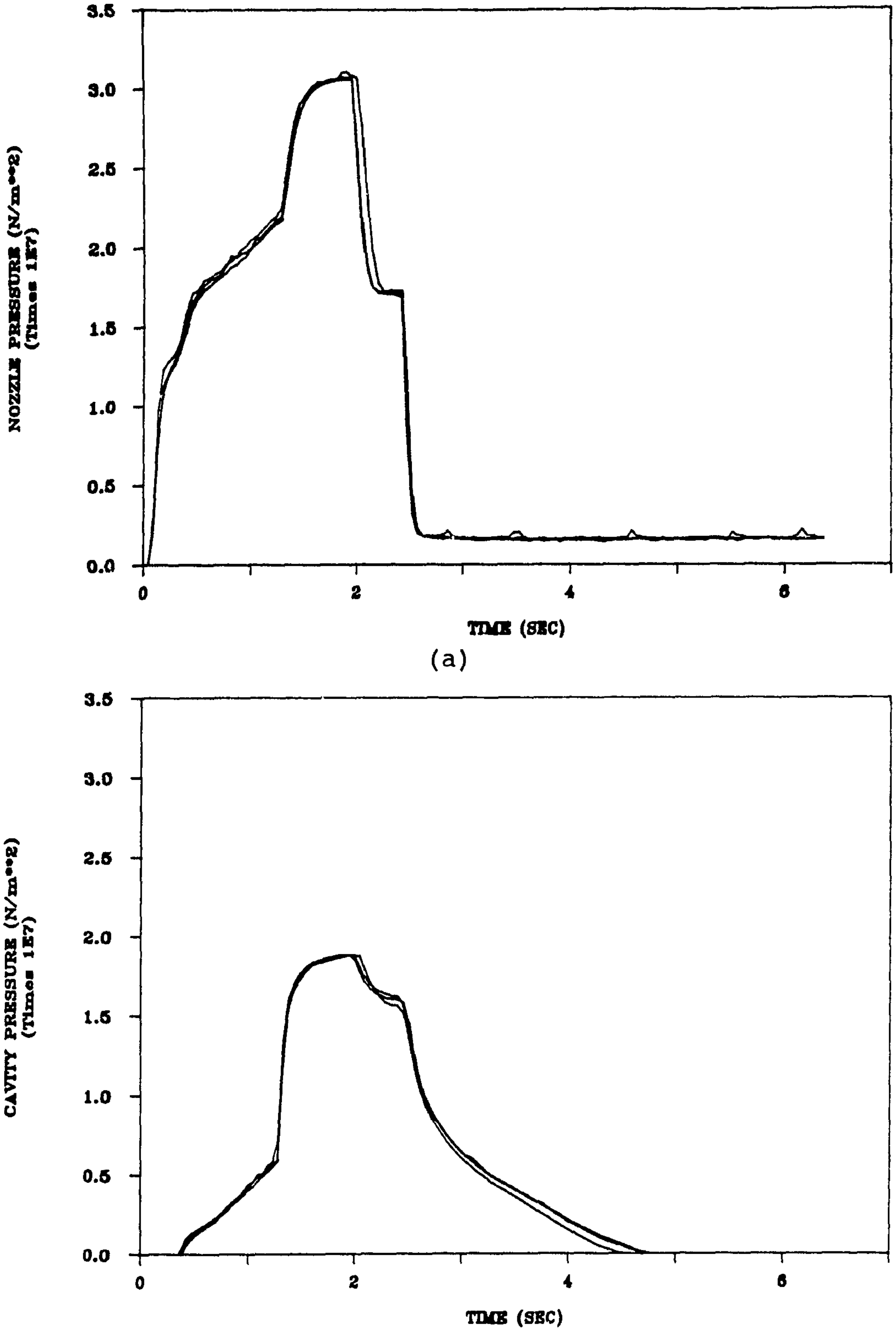

(a)

(b)

Figure 5.2 Replicates showing (a) the nozzle, and (b) cavity pressure profiles (Condition ZCEN).

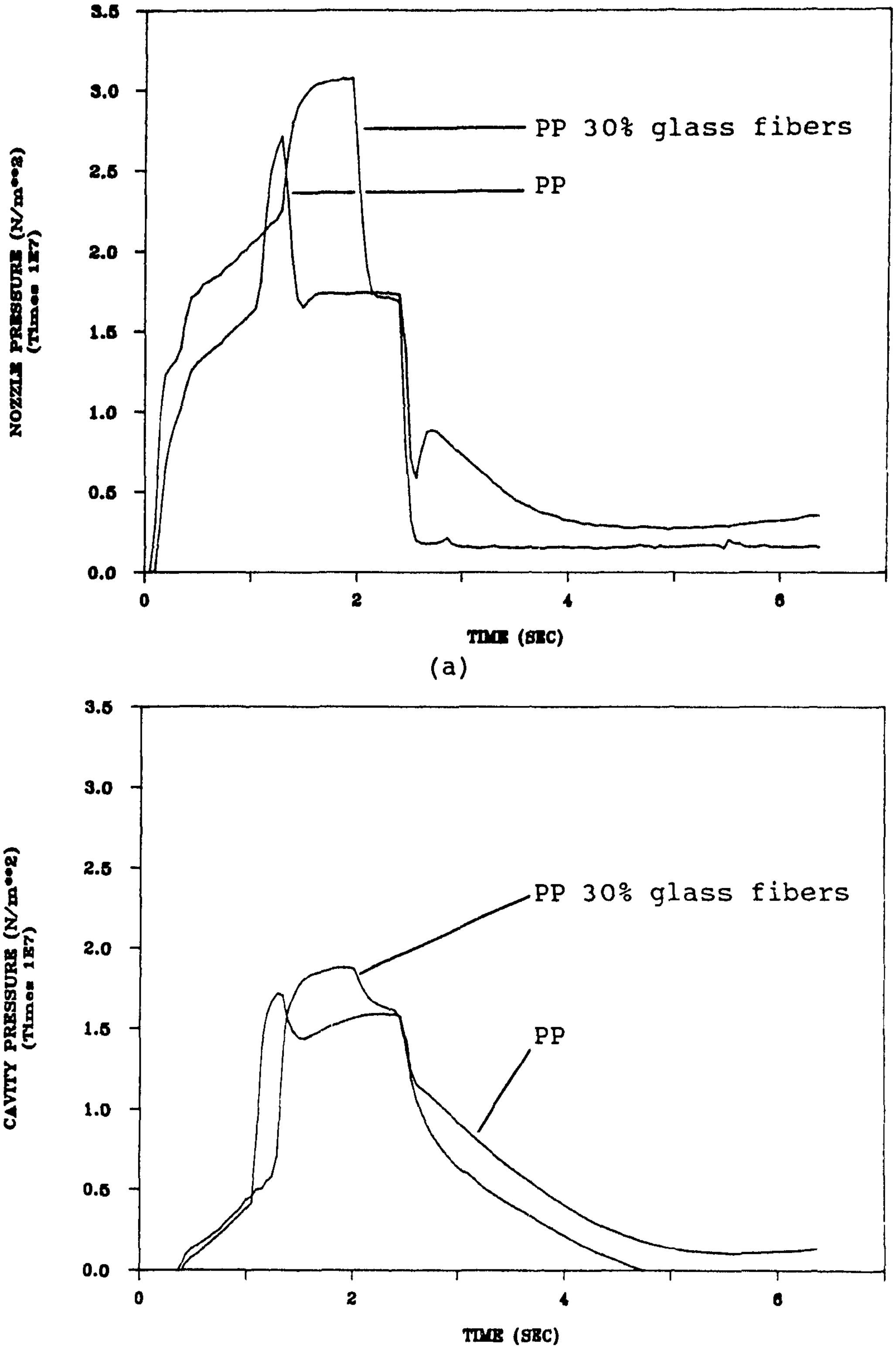

(b)

Figure 5.3 (a) Nozzle, and (b) cavity pressure profiles obtained with reinforced and unreinforced polypropylene (Conditions ZCEN, YCEN).

obtained for reinforced and unreinforced material processed under the same conditions (ZCEN and YCEN, see Table 4.2). The data show that the pure polypropylene fills the mold cavity faster, as a result of its lower viscosity [111]. The peak pressure at the nozzle does not build up to a high value when it is switched to the holding pressure of 1.03×10^7 N/m^2. The reinforced material shows a higher nozzle pressure and peak cavity pressure than that of the unreinforced material.

The cavity pressure for the unreinforced material drops to zero more slowly than for the reinforced material. This may be due to the higher thermal conductivity of the composite material which aids cooling and solidification. Although the filling time is longer, the cooling time needed is shorter for the composite material. In fact, the overall cycle is shorter for the composite.

The thermal properties of the reinforced material can have a profound effect on processing. Boldizar and Kubat [137] showed that there are significant variations in sealing time with polypropylene and polystyrene composites using different filler systems. They attributed this to corresponding variation in α, thermal diffusivity values. Thus, faster cycle times can be achieved by incorporating thermally active fillers into standard polymer melts. Large pressure overshoots in the nozzle pressure with filled melts have been observed [138]. Slow pressure build-up for the composite melts is expected because of the fast cooling.

The effect of melt temperature on the composite molding was quite dramatic, as seen in Figure 5.4. At a melt temperature of 280 °C, the maximum cavity pressure was substantially lower than at 200 °C. Filling was much faster at the high temperature, and both the cavity and nozzle pressures were quite low.

The effect of higher melt temperature is to decrease the viscosity of the polymer melt [5,111]. This lowers the filling time. However, the time needed to cool the part would be longer. In general, higher melt temperatures lead to shorter filling times but longer cycle times [139,140]. With low melt temperature, low mold temperature or thin cavities, the filling pressure is much higher because of the higher melt viscosity and polymer solidification during flow [141].

Figure 5.5 shows the effect of filling time. The rate of pressure build-up is faster in the 1 sec fill time condition. However, the cavity pressure does not achieve the same values as in the slower filling condition. At the slower filling time, the maximum cavity pressure is greater. The area under the pressure-time curve is much smaller for the faster filling condition. The faster filling rate shortens the overall cycle time.

Cox and Mentzer [142] showed that for short fill times, the viscous forces are high. The high shear stresses may give rise to viscous heating to increase the melt temperature. With decreasing fill time, the filling pressure passes through a

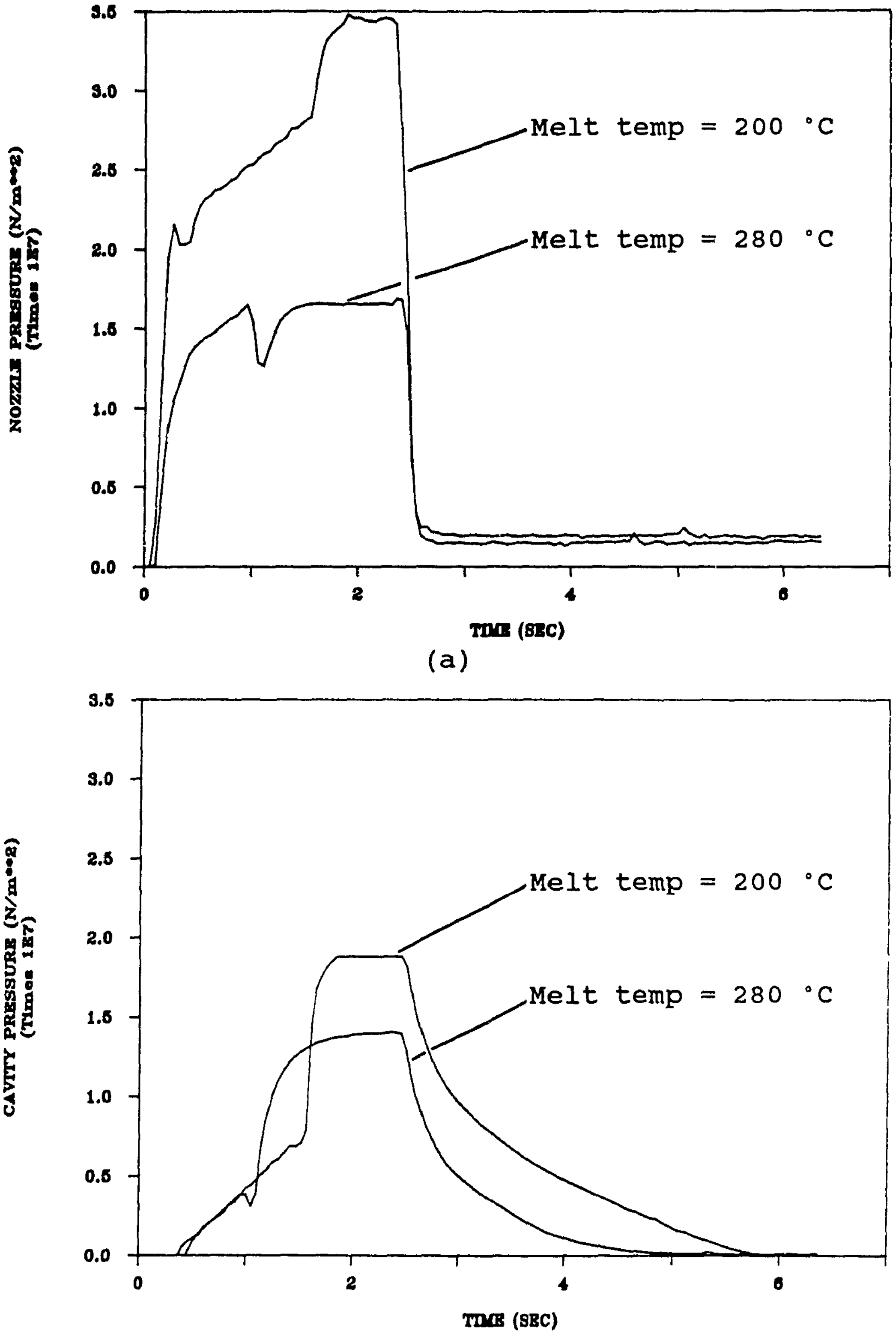

(a)

(b)

Figure 5.4 Effect of melt temperature on (a) the nozzle, and (b) the cavity pressure profiles (Conditions ZLMT, ZHMT).

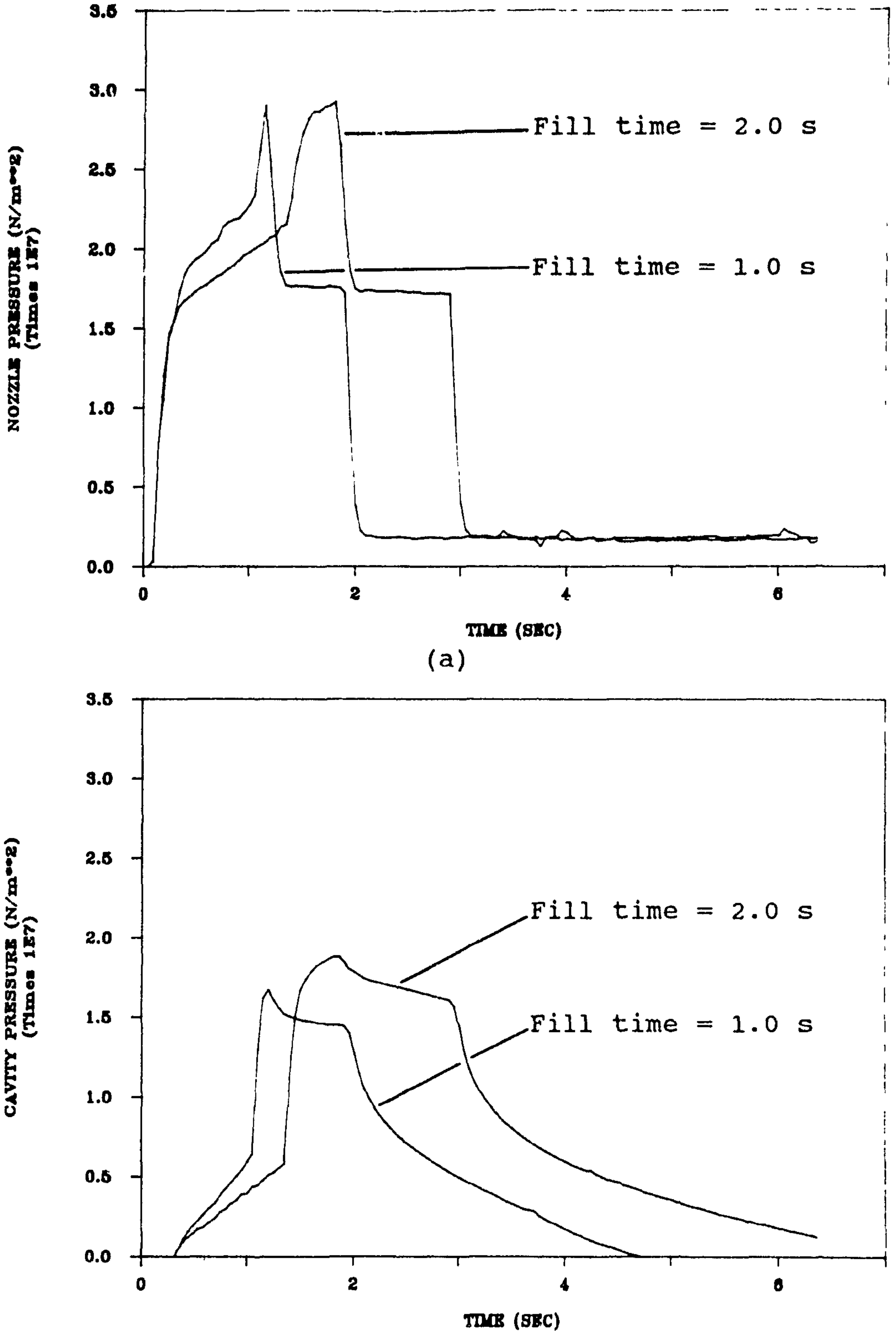

(a)

(b)

Figure 5.5 Effect of filling time on (a) the nozzle, and (b) the cavity pressure profiles (Conditions ZLIT, ZHIT).

minimum, then increases. In this region, the flow is heat transfer controlled. The fill time is dependent on such factors as mold geometry, heat transfer and hydrodynamic pressure.

Figure 5.6 shows the effect of holding pressure. The pressure profiles are the expected ones. The front portion of the profiles are the same. However, when the pressure switches to holding, the pattern changes. The cavity pressure is maintained throughout the holding time for the higher holding pressure while it decreases for the holding pressure of 1.03 x 10^7 N/m^2. After the holding pressure is removed, an unexpected result is seen. The cavity pressure drops lower for the higher holding pressure. The most plausible explanation is that the gate does not freeze with a high packing pressure because of continual flow of the hot polymer melt. Thus, after the pressure is removed, there is back-flow. With lower pressure, there is little or no flow: thus, the gate freezes. When a high packing or holding pressure is used, the holding time should be extended to allow the gate to freeze.

Figure 5.7 shows the effect of holding time. The front regions of the profiles are the same. With no holding time, the nozzle and peak cavity pressures drop very sharply. This is a result of back-flow through the still molten gate.

Usually, the cavity pressure decreases slowly during the cooling stage. At the point when the nozzle pressure drops, the cavity pressure does not show the same sharp decrease.

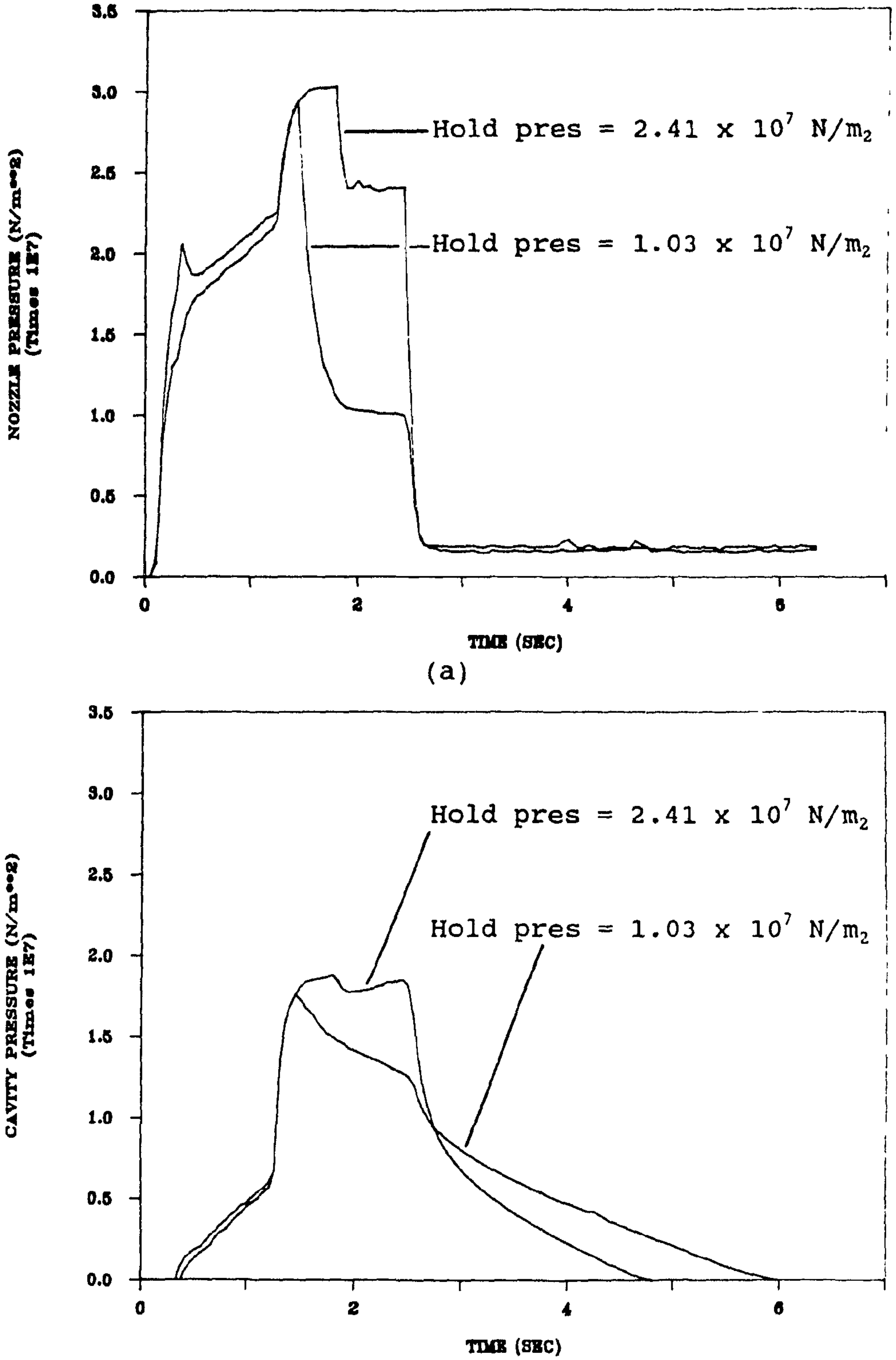

(a)

(b)

Figure 5.6 Effect of holding pressure on (a) the nozzle, and (b) the cavity pressure profiles (Conditions ZHHP, ZLHP).

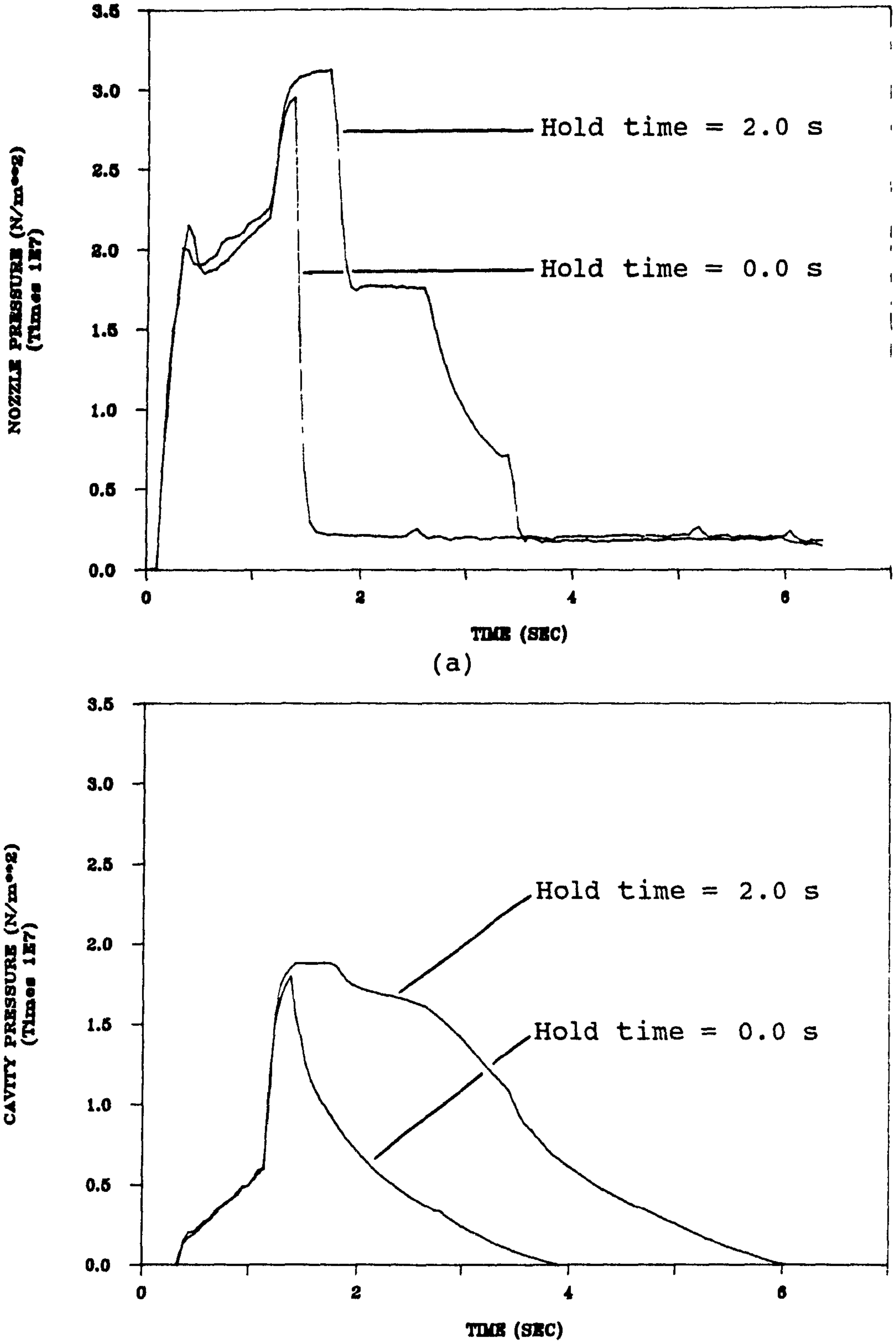

(a)

(b)

Figure 5.7 Effect of holding time on (a) the nozzle, and (b) the cavity pressure profiles (Conditions ZLHT, ZHHT).

The gate region is frozen in this case, preventing back-flow. The sealing time for this set of conditions is less than 2 seconds. However, for other systems, the sealing time would change depending on the thermal characteristics. In general, decreasing the holding pressure time, enhances the back-flow tendency of the melt, thus reducing part weight and dimensions [143].

Packing pressure effects on part dimensions, warpage and mechanical properties have been documented [144-149]. Packing pressure results in more material being compressed into the mold. Greener [147] showed that density variations in the molding were attributed to the different values of pressure prevailing at the times of solidification of various polymer segments in the mold. Kamal, et al. [4,140] measured pressure variation at several points in the cavity during the filling and packing stages. The pressure was shown to decrease with the distance from the gate.

Koita [144] showed that melt temperature and part thickness have different effects on the packing pressure and on the filling pressure. Increasing the melt temperature or the thickness causes the filling pressure to decrease sharply, while the packing pressure shows increases. Thus, for thick parts or high melt temperature, the process is packing limited, while for low melt temperature or thin parts, the process is filling limited.

Darlington, et al. [148] studied pressure losses in the packing stage. They showed that the peak cavity pressure is always much lower than the nozzle pressure and it decreases from the gate even under isothermal conditions. This effect increases with increasing packing pressure. The melt flow in the packing stage is too small to account for the large observed pressure drop. Darlington attributed these effects to time-dependent properties of the polymer.

Only limited effort has been reported regarding the theoretical description and computer simulation of the packing stage [53,149].

5.2 Mold Shrinkage

Upon solidification in the mold, the part shrinks, unless additional material is compressed into the mold to compensate for this shrinkage. Occasionally, there are warpage effects due to inhomogeneous shrinkage brought about by nonuniform cooling or nonuniform relaxation of molecular orientation [150].

Part shrinkage was measured in the thickness direction at selected positions for five samples and then averaged. Shrinkage in the thickness direction was quite large compared to that in the longitudinal direction. Cox and Mentzer [142] showed that shrinkage in the thickness direction in composites was much higher than in the length direction, because of the constraints due to the glass fibers. The glass fibers inhibit relaxation of molecular orientation in the amorphous phase [150]. Shrinkage in the thickness direction is higher, since very few fibers are oriented in the thickness direction. Thus, shrinkage in this direction is not restrained by fibers.

Shrinkage is related to the Pressure-Volume-Temperature (P-V-T) characteristics of the material. The specific volume of the melt is defined at the melt temperature and the packing pressure. After cooling in the cavity, the average specific volume assumes its characteristic value at the temperature and pressure which prevail at the end of the molding cycle. However, the state of the matrix, i.e. crystallinity and molecular orientation are additional factors that are very important in defining the specific volume, and thus shrinkage, of the material [3,28]. A more crystallizable material will show higher shrinkage because of the higher packing assumed by the higher crystalline fraction. Oriented material will also show higher shrinkage when the molecules resort to random configurations during relaxation.

Figure 5.8 shows the mold shrinkage in the thickness direction, within ± 1 standard deviation of the mean for an injection molded composite sample. The shrinkage decreased from the gate to the far end of the mold as can be seen from the changes in positions 1 to 3 and 4 to 6. The positive values for mold shrinkage are probably the result of mold deformation during the molding cycle. The high pressure inside the mold sometimes deforms or separates the mold plates apart especially during packing and holding, when the highest pressures are experienced.

In general, for all samples, the mold shrinkage varied from 1 to 10 %, depending on the processing conditions. Figure 5.9 shows the mold shrinkage for reinforced and unreinforced injection molded samples. Both samples were processed at the same conditions. The reinforced samples show more shrinkage compared to the unreinforced material. This result has also been documented by Kubat et al. [151]. The thermal expansion of the glass fibers is negligible in comparison to the polymer. Since the composite has a lower

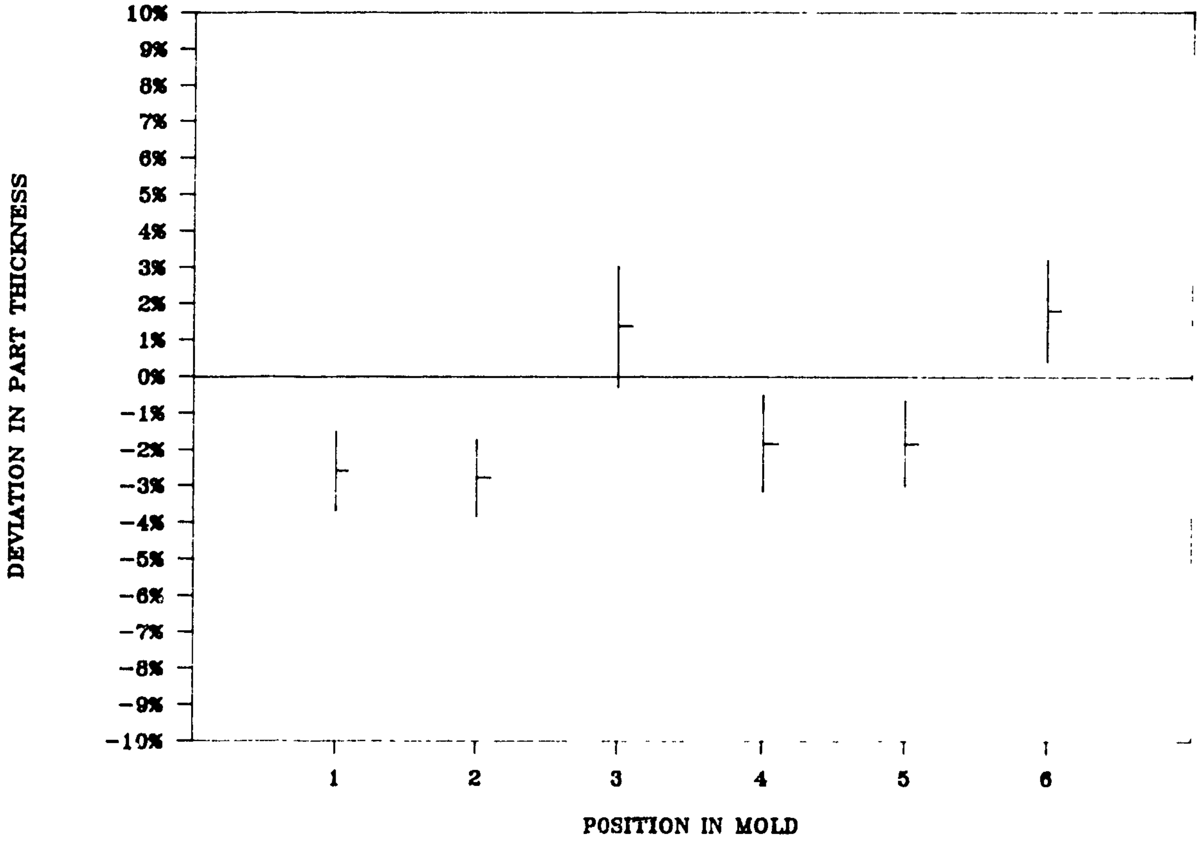

Figure 5.8 Mold shrinkage in injection molded samples, showing the mean ± 1 standard deviation (Condition ZCEN).

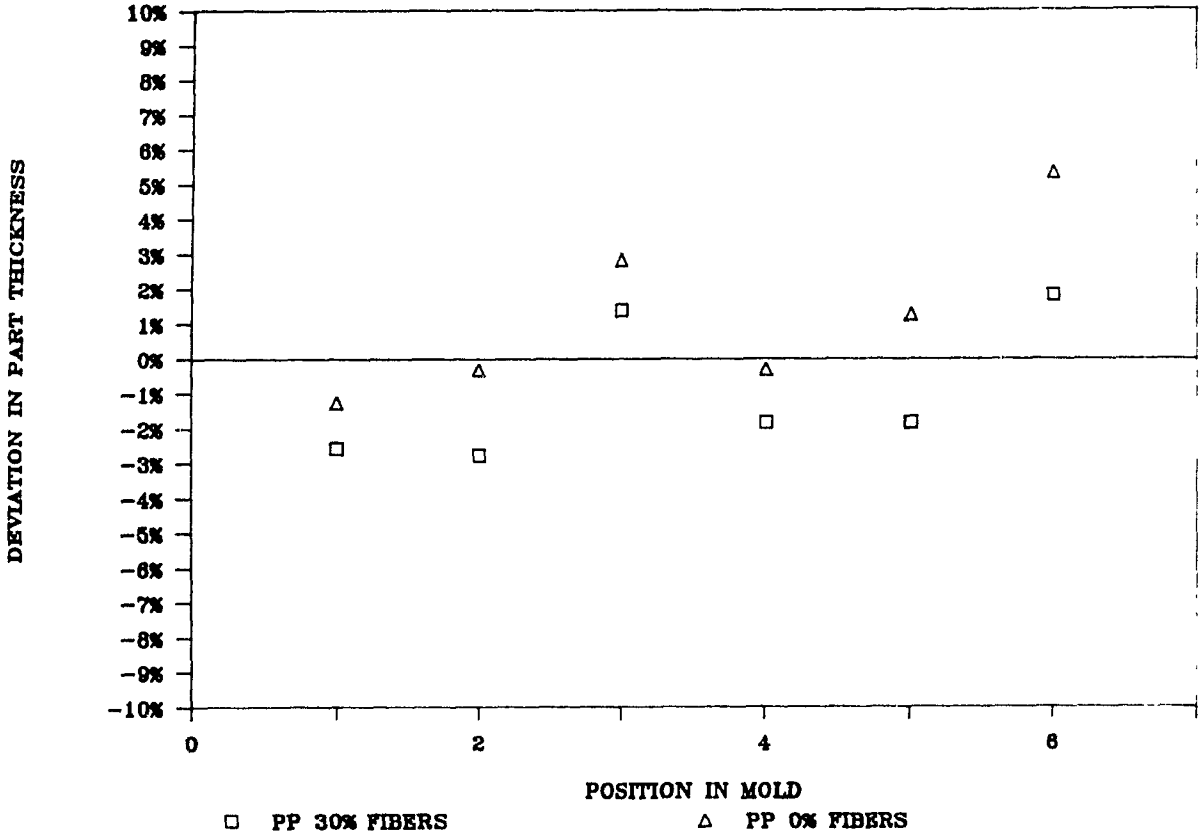

Figure 5.9 Mold shrinkage for reinforced and unreinforced polypropylene in injection molded samples (Conditions ZCEN and YCEN).

fraction of polymer, it would be expected that it should show a smaller shrinkage. The opposite results suggests that the glass fibers influence the shrinkage process. As will be shown later in the chapter, the molecular orientation in the composite samples is higher than in the pure polypropylene sample. The higher orientation due to the fibers leads to greater shrinkage when the oriented or deformed molecules are relaxed to their random conformation state.

Another point is that unreinforced polymer shrinks more in the flow direction (being unrestricted by glass fibers). This probably overpowers the shrinkage in the thickness direction, which is not the case with reinforced polypropylene.

The effect of the processing conditions on the shrinkage of the reinforced resin was also examined. Figure 5.10 shows the dramatic effect of melt temperature. With increasing melt temperature, the shrinkage increases. One reason for this is the larger difference in specific volume between the higher melt temperatures and the solidification temperature, as observed in the P-V-T relationship. Another reason is the enhanced molecular relaxation at the higher temperatures. Also, crystallinity tends to be greater for moldings obtained at the higher melt temperatures because of the longer cooling times.

Figure 5.11 shows the effect of filling time. The shrinkage is greatest at the fastest filling time.

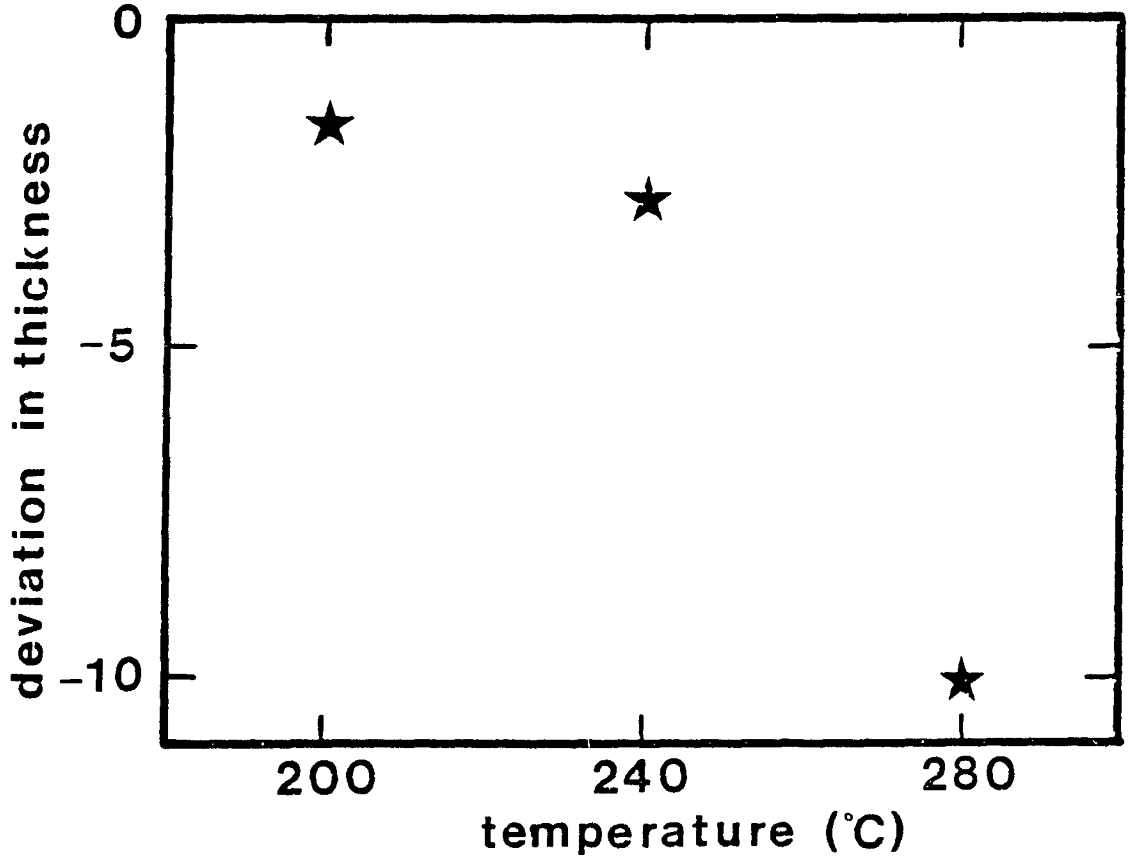

Figure 5.10 Effect of melt temperature on mold shrinkage.

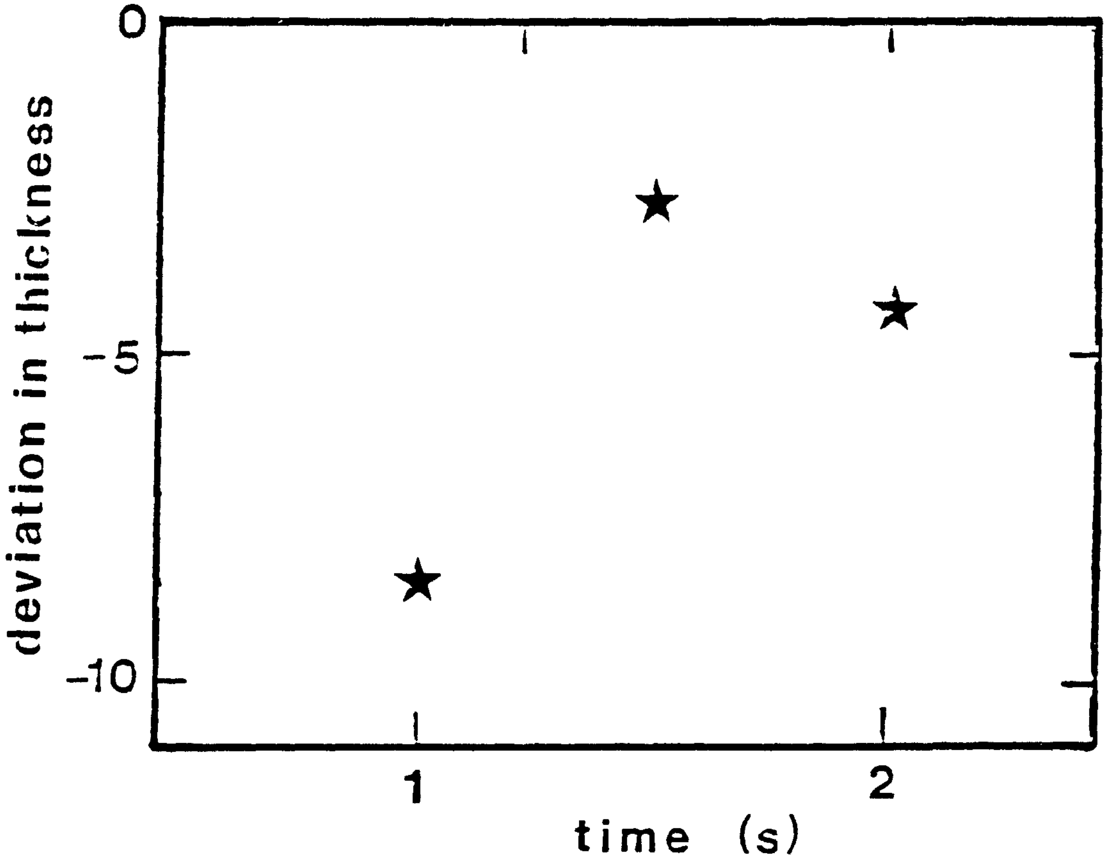

Figure 5.11 Effect of filling time on mold shrinkage.

Mold shrinkage appears to reach a minimum at a filling time of 1.5 seconds. Similar results have been found by Cox et al. [142], who observed a minimum of shrinkage at a fill time of 1 second. It appears that there are two competing processes for shrinkage. At low injection speeds, cooling of the melt raises the viscosity and produces higher stresses and orientation, thus yielding high shrinkage. At high injection speeds, high shear rates are obtained, thus causing higher orientation and shrinkage. In the intermediate range, a situation arises where the two effects are minimized, thus yielding the minimum in Figure 5.11.

The effect of holding pressure is shown in Figure 5.12. Mold shrinkage decreases with increasing holding pressure. This is expected, since more material would be packed into the mold with higher pressure. P-V-T data show that the volume change from a molten state at higher pressure to the frozen state is smaller than if the pressure is lower.

Figure 5.13 shows the effect of holding time. With no holding time, the shrinkage is large. The gate is not yet frozen and back-flow occurs as soon as the injection pressure is removed. A holding time of 1 second shows a marked effect on mold shrinkage. More material is packed into the mold and backflow is reduced or eliminated. Increasing the holding time to 2 seconds does not decrease the shrinkage significantly. Increasing the holding time beyond the time when the gate freezes does not decrease the shrinkage further since the melt

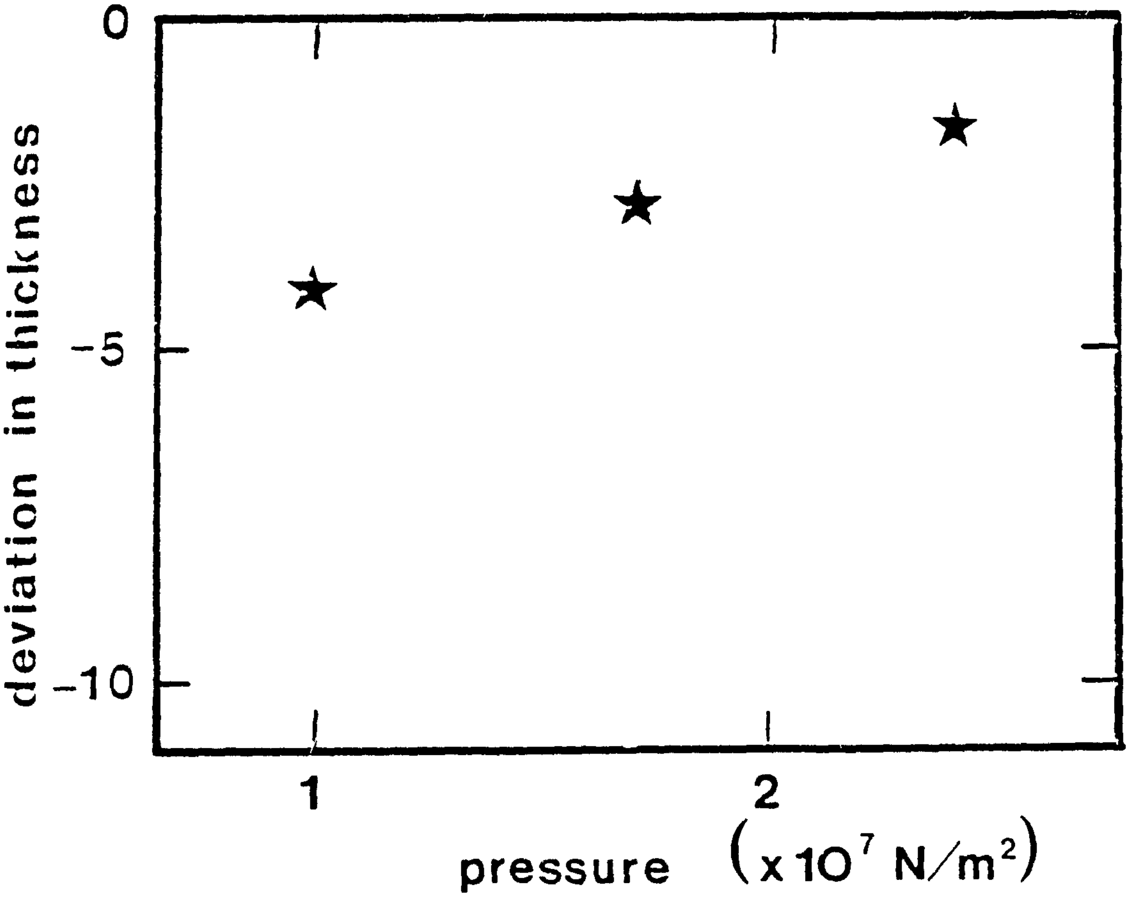

Figure 5.12 Effect of holding pressure on mold shrinkage.

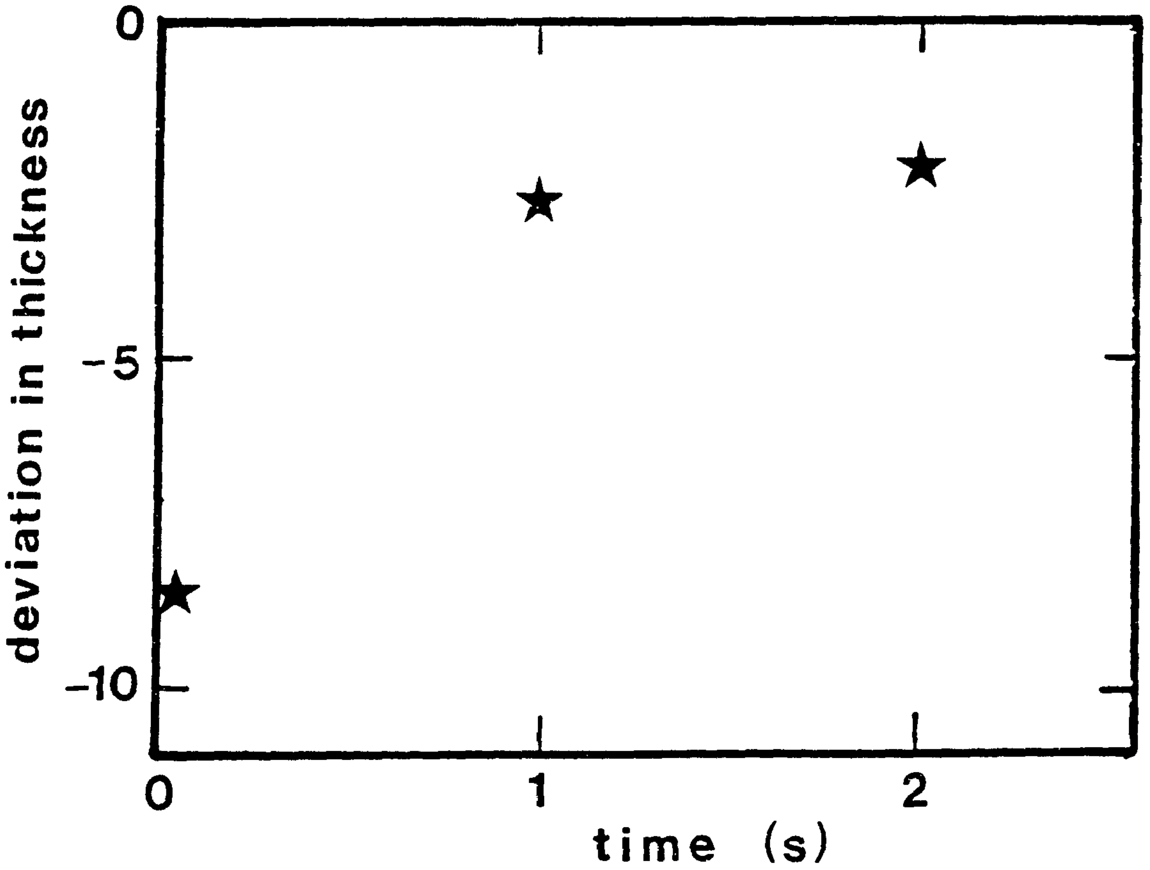

Figure 5.13 Effect of holding time on mold shrinkage.

in the cavity is isolated from the nozzle.

Gilmore and Spencer [139] showed that mold shrinkage was strongly affected by injection pressure as well as the holding time. Lower mold temperatures yielded lower mold shrinkage. They described the effect of processing variables on mold shrinkage with the help of empirical equations. These equations are useful for a limited number of materials and molds [152].

The final shrinkage can be seen to be related to the maximum cavity pressure as well as to the area under the pressure-time profiles. A greater area or maximum pressure yield lower shrinkage [72].

Shrinkage that is related to the frozen-in orientation is caused by the polymer melt flow. The differences in orientation from skin to core lead to skin-core variation in the shrinkage. Menges and Wubken [28] showed that the shrinkage in the flow direction was maximum at the surface. Near the surface, it decreased then passed through another maximum before dropping to zero at the core. The shrinkage in the transverse direction was also maximum at the surface and zero at the core but no maximum was present. This suggested the presence of biaxial orientation in the skin layer, high flow direction orientation in the intermediate shear zone layer, and complete relaxation in the core.

5.3 Photomicrography

The microtomed specimens were examined with the aid of cross-polarized light microscopy, in order to view the morphology of the samples. Injection molded polyethylene samples were also examined for comparison. The morphology of injection molded polyethylene has been studied extensively and is well established [12-23].

The morphology of injection molded polyethylene samples examined in the present study is in agreement with the results of other reported studies. The polyethylene morphology reveals the following features as shown in Figure 5.14:

(Ia) a trans-crystalline skin with no visible spherulites. At high magnification, a z-direction striations was observed;

(Ib) a clear intermediate layer with random spherulites growing in the direction of the core. It is not clear if this region, which is not quenched quite as quickly as the outermost layer, forms a part of the skin layer;

(Ic) next to the above two layers, there is an extremely curious structure. It can be seen as lines lying at a small angle to the flow;

(II) a region of broken spherulites. The spherulites are easily seen, however, they are not as large as in the centre;

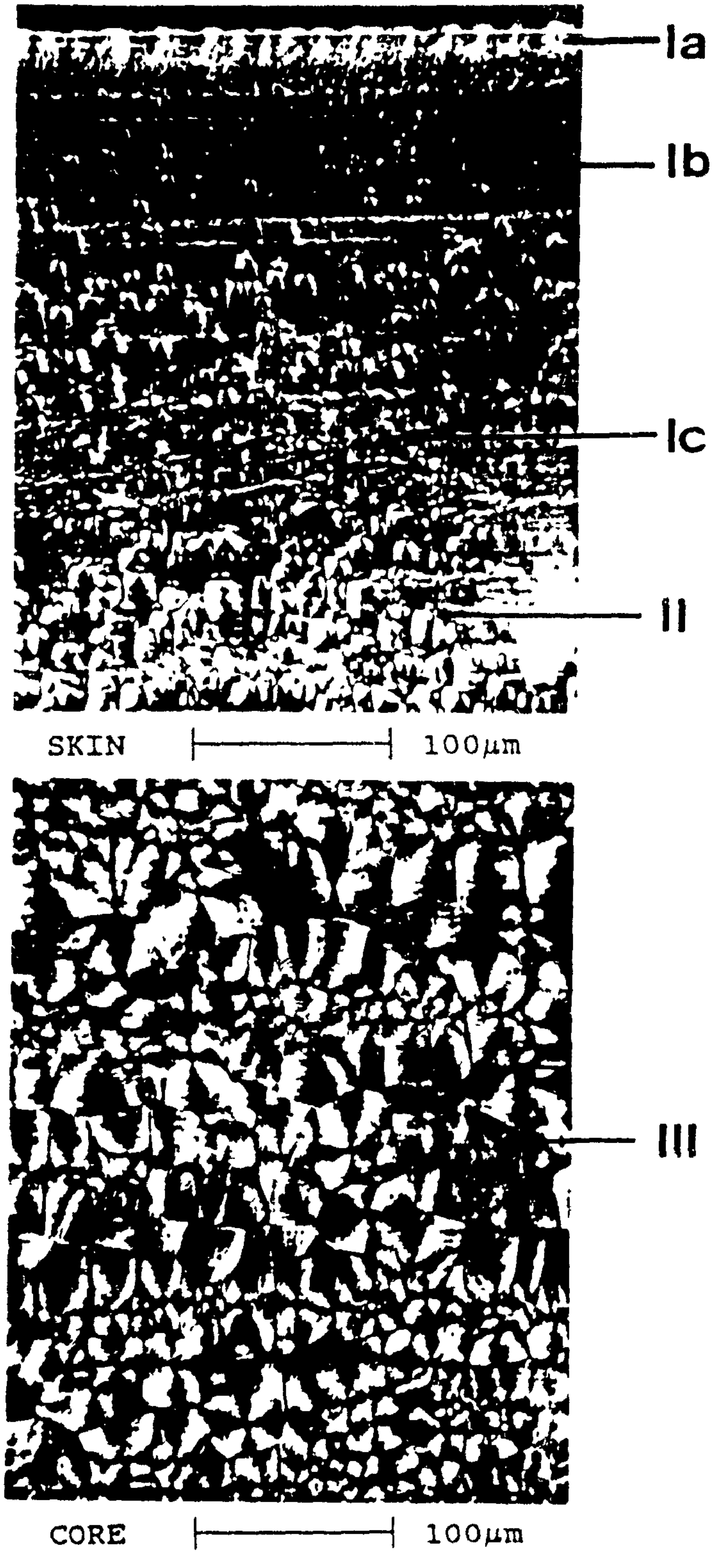

Figure 5.14 Cross-polarized photomicrographs showing the morphological characteristics of injection molded polyethylene (Condition YCEN).

(III)the core region takes up the majority of the thickness. The spherulites are clearly seen, increasing in size from the outer region to the centre. The spherulites are nucleated in a straight line running in the flow direction.

The evidence reveals that there are several morphological zones in the injection molded sample. It is usual to group these zones into three distinct layers designated as the skin, the intermediate layer and the core layer, or, even four distinct layers as indicated by Kantz [13], Menges, et al. [20], Fitchum, et al. [21], and Kamal, et al. [3,23]. These represent layers formed by different processes, whereas the assimilated layers may reflect transitions zones between two type of disparate structure. It has been proposed that the layers are formed during the filling, packing and cooling stages of the injection molding process [15]. Normally, the thickness of the skin layer is smaller than the layer solidified during the filling stage [23].

The skin layer (Ia - Ic) has a thickness of 0.05-0.25 mm, which changes with the position in the molded part and with the material used [13,15,23]. This layer consists of stacks of lamellae with chain axes in the flow direction and growing in the depth direction. This is the effect of the steep temperature gradient from the skin to the core. The lower temperature on the skin side induces rapid nucleation but inhibits growth on this side, resulting in spherulites elongated towards the core [23].

The intermediate layer (IIa - IIb) has a thickness in the range 0.25-0.80 mm, and is affected similarly as the skin [3]. It is composed of very small spherulites close to the gate, and increasingly larger spherulites away from the gate [3]. It has been proposed that the intermediate layer is formed during the packing stage, with crystallization of the lamellae taking place under high pressure [5,15]. The increase in pressure induces a higher melting point and increases the rate of crystallization, leading to thicker lamellae [153].

The core layer (III) consists of the majority of the material. The increase in size of the spherulites towards the centre is evidence of the decrease in cooling rate towards the centre. The location of the spherulites in a straight line along the flow path indicates that flow may play a role in the nucleation process.

The rate of spherulitic growth is the result of competition between the nucleation rate and the growth rate. The nucleation rate is proportional to the degree of undercooling ((T_m-T_c), the difference between the melt temperature and that at which crystallization is occurring). For example, at low crystallization temperature, T_c, the nucleation rate is high. The growth rate is inversely proportional to the undercooling, and it increases with increasing crystallization temperature. The maximum overall rate of crystallization occurs at a temperature in between the glass transition temperature (T_g) and the melting temperature (T_m) [153]. Higher temperatures lead to larger, less numerous spherulites, while lower temperatures lead to smaller, more numerous spherulites.

At fast cooling rates, the molecules do not have sufficient time to arrange themselves into well ordered crystallites. This results in lower crystallinity and less ordered crystals. With slower cooling rates, there is sufficient time for crystallization to occur in the form of more ordered and larger crystallites.

The photomicrographs for injection molded polypropylene, with and without glass fiber reinforcement, are shown in Figure 5.15 and 5.16, respectively. The photomicrographs of the polypropylene samples reveal no sharp, distinct spherulitic structure, as was obtained in the polyethylene samples. The structure consists of very small dark and bright patches of very small broken spherulites. It appears that the nucleation rate is much faster than in the polyethylene sample. The factor to consider is the presence of heterogenous nuclei [154]. This is likely because of the addition of a nucleating agent in the polymer by the manufacturer. The abundance of nucleation sites per unit volume will determine the size of the infringed spherulites.

The results show similar changes in structure from skin to core for both polypropylene and polyethylene samples, as

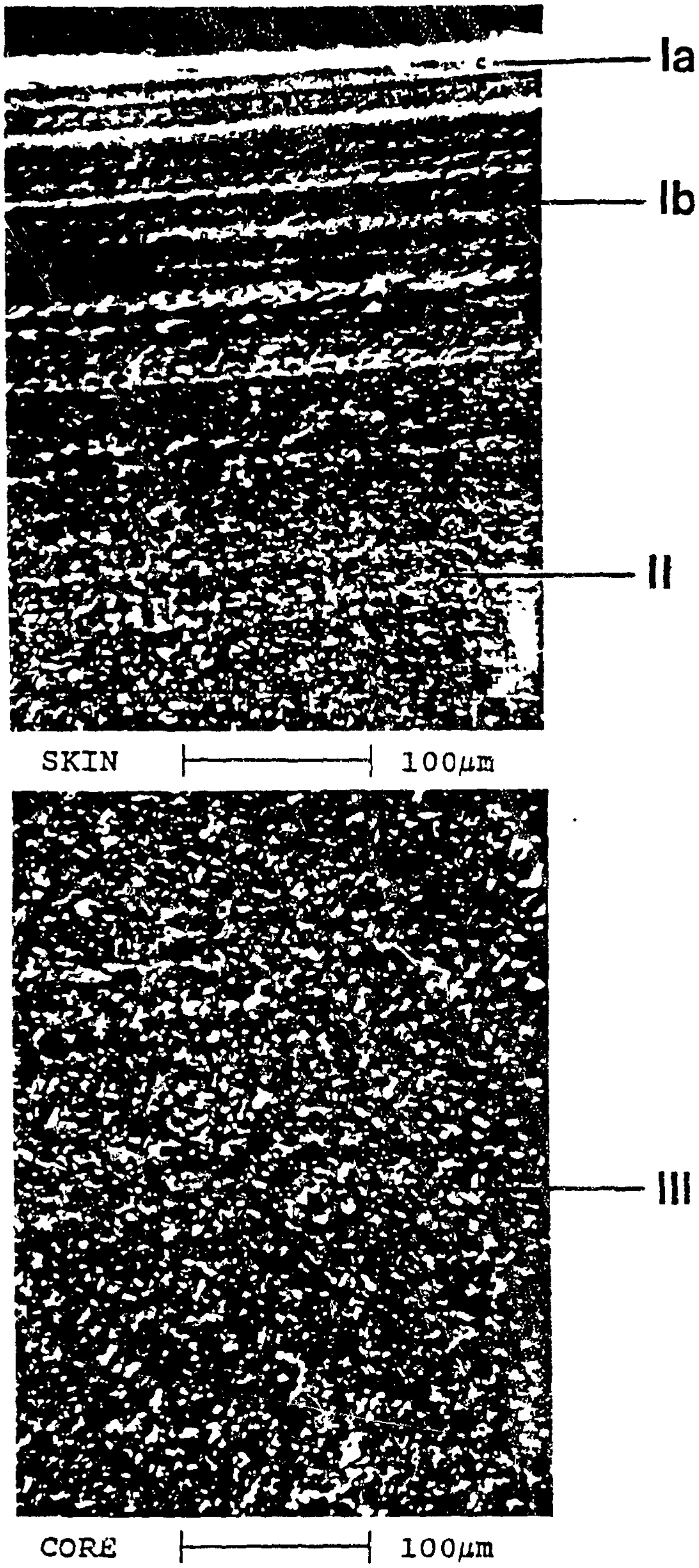

Figure 5.15 Cross-polarized photomicrographs showing the morphological characteristics of injection molded polypropylene (Condition YCEN).

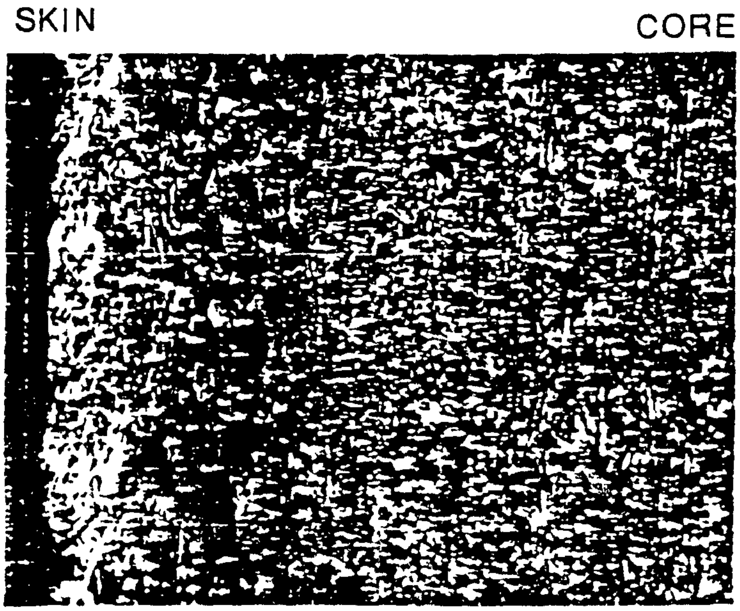

POLYPROPYLENE COMPOSITE

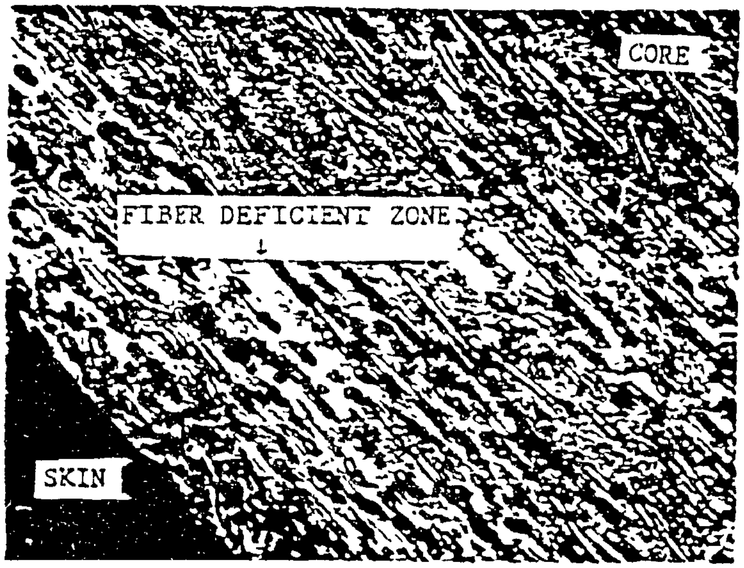

POLYPROPYLENE COMPOSITE

Figure 5.16 Cross-polarized photomicrographs showing the morphological characteristics of injection molded polypropylene composite.

seen by the light and dark bands in Figures 5.14 and 5.15. The crystal structure of polyethylene is more developed with larger spherulites, whereas the spherulites are not discernable at the same magnification in polypropylene.

It is difficult to discern the microstructure of the reinforced polypropylene, because of the optical interference of the glass fibers. In some cases, there is a layer with relatively few fibers as seen in Figure 5.16. This is seen mainly near the gate region. This layer may be produced by the high shear rate at the interface of the frozen layer and the melt.

5.4 Electron Microscopy

Scanning Electron Microscopy revealed useful qualitative information regarding the microstructure, in terms of fiber orientation and fiber-matrix bonding. It showed fibers that were lying in the plane of view as well as those perpendicular (i.e. protruding from the matrix). Holes were observed where the fibers were pulled out either perpendicular or at some angle to the crack surface of the matrix. The dislodging of fibers lying parallel or close to parallel to the crack surface resulted in long furrows.

Figures 5.17 show photographs of a sample broken in the y-direction so as to reveal the microstructure in the y-z plane. The surface region is shown at a magnification of 200. The change in fiber orientation from the surface to a depth of approximately 0.6 mm is quite complex. The fibers at the surface lie perpendicular to the plane of the photograph. This suggests orientation in the x-direction (flow direction). Next to the surface layer, there is a region where the fibers are parallel to the y-direction. Immediately following this, is a region of many holes, signifying more x-axis orientation. The amount of this x-axis orientation decreases as the centre of the molding is approached.

In the intermediate layer, the change of fiber orientation continues. The fibers change orientation from the x-direction to the y-direction. At the left of the photograph, DEPTH 0.00 TO 0.51 mm

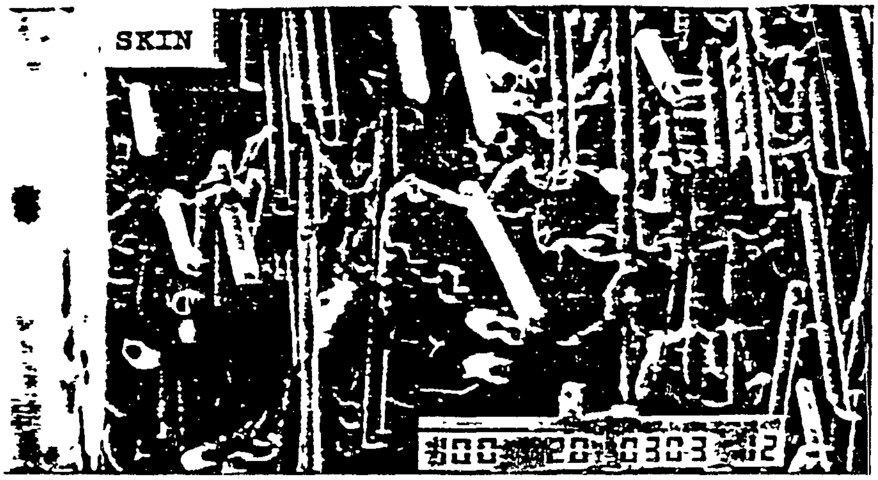

DEPTH 0.51 TO 1.10 mm

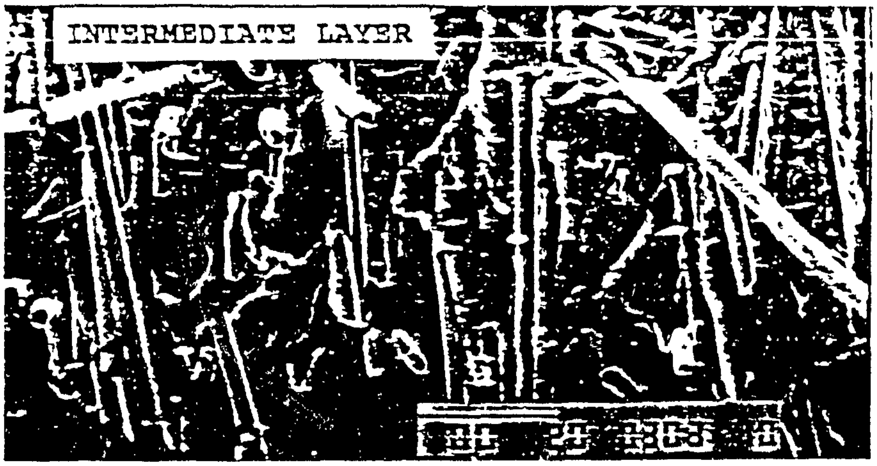

DEPTH 1.10 TO 1.70 mm

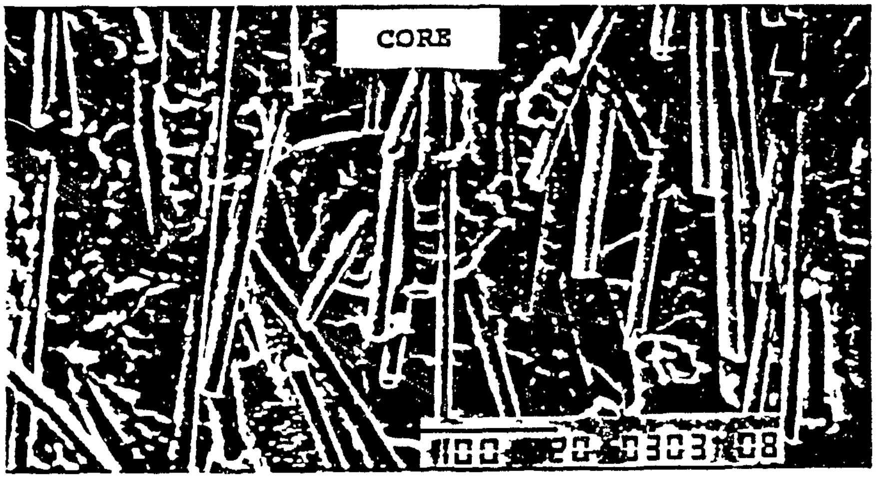

Figure 5.17 SEM photographs of an injection molded sample broken in the Y-Z plane (Condition ZCEN).

there are more holes and protruding fibers than on the right. In the region near the centre of the molding, the y-direction orientation of the fibers can be seen quite conclusively. There are almost none of the protruding fibers or holes in the photograph. In all of the photographs, practically none of the fibers can be seen to lie in the z-direction.

Figure 5.18 shows the photographs taken of the sample broken in the x-direction (i.e. showing the x-z plane). It shows the expected patterns. In the region close to the surface, the fibers lie in the plane of the photograph, in the x-direction. The change in fiber orientation from the surface to the centre follows the same trends as seen in the sample broken in the y-direction. At the centre, the fibers protrude out of the plane of the photograph. Thus, the orientation of the fibers is in the y-direction.

Scanning electron microscopy results show a clear trend, in which the fibers are highly aligned in the x-direction at the surface and at an intermediate depth and are highly oriented in the y-direction in the core. The results also show that all of the fibers are in the x-y plane i.e. none of the fibers lie in the z-direction (thickness direction).

Insight into the fiber-matrix interface can be gained from the photographs in Figure 5.19, which shows close-ups of the interface. Although the fiber-matrix contact appears good, there is evidence of poor bonding at the interface. The large number of furrows and holes in Figures 5.17 and 5.18 indicates

DEPTH 0.00 TO 0.51 mm

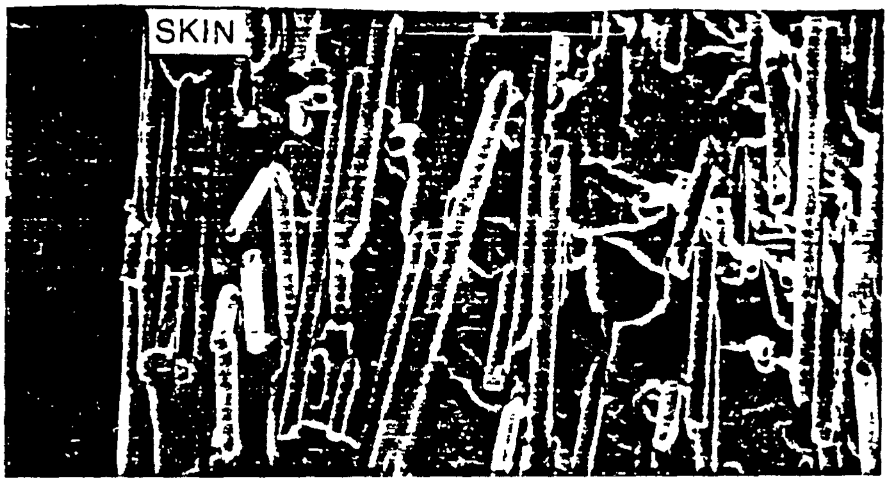

DEPTH 0.51 TO 1.10 mm

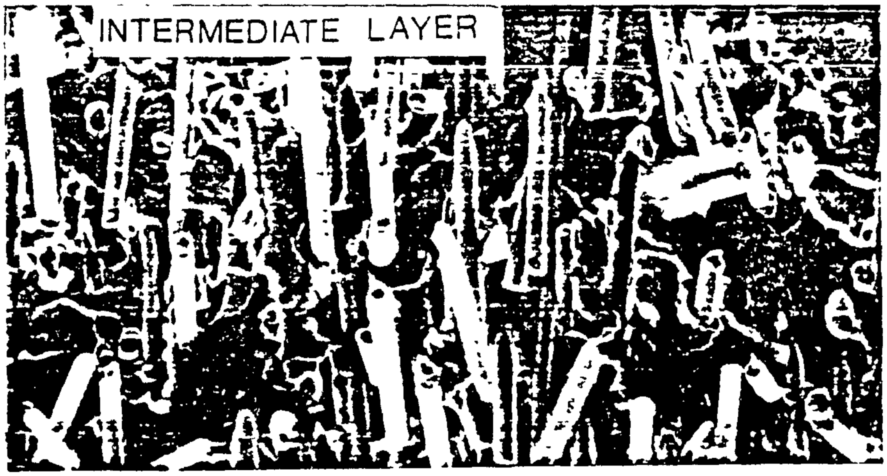

DEPTH 1.10 TO 1.70 mm

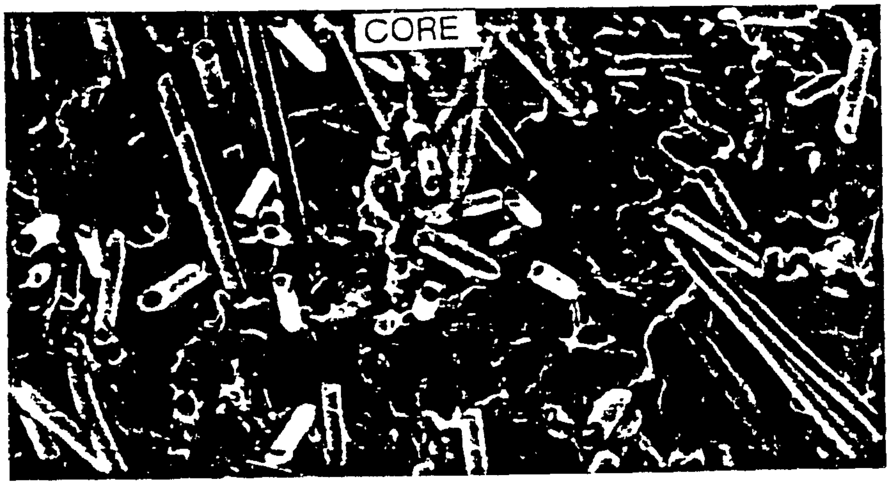

Figure 5.18 SEM photograph of an injection molded sample broken in the x-z plane (Condition ZCEN).

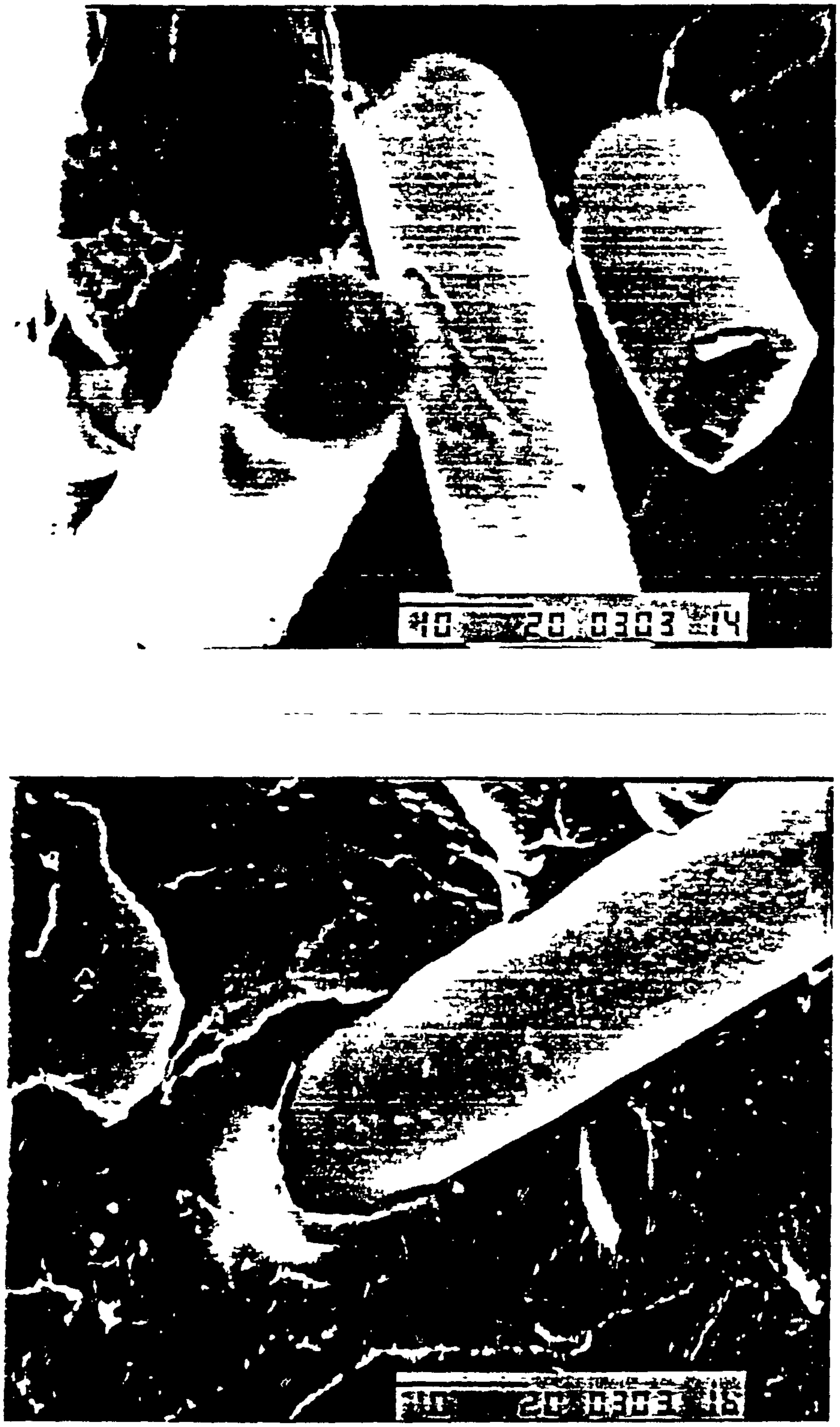

Figure 5.19 SEM photographs showing close-ups of the fiber-matrix interface.

that there are weaknesses in the fiber-matrix bonding. The close-up reveals a small gap between the fiber and matrix. The gap forms when the matrix material shrinks around the fiber due to density changes during cooling. The contraction forces appears to be stronger than the bond strength, thus causing the matrix to de-bond from the fiber. This suggests that the physical bonding between the fiber and matrix, provided by the silane coupling agent, is not strong. Also, shrinkage during crystallization may be more concentrated near the interface. The interfacial zone, crystallized epitaxially around the fibers, has been shown to have strong influence on stress transferral between the fibers and the matrix [155].

5.5 Thermal Behaviour

Many studies have been reported regarding the relation between crystalline structure and thermal behaviour of pure polypropylene [156-166]. There are conflicting explanations of the transition peaks that are observed during thermal analysis. It is generally agreed, however, that polypropylene is polymorphic, i.e. it can assume a variety of crystalline forms [49,156].

In this work, thermal analysis of both polypropylene and polypropylene composites has shown that the resin has a major melting peak, with a maximum at about 162 °C. Most scans also show a shoulder on this peak, on the lower temperature side, that moves from 155 °C to 158 °C.

There are also two shoulders on the lower temperature side of the main peak that only occur in the composite samples They are very small slightly overlapping peaks, designated as peaks I and II for the lower and higher temperature peaks, respectively. These sometimes exist as separate peaks. They are located at 140 °C and 147 °C. One peak at 142 °C can be seen in compression molded composite samples. The slight emergence of a shoulder at 142 °C can be barely noticeably in such samples.

The major peaks, which overlap to a great degree, are designated as peak III and peak IV. The major peak, in most cases, is IV but can be either III or IV, depending on the sample.

There have been many explanations for the double peak effect [35,157,158,160]. Melting peak III may be attributed to the fusion of the original crystals, its position being determined by competition between melting and recrystallization processes. Peak IV may be attributed to the fusion of crystals generated by the recrystallization process. This recrystallization effect has been used to explain the changes in relative amounts of III and IV peaks with various heating rates and temperatures. Samuels [35] has shown that two peaks, with ultimate melting points of 185 °C and 220 °C, were produced even in isothermally crystallized samples. Multiple peak endotherms are produced when two or more crystalline species are involved.

Yadav and Jain [157] observed the double peaks under isothermal crystallization conditions. They also concluded that the first peak was originally formed during the crystallization process, and the second peak was due to the melting of crystals of higher stability formed due to recrystallization of the original crystals.

Keith and Padden [158] studied the cross-hatched morphology of positive spherulites crystallized at 130 - 140 °C as an effect of branching. They attributed this morphology to small amounts of triclinic γ-form crystals formed at the α-form growth fronts. Jacoby, et al. [159] also studied multiple crystalline morphologies that melted around

150 °C, which they attributed to the β-form crystallites.

Another explanation of the double peak was given by Guerra, et al. [160]. They showed that both oriented and unoriented polypropylene exhibited a double peak, even though it was shown by x-ray analysis to have only α-form crystals. They proposed that the α form took two limiting forms, α_1 and α_2. Form α_1 is an ordered limiting structure having crystallographic symmetry with a well defined disposition of up and down helices in the unit cell. Form α_2, on the other hand, is the limiting modification with random distribution of up and down chains in each site of the unit cell. The first peak is related to the melting of the crystals having a structure nearer to the α_1 modification, and the second is related to the melting of the crystals of the α_2 modification. The α_1 to α_2 modification is reached only by passing through the melt. Thus, the double peak shape of the overall melting endotherm is explained in terms of competition of melting and recrystallization.

The first two peaks (I and II) observed in this work have not been reported by other researchers for normal crystallization processes. The only occurrences have been under high pressure crystallization in pure polymer samples [156,48]. The same types of peaks are observable in pressure crystallized polyethylene [161-166]. High pressure crystallization leads to both folded and extended chain crystals in the γ-form. This effect is reported to occur in low molecular weight fractions under high pressure. Separation of lower molecular weight polymer molecules may be induced by flow [167], hence making γ-type crystallization in injection molded samples very credible. At a pressure above 1500 atm., the majority of the sample crystallizes in the γ-structure. The stability of the γ-type crystal modification is probably due to the decreased volume available for packing of the helical chains into a crystalline lattice [48].

Prime and Wunderlich [165] showed the pre-peaks in polypropylene to be due to extended chain γ-type crystals of the low molecular weight portion. These were formed by crystallization of broad molecular weight distribution polymer under pressure. During crystallization under elevated pressure, the low molecular weight portion of the polymer segregates preferentially into a limited number of mixed crystals, each including a narrow molecular weight distribution. On faster crystallization, the molecular weight distributions become broader and overlap increasingly to obliterate the separate peaks.

A γ-to-α transition is observed at atmospheric pressure at around 145 - 150 °C. This is most likely due to the melting of the γ-phase, followed by recrystallization to the α-phase. This polymorphic transition takes place in the solid state and involves distortion but not breakdown of the lattice network. The α-cells can be obtained from the γ-form by slightly deforming the γ-lattice. This is quite different from the βto-α transformation, which must occur through a melt recrystallization process, since the two cells are very different.

5.5.1 Effect of Cooling Rates on Morphology

The experiments were carried out on thin compression molded samples that were cut to fit in the sample pan. This was done to obtain specimen of exact shape and size. They were heated in the DSC to 240 °C and held at that temperature for 5 minutes for complete melting and stress relaxation. They were then cooled at the set cooling rates, either in the DSC or in a quenching bath, to room temperature. Measurements were then made by heating the sample at 10 °C/minute to 240 °C. Figure 5.20 shows the DSC curves for samples cooled at various rates. At very high cooling rates, obtained by quenching in ice water bath and in a liquid nitrogen bath, there is only a broad α_2 peak. The α_1 peak appears at the rate of 80 °C/min, where it is the major peak. Upon lowering the cooling rates, the lower temperature α_1 peak increases at the expense of the other peak and shifts towards a higher temperature. At very low cooling rates, the α_1 peak appears alone and is now shifted to a position close to that previously held by the second peak. With slower cooling rates, the perfection of the more ordered α_1 crystals increases, thus resulting in a higher melting point.

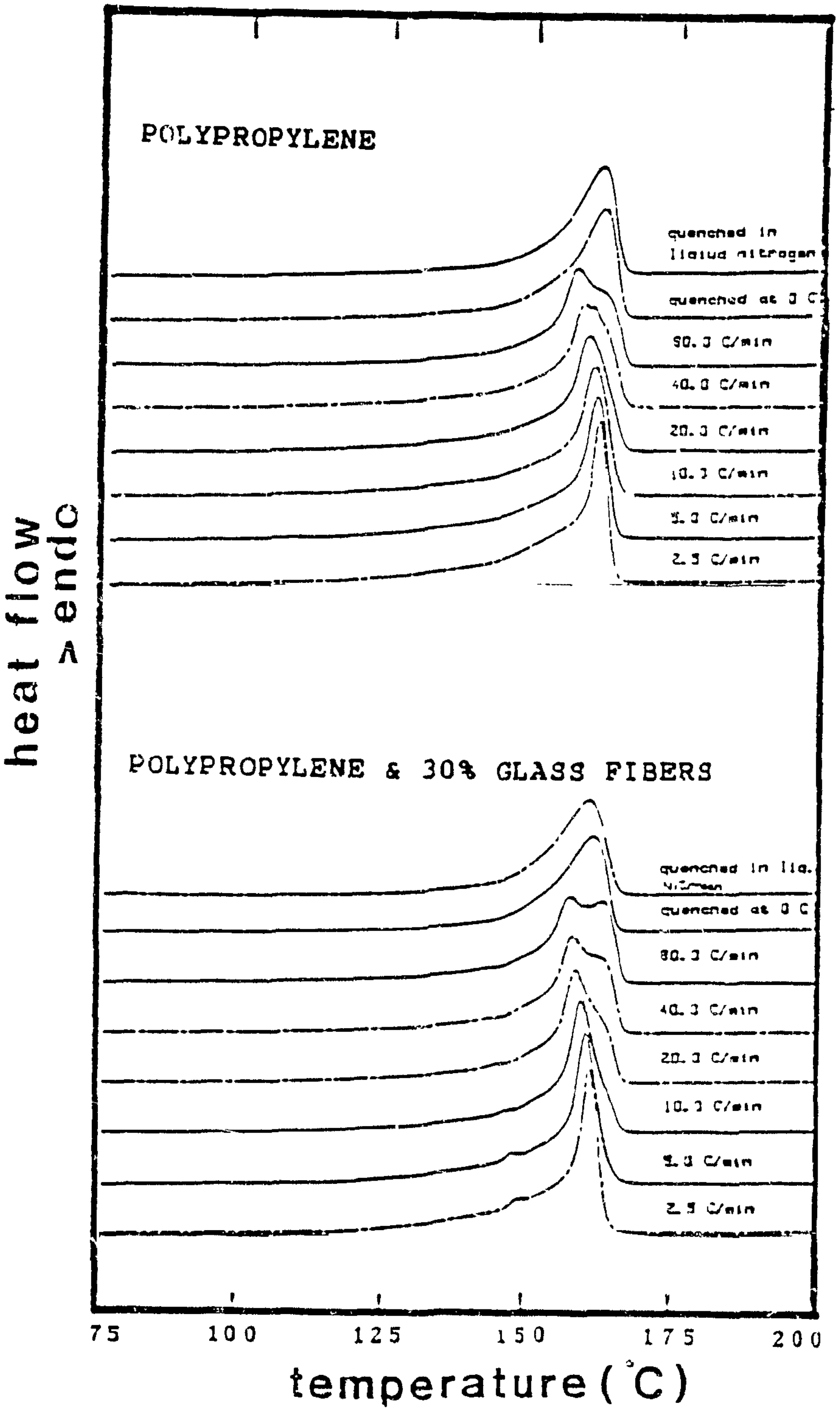

Figure 5.20 DSC melting curves for (a) polypropylene (YCEN) and (b) reinforced polypropylene crystallized at various cooling rates (ZCEN).

The DSC curves for the composite samples show the same trends. However, the α_2 peak is stronger at the same cooling rates. Fibers appear to affect the type of crystallinity by contributing to restraining the motion of the chains, thus interfering with structural changes. All the peaks are shifted by about 2 °C towards the lower temperature side. At the cooling rate of 80 °C/min, an additional peak appears. This peak is found in all the samples cooled at the lower cooling rates, but not in the quenched samples. It is observed at 140 °C at 80 °C/min and moves to higher temperatures with lower cooling rates, appearing at 148 °C with a cooling rate of 2.5 °C/min. Furthermore, it was observed only in the composite samples. It might be due to either β- or γ-type crystallinity produced at the fiber surface.

The heats of fusion and the peak melting temperatures are plotted versus the logarithm of the cooling rate in Figure 5.21. The heat of fusion of the composite was corrected by dividing by the fraction of matrix. The heat of fusion of the composite is consistently lower than that of the pure polymer by 3 to 5 percent. These results again reflect the effect of glass fibers in restraining conformational changes in the polymer molecules. The heat of fusion, for both the polymer and the composite, decreases with increasing cooling rate, following approximately a linear relationship with the logarithm of the cooling rate.

The onset temperature for the main melting peak increases

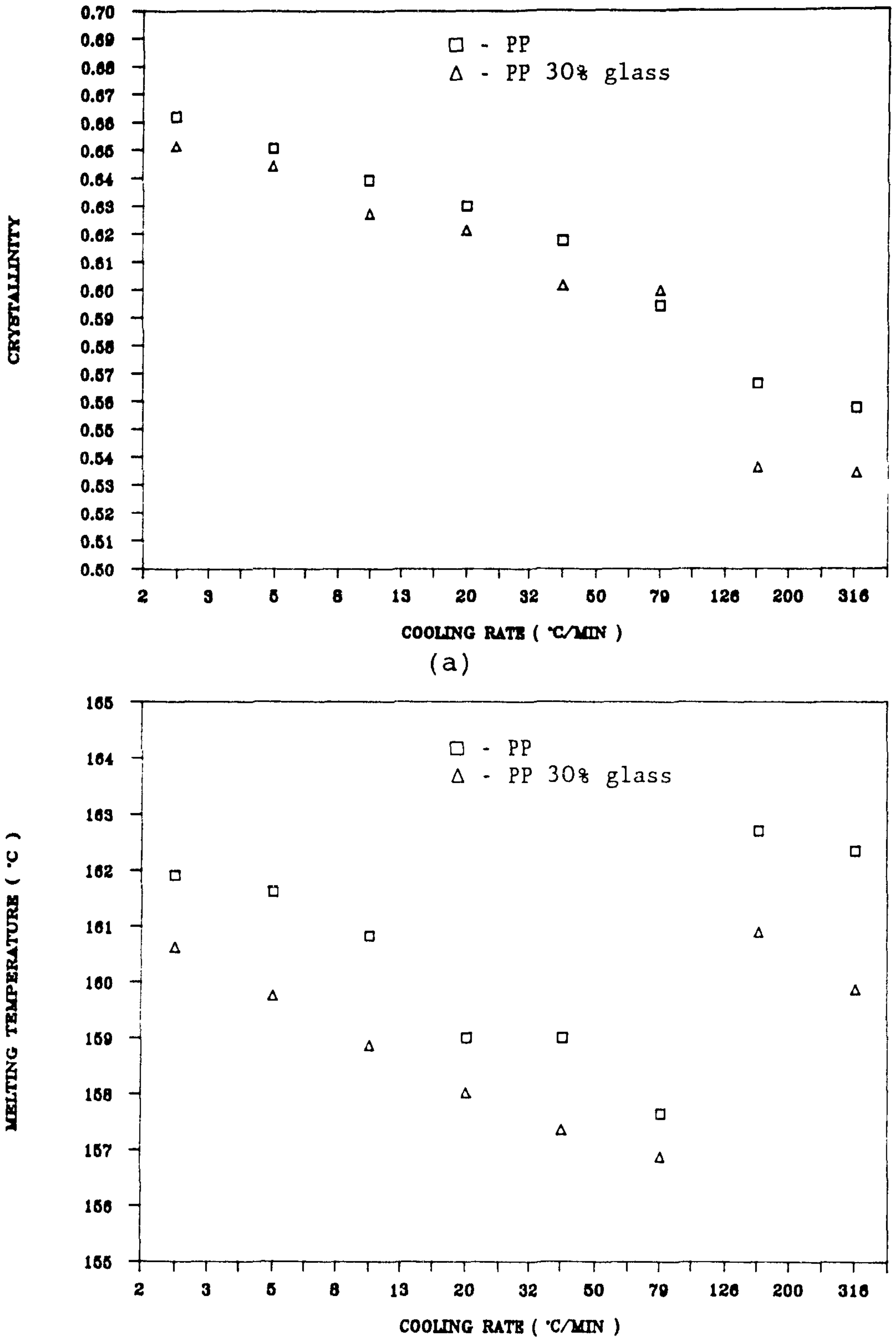

(a)

(b)

Figure 5.21 (a) The heat of fusion and (b) melting temperature of polypropylene and composite crystallized at various cooling rates (Conditions YCEN and ZCEN).

with decreasing cooling rate. The slower cooling rates favour the formation of the more ordered α_1 structure. The perfection of these crystals improve at the higher temperatures available with slower cooling rates. The peak temperature for the composite is consistently lower than that of the pure polypropylene by 1 or 2 °C (Figure 5.21b).

Crystals form in a more ordered manner and to a larger extent when cooled slowly. The samples cooled at slower rates will have larger crystallites than the samples cooled at faster rates. As a result, these samples will melt at a higher temperatures and with larger heats of fusion. This result is observed with the α_1 structure. In the quenched samples, the crystallites do not have time to grow to the fullest extent and are frozen in with a larger variation of sizes. The melting peak is thus much broader with a lower heat of fusion. The α_2 transition peak appear to be as high for the quenched samples and the slowly cooled samples as seen in Figure 5.21b. An explanation for this is that quenching produces a continuum of the two intermediates α_1 and α_2 modifications, and thus, it results in a single broad peak [160]. However the results of this study shows that the quenched samples produce only the α_2 structure, which melts at a higher temperature than the α_1 structure.

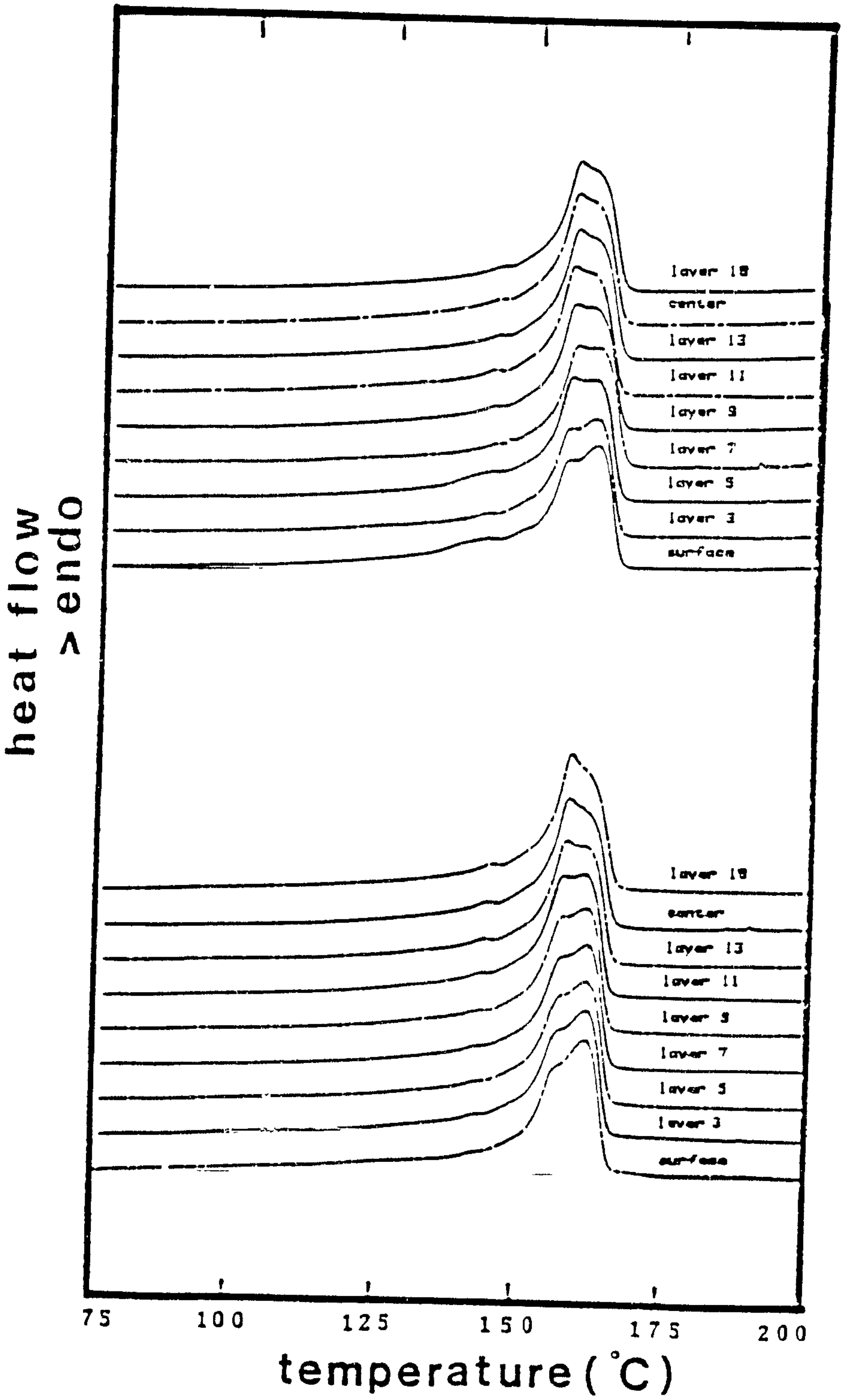

Figure 5.22 Replicate DSC melting curves for compression molded polypropylene composite from surface to centre.

5.5.2 Compression Molded Polypropylene Composite

The DSC curves for the compression molded composite samples, shown in Figure 5.22 exhibits three peaks that are consistently seen in all the layers. The γ peak is very small and occurs at 142 °C. It is present in every layer from the surface to the centre, and it appears to remain unchanged from one layer to the next. This is most likely due to the formation of a small amount of γ-type crystals, under the effect of the pressure employed during compression molding. It is aided by the role of fibers as nucleating sites. The α_1 and α_2 peaks are larger and overlap to a large degree. The α_1 peak is smaller than the α_2 peak at the surface, but it grows progressively to become greater in the centre layers. The more ordered α_1 crystals are favoured at the slower cooling rates found near the centre of the moldings.

5.5.3 Injection Molded Polypropylene

In an injection molded sample, different melt elements experience distinctive temperature, pressure and flow histories. Thus, the type and amount of crystallinity is expected to vary throughout the molded part.

The skin, being molten material quenched on a cold mold wall, experiences the greatest cooling rate, and the most rapid nucleation rates. In the case of polypropylene, this condition favours the formation of the random α_2 type crystals. In the intermediate layer, there is high shear occurring between the frozen layer and melt. After the filling stage, this layer is influenced by the packing stage, and probably freezes under the packing pressure. The γ-type crystals are favoured under these conditions of shear and pressure. In the core, the cooling rate is smallest with low nucleation rates. There are no pressure or shear influences. In this case, the more ordered α_1 type crystals are supported.

The DSC curves for the injection molded pure polypropylene are given in Figure 5.23. The samples were taken at the centre of the mold at position 2. Layers, 100 μm in thickness were removed from the surface down to the core. The surface layer shows a single α_2 peak. In layer 3, there is a slight trace of the α_1 peak. The α_1 peak grows to almost the same size as the α_2 peak in the centre (layer 15). However, the α_1 peak never reaches the same relative strength as seen in the compression molded sample as seen in Figure 5.22. The cooling rates are much greater in the injection molded samples, thus the more ordered α_1 crystals do not have as much time to form. The γ-type crystals are not observed in the case of the unreinforced polypropylene sample, supporting the hypothesis that the fibers act as nucleating sites for this crystalline type.

There was no practical way of resolving the individual peaks. Thus, the height of the α_2 peak was plotted to

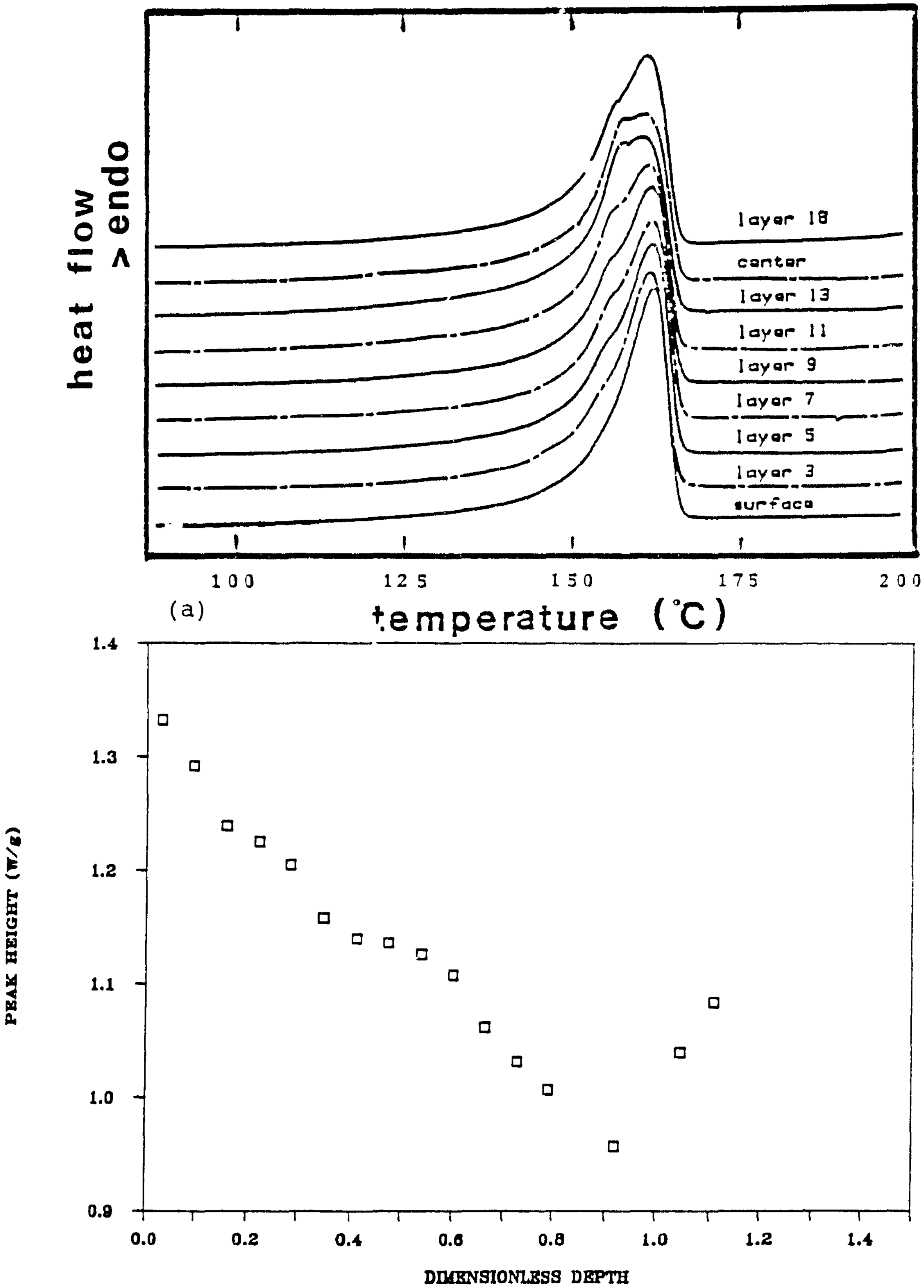

(b)

Figure 5.23 (a) DSC melting curves and (b) peak IV height for injection molded pure polypropylene (Condition YCEN).

illustrate the changes in relative amounts of crystalline specie. The peak height decreases continuously towards the core, depicting the relative decrease of the α_2-type in comparison with the α_1-type crystals.

5.5.4 Injection Molded Polypropylene Composite

The reinforced injection molded samples were characterized at positions 1 to 6 for samples molded at the intermediate condition (ZCEN). All the DSC curves at the various positions showed the same peaks and trends for layers starting from surface and proceeding to core layers, as shown in Figures 5.24 and 5.25. However there were some variations from position to position.

The surface layers are characterized by a single peak, designated as the α_2 peak. The surface material is quenched, and only the random α_2 type crystals are found. The same trend regarding the α_1 and the α_2 peaks is seen as in the case of compression molded samples. In the interior of the mold, increasing proportions of the more ordered α_1 type crystals are observed. However, in the injection molded composite samples, the α_1 peak remains lower than the α_2 peak. The α_1 peak only begins to appear at some depth from the surface unlike the case of the compression molded samples. The results suggest that the cooling rates in the interior of the injection molded composite samples are faster than in the case

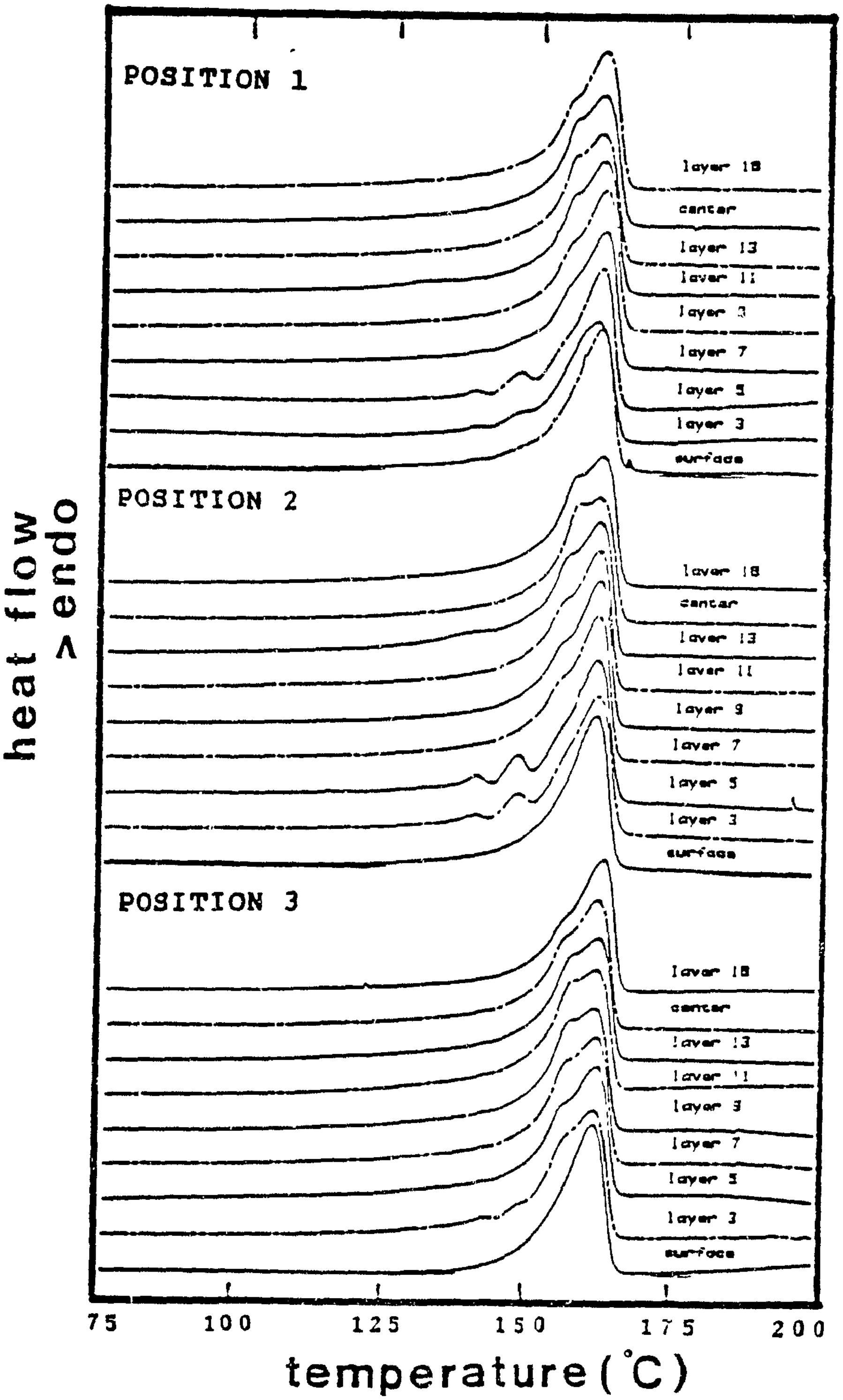

Figure 5.24 DSC melting curves for injection molded polypropylene composite at positions 1-3 (Condition ZCEN).

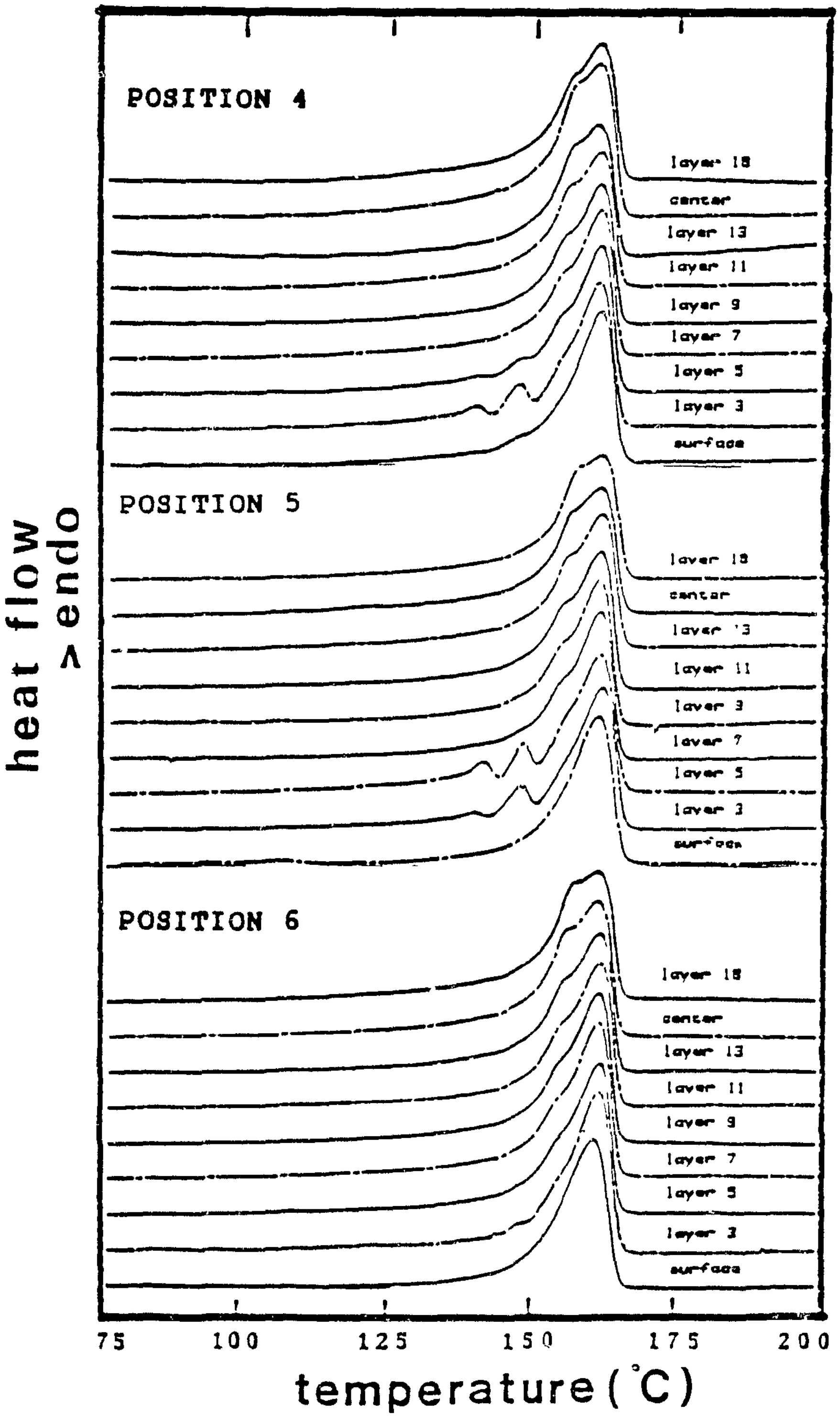

Figure 5.25 DSC melting curves for injection molded polypropylene composite at position 4-6 (Condition ZCEN).

of either the injection molded pure polypropylene samples or the compression molded samples. The higher thermal conductivity of the composite should be a contributing factor.

Two γ-type crystalline peaks appear only in certain layers close to the surface, depending on the location of the samples in the mold. The presence of the γ-type crystals below the skin layer suggests that high shear stresses are encountered in this region, probably during the packing stage when high shear stresses arise at the interface between the solid frozen layer and the flowing melt. The material, under high shear stress and pressure, crystallizes as oriented γ-type crystals. This phenomenon is not observed with the pure polypropylene samples molded under similar conditions. The reinforcing fibers appear to play an important role in the formation of the γ-type crystals. One factor, as was observed in the case of compression moldings, is that the fibers may act as nucleation sites. Another factor, is that the presence of the reinforcement could produce higher shear rates (or stresses) in the spaces between the fibers, which enhances the formation of the γ-type crystals.

The most significant difference that can be seen from the DSC curves of layers taken at positions 1 to 6 is in the relative amounts of the γ-type crystallinity. The amount of the γ crystals was greatest at positions 2 and 5 in the middle of the mold, i.e. away from the gate region and the flow front region. The amount is somewhat smaller in the gate region (positions 1 and 4), while it is minimal at the far end of the mold (positions 3 and 6). This suggests that the effects of shear and pressure are greatest at the mid-mold positions and least at the far end of the mold. Although the gate region experiences high levels of shear and pressure, the melt also experiences the highest temperatures in this region. This might explain the slightly lower levels of γ-type crystals near the gate. It should be noted that the frozen-layer is thicker in the middle of the mold than at the far end of the mold or near the gate. Thus, shear rate effects may be highest in that zone, due to the smaller cross-sectional area available for flow.

Figure 5.26 shows the peak height profiles for positions 1 to 6. The peak height profiles for positions 1 to 3 show a minimum below the surface. The peak height then increases to a maximum before decreasing again towards the centre for positions 1 and 2. The patterns at positions 4 to 6 show similar, though not identical features. However, at these positions near mold edges, the minima and maxima with peak height are shifted closer to the wall. It should be pointed out that the peak height profile of the pure polypropylene sample does not show a minimum near the surface.

The decrease in height of peak IV towards the centre of the samples represents the decrease in the more random α_2 crystal type. This is being replaced by the more ordered α_1 type crystals as seen in the DSC curves. In the shear layer,

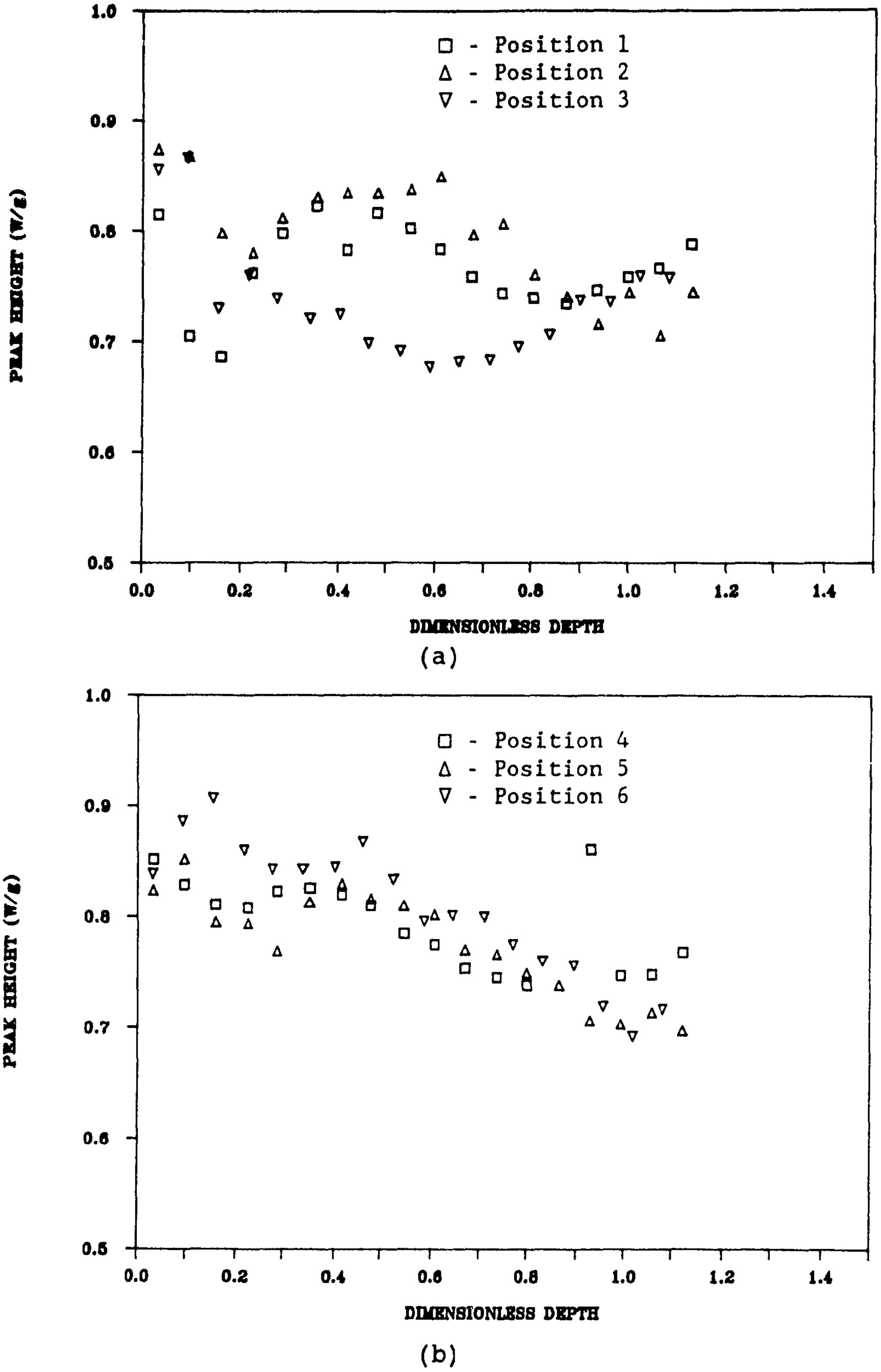

Figure 5.26 Peak height profiles for (a) positions 1-3, (b) positions 4-6 (Condition ZCEN).

γ-type crystals have replaced some of the α_2 crystals, and this accounts for the decrease in the peak height at that position. However, the peak height shows the sharpest drop at position 1 nearest to the gate, and, this is not supported by the DSC curves which show only a small amount of the γ-type crystals. This can be explained by the fact that the overall crystallinity has dropped, and, that it is not just one crystal type being more dominant than another. In a later section, it will be shown that very low crystallinity values prevail near the surface at position 1.

5.5.4.1 Effect of Processing Conditions

Injection molded samples of the polypropylene composite were obtained by using different molding conditions, in order to evaluate the effects of the following variables: melt temperature, injection time, holding pressure and holding time. DSC studies were carried out on these samples at position 2 in the centre of the cavity.

Samples were obtained at different melt temperatures. The limits of the melt processing temperatures were used, 280 °C and 200 °C. The DSC curves are presented in Figure 5.27. The trends shown in Figure 5.27 are typical of the behaviour observed in the other injection molded samples. The notable effect of melt temperature is seen in the relative amounts of γ-type crystals found in the sub-skin layers. At a melt

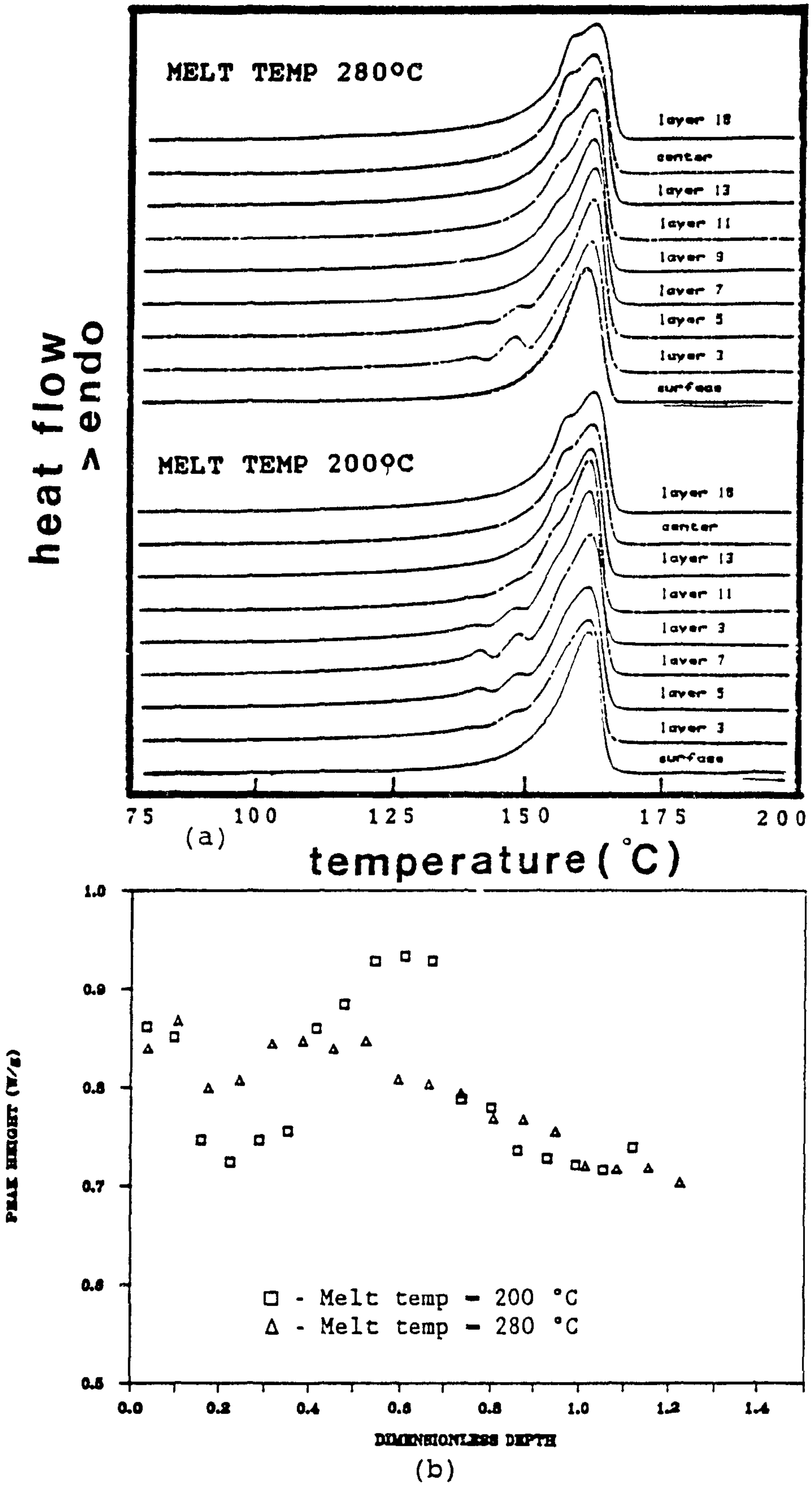

Figure 5.27 (a) DSC melting curves, and (b) peak height for polypropylene composite with a melt temperature = 200 °C and 280 °C (Conditions ZHMT and ZLMT).

temperature of 200 °C, γ-type crystals are observed over a wider region. The maximum amount occurs at a greater depth than with a melt temperature of 280 °C. At the lower melt temperature, the frozen layer grows at a faster rate and the pressure during filling is higher. Thus, shear effects will spread over a wider area. Also, the higher pressure will enhance the development of the γ-type crystals in this expanded area.

The height of peak IV was plotted versus depth, and it shows that the amount of α_2 drops sharply from the second layer in both cases, with the high temperature sample showing a less dramatic drop. The drop is probably due to the transformation of some material near the surface into γ crystals rather than α_2 crystals. Both samples exhibit a peak maximum between the 8th and 10th layers, reflecting the combined effects of shear, pressure, and cooling rate which must be most favourable for formation of the α_2 crystals in that zone. The maximum in the amount of α_2 crystals in that zone corresponds to a maximum in the total crystallinity in each case as seen in section 5.6.

Injection or filling times of 1 and 2 seconds were evaluated as shown in Figure 5.28. In the faster injection condition, the γ peaks are sharper and limited to layer 3. The fast injection time is accompanied by high shear rates at the interface. However, because of the time constraint, the thickness of the frozen layer during filling is limited.

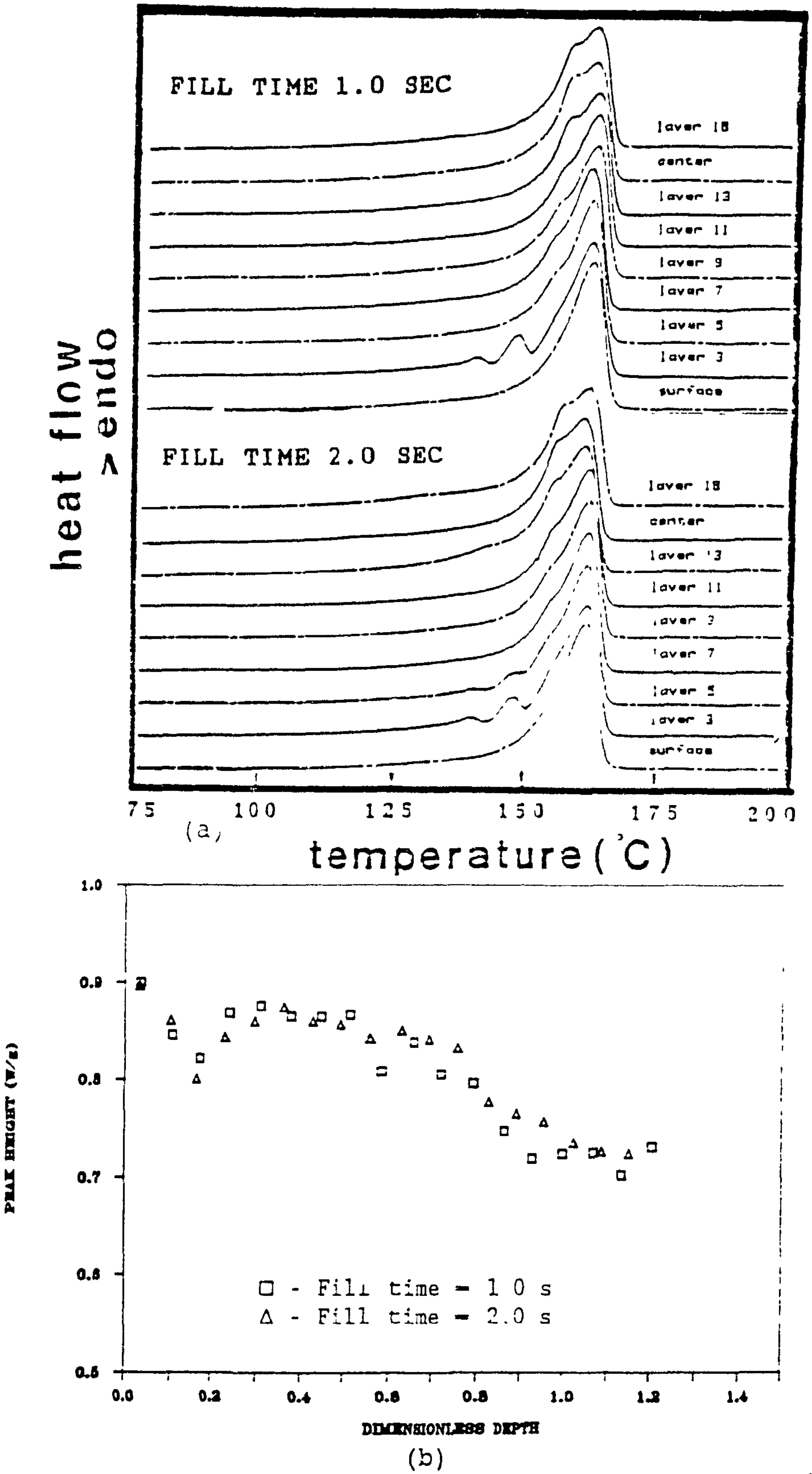

Figure 5.28 (a) DSC melting curves, and (b) peak height for polypropylene composite with a filling time of 1.0 and 2.0 seconds (Conditions ZLIT and ZHIT).

With the slower injection speed, the shear effects are lower, but they are spread over a thicker frozen layer. The plots of the α_2 peak height versus depth reveal that there are no dramatic differences between the relative amounts of α_2-type crystals for the two injection speed conditions. This is expected since this type of crystalline structure is not influenced by shear, and the amount of γ-type crystals is not so different so as to significantly decrease the amount of α_2-type crystal.

The samples obtained at holding pressures of 1.03 x 10^7 N/m^2 and 2.41 x 10^7 N/m^2 (ZLHP,ZHHP) were evaluated as shown in Figure 5.29. The amount of γ crystals is greater in the higher holding pressure with no apparent effect on the frozen layer. These observations are evidence that the γ-type crystals are also induced by pressure. The temperature profile should remain the same in both conditions. Since the cooling rates and nucleation rates are effectively the same, only the crystal modification that is affected by pressure should be influenced by changing holding pressure. The peak height profiles are similar for both samples, except near the intermediate layer. In this region, the influence of pressure is expected to be greatest.

Figures 5.30 show the DSC curves for the two holding times of 0 and 2 seconds (ZLHT,ZHHT). The amount of γ-type crystals increases for the sample obtained at the longer holding time, as expected because of the influence of

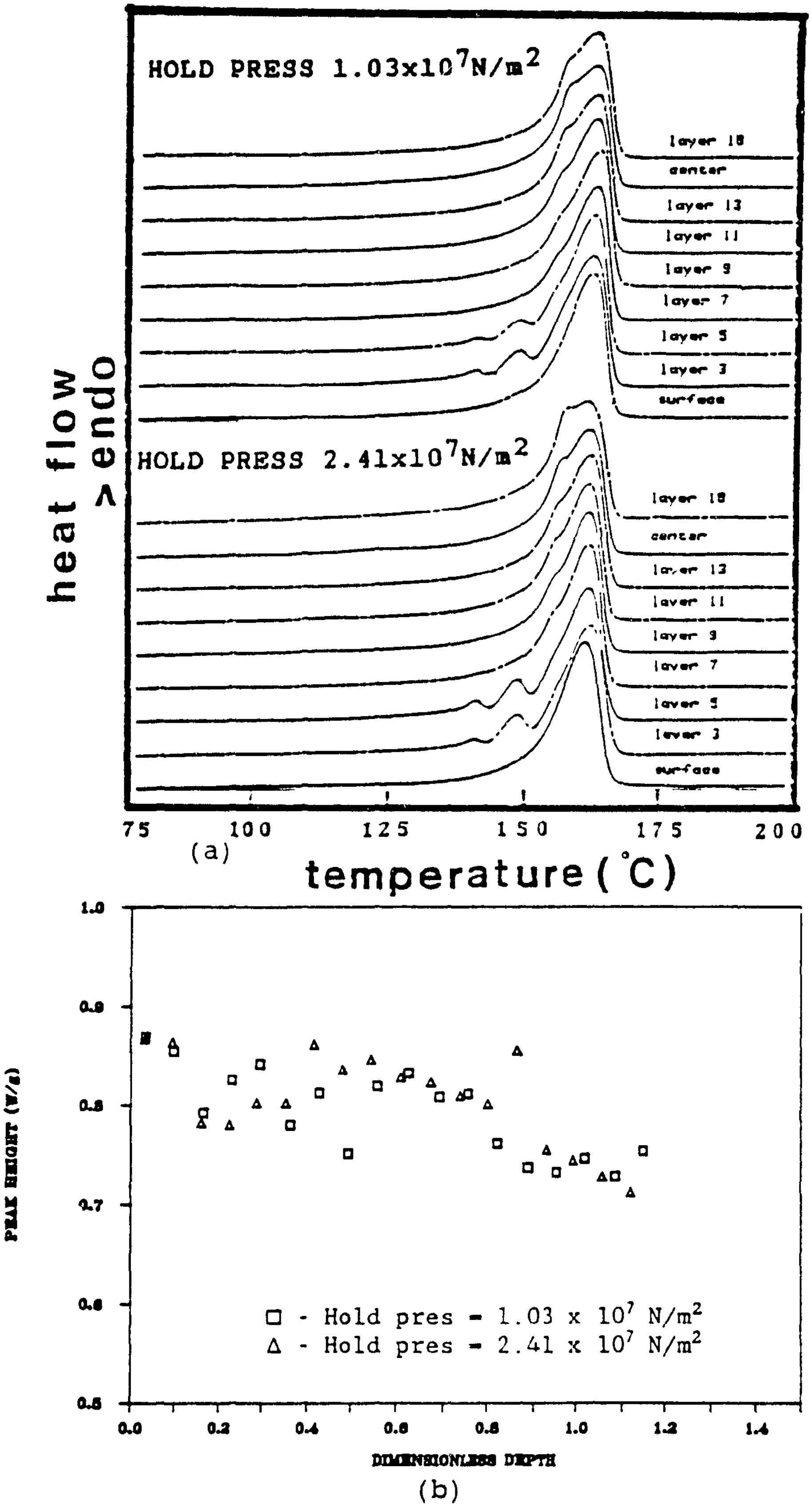

(a)

(b)

Figure 5.29 (a) DSC melting curves, and (b) peak height for polypropylene composite with holding pressure of 1.03 and 2.41 x 10^7 N/m^2 (ZHHP and ZLHP).

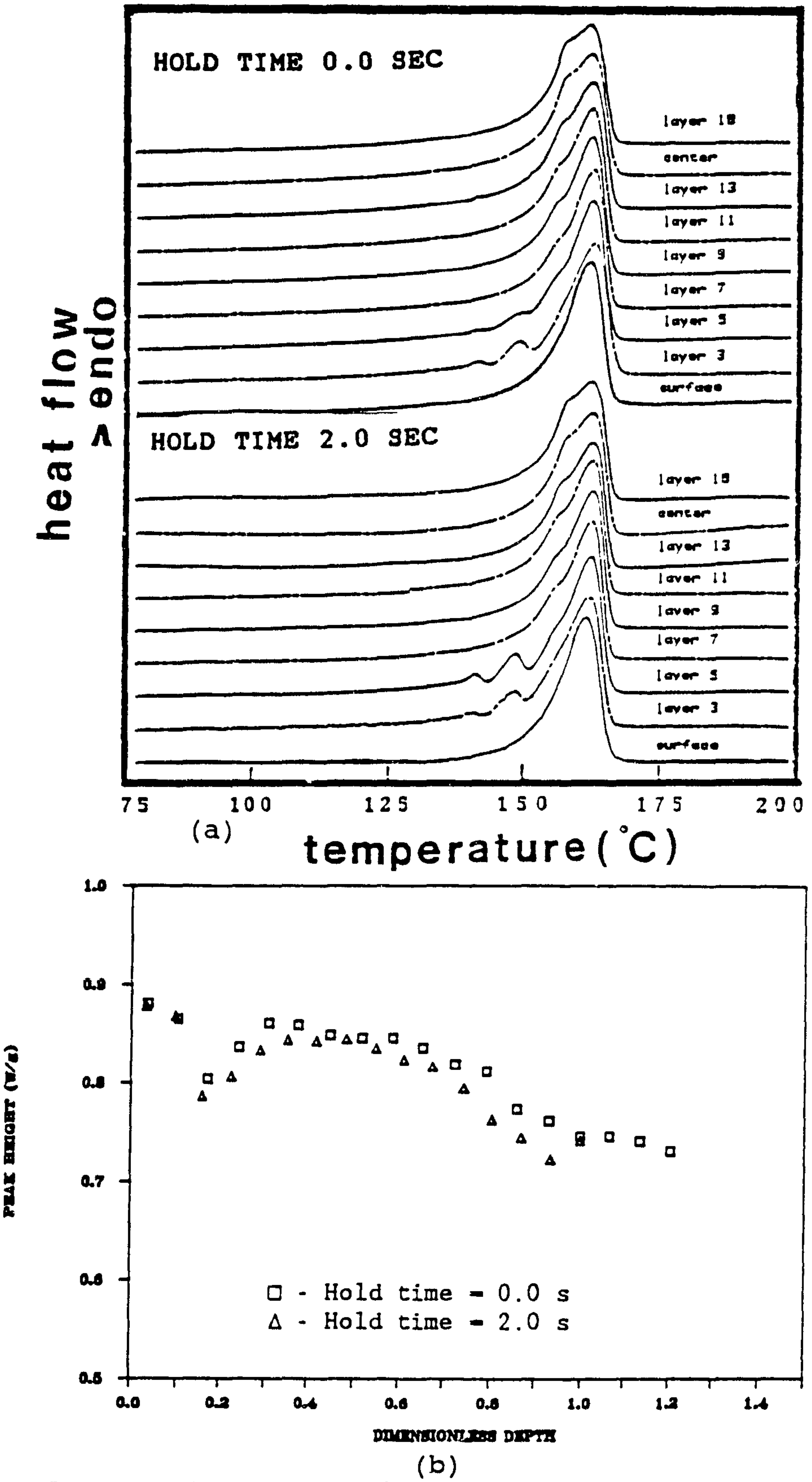

Figure 5.30 (a) DSC melting curves, and (b) peak height for polypropylene composite with a holding time of 0.0 and 2.0 seconds (Conditions ZLHT and ZHHT).

pressure. The peak height versus the depth results are similar for both conditions.

Trotignon and Verdu [168] measured the β-type crystal fraction index from skin to core in injection molded samples using a Wide Angle X-Ray Spectrometer (WAXD). They showed that the β phase existed in a sharp range at a depth of 200 - 500 μm, with the maximum occurring at 300 - 400 μm. In this region, the conditions are ideal for β phase nucleation and growth. There is high molecular orientation in the melt, quick cooling to 100 - 125 °C (i.e. below the range of maximum rate of crystallization for the α form) and high pressure. They also showed that there is high degree of orientation in the low crystallinity region. This corresponds to the region where the γ-type crystals are observed in this study. It appears that there is some confusion whether the crystals observed in this region are of γ-type or β-type. However, the selection is for the γ-type [48,165].

Trotignon and Verdu [168] showed that pressure had a large effect on crystallization. The secondary maximum was shifted towards the core with higher holding pressure. The effect of an increase in pressure on packing increased the equilibrium melting point and the rate of crystallization.

A summary of the morphological features reveals that polypropylene is polymorphic. It crystallizes in the form of randomly nucleated α_1 and α_2 type crystals, and a γ-type crystal which has been observed only in the composite samples.

The α_1 type of crystals is a more ordered helix structure which is found in the slow cooling zones with slower crystallization rates in the core. The α_2 type crystals are found in the quenched skin where there is rapid nucleation. The γ-type crystal shows two peaks in DSC curves. It is formed in the intermediate region which undergoes high shear and freezes under pressure. It is the result of the ordering of shear extended molecules or fractions of flow separated small molecular weight molecules.

The high cooling rates experienced by the polymer during injection molding favour the type of crystallites that has the highest growth rate at these conditions. Under these circumstances, the α_2 type crystals dominate. In the skin, which is quenched, the evidence reveals only α_2 type crystals.

5.6 Crystallinity

From the DSC curves, it is seen that the injection molded samples contain a variety of crystallite types. The variability of crystalline types in a sample renders the analysis of crystallinity distribution more difficult than with a sample consisting of a single crystalline species. As has been noted earlier, the crystalline specie are formed under different conditions and have quite different properties. The degree of crystallization of each species would depend on the conditions of crystallization.

The measured area under the DSC curves is the total area of all the peaks. It represents the total heat of fusion of all the crystalline material present. Individual heats of fusion for the different crystalline specie could not be obtained because of the difficulty in resolving the individual peaks.

The theoretical heat of fusion of 100% crystalline polypropylene is also a source of difficulty. Values reported in literature are in the range from 64.5 to 260 J/g [49]. A value of 153 J/q [169] is used here to calculate the apparent crystallinity, resulting in values around 60%. Typical values for the degree of crystallinity of commercial polypropylene samples have been found to be between 0.6 and 0.8 [169,170]. However, the theoretical heat of fusion of the 100% crystalline material cannot be defined because the different crystalline specie have different heats of fusion, and the relative amounts of each specie in the sample are dependent on processing history. The glass fiber concentration was taken into account in obtaining the heat of fusion of the matrix phase. The percent crystallinity in the matrix was obtained by using thermo-gravimetric analysis to obtain the actual fiber concentration of each layer.

The crystallinity profile for a compression molded sample is quite flat as seen in Figure 5.31. Although the DSC curves show changes in relative amounts of α_1 and α_2 type crystallinity, the total crystallinity remains essentially uniform across the thickness. This uniform crystallinity across the thickness of the material signifies an essentially homogenous cooling rate across the thickness of the sample.

The percent crystallinity for pure and reinforced polypropylene are remarkably similar as shown in Figure 5.32. Generally, there is low crystallinity at the surface, and the crystallinity increases steadily towards the centre. It was expected that the crystallinity of the composite would be greater than that of the neat resin molding, since the fibers might act as nucleation sites for crystalline growths. However the higher thermal conductivity of the composite melt would increase the cooling rate and thus lower the crystallinity. The similarity in the crystallinity may be that the effects of nucleation sites in the matrix and the increased cooling rate are in relative balance. Although there are additional

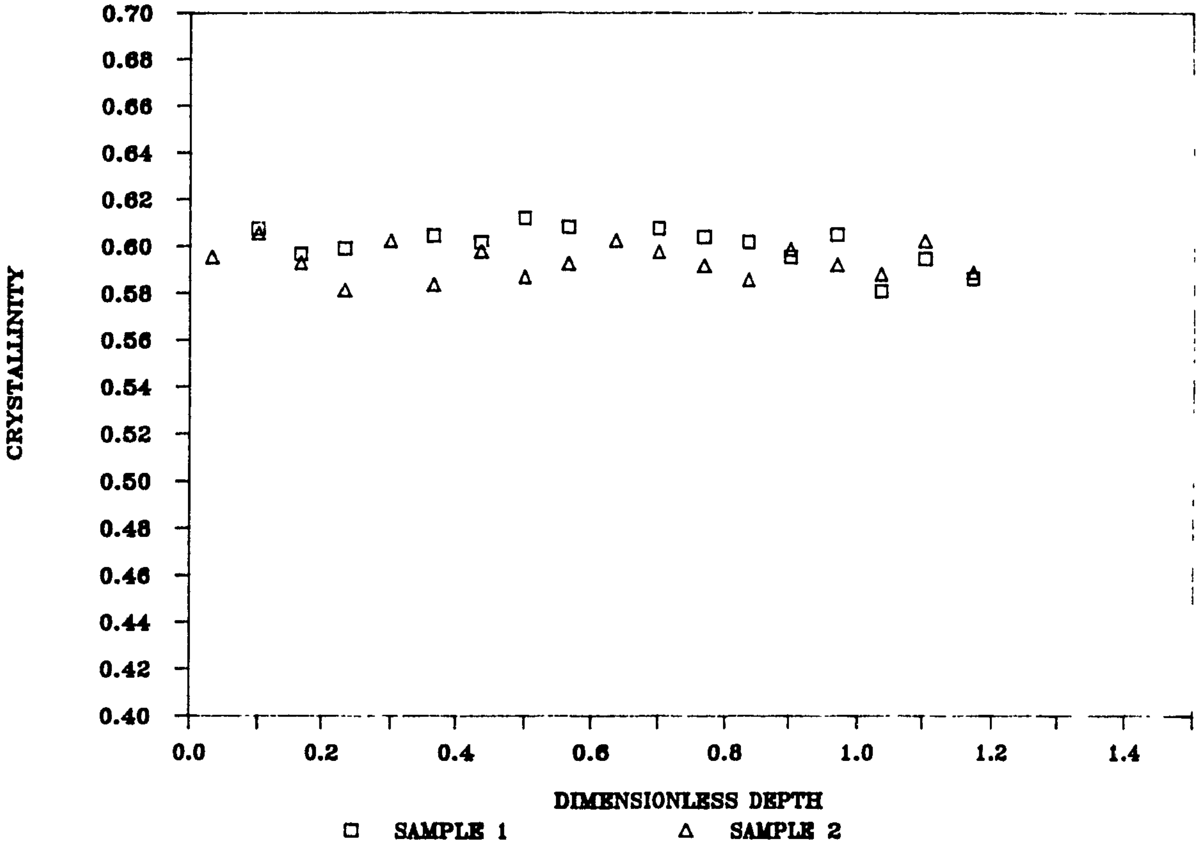

Figure 5.31 Replicate crystallinity curves for compression molded samples at the same conditions.

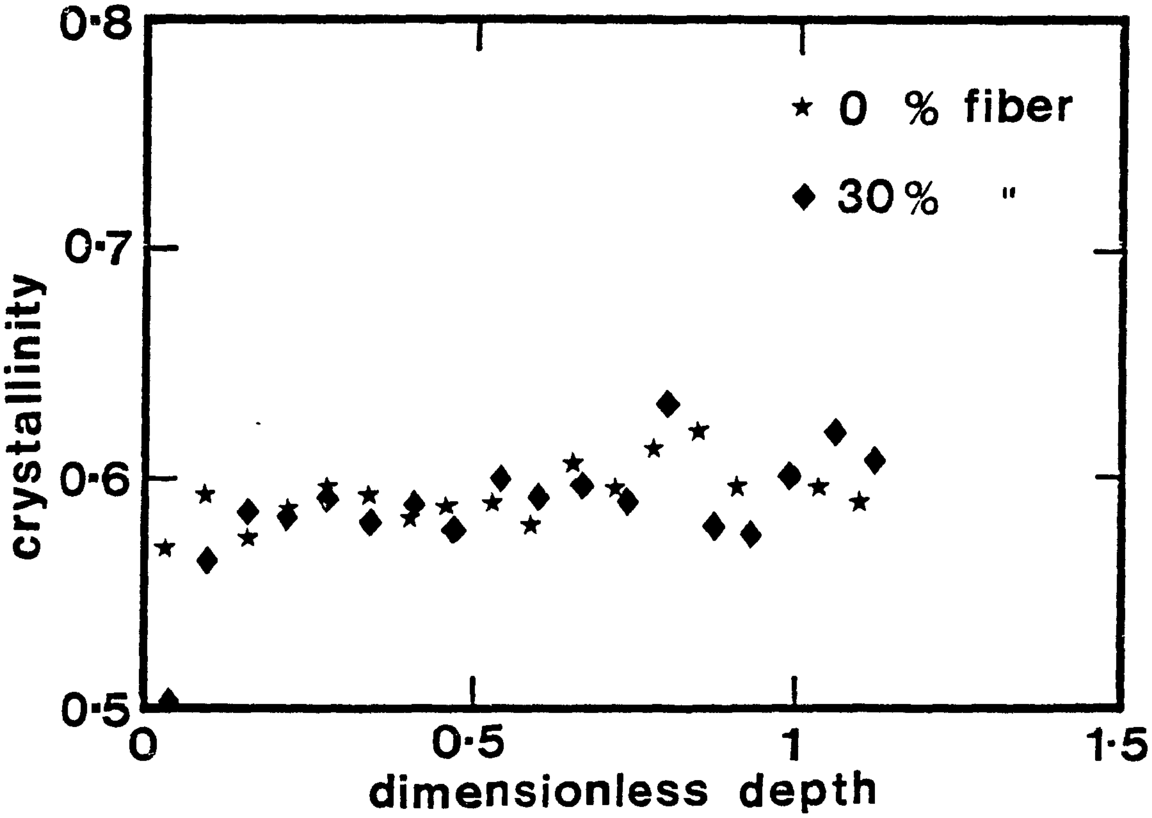

Figure 5.32 Effect of glass fibers on the crystallinity profiles for injection molded samples (Conditions YCEN, ZCEN).

amounts of γ-type crystals in the composite molding, it appears that this occurs at the expense of the α_1 and the α_2 crystals, so that the overall crystallinity is not affected.

Garton [171] showed that crystallization of polypropylene occurred preferentially on the surface of mica platelets. The evidence with DSC was that the crystallization exotherms of the composites were preferentially shifted to higher temperatures. The addition of silane coupling agents greatly diminished this nucleation effect. In the present study, DSC thermograms for the cooling of polypropylene samples at 10 °C/min show that the crystallization exotherm of the reinforced sample was shifted by about 3 degrees to lower temperatures, as shown in Figure 5.33. There appears to be a supercooling effect in the composite, which reinforces the hypothesis that the presence of the fibers hinders changes in molecular conformations associated with crystallization.

Figure 5.34 shows the crystallinity profiles in an injection molded composite sample for position 1 to 6. Generally, the crystallinity increases steadily from a minimum at the surface to a maximum at the centre. This trend in crystallinity profile from skin to core has been reported in several similar studies [3,72,172]. The low crystallinity values near the surface are attributed to lower rates and duration of crystallization due to the rapid cooling of the melt near the cold mold surface [173]. The quenching at the surface does not allow the material sufficient time for

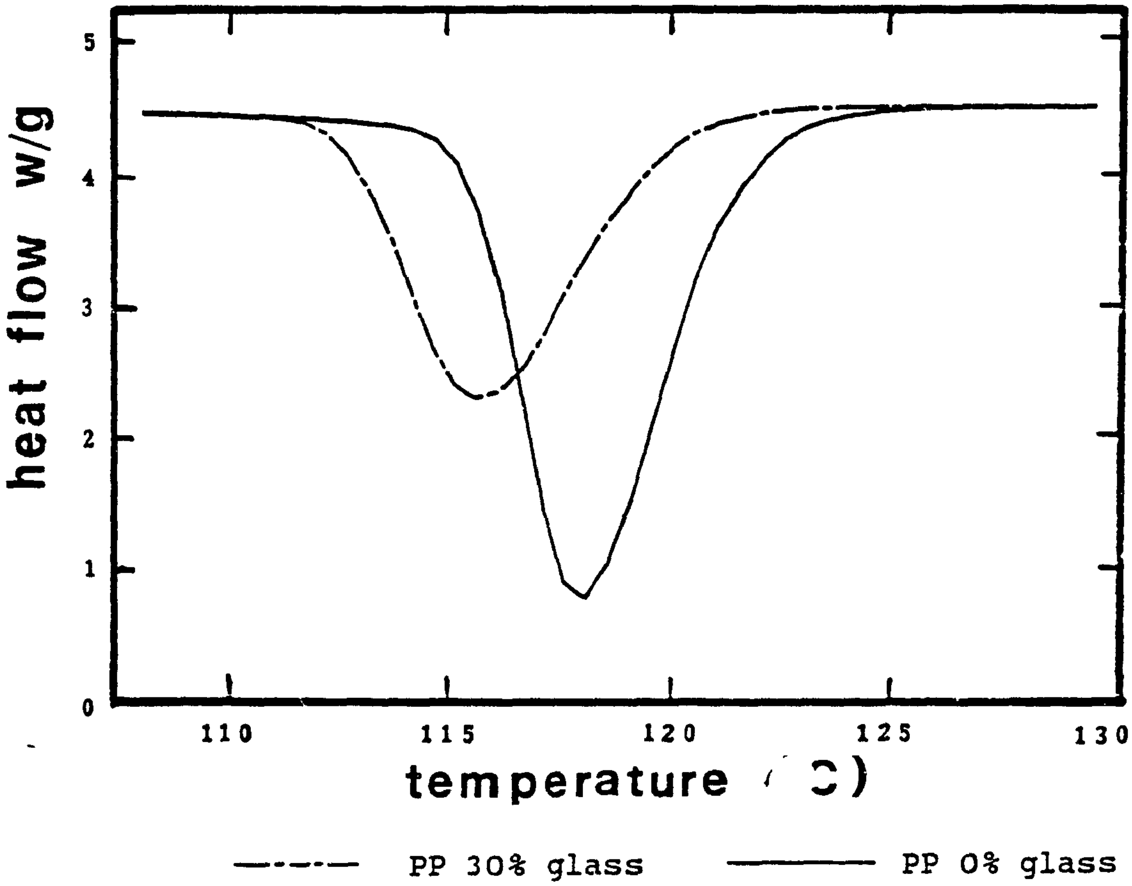

Figure 5.33 Crystallization exotherms for reinforced and unreinforced polypropylene (Conditions ZCEN, YCEN).

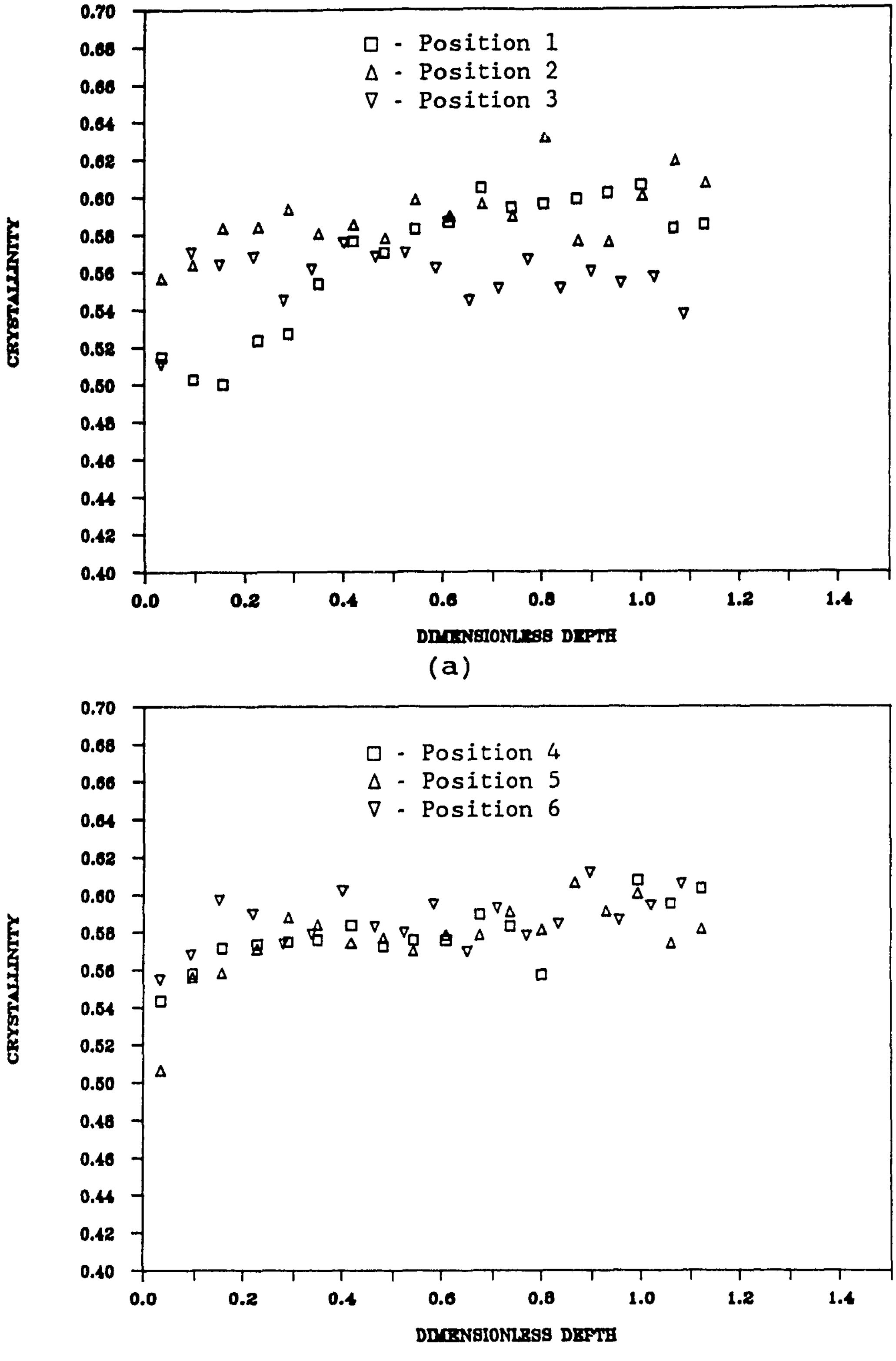

(a)

(b)

Figure 5.34 Distribution of the crystallinity profiles in injection composite molded samples, (a) positions 1-3, (b) positions 4-6 (ZCEN).

crystallization [172]. At the core of the samples, the thermal gradients are smaller, resulting in lower cooling rates. This produces higher crystallization rates and durations which increase the amount of crystallinity in the core.

The variations from positions 1 to 3 are quite interesting. At position 1, the surface and close-by regions (up to 500μm depth) show very low crystallinity. At positions 2 and 3, the variation in crystallinity is smaller than at position 1. Both positions 2 and 3 show higher crystallinity near the wall than position 1. However, in the core, the crystallinity is lowest at position 3. Other workers have shown high crystallinity values near the gate position and the lowest for the farthest location [3,72,172,173]. This has been attributed to the longer cooling times and higher packing pressures that prevail near the gate [26,172]. The trend in the core is similar to that observed above. However, at the surface, the results deviate. The possible explanation is that the melt temperature is highest near the gate. Thus high cooling rates prevail near the mold surface, producing low crystallinity. Shear rate influence on the crystallization process has been recognized in previous studies in pure polymer [173] and in the composite samples [46]. The low crystallinity region corresponds to the high shear zone as observed by Houska and Brummel [174].

The off-centre positions 4 to 6 show very similar crystallinity profiles since flow and thermal histories in these regions are quite similar. They are away from both the centre-line and the gate, while being close to the mold side wall. They all show steady, but slow increase of crystallinity from the surface towards the centre. The major difference between the crystallinity profile at the centre-line positions (1 - 3) and the off-centre position (4 - 6) lies in the surface region.

The melt temperature appears to have the largest effect on the crystallinity profile, as shown in Figure 5.35. Crystallinity is generally higher, when a lower melt temperature is employed. The greatest differences are observed in the intermediate zone, where the crystallinity values for the 200 °C melt temperature sample are exceptionally high. Increasing injection melt temperature has been observed by other workers to marginally increase the crystallinity in the whole part due to lower average cooling rates and longer cooling times associated with the higher temperature [3,172], and also, decrease crystallinity at the off-centre positions [3]. The explanation given was the faster crystallization rates prevailed as a result of higher cooling rates due to a higher cooling area in these regions. The explanation for the results observed in this study is probably more complicated than that given. The high crystallinity values in the 200 °C melt temperature sample is observed in the same zone as the γ-type crystals. The higher melt temperature sample has a less pronounced γ-type crystal formation with no corresponding high

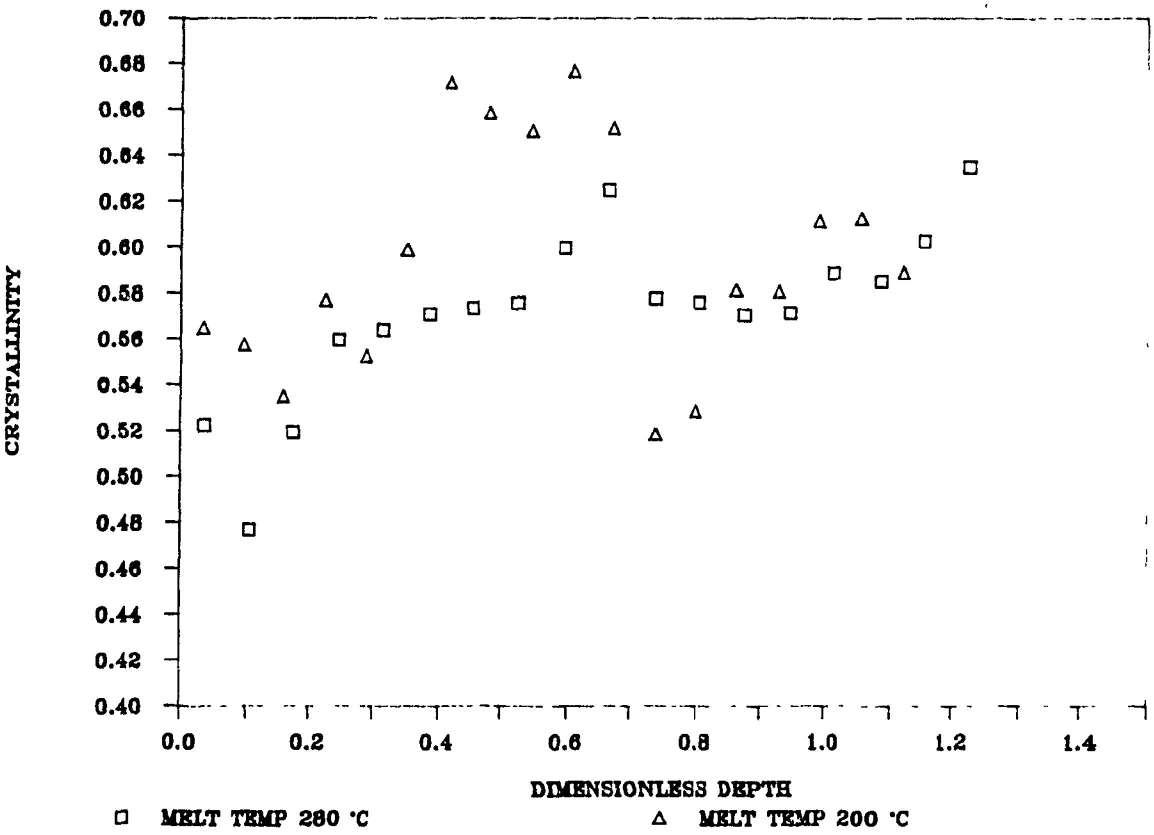

Figure 5.35 Effect of melt temperature on the crystallinity profiles for injection molded composite samples (Conditions ZHMT, ZLMT).

crystallinity region. A reasonable explanation is that more shear oriented γ-type crystals are formed at the lower temperature because of higher shear and higher pressures. The γ-type crystals produced undergoes relaxation at the higher temperature. The lower melt temperature also produces lower rates of cooling which increases crystallinity.

The other processing variables did not affect the crystallinity distribution as significantly as the melt temperature. The results are shown in Figures 5.36 to 5.38. The same trends of low crystallinity at the surface with an increase towards the centre are seen in all the cases. It appears that the crystallinity in the intermediate layers is somewhat higher when a higher hold pressure is employed. It has been observed that increasing packing pressure leads to an increase in the crystallinity [3,172].

The results of the crystallinity distribution measurements in injection molded composite samples can be summarized as follows:

(i) Crystallinity values are low at the surface, and increase steadily to a maximum at the core.

(ii) Crystallinity is lowest at the surface near the gate position and increases downstream. The crystallinity at the core is highest near the gate and decreases downstream.

(iii) A lower melt temperature was found to increase the crystallinity substantially in the intermediate

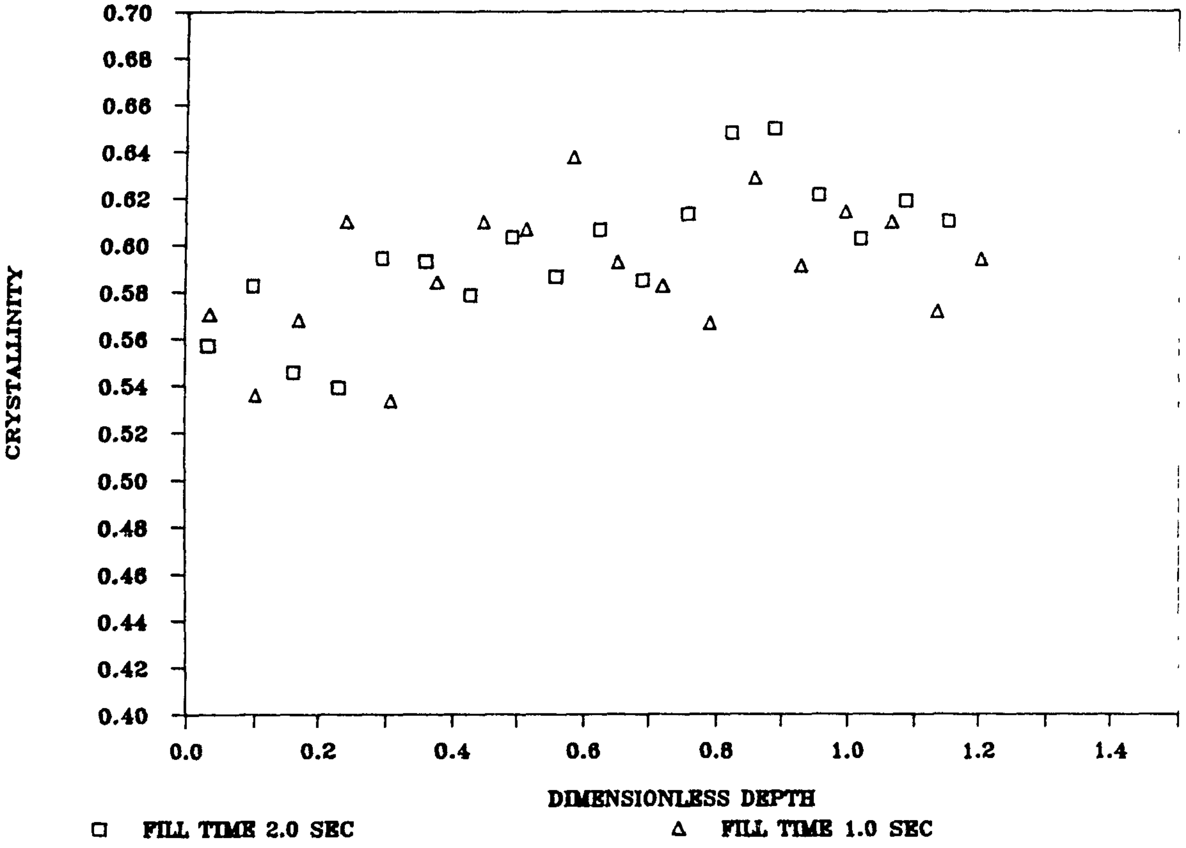

Figure 5.36 Effect of filling time on the crystallinity profiles for injection molded samples (Conditions ZHIT, ZLIT).

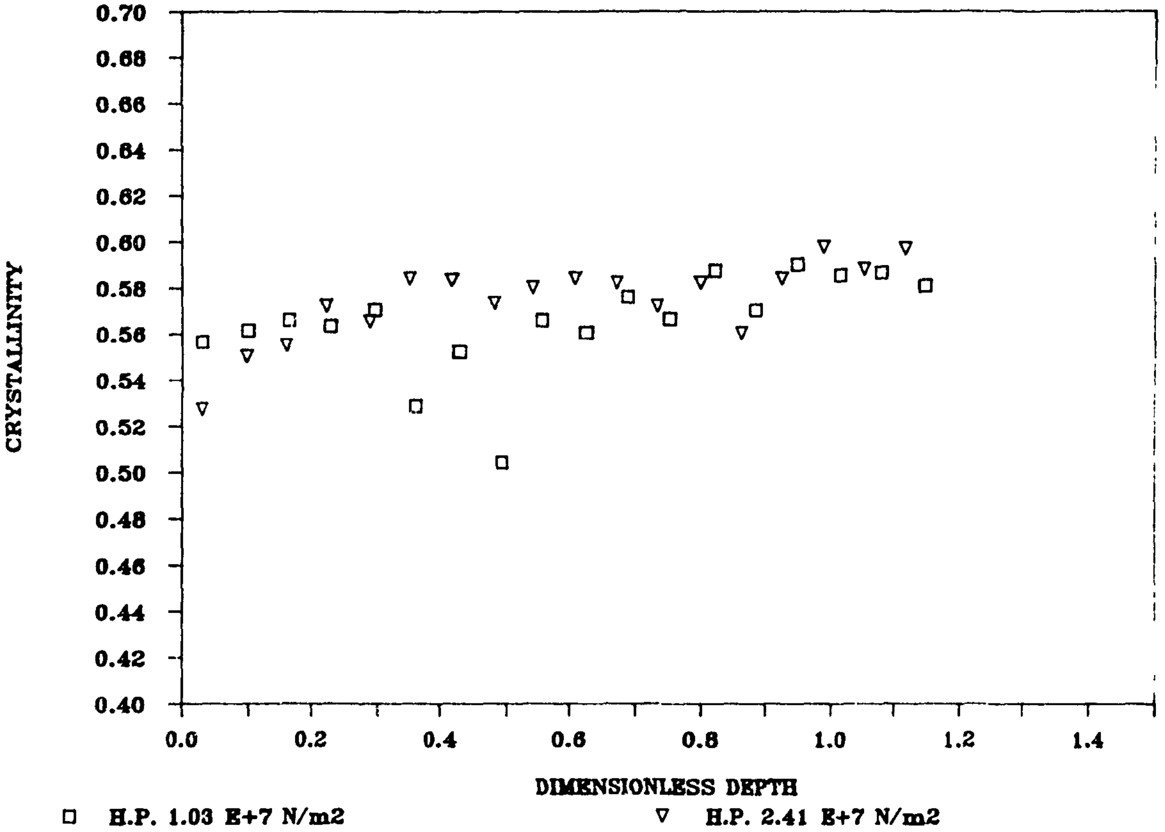

Figure 5.37 Effect of holding pressure on the crystallinity profiles for injection molded samples (Conditions ZHHP, ZLHP).

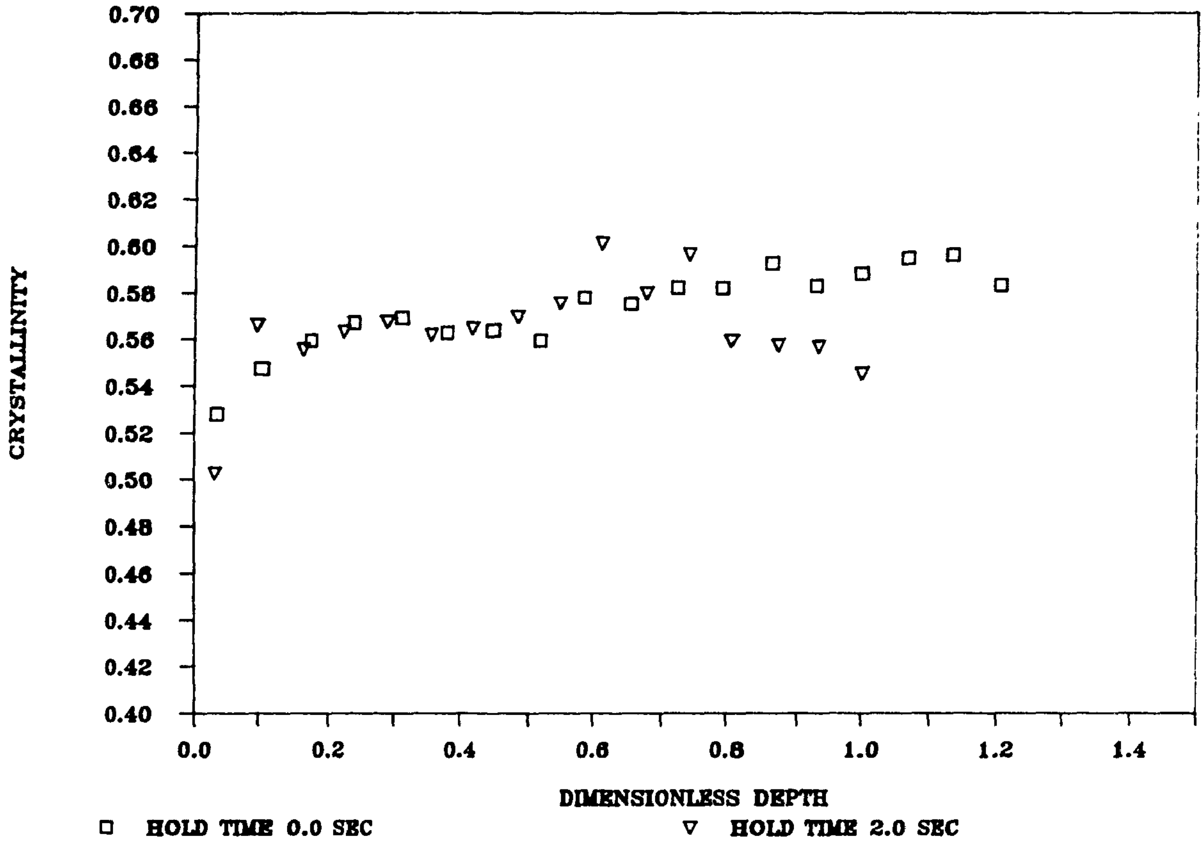

Figure 5.38 Effect of holding time on the crystallinity profiles for injection molded samples (Conditions ZHHT, ZLHT).

region. Packing pressure increases crystallinity slightly. Other molding conditions did not show significant effects.

(iv) Although reasonably simple explanations of the results have been given here and by other workers [3,172], a complete explanation of the observed phenomena requires more detailed analysis of the interactions of various factors, such as cooling rates nucleation rates, pressure, shear, and relaxation.

5.7 Molecular Orientation

Molecular orientation was measured using a method proposed by Kissin, et al. [136]. Another method, described by Samuels [35], uses dichroic ratios to determine uniaxial orientation, as in drawing processes. The orientation of the crystalline and amorphous phases can be described relative to one direction. However, Kissin's method involves measuring crystalline orientation in three mutually perpendicular axes. Therefore, it would be useful for studying biaxial orientation, as in the case of injection molding. The method permits the calculation of the proportions of polymer chains with chain axes aligned in the respective reference direction. In the discussion, the orientation of the molecular chains is described relative to the x-axis, i.e. the flow direction. The method is described in detail in Appendix I.

5.7.1 Crystalline Phase

Bulk measurements suggest that the molecular orientation in the injection molded fiber reinforced composites is different from that in the unreinforced material. This view is substantiated by the occurrence of warpage in glass fiber reinforced polypropylene [150]. Differences occur due to the interactions between the glass fibers and the polypropylene matrix.

Figure 5.39 shows the crystalline and amorphous orientations described relative to the x-direction for both the reinforced and unreinforced injection molded polypropylene samples. The values were obtained using the method described in Appendix I. The orientation function used is a Hermans type orientation function [175]. A value of 1 signifies perfect orientation in the x-direction, -0.5 signifies perfect transverse orientation while 0 is random orientation.

The curves show that there are not very high orientation effects in the crystalline phase. The orientation function values are limited to the range between +0.35 and -0.25. The crystalline orientation is higher near to the surface than in the rest of the thickness in both samples. In the unreinforced sample, the oriented surface layer is spread out extending to about a quarter of the thickness. This layer is thinner in the reinforced sample, but slightly more oriented. The unreinforced material shows low or near random orientation in the core. In the case of the reinforced material, there is a slightly transverse orientation in the core. This transverse core orientation is only observed in the composite samples molded at this condition, as will be seen later.

Houska and Brummel [174] showed maximum orientation of $f_c \approx 0.25$ for unreinforced injection molded polypropylene at approximately 300 μm from the surface. This changed gradually to random orientation at the centre. Orientation of the molecular chains (i.e. c-axis orientation) in the crystalline

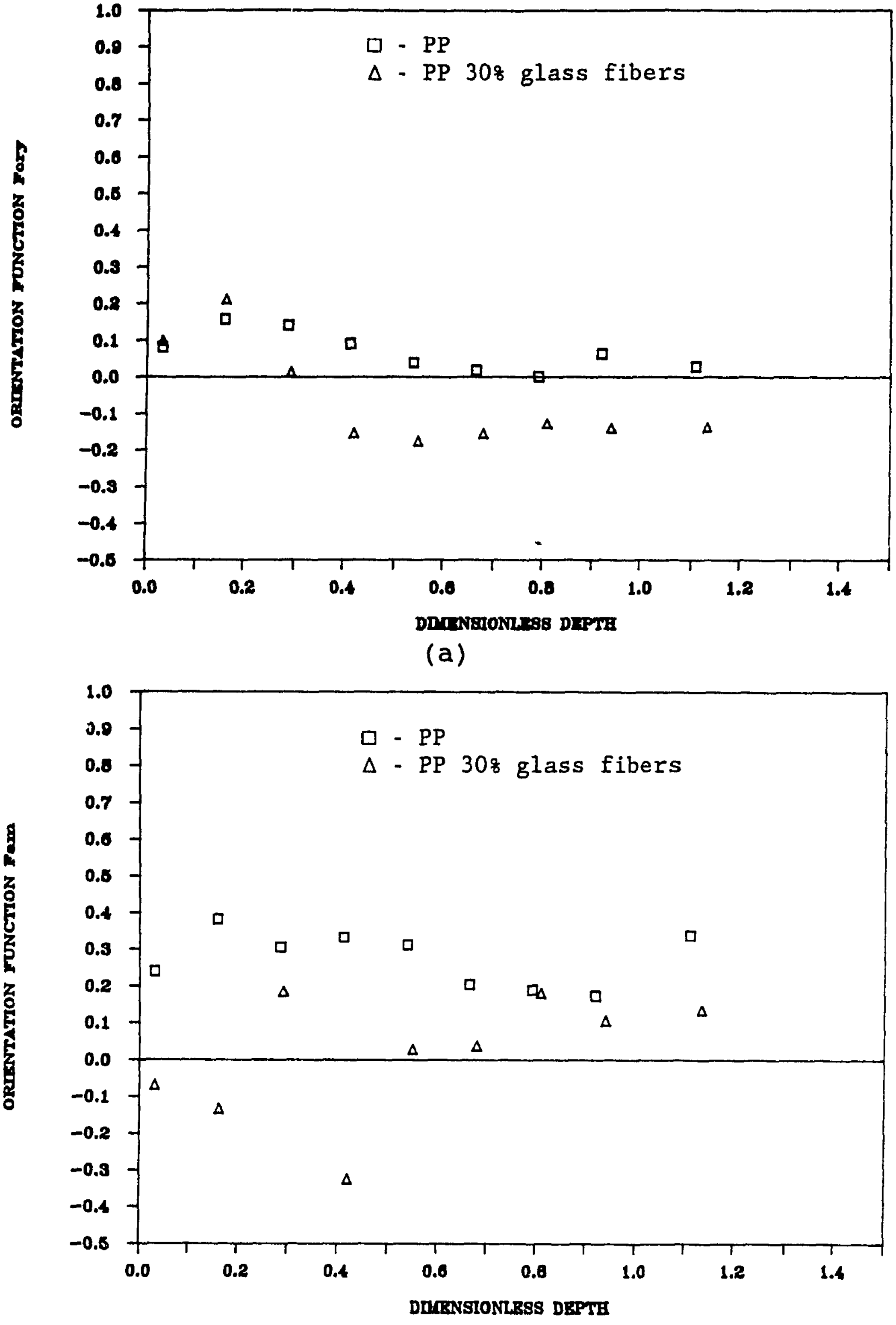

(a)

(b)

Figure 5.39 (a) Crystalline and (b) amorphous orientation of injection molded polypropylene and polypropylene composite (Conditions YCEN,ZCEN).

phase of injection molded polyethylene has been observed to be maximum at or near the surface [3]. The c-axis orientation below the surface is attributed to crystallization during shear flow (i.e. shear induced crystallization) at the interface of the frozen layer and the melt [5,176]. The orientation of the surface material is a characteristic of fountain flow in the melt front region [7]. The core shows predominantly a-axis orientation in this case. The increase of a-axis orientation from the surface to the core is attributed to the increase in time available for the molecular chains to relax due to the longer cooling times towards the centre of the molding [3].

The evidence is strong that the fibers affect the molecular orientation distribution in injection molded composites. The highly non-Newtonian, high viscosity reinforced melt produces high shear stresses close to the solid melt interface. This is manifested in high flow orientation that is limited to the zone close to the walls. The pseudo-plastic nature of the reinforced melt causes the velocity profile to be flat (plug flow) away from the wall. In the unreinforced melt, non-Newtonian effects are not as large, thus the velocity profile is not as flat and shear effects cover a broader region.

As observed previously, the fibers play an important role in restricting changes in molecular conformation and relaxation effects. This explains why the molecular orientation in the pure polypropylene has relaxed to a random distribution in the core, whereas some residual transverse orientation remains in the composite core. The presence and orientation of the glass fibers inhibit the relaxation of the oriented amorphous material, which causes c-axis orientation of the crystalline regions after the primary and secondary crystallization of the material [150].

The FTIR method provides reproducible results for the crystalline orientation, as seen in Figure 5.40, which compares the results obtained for two samples. However, the amorphous orientation, estimated by this method, shows large variability. The reason could be due to the great influence of fibers on the orientation of the amorphous phase. In support of this hypothesis, it has been found, in this work, that more consistent orientation data are obtainable with unreinforced injection molded samples than with reinforced composites.

In Figure 5.41, the crystalline orientation for a composite sample at positions 1 to 3 is examined. All the profiles show orientation in the flow direction near the surface. At position 1 and 3, the orientation is highest at the surface and decreases towards the centre. The maximum is highest at position 1. The maximum orientation lies at some depth below the surface at position 2. It can also be seen that in the core region the orientation is transverse to the x-direction. The orientation is random at some point below the

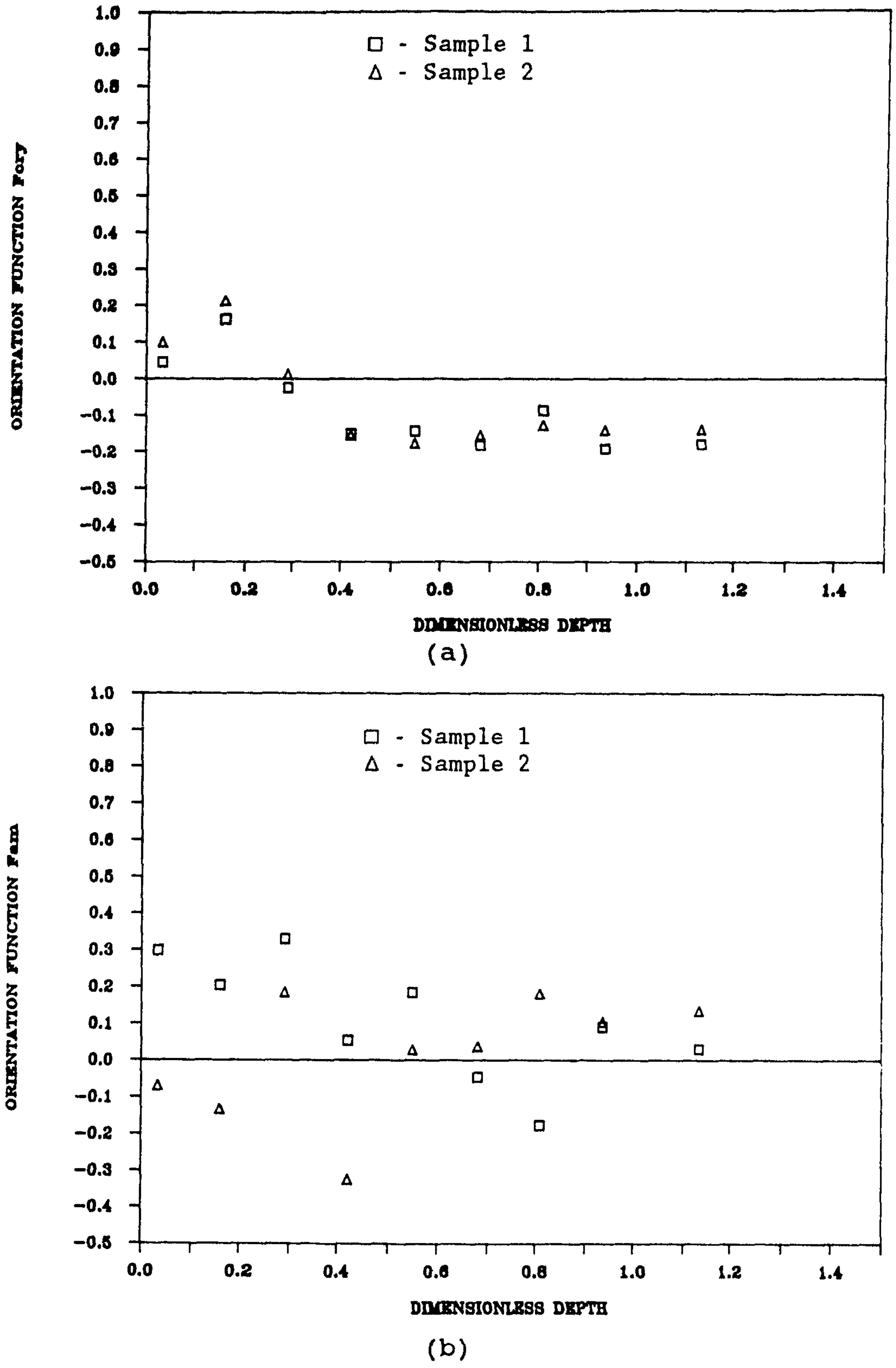

Figure 5.40 (a) Crystalline and (b) amorphous orientation of injection molded samples (Condition ZCEN).

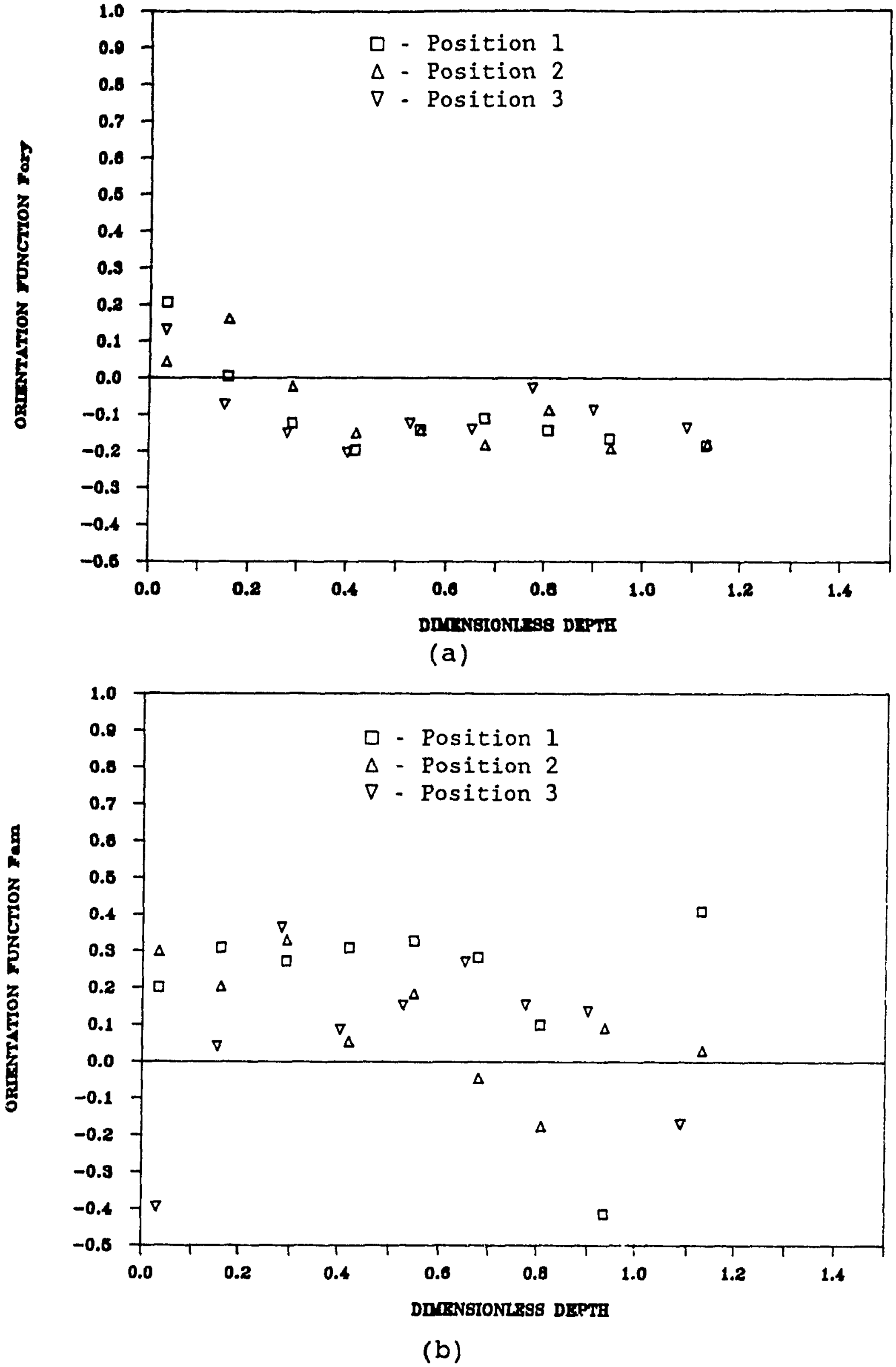

Figure 5.41 (a) Crystalline, and (b) amorphous orientation at positions 1 - 3 in the mold (Condition ZCEN).

surface (0.1 - 0.3 dimensionless depth).

The results appear consistent with other studies that have reported high flow direction orientation at or just below the surface [3,174]. The intensities of the maximum become lower as the distance from the gate increases. This is similar to observations made by Kamal and Moy [177]. Magila, et al. [150] showed that the a and c-axis of crystals were oriented parallel to the direction of flow, with the highest orientation near the gate region.

The variation in the depth of the position of maximum orientation is in good agreement with the analysis of the development of the frozen layer growth analysis given in chapter 6. The orientation is maximum at the surface near the gate and at the end of the mold, where in both cases the frozen layer at the end of filling is the thinnest. Position 2 has a thicker frozen layer at that time, and thus shows the maximum orientation below the surface, where the solid-melt interface is encountered.

The effect of processing variables was also examined. The samples were examined at position 2 at the centre of the mold. The results are presented in Figures 5.42- 5.45. In general, the crystalline orientation has a maximum below the surface, and orientation becomes random in the core. The maximum occurs at a dimensionless depth of 0.2 at a melt temperature of 200 °C compared to 0.3 for the higher melt temperature. Orientation in the flow direction is more predominant in the

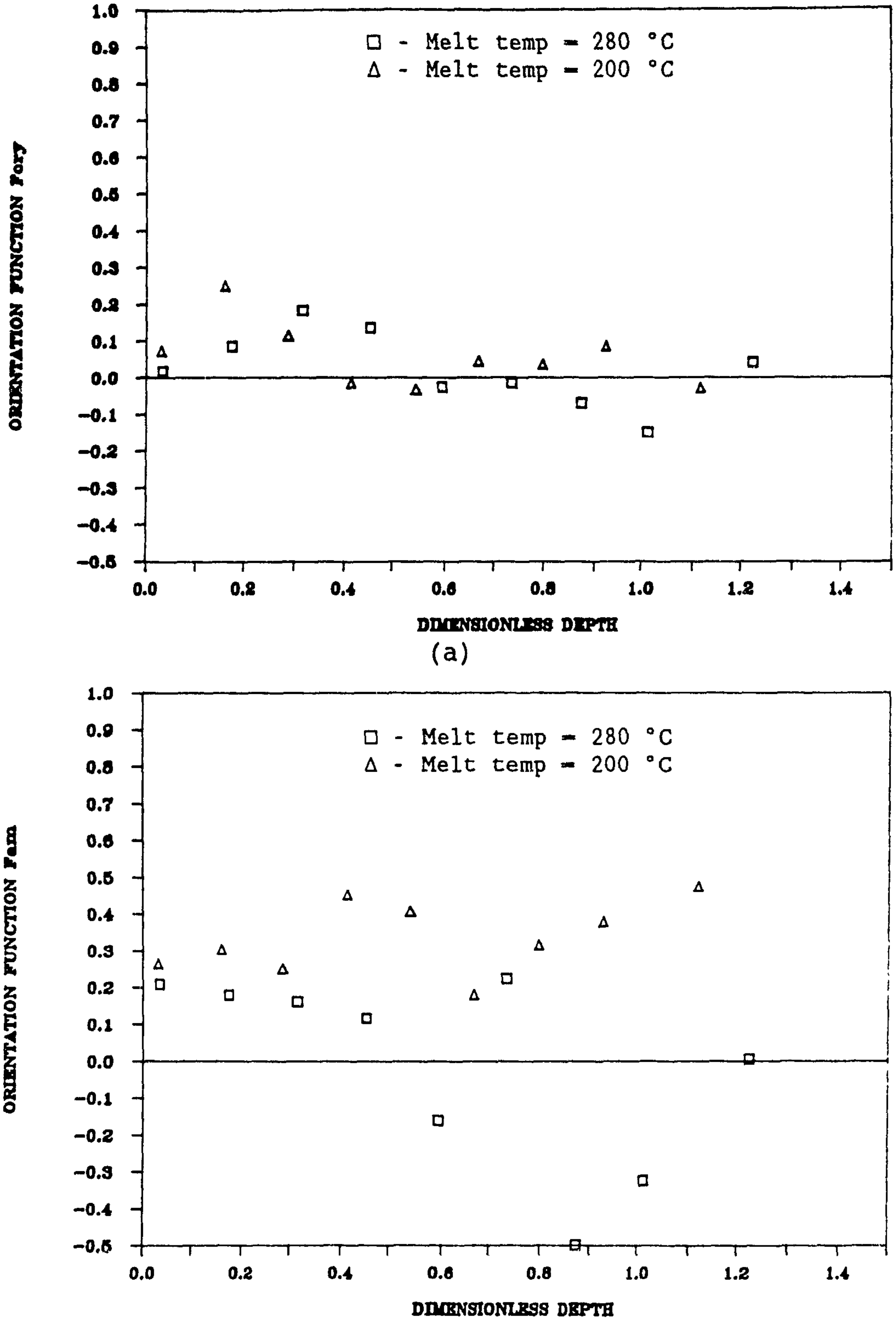

(a)

(b)

Figure 5.42 Effect of melt temperature on (a) crystalline, and (b) amorphous orientation (Conditions ZLMT, ZHMT).

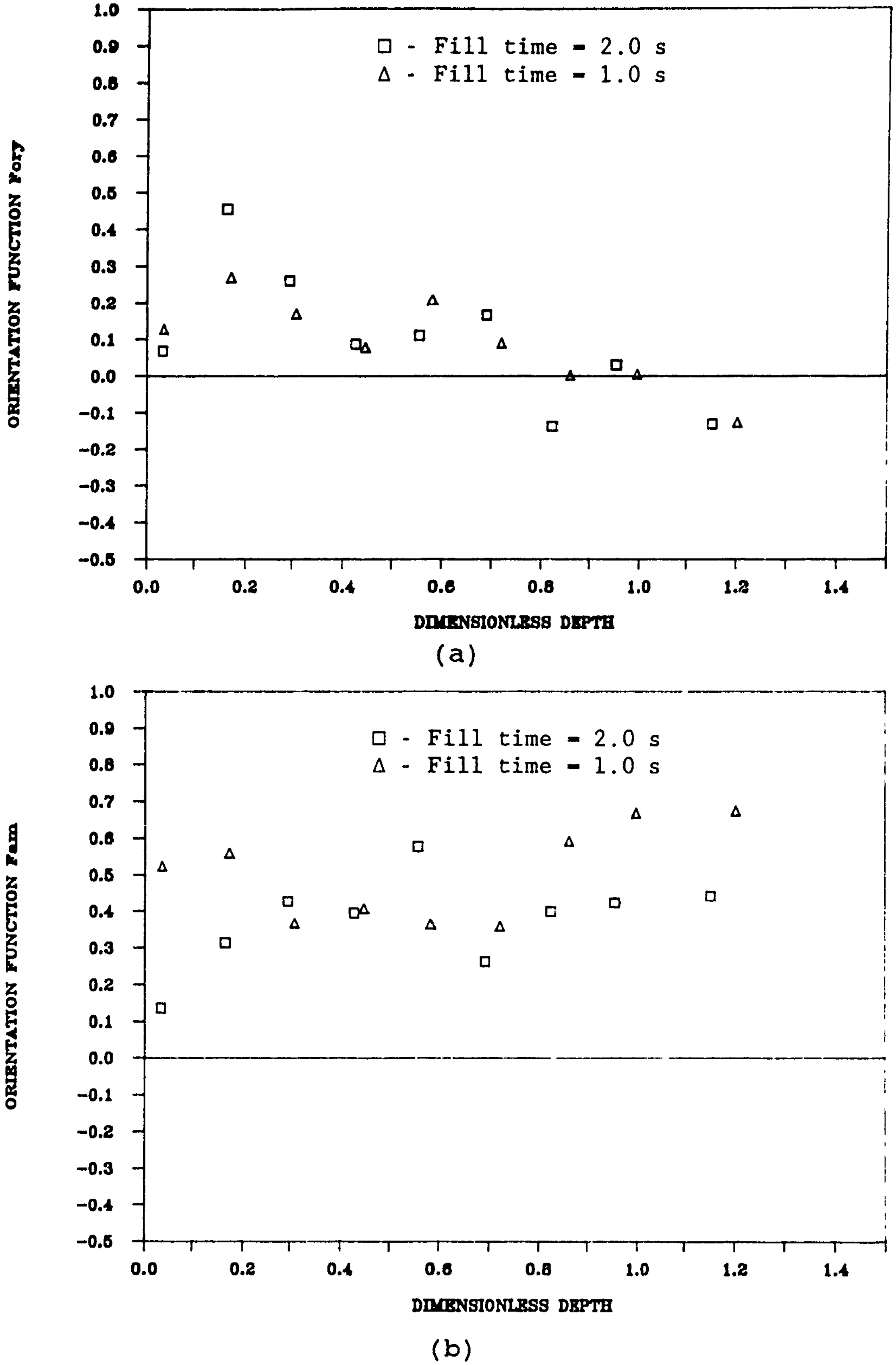

Figure 5.43 Effect of filling time on (a) crystalline, and (b) amorphous orientation (Conditions ZLIT, ZHIT).

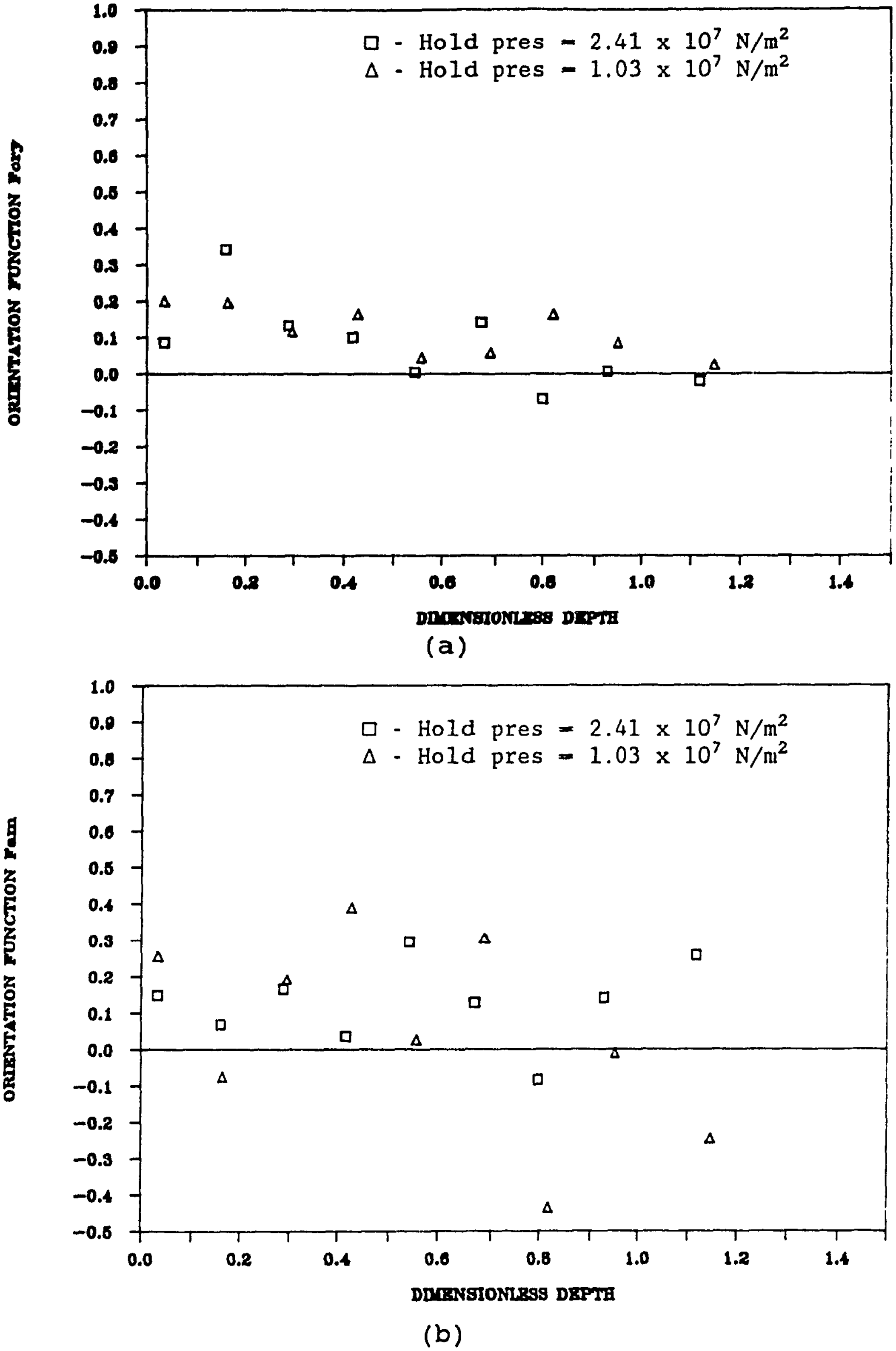

Figure 5.44 Effect of holding pressure on (a) crystalline, and (b) amorphous orientation (Conditions ZLHP, ZHHP).

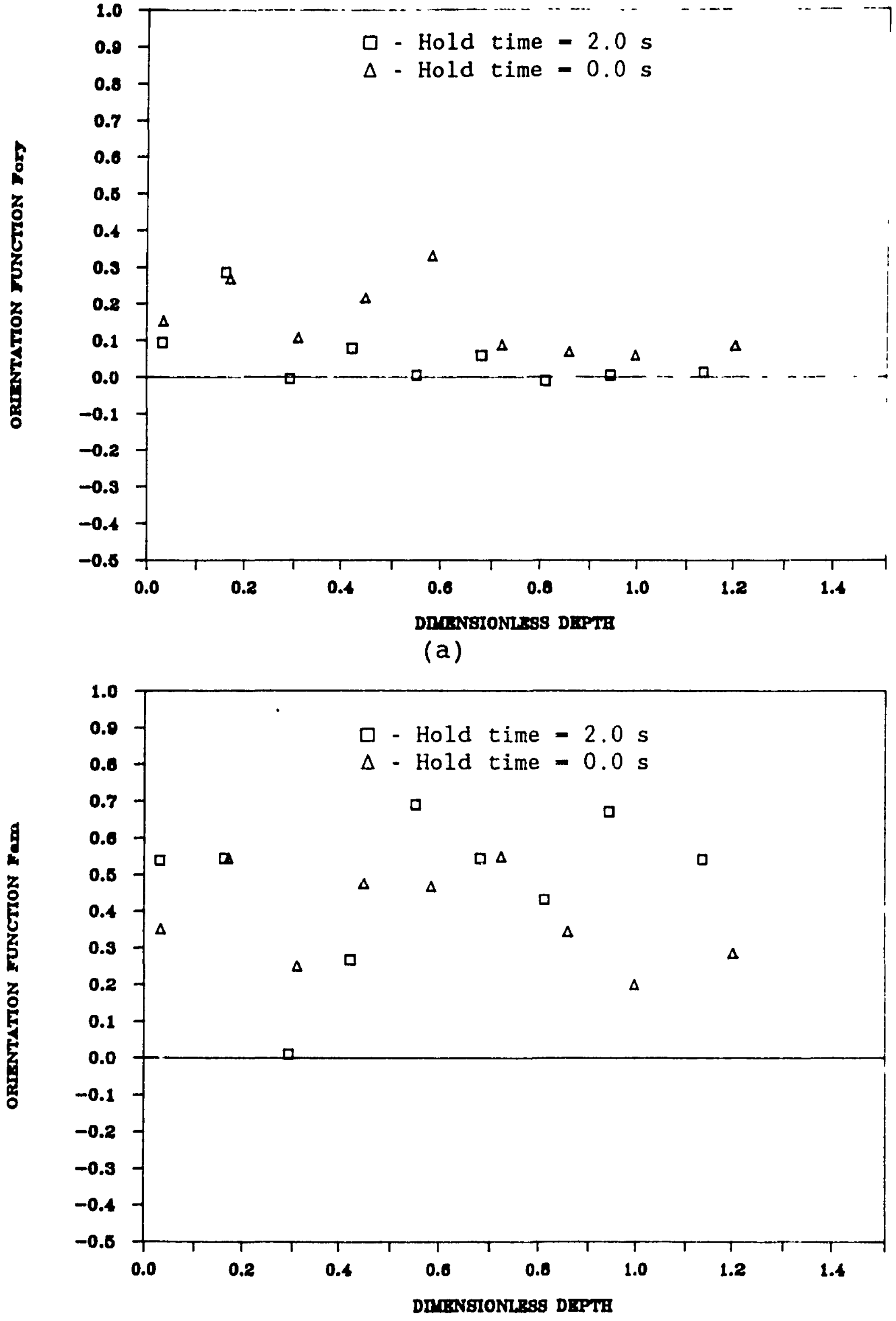

(a)

(b)

Figure 5.45 Effect of holding time on (a) crystalline, and (b) amorphous orientation (Conditions ZLHT, ZHHT).

low melt temperature sample. This is in agreement with other results reported in the literature [178]. The effect of higher shear stresses is expected to increase the orientation in the flow direction. An additional consequence is that at lower temperatures, the polymer has less time to relax, thus the orientation persists at the end of the filling stage. The effect of slower injection time on orientation is comparable to the effect of lower melt temperature. The longer filling time shows a greater maximum orientation. The slower flow rate allows for increased cooling while the material flows into the cavity. With the colder material, the shear stresses are greater, resulting in higher orientation, and, the relaxation effects are smaller.

At higher packing or holding pressure, the orientation in the sub-skin layer becomes higher and the maximum near the surface becomes sharper. The role of increasing pressure appears to be inhibiting the molecular relaxation process. Similar results have been reported by Heckmann and Johnsen [178]. Holding time does not appear to have a significant influence on the distribution of crystalline orientation.

In general, crystalline orientation in injection molding composites is characterized by:

(i) Maximum orientation at or near the surface layer. The surface orientation is a result of fountain flow. The orientation below the surface is caused by shear flow after the flow front has passed. In composite samples, the orientation peak is narrow, while it is broader in the unreinforced material. This emphasizes the stronger non-Newtonian behaviour of the composite melt.

(ii) The orientation in the core of the samples is random. Competing with the orientation process, is a relaxation process. The relaxation process dominates in the core where the cooling rate is slow. In the case of the composite sample molded at condition ZCEN, there is transverse orientation remaining in the core.

(iii) Molecular orientation is the result of the competition of orientation and relaxation processes. The two processes are affected by a variety of factors such as temperature, pressure shear, etc., as discussed above.

5.7.2 Amorphous Phase

The unreinforced sample exhibits orientation essentially in the x-direction. High orientation is observed near the surface. The orientation shows a maximum below the surface and decreases towards the centre. Other workers have shown transverse orientation at the surface, maximum flow direction orientation just below the surface, and decreasing flow direction orientation towards the core [3,28]. Menges and

Wubken [28] showed maximum orientation at the surface in injection molded polystyrene.

The source of the skin orientation is attributed to elongational forces developed during fountain flow of the advancing melt front during the filling process [7,28,179]. The surface layer solidifies, retaining the x-direction orientation. The second sub-skin layer of flow direction orientation is formed by shear stress during flow after the melt front has passed [7]. During filling, a frozen layer is formed at the walls. This decreases the cross-sectional area available to flow, and produces high shear stresses at the solid-melt interface. The maximum orientation occurs close to the surface at a depth of 220 - 250 μm, where the solid-melt interface and maximum shear stress occur. The decrease in orientation towards the core may be the result of decreasing shear effects at the centre of the flow, as well as increasing molecular relaxation effects in the higher temperature core region. Jackson and Ballman [31] studied the effects of processing conditions on molecular orientation. They showed that shear flow is the main source of molecular orientation and that the process of molecular relaxation reduces this orientation. Crystallization also occurs in a way to relieve the stresses.

Tadmor [7] proposed a semi-quantitative model, incorporating flow and heat transfer and molecular theories, to estimate orientation effects. However such a model is not applicable to fiber reinforced systems. Kamal, et al. [9,180] have simulated the injection molding of a visco-elastic polymer with fountain flow. The results obtained have been used to explain experimental observations of orientation effects.

The amorphous orientation function for the reinforced samples shows large variability as can be seen in Figure 5.40. This is probably due to the influence of the glass fibers, which cause local orientation effects [150]. The presence of glass affects the uniformity of the relaxation of the amorphous material, as well as the orientation of the crystalline regions caused by primary crystallization in the presence of the fibers.

With due allowance for the observed variability of the measurements, an overall trend of flow direction orientation of the amorphous phase in the composites can be presumed. However, analysis of the effects of processing conditions on the amorphous orientation was not attempted. In summary, the molecular orientation in the amorphous phase can be described as follows:

(i) In the unreinforced material, flow direction orientation at the surface increased to a maximum just below the surface, then decreased to a minimum at the core. The orientation was in the flow direction throughout the thickness. The amorphous phase orientation was higher than the crystalline phase orientation in the pure polypropylene sample.

(ii) The orientation was irregular in the composite samples, due to the localised orientation effect of the glass fibers. The general trend was of flow direction orientation.

(iii) The orientation profile in the amorphous phase is very similar to that in the crystalline phase. It appears that both are determined by the same processes, i.e., fountain flow, shearing at the solid melt interface, etc. However, the observation of lower crystalline orientation suggests that crystallization occurs in such a way as to relax molecular orientation.

5.8 Fiber Phase Properties

5.8.1 Fiber Concentration

The effect of processing conditions on the fiber concentration distribution was investigated. At positions 1 to 6, the whole thickness was removed from the molding. This was also done at the sprue which is designated position 0. The sections were analyzed by Thermo-Gravimetric Analysis (TGA) in order to determine the glass content. The glass weight concentration value (X%) obtained was converted to percent deviation in fiber concentration by the formula:

$$\left\{ \%\ \text{deviation} \right\} = \left\{ \frac{X\% - \text{fiber conc. in pellet)}}{\text{fiber conc. in the pellet}} \right\} \qquad (5.1)$$

Positive values indicate an accumulation of fibers, while negative values indicate a depletion of fibers in that area.

Figure 5.46 shows the depletion of fibers at the front end of the mold and accumulation at the back end. Positions 0 and 4 have lower concentration of fibers than the pellet while positions 3 and 6 show slightly higher values. This phenomenon has been observed by Kubat and Szalanczi [181]. The average concentration of fibers was observed to be lower near the entrance of a spiral mold and higher at the end of the mold. This difference was shown to increase with fibers of greater aspect ratio.

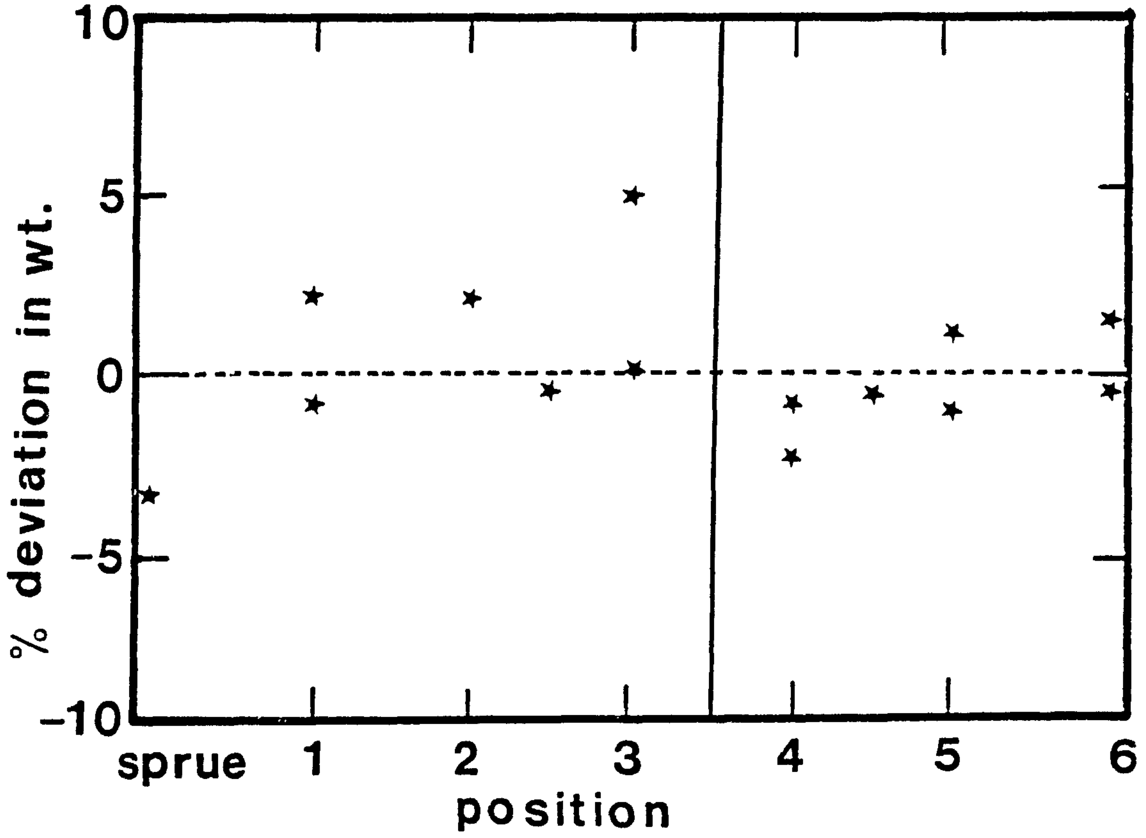

Figure 5.46 Fiber concentration distribution in injection molded samples (Condition ZCEN).

Layers were microtomed with thicknesses of 100 and 200 μm at position 2 in injection molded samples. The percent fiber concentration deviation is plotted versus the dimensionless depth.

The results are presented in Figure 5.47. The following observations can be made:

(i) there is fiber depletion in the region close to the surface;

(ii) fiber accumulation occurs at a region that is intermediate between the skin and core;

(iii) fiber concentration at the central or core region is equal to the average concentration, i.e. no concentration or depletion is observed.

Fibers appear to migrate away from high shear to lower shear regions. The fibers that migrate away from the surface region, accumulate in the intermediate zone. The core is not affected by any fiber migration process.

The drop in fiber concentration at the surface is quite sharp. This raises further evidence of a fiber deficient zone, as was observed with optical microscopy.

5.8.1.1 Effect of Processing Conditions

The effect of melt temperature on the fiber concentration distribution in the thickness direction is illustrated in Figure 5.48. For the higher melt temperature, there is

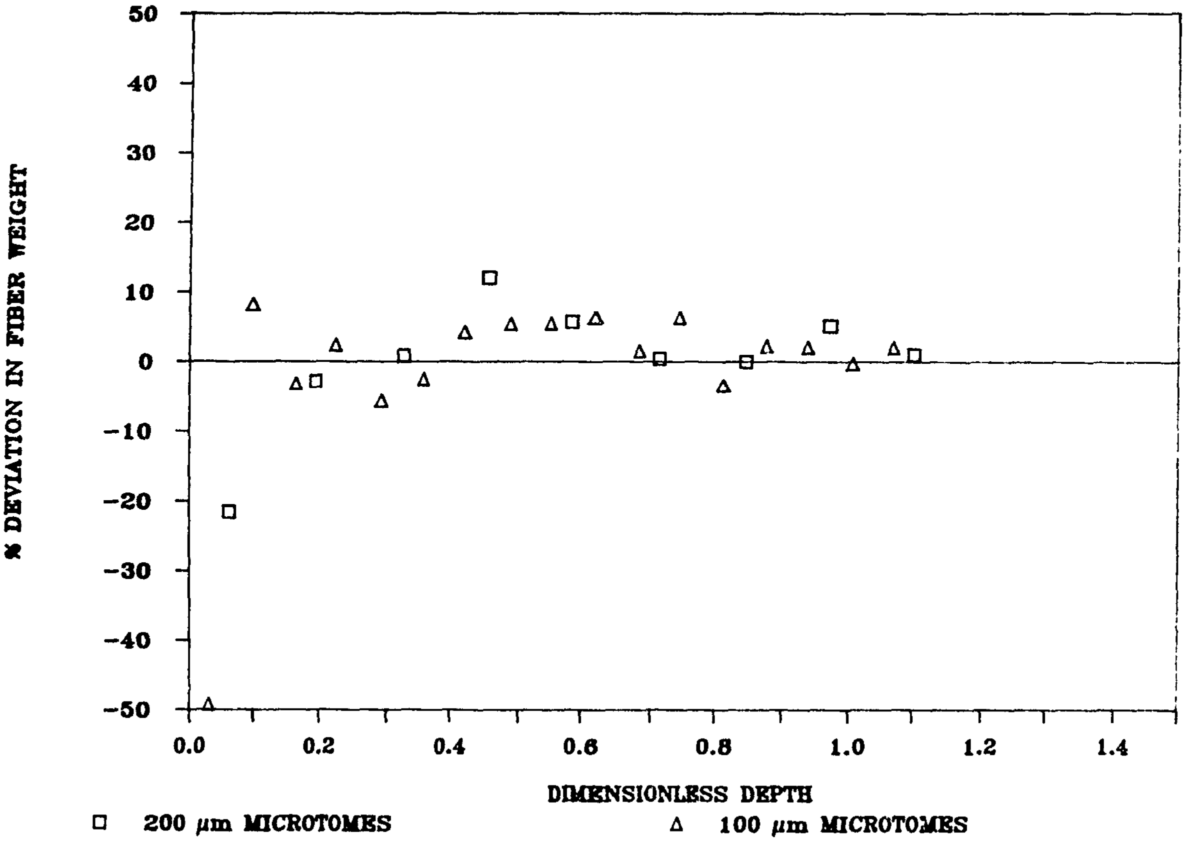

Figure 5.47 Replicates of fiber concentration distribution in the depth direction in injection molded samples (Condition ZCEN).

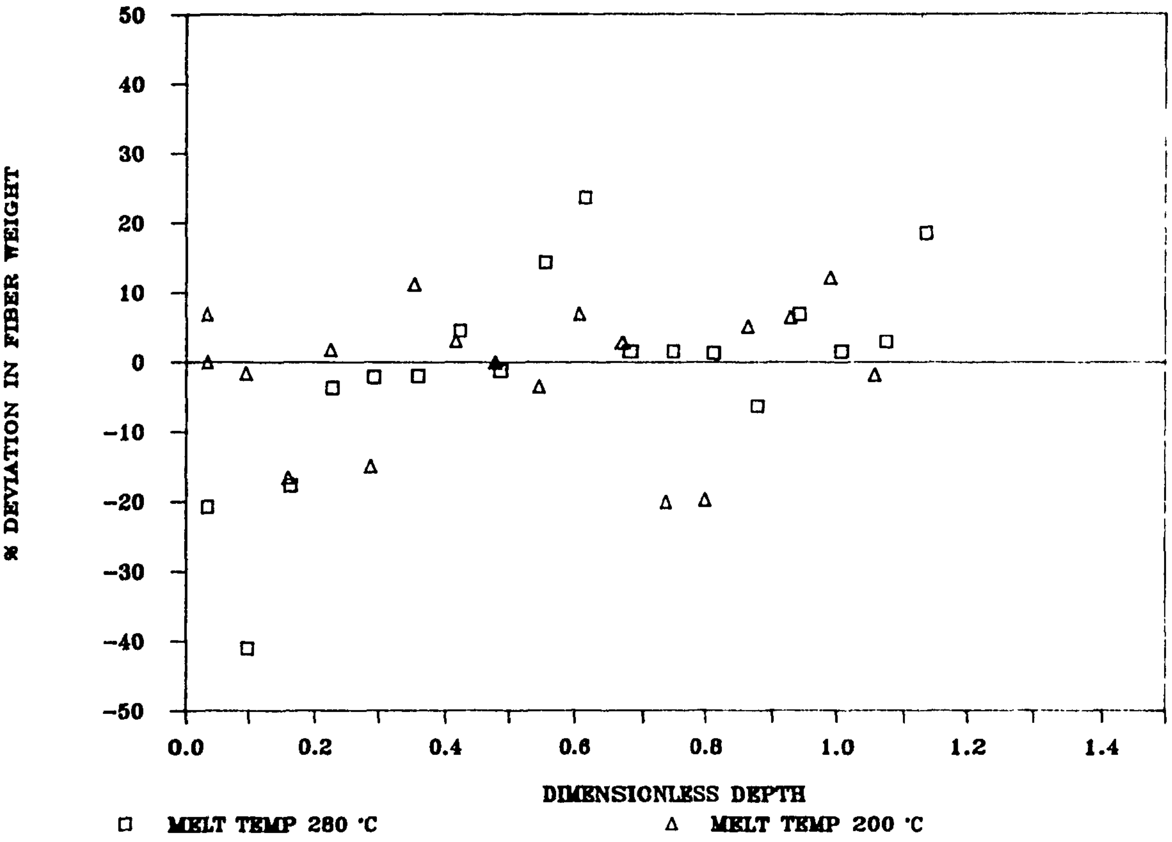

Figure 5.48 Effect of on melt temperature on fiber concentration distribution in injection molded samples (Conditions ZHMT, ZLMT).

depletion of fibers close to the surface. The depletion is not evident in the lower melt temperature molding. Lower viscosity appears to be a helpful factor in the fiber migration process.

The effect of filling time on the fiber concentration distribution is shown in Figure 5.49. The results show that there is a region of fiber depletion near the surface. It seems that depletion is more pronounced at higher fill rates. It should be noted that higher fill rates are associated with higher effective melt temperature and higher shear rate during filling. Thus, the observed effect may be due to both temperature and shear rate differences.

Significant fiber migration during flow has been observed by other researchers [76,138]. Wu [76] showed that fibers migrate to low shear rate zones in the flow. Fiber migration occurs in extrusion when there are normal stresses or eccentric rotation of fibers. Maximum fiber concentration was found at the centre of extrudates with the minimum at $(r/R) = 0.63$.

Evidence of a fiber free region near the surface was found in the sprue. Sometimes, the phenomenon is observed in the molding depending on the processing conditions. In most of the samples, the conditions were not ideal for the region to be formed. Akay [138] found that if the injection speed, mold temperature or melt temperature were high, then the fiber free region near the surface would penetrate well into the

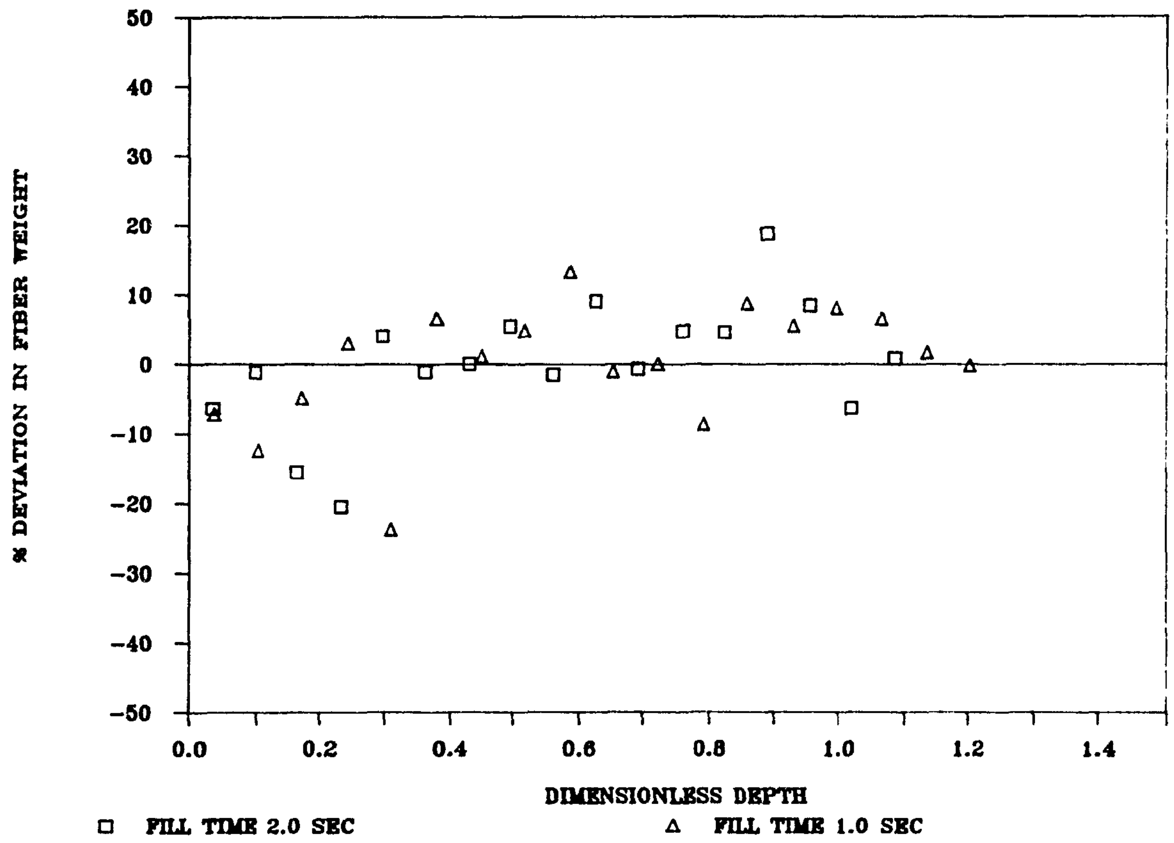

Figure 5.49 Effect of filling time on fiber concentration distribution in injection molded samples (Conditions ZHIT, ZLIT).

molding in the direction of flow. If they were low, the fiber free region is away from the surface. The fiber free region is found adjacent to the highly oriented region in which fibers are aligned in the flow direction.

In an isothermal case, the fiber free region should be expected next to the surface. However, in the case of injection molding, a frozen layer is formed during fountain flow. This acts as a new surface, forcing the fiber free zone to be formed some distance from the surface.

Flow induced crystallization could play a significant role in the formation of the fiber free layer. The highly oriented structures that are formed exclude the smaller molecules and push them into the amorphous regions [182,183]. Similarly, flow induced crystallization can cause fiber migrations to yield fiber deficient regions. In injection molding, the conditions of flow, shear rate and melt temperature are suitable for this type of crystallization to occur at the melt-solid interface.

5.8.2 Fiber Length

Fiber length distribution in the injection molded article is important in determining the mechanical properties [83]. The fiber length in the final molded article is determined not only by the original length of fibers before processing, but also by processing conditions and the geometrical aspects of the design of the plasticating unit, the delivery channels, the gate, and the mold [81,82]. The fiber length distributions in the pellet and in the injection molded sample are compared in Figure 5.50, which shows significant attrition or reduction in fiber length during processing. The average fiber length is reduced from 560 μm to 280 μm on processing in an injection molding machine.

Most of the fiber breakage occurs in the screw melting zone and injection unit with some additional breakage in the mold and runners [81,82]. The mechanism of fiber attrition is described as a two-stage phenomenon [82]. Fibers which are exposed by the surface melting of granules close to the barrel wall of the extruder, experience a bending moment due to one end being in the melt flow and the other anchored in the solid granule. This results in fiber breakage. The broken pieces flow with the melt and experience further breakage due to post-buckling deformation [82]. The initial fiber length appears to have a minor influence on the final fiber length [97,184].

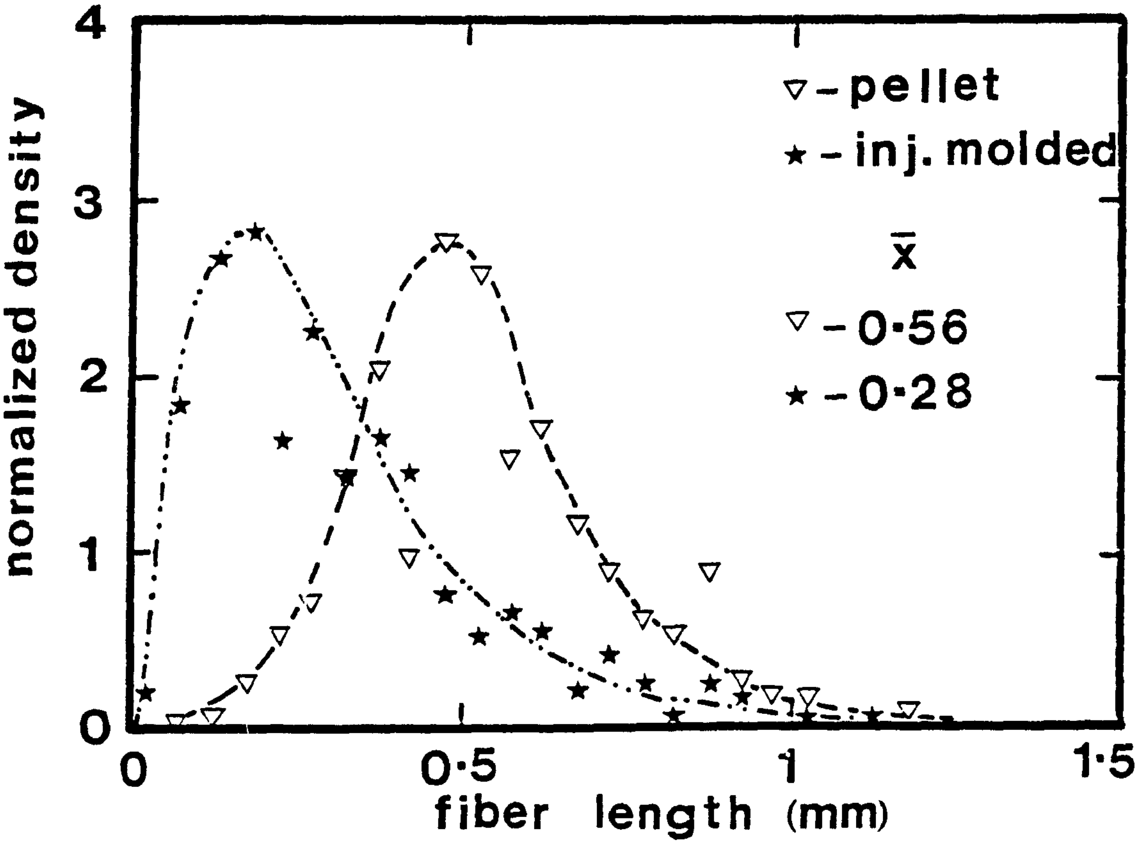

Figure 5.50 Fiber length distribution for material in pellet and in an injection molded sample (Condition ZCEN).

The average fiber length in microtomed layers 100 μm thick in the depth direction was plotted for various injection molded samples. Scanning electron microscopy revealed that the fibers were essentially located in the xy plane. Thus, microtoming should have had a minimal effect on fiber length measurements. However, the average fiber length across the thickness taken from the individual microtomed layers was significantly different from that obtained from an entire cross-sectional sample. The average fiber length in the whole cross-sectional sample was measured to be 280μm, whereas, it was approximately 190μm, averaged from individually microtomed layers. This discrepancy was probably due to some fiber breakage during microtoming and fiber image cut-off in the photographing and digitizing processes.

The average length distributions at positions 1 to 6, as shown in Figure 5.51, reveal a number of trends. In general, the fiber length varied from 100 to 280 μm. The fibers are longest at or near the surface and the length decreases to a minimum at the core. In a majority of the samples, the maximum length is observed at a depth of 150 to 200 μm. Some of the samples show a relative minimum of fiber length in the vicinity of the wall. Centre-line positions 1 to 3 show sharper gradients of fiber length than at positions 4 to 6. Figure 5.52 shows fiber length data for replicates of samples processed at the same conditions. The results suggest good reproducibility, with similar trends in both samples.

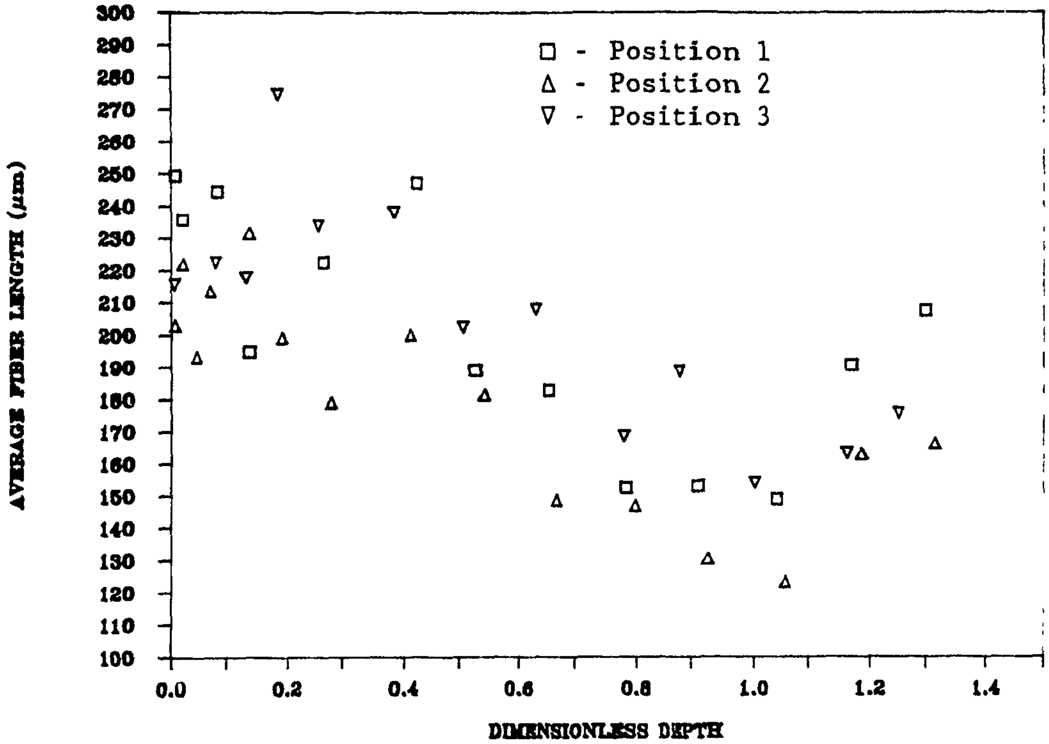

(a)

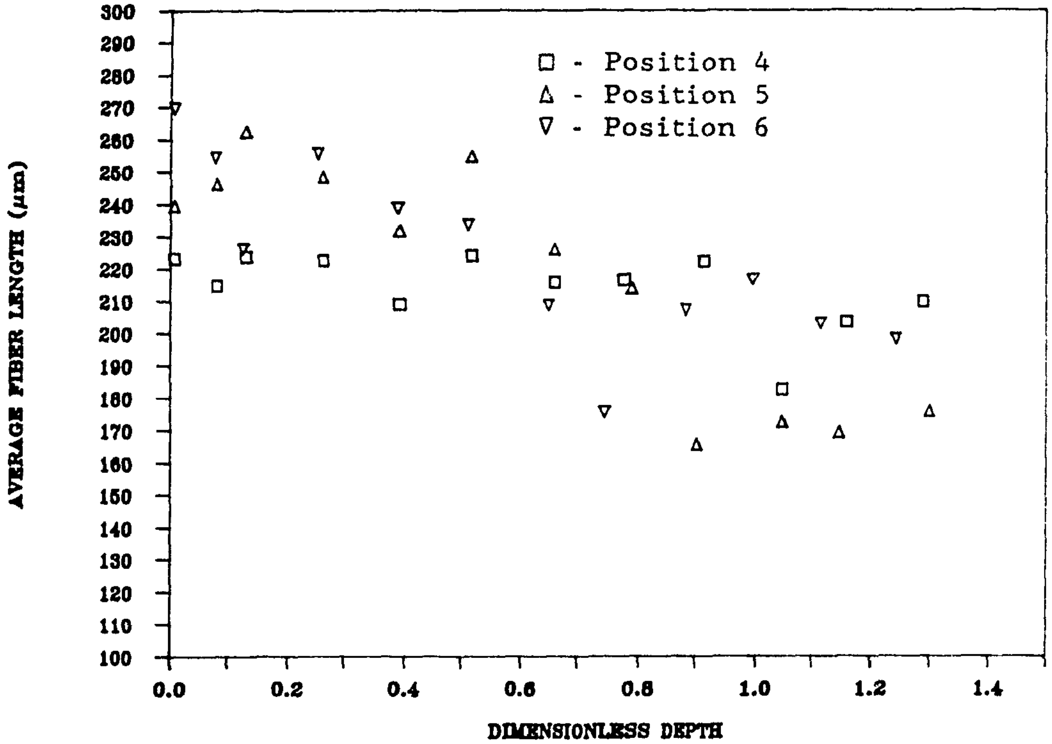

(b)

Figure 5.51 Average fiber length distribution in injection molded samples, (a) positions 1-3, (b) position 4-6 (Condition ZCEN).

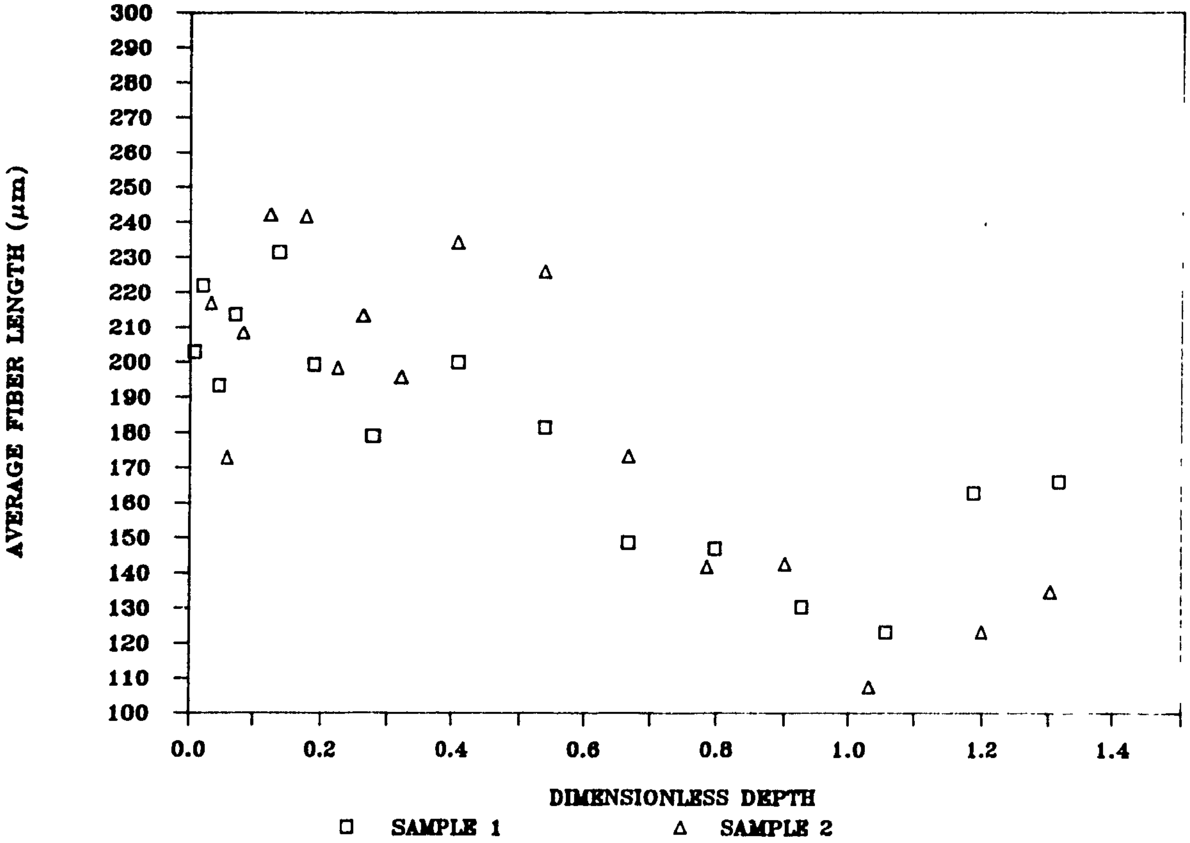

Figure 5.52 Replicates of average fiber length distribution in injection molded samples (Condition ZCEN).

It has been suggested that the major cause of fiber breakage is viscous loading rather than fiber-fiber or fiber-surface interactions [81,184].

Mason [97] developed a theory relating the bending behaviour of fibers suspended in a viscous liquid subjected to laminar shear. The fluid shear stress τ required to bend a straight fiber was related to the fiber aspect ratio (L/D) and modulus E as follows:

$$\tau = \left\{ \frac{E[\ln(2L/D) - 1.75]}{2(L/D)^4} \right\} \tag{5.2}$$

They found that a sufficiently high shear stress would produce buckling, and that the threshold values of such stress for long fibers would be significantly lower than stresses encountered during processing. The implication is that, during processing, long fibers would break down into successively shorter fibers, until the resulting fibers are too short to be broken by the shear stresses. The above is in agreement with the observations made by other workers [81,82]. However, these predictions are not confirmed by the results shown in Figure 5.51, where a comparison is made between the lengths of fibers in the downstream and upstream positions.

It will be shown later, that, in injection molding, fibers near the wall are usually oriented in the flow direction, while, in the core, they are oriented transverse to the direction of flow. The shear stresses acting on the fibers near the wall are less effective because they act along the length of the fibers. In the centre, where the fibers are aligned in the transverse direction, stresses acting on the fibers involve bending and could cause them to break. The force needed to bend and break a fiber is much lower than that required to pull it apart. Thus, greater fiber breakage occurs in the core than near the walls, as shown in Figures 5.51 and 5.52.

There are some deviations in fiber length distribution close to the wall along the depth direction, which do not conform to the above observations. They might be attributable, in part, to solidification effects where fibers near the wall are trapped partly in the solidifying skin and partly in the melt zone. Under such conditions, fibers would be broken by the shear stresses at the solid-melt interface during filling and packing. This is similar to the phenomenon observed in the melting zone of an extruder [82].

The effect of processing conditions on the average fiber length in the layers was not very large. The results are shown in Figures 5.53 to 5.56. The general trend of a decrease in average fiber length towards the core is present in all cases. The largest differences occurred in the intermediate layer. The melt temperature of 280 °C produced much shorter fiber length in the intermediate layers. At the surface, the average fiber lengths were similar for both melt temperatures of 280 and 240 °C.

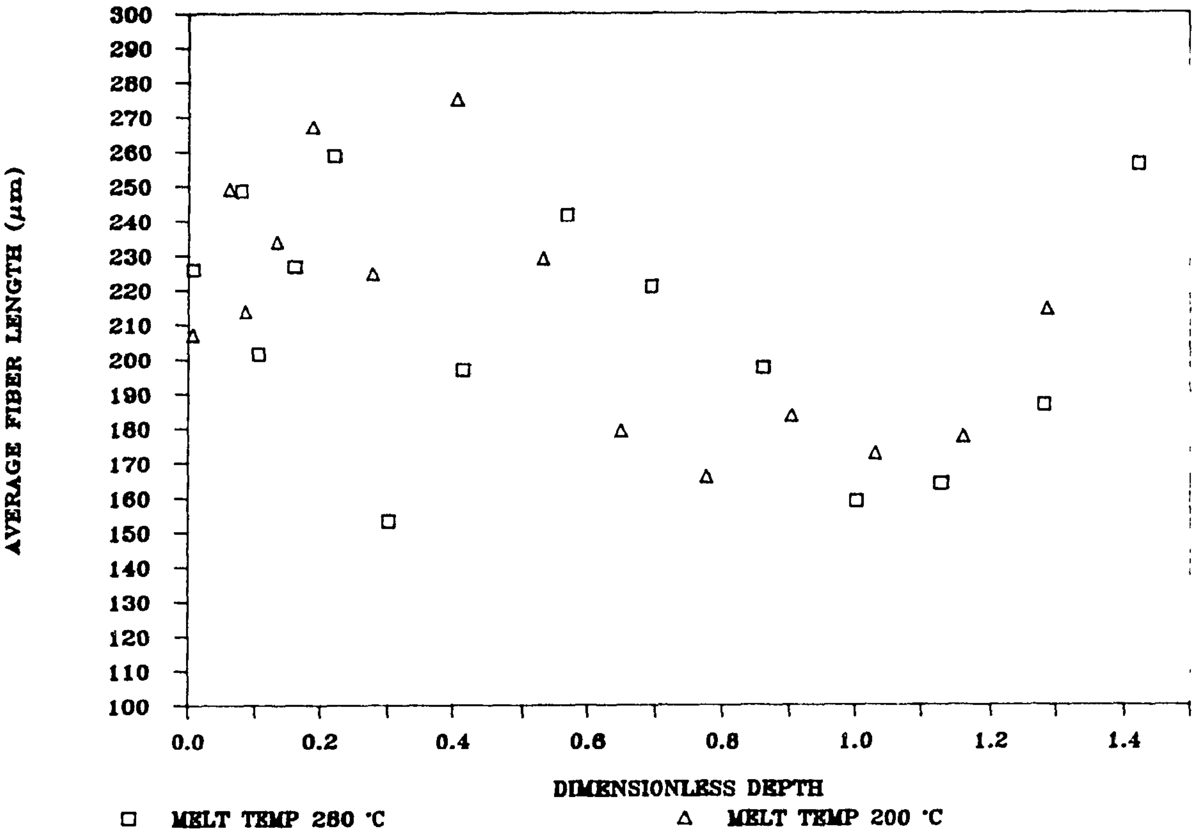

Figure 5.53 Effect of melt temperature on average fiber length distribution in injection molded samples (Conditions ZHMT, ZLMT).

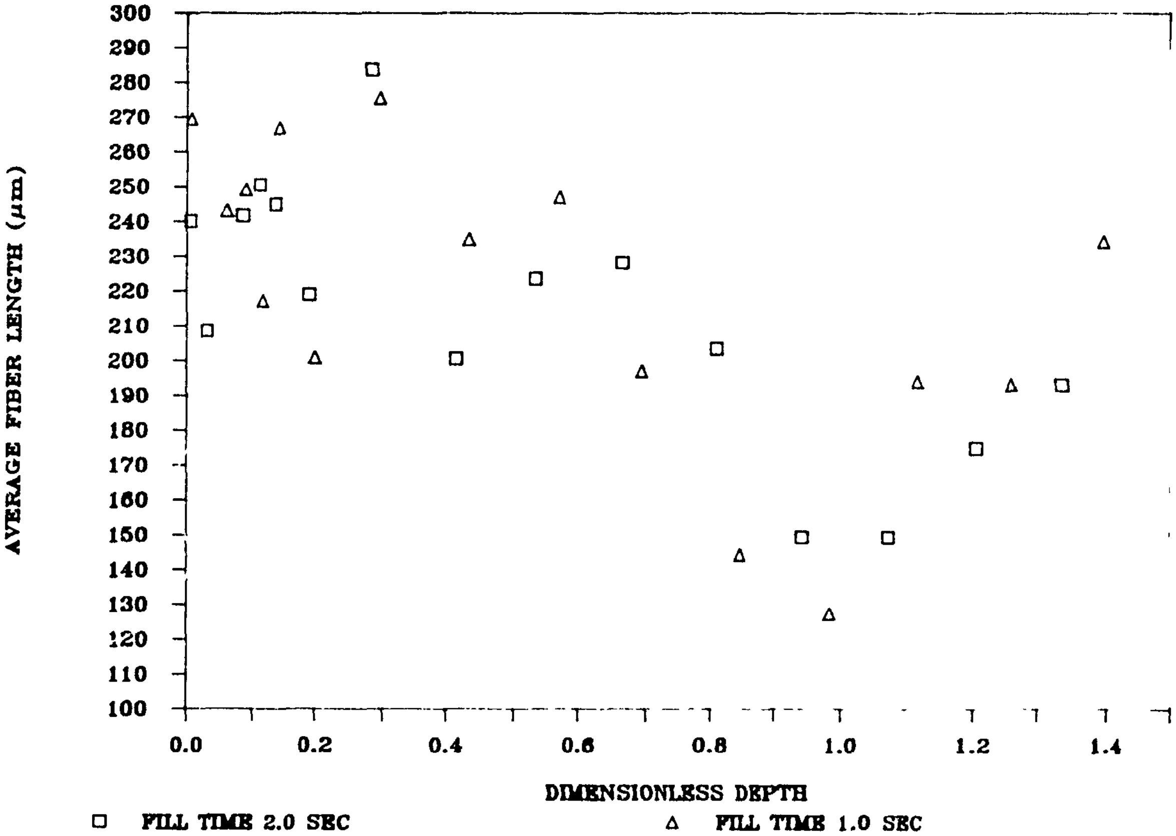

Figure 5.54 Effect of filling time on average fiber length distribution in injection molded samples (Conditions ZHIT, ZLIT).

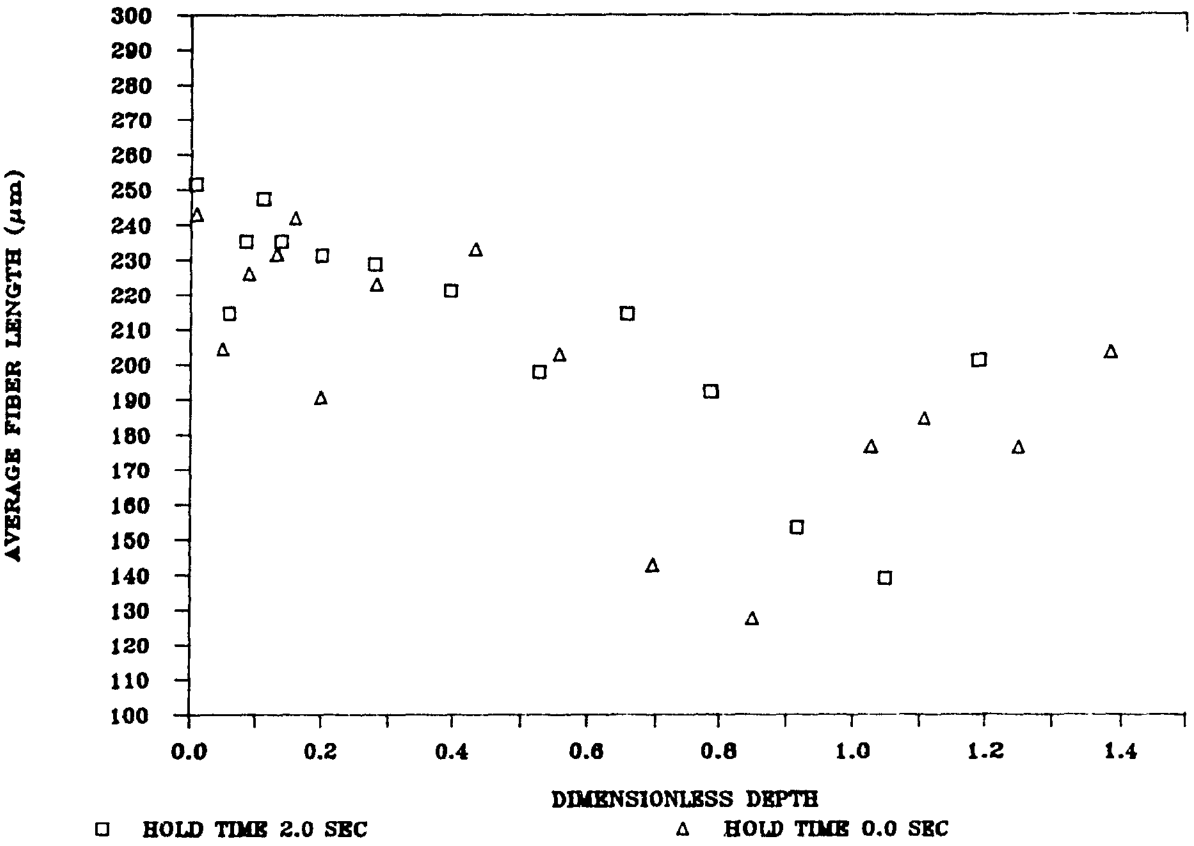

Figure 5.55 Effect of holding time on average fiber length distribution in injection molded samples (Conditions ZHHT, ZLHT).

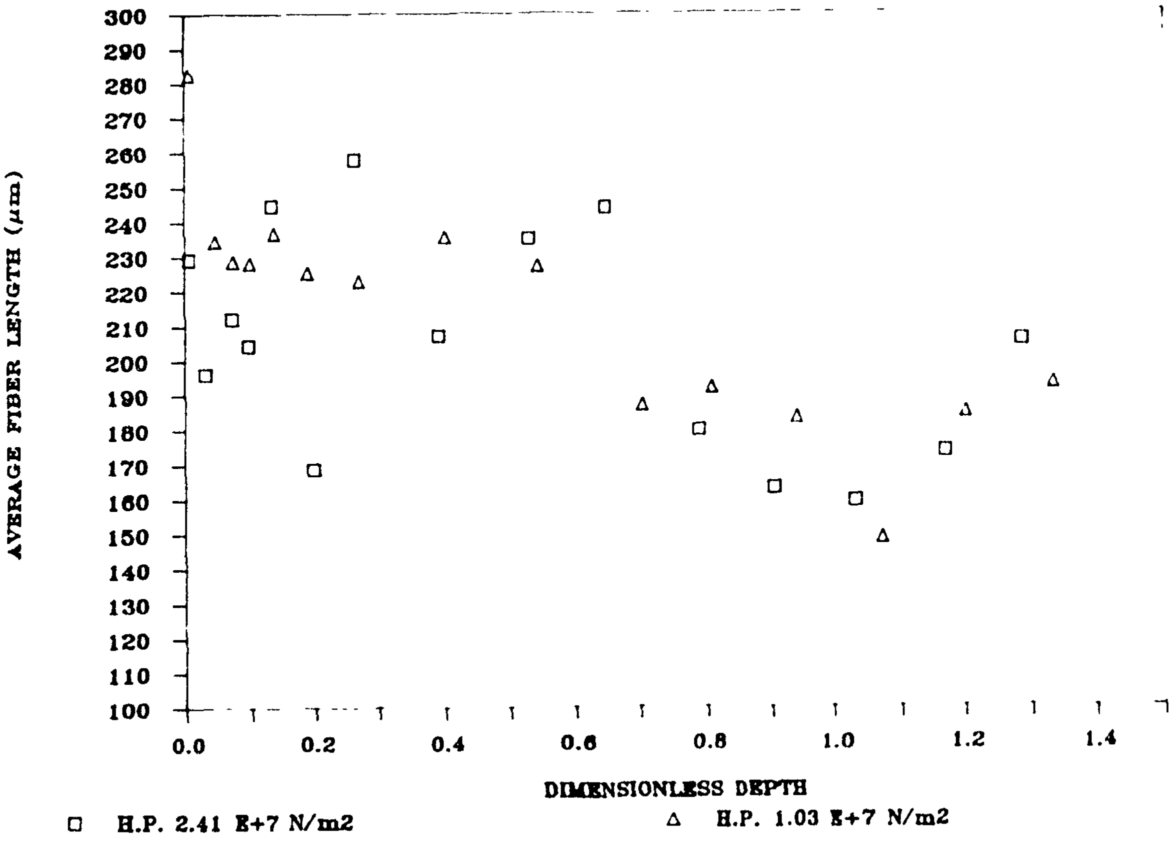

Figure 5.56 Effect of holding pressure on average fiber length distribution in injection molded samples (Conditions ZHHP, ZLHP).

5.8.3 Fiber Orientation

Figures 5.57 to 5.60 show the variation of the fiber images obtained at selected layers at progressive depths in the thickness direction. The fibers are predominantly oriented in layers in the x-y plane, and this result has been verified in other reported studies [92,185,186]. This facilitates the measurement of fiber orientation by microtoming layers from skin to core. The digitized images, reproduced from the end point coordinates, show complex changes in fiber orientation from the surface to the centre of the samples.

In each layer, the orientation can be described by the distribution of fiber angles as in Figure 5.61, however this scheme is cumbersome. The fiber orientation was described in this study by the use of orientation function, f_p, described in Appendix II. The orientation function, f_p, is defined as follows:

$$f_p = \frac{1}{2}\left\{ 3\langle\cos^2(\pi/2-\phi)\rangle - 1 \right\} \tag{5.3}$$

$$\langle\cos^2(\pi/2-\phi)\rangle = \int_{-\pi/2}^{\pi/2}\left\{ N(\pi/2-\phi)\cos^2(\pi/2-\phi)\,d(\pi/2-\phi) \right\} \tag{5.4}$$

where

$N(\pi/2-\phi)$ = the weighting function for the normalized distribution corresponding to the percentage of fibers at an angle of $(\pi/2-\phi)$ measured from the principal coordinate system.

CENTRE OF MOLD (POSITION 2) INJECTION DIRECTION ↓
(d.d. = depth/half thickness)

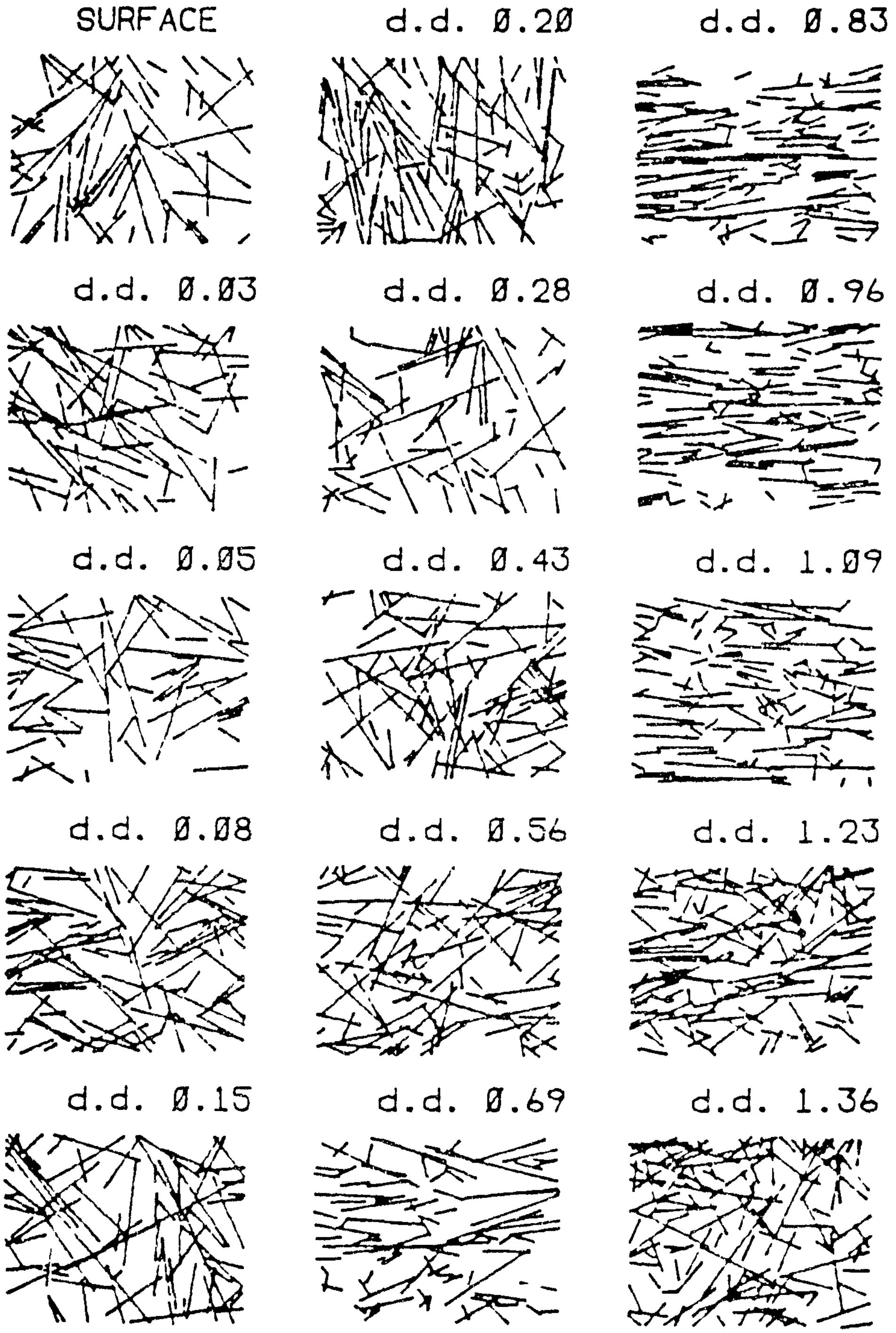

Figure 5.57 Fiber images taken of selected layers at various depths in the thickness direction near the centre of the mold, position 2 (Condition ZCEN).

OFF-CENTRE OF MOLD (POSITION 5) INJECTION DIRECTION ↓
(d.d. = depth/half thickness)

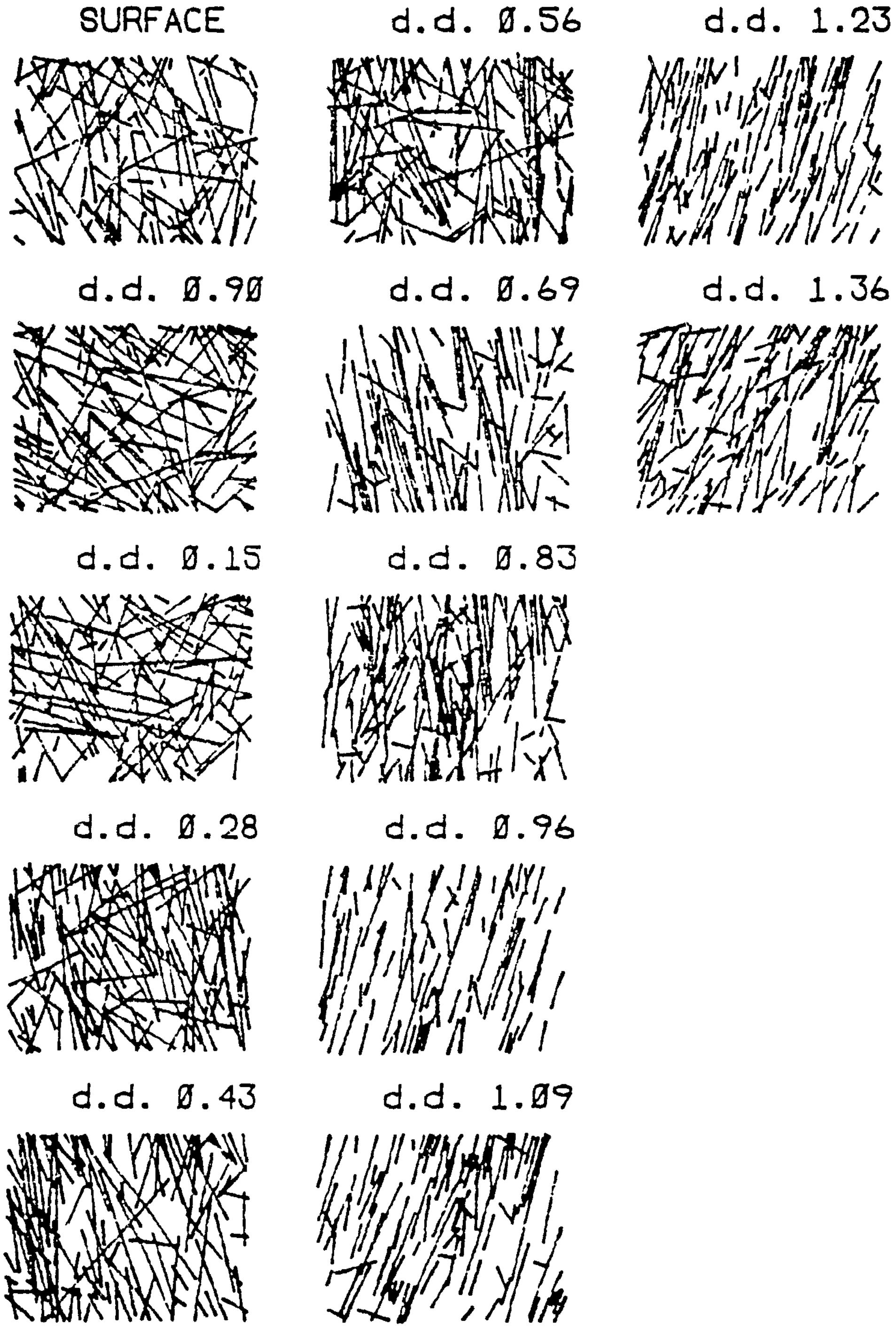

Figure 5.58 Fiber images taken of selected layers at various depths in the thickness direction near the off-centre of the mold, position 5 (Condition ZCEN).

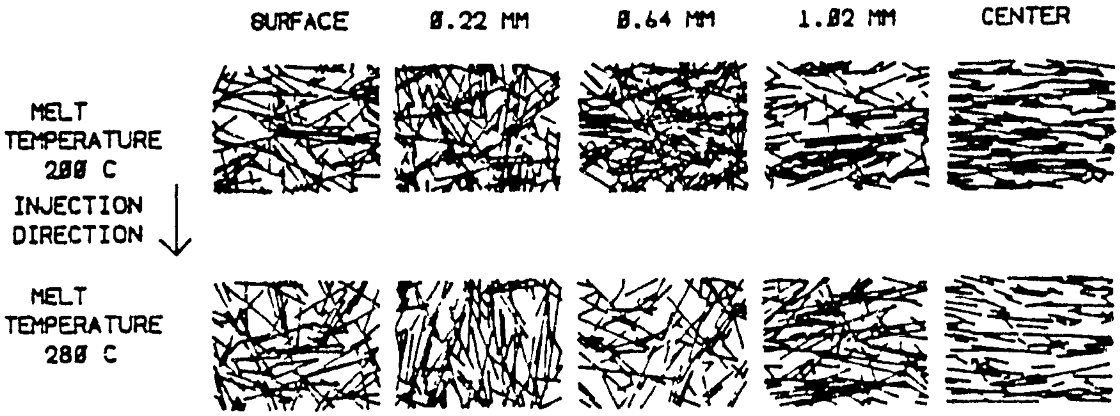

THE EFFECT OF MELT TEMPERATURE ON FIBER ORIENTATION DISTRIBUTION FOR INJECTION MOLDED COMPOSITES

(a)

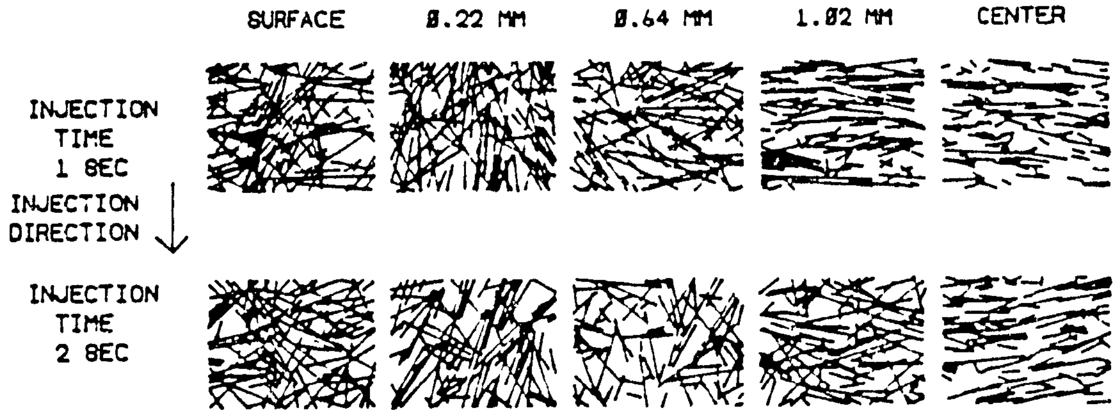

THE EFFECT OF INJECTION TIME ON FIBER ORIENTATION DISTRIBUTION FOR INJECTION MOLDED COMPOSITES

(b)

Figure 5.59 Fiber images taken of selected layers at various depths in the thickness direction at the centre position showing the influence of (a) melt temperature, and (b) filling time.

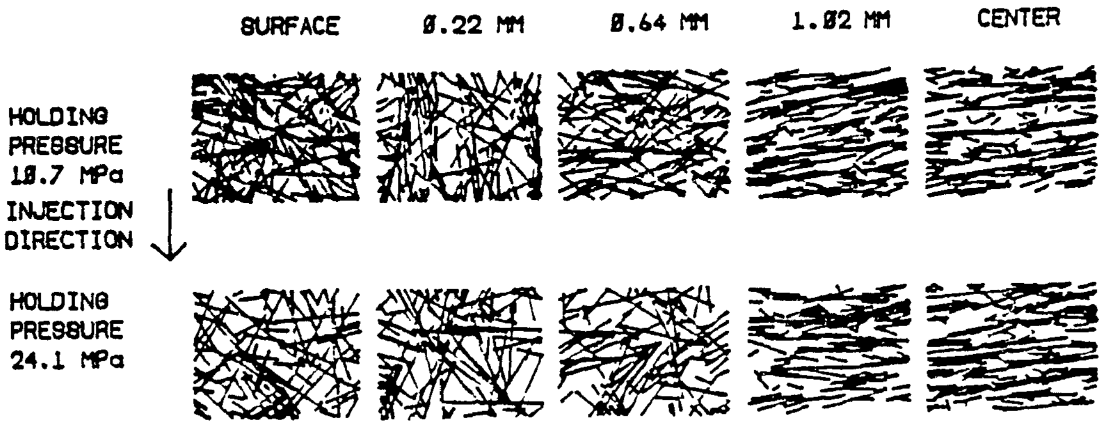

THE EFFECT OF HOLDING PRESSURE ON FIBER ORIENTATION DISTRIBUTION FOR INJECTION MOLDED COMPOSITES

(a)

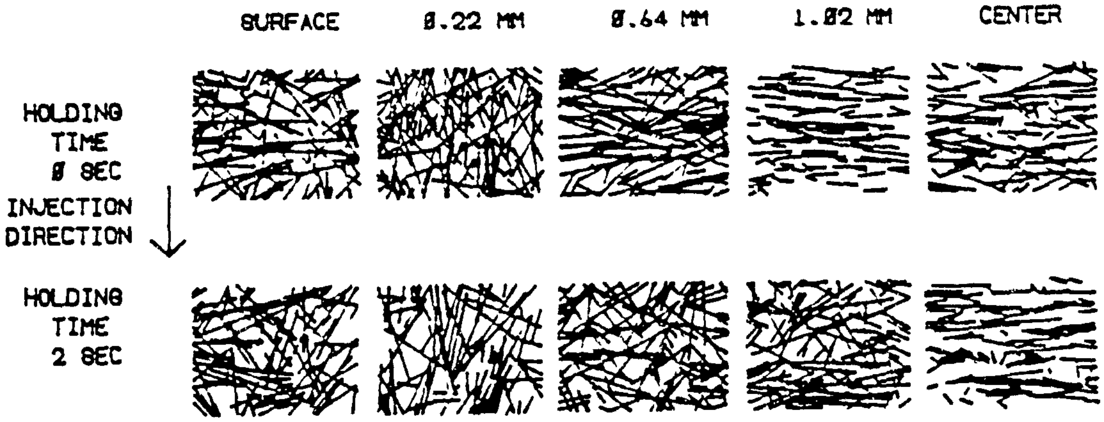

THE EFFECT OF HOLDING TIME ON FIBER ORIENTATION DISTRIBUTION FOR INJECTION MOLDED COMPOSITES

(b)

Figure 5.60 Fiber images taken of selected layers at various depths in the thickness direction at the centre position showing the influence of (a) holding pressure, and (b) holding time.

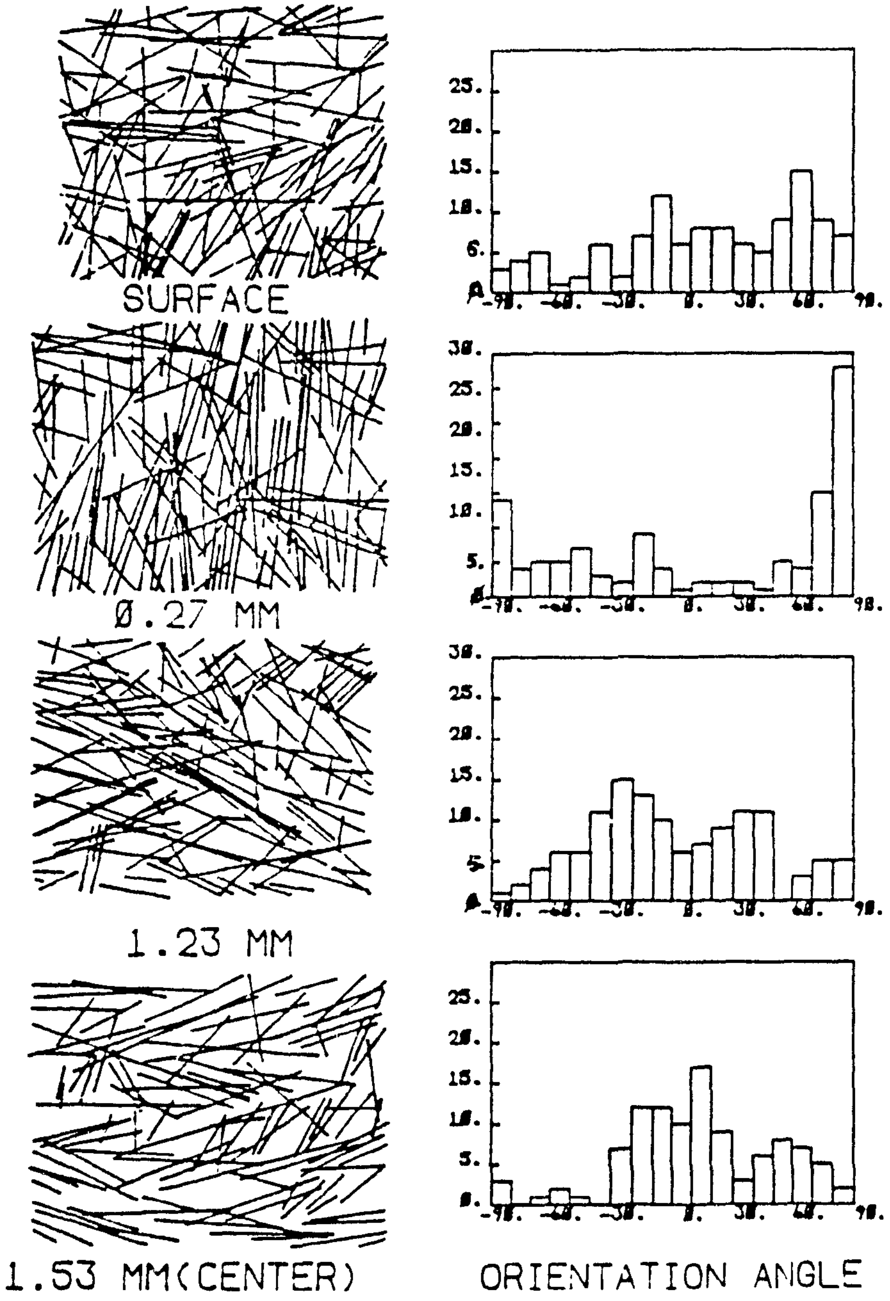

Figure 5.61 Fiber images taken of selected layers shown along with histograms of fiber orientation angles.

f_p = 1 signifies perfectly parallel orientation;

f_p = 0 signifies random orientation;

f_p = -0.5 signifies perfectly perpendicular orientation.

The orientation parameter f_p is similar to that used to describe the molecular orientation of the crystalline and amorphous phases. $(\pi/2-\phi)$ is defined as the angle that the fiber makes with the reference direction i.e. the injection direction as described in Figure 6.6. $\langle\cos^2(\pi/2-\phi)\rangle$ is calculated for discrete fiber angles as follows:

$$\langle\cos^2(\pi/2-\phi)\rangle = \left\{ \sum_{i=1}^{i=n} w_i \cos^2(\pi/2-\phi)_i \right\} \Big/ \left\{ \sum_{i=1}^{i=n} w_i \right\} \qquad (5.5)$$

where w_i is the weighting function.

Many authors have used w_i=1 where the angle of each fiber makes an equal contribution regardless of the length of the fiber [89,102,208]. In order to obtain a weighted average fiber orientation, the length of each fiber is used as a weighting function [82]. Thus:

$$\langle\cos^2(\pi/2-\phi)\rangle = \left\{ \sum_{i=1}^{i=n} l_i \cos^2(\pi/2-\phi)_i \right\} \Big/ \left\{ \sum_{i=1}^{i=n} l_i \right\} \qquad (5.6)$$

In the quantity, $\langle\cos^2(\pi/2-\phi)\rangle$, there is no differentiation whether the angle that the fiber makes with the reference direction is negative or positive. At position 1,2 and 3 at the centre-line of the plaque, this distinction is not required. However, at positions 4,5 and 6, which are off-centre positions, there is a need to distinguish positive and negative angles. One way of dealing with this is to obtain another parameter such as the mean angle.

In all the samples, the fiber orientation distribution in the depth direction along the flow axis (positions 1 - 3) followed the same general profile as shown in Figure 5.62. This type of fiber orientation profile in injection molded composites has not been reported elsewhere. However, the profile is remarkably similar to the fiber-orientation efficiency factor in injection molded test bars by Smith _et al._ [187]. The surface layer or an adjacent layer possesses parallel fiber orientation, i.e. fibers are oriented in the direction of flow. This is sometimes followed by lower parallel orientation or in some cases random orientation. In some of the samples, the random orientation was observed in the skin layer. The parallel orientation increases to a maximum and then subsequently decreases with increasing depth. At some point in the depth, the orientation changes from parallel to transverse, where the fibers are aligned perpendicular to the flow direction. The transverse orientation increases towards the centre of the molding, at which point the fibers are essentially oriented perpendicular to the flow.

In the vicinity of the gate, expansion flow occurs. The equilibrium fiber orientation is perpendicular to the streamlines or flow direction [90,94,95,102,103]. At the

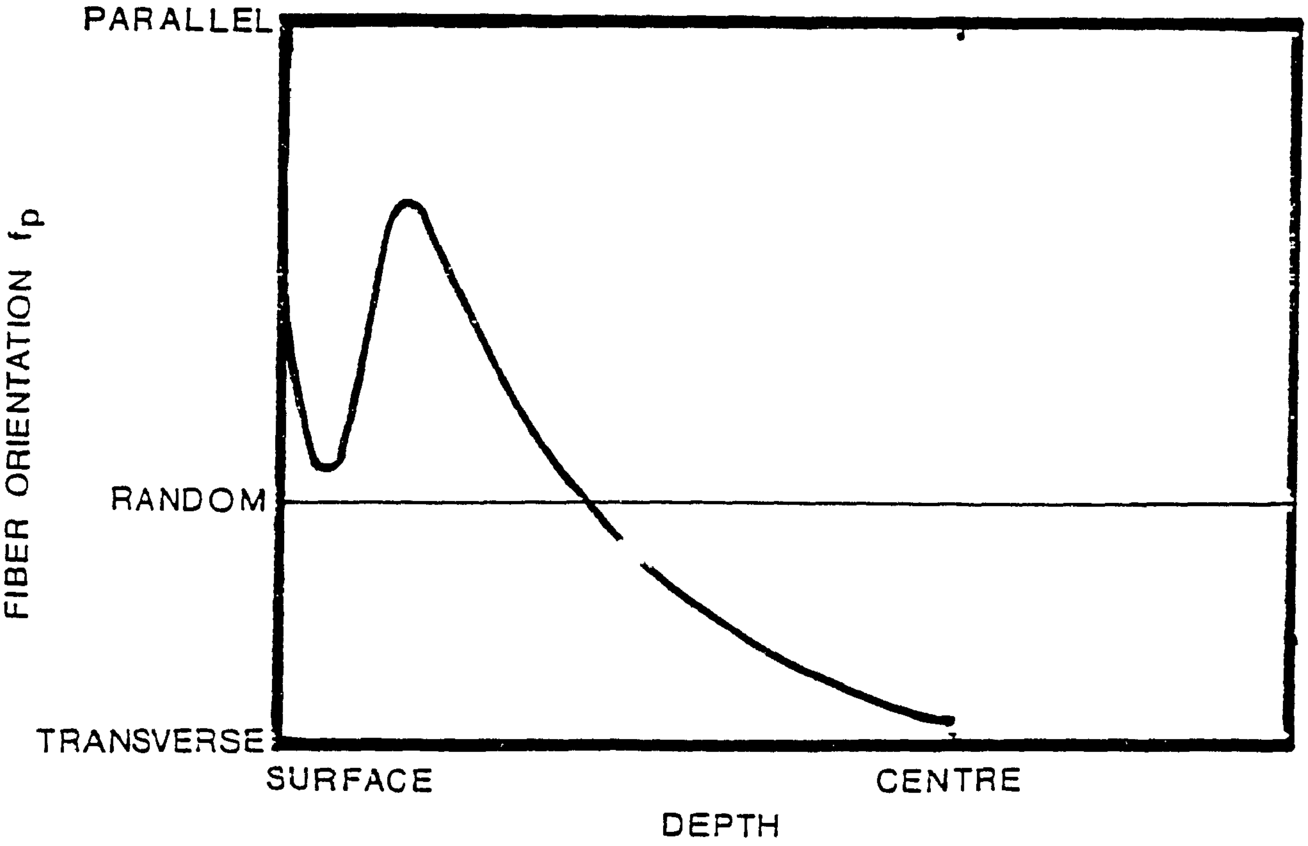

Figure 5.62 General profile for the fiber orientation function in the depth direction.

entrance of the mold, the sudden expansion from the gate to the mold produces transverse flow in the xy plane, as shown in Figure 3.2. The fibers will align tangential to the semi-circular flow front which develops initially near the gate. This results in fiber orientation transverse to the x-direction near the gate and fiber orientation in the x-direction away from the gate in the off-centre positions. This is a result of the semi-circular nature of the flow front near the gate.

During the filling process, shear flow occurs. In the mold cavity, velocity gradient exists in two directions with dissimilar influence on the fiber orientation. The velocity gradient in the y-direction, $\partial v/\partial y$, tends to align the fibers in the flow direction (x-direction) in the x-y plane along the mold wall ($y = \pm W/2$). The velocity gradient in the z-direction, $\partial v/\partial z$, tends to align the fibers in the flow direction (x-direction) in the x-z plane along the mold walls ($y = \pm H/2$). This effect is illustrated in Figure 5.63. The cone of average free volume (i.e. volume taken by fiber rotating about its axis) available to a fiber becomes elongated. The fibers, being restricted to that volume, thus reorient to the new shape of the free volume. In a flat rectangular mold with the y dimension much larger than the z dimension, the velocity gradient in the z-direction, $\partial v/\partial z$, is much greater than the y-direction velocity gradient, $\partial v/\partial y$, and thus controls the fiber orientation. The influence of the

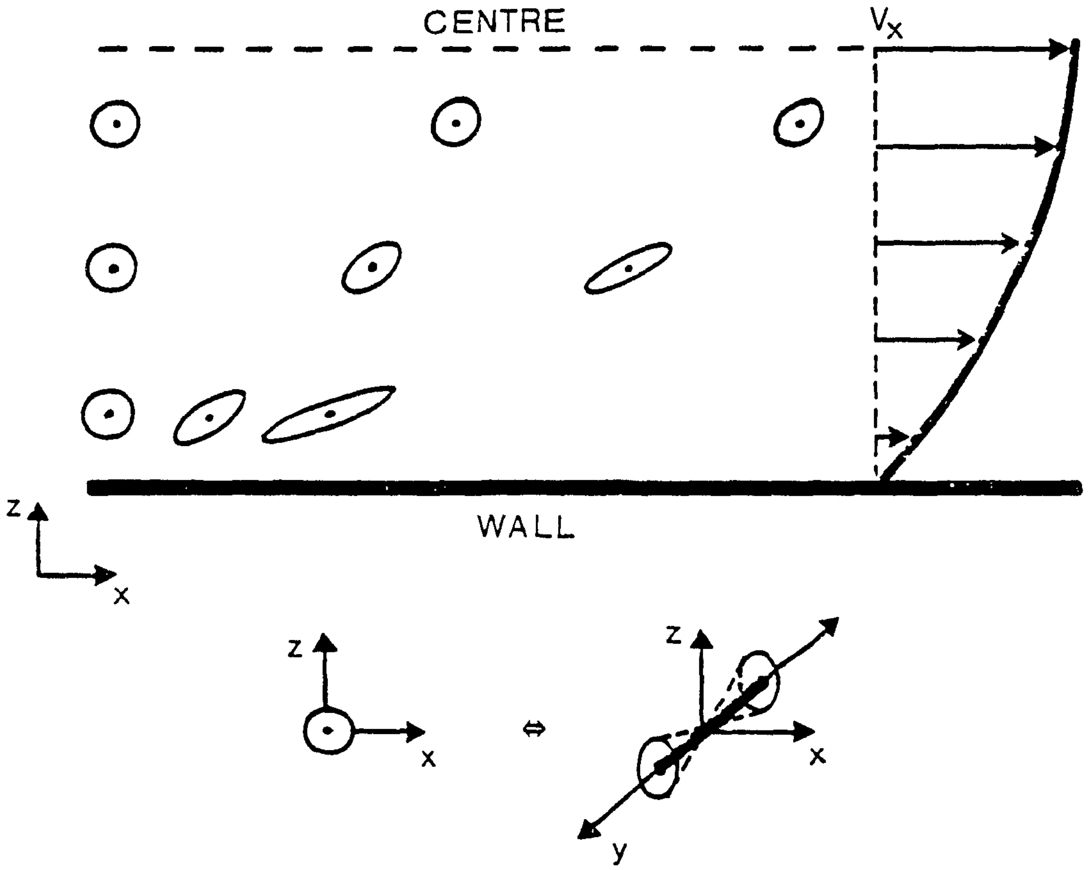

Figure 5.63 Effect of shear flow on fiber orientation.

y-direction velocity gradient is greatest near the walls ($y = \pm H/2$).

In the interior of the flow profile, the velocity gradients are small because of plug flow of the non-Newtonian composite melt. Thus, shear flow has a minor influence on fiber orientation in the core. The fiber orientation produced in the gate region, (i.e. transverse orientation) essentially remains in the core, with fiber alignment in the flow direction in the outer regions. Malzahn and Schultz [186] attributed the transverse core orientation to stresses developed during the packing stage of the injection molding process. However, in this study, different packing pressures and packing times did not significantly influence the fiber orientation profile. Other workers have shown that the transverse core orientation is a result of spreading flow in the gate region [90,94,95,102,103]. Thus, the role of packing pressure in influencing fiber orientation in the core does not appear to be large.

The combination of the above processes should produce a fiber orientation profile with transverse orientation in the core and orientation in the flow direction in the skin layer. Fiber orientation simulations based on these principles yield similar results [102,103]. However, experimental observations show that this is an oversimplification of the fiber orientation process in injection molding.

One complication arises due to the non-isothermal nature of the process. A frozen layer accumulates at the wall with the progression of filling. This restricts the cross-sectional area available to flow, thus increasing the shear rates. The result is a high shear region at the interface of the frozen layer and melt. The shear rates become highest when the frozen layer is thickest during filling.

Another complication is the free surface flow as the material enters the mold cavity. This causes fibers to be aligned along the free surface and to be deposited at the mold walls aligned in the flow direction [103]. Fibers slightly away from the free surface are less aligned. The effect of this fountain flow on particle orientation is shown in Figure 5.64 [9]. The fountain flow effect produces extensional stresses in the central core of the advancing flow front, producing stretched fluid particles which are deposited at the walls, as illustrated in Figure 5.65 [9]. For a fully developed flow of a power law fluid between parallel plates, the extensional rate is give by [7]:

$$- \epsilon = \left\{ \frac{n}{n+1} \right\} \left\{ \frac{<\nu>}{H} \right\} \tag{5.7}$$

where

$<\nu>$ = the mean velocity of the fluid

The material that was originally oriented in the y-direction becomes oriented in the x-direction because of this extensional flow. This changes sharply with depth to

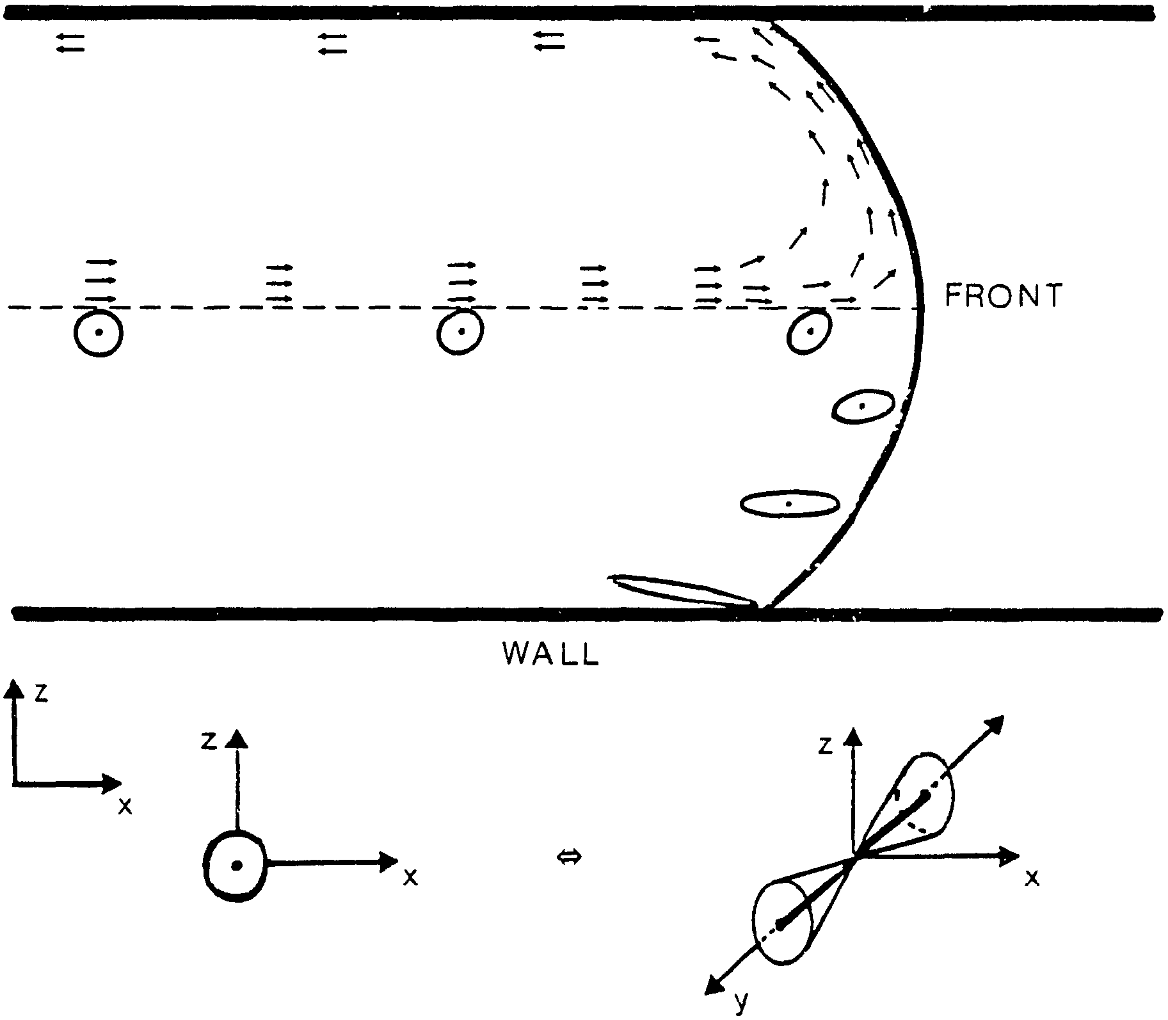

Figure 5.64 Effect of fountain flow on fiber orientation.

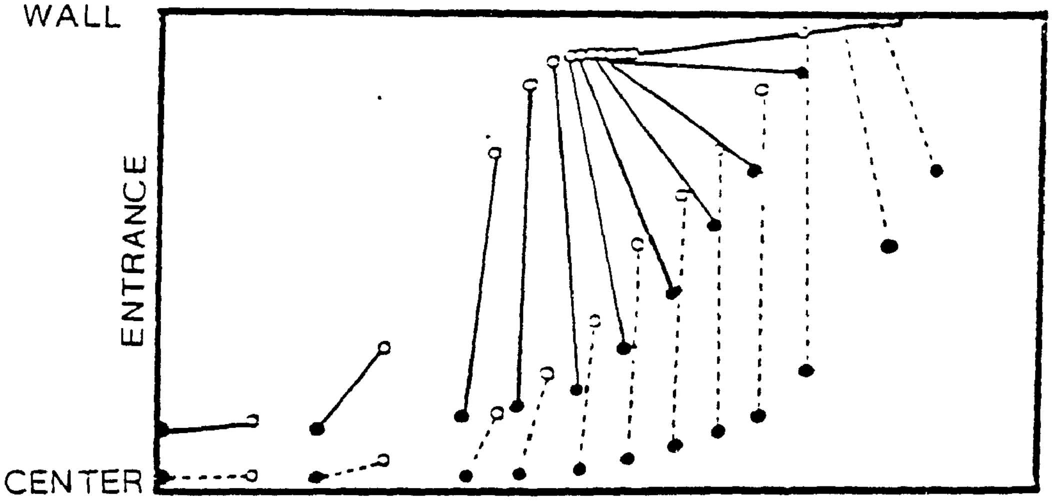

Figure 5.65 Effect of fountain flow on stretching and orientation of fluid particles [9].

transverse orientation for the major part of the core area. As the material flows into the mold, the front hits the mold surface and the polymer freezes on contact with the cold mold surface in a very thin skin layer. This essentially freezes the fiber orientation profile. It consists of the very thin x-direction oriented layer followed by a randomly, or in some cases, a transversely oriented layer.

The above processes combine to produce the experimentally observed fiber orientation profile. This is characterized by high flow direction orientation at the surface, followed by a lesser oriented layer, a maximum below the surface, and transverse core orientation.

When a cross-section of fiber reinforced melt enters the cavity, the faster moving central region reaches the front first. Fountain flow forces it to the wall with a flow direction orientation which becomes frozen in. The slower moving region (i.e. slower than the average velocity) never reaches the front, and, thus it is subjected to shear forces. This is illustrated in Figure 5.66. This is very similar to observation of tracer particles by Gogos et al. [179], as shown in Figure 5.67. The region that is deposited near the walls by fountain flow now assumes a slower velocity and is influenced by shear forces. Thus, the effects of fountain flow on particle orientation are wiped out by the shear flow region, with the only exception being the frozen surface orientation. For the molten region, flow continues with

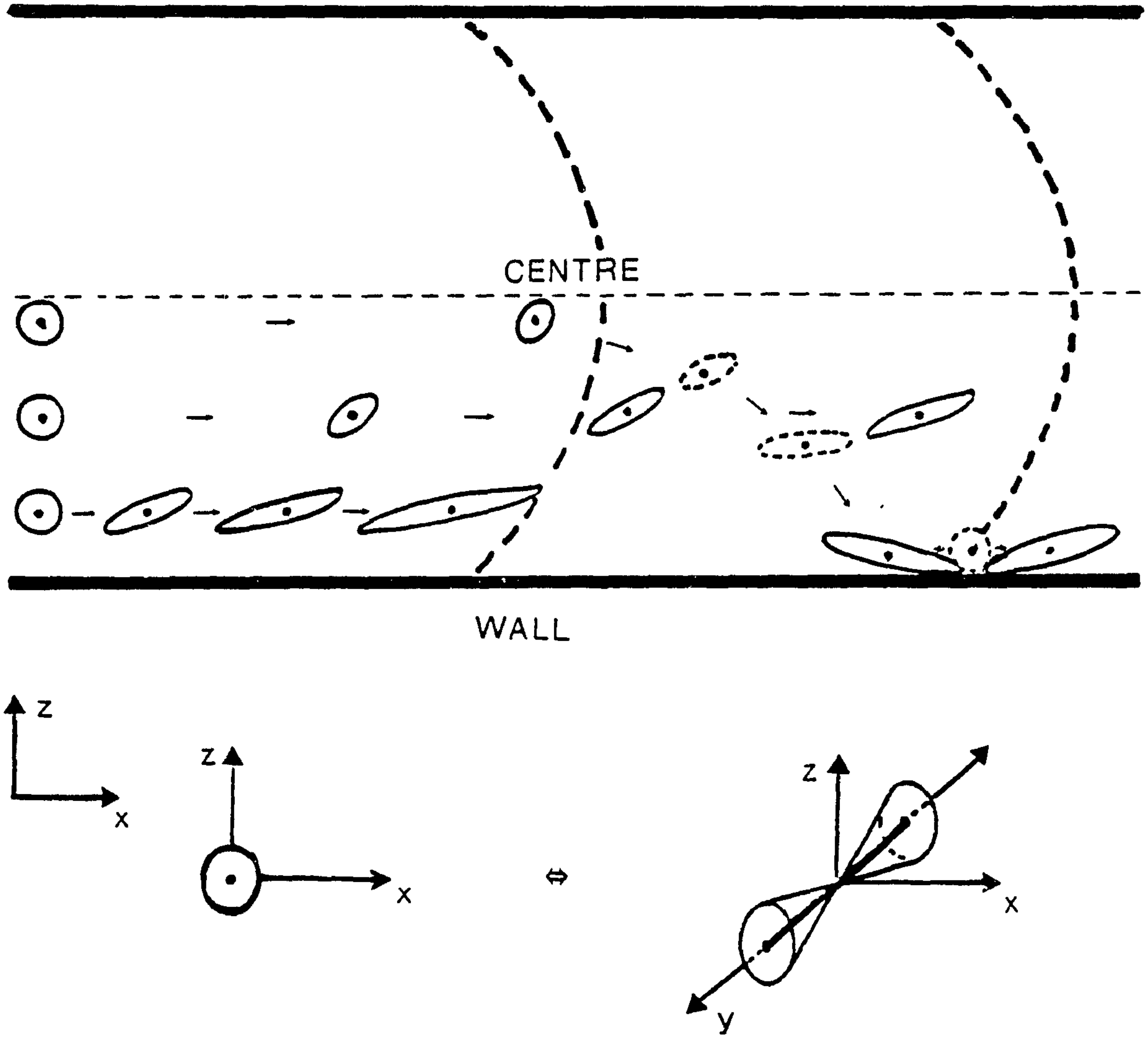

Figure 5.66 Effect of fountain flow and shear flow on fiber orientation.

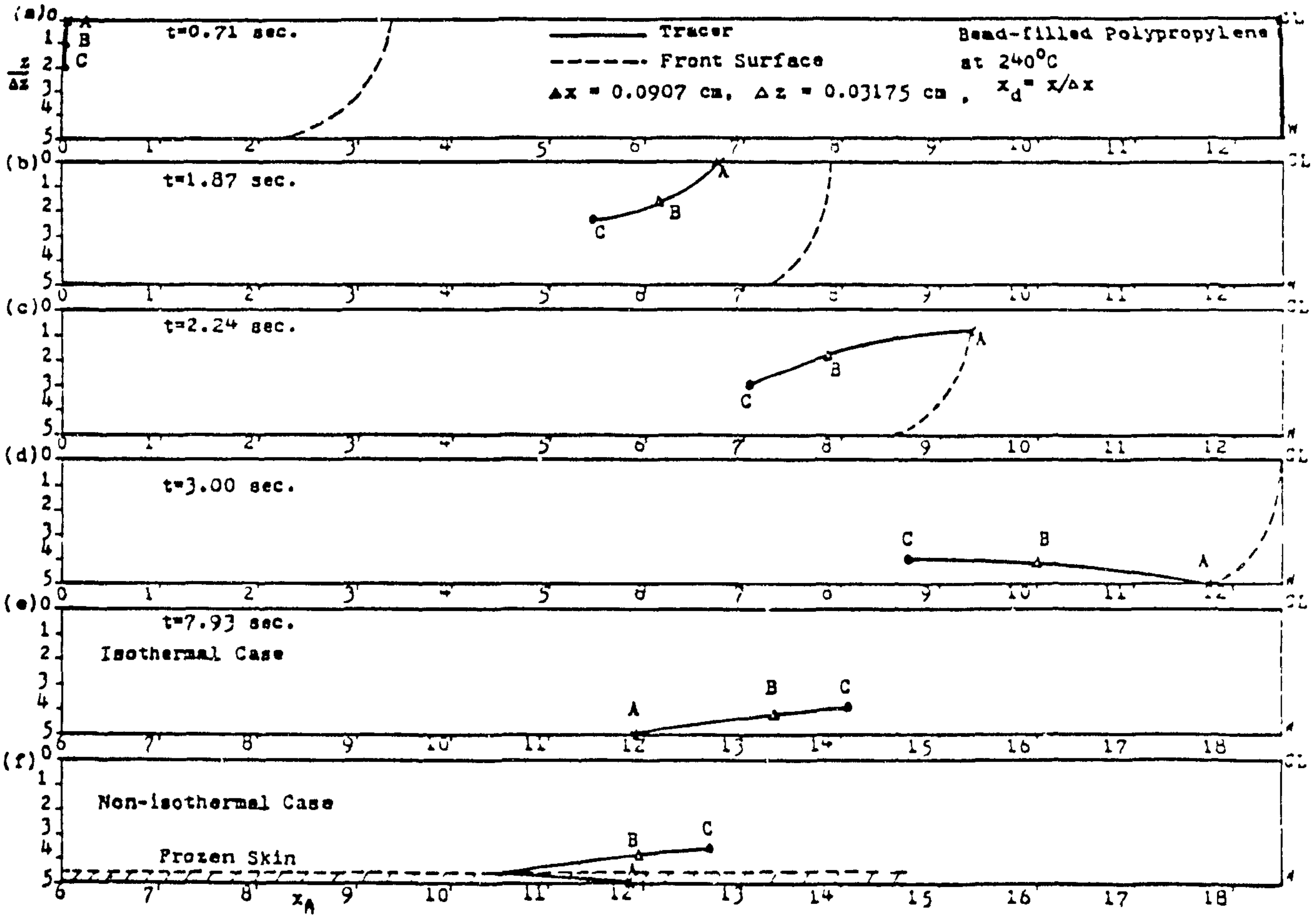

Figure 5.67 (a-e) Tracer location during isothermal mold filling with bead filled polypropylene indicating the experimentally obtained tracer shape at the wall (f) Postulated mechanism for the formation of the V-shape tracer shape during non-isothermal flow due to the formation of a frozen skin layer during filling [179].

shearing now playing an important role in aligning the fibers in the flow direction. The bulk of the melt experiences plug flow in the core with most of the shear occurring close to the solid-melt interface region. After traversing in the mold for some time, the fibers continue to acquire orientation in the flow direction. This increases the thickness of the layer near the surface with x-direction orientation. Thus, the amount of transverse orientation decreases away from the gate. The growth of the frozen layer, which determines the position of the interface, plays an important role in establishing the overall orientation distribution. The analysis of the development of the frozen layer is given in chapter 6.

5.8.3.1 Orientation Distribution in Molding

Fiber orientation distribution profiles in the depth direction are given in Figure 5.68 for condition ZCEN at positions 1 to 6. A comparison of data obtained with replicate samples at position 2 is shown in Figure 5.69.

At position 1, the orientation increases from the surface to a maximum and then decreases to transverse towards the centre. At positions 2 and 3, the orientation decreases from the surface towards a region where it becomes random or close to random. It then increases to a maximum whereupon it decreases towards the core. The layer of random fiber orientation is observed at or near the surface only at

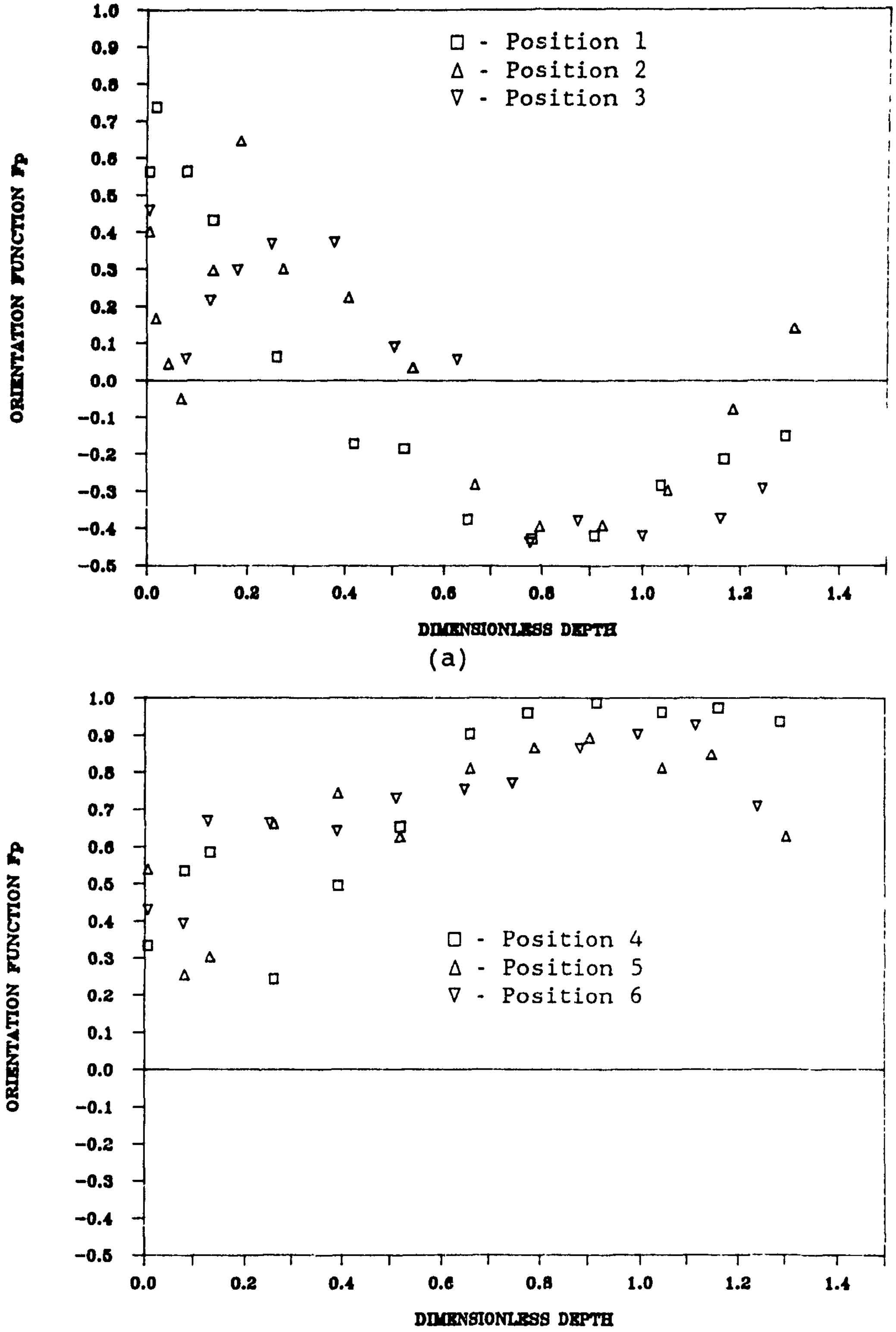

(a)

(b)

Figure 5.68 Fiber orientation distribution in injection molded samples, (a) positions 1-3, (b) positions 4-6 (Condition ZCEN).

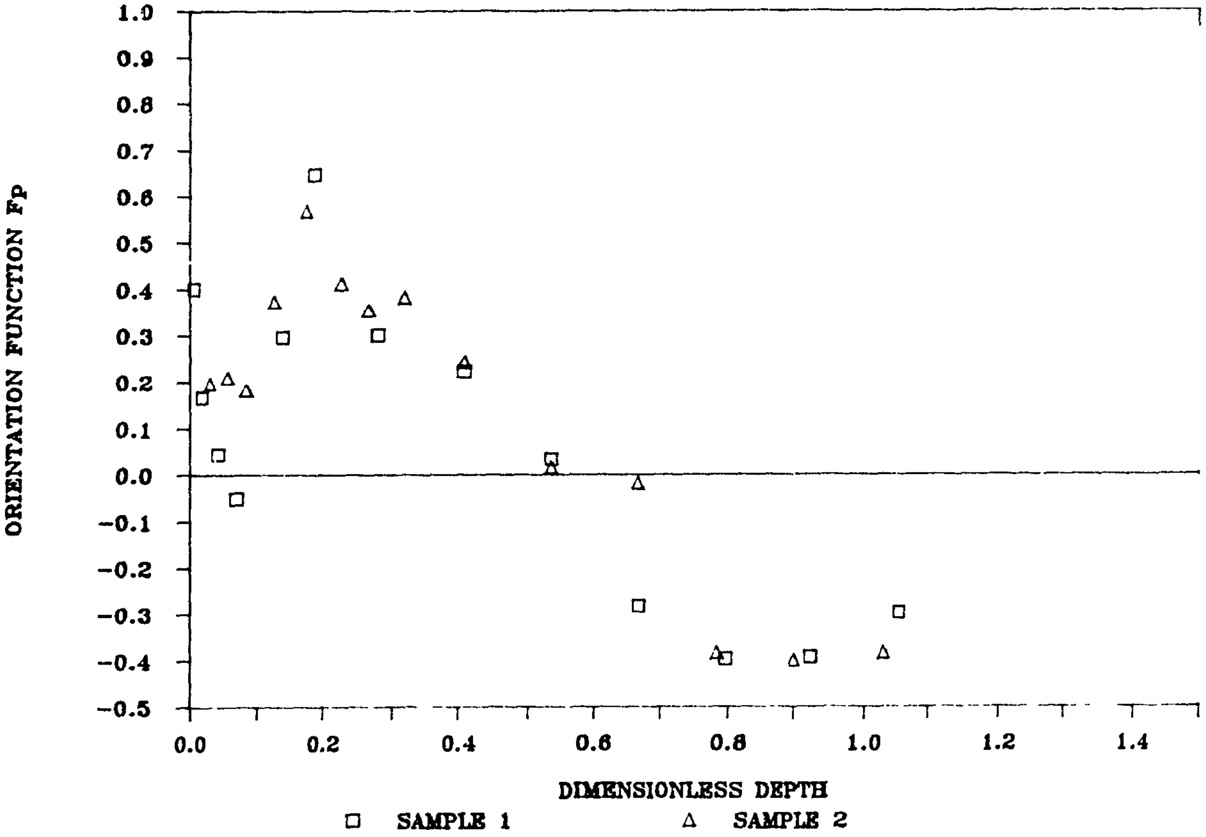

Figure 5.69 Replicates of fiber orientation distribution in injection molded samples (Condition ZCEN).

positions 2 and 3.

The maximum orientation function decreases with distance from the gate, i.e. from positions 1 to 3. The maximum values of the orientation function for position 1 to 3 are 0.78, 0.65 and 0.37, respectively. The distance of each maximum from the surface increases with distance from the gate. The depths from position 1 to position 3 are 0.04, 0.30 and 0.62 mm respectively. The amount of transverse orientation (width of the transverse core) is much greater near the gate at position 1 than at downstream positions 2 or 3. The width of the transverse zone is 1 mm thick at position 1 and 0.5 mm at positions 2 and 3.

At position 1, the melt-solid interface remains essentially close to the mold walls. A small area near to the wall has fibers oriented in the flow direction, while the major part shows transverse fiber orientation. At position 2, the melt-frozen layer interface moves inwards as the frozen skin layer grows in thickness. The orientation becomes frozen-in at those locations. The flow cross-sectional area decreases, thus causing an increase in the velocity and shear rate and resulting in higher orientation at the interface. The thickness of the frozen layer increases downstream, except near the flow front, until the mold is filled. Thus, the depth of the x-direction orientation below the surface increases with the downstream position of the melt. The final fiber orientation profile is a combination of the orientation in the skin, that frozen in the frozen layer during filling and that remaining in the melt when the mold is filled.

The orientation at position 3 should be similar to that at position 2. However, complex flows at the end of the mold influence the final fiber orientation.

Positions 4, 5 and 6 show somewhat different orientation profiles. The orientation with respect to the reference x-direction increases from surface to core, with maximum occurring in the core. The initial fiber orientation in the case of the off-centre position is in the x-direction. The proximity of the fibers to two mold walls in this region also causes fiber orientation in the x-direction to be dominant.

One of the most interesting and somewhat surprising observations in this study relates to the coexistence near the mold surface of two adjacent layers: one with characteristic fiber orientation in the flow direction and the other exhibiting random or nearly random orientation. This observation is particularly true for samples along the centre axis of the molding. Thus, in practically all samples examined in the present study, a skin layer (at or near the surface) with characteristic x-direction orientation was observed, as expected. In addition, adjacent to the above layer, another layer with random or nearly random fiber orientation was also observed. In some instances, the layer with the random orientation was at the surface. It is difficult to explain the presence of the layer with the random orientation at or so close to the surface. However, it appears from the flow and heat transfer analysis given in Chapter 6 that the initial orientation of the fibers at the entrance of the cavity may play an important role in this regard.

The average fiber angle at the core of positions 1 to 6 is shown in Figure 5.70. This fiber angle represents the orientation of the fibers in the core region which is unaffected by shear effects from the wall. The results suggests that the fiber orientation in the core is influenced by the spreading flow, as the melt enters the mold cavity from the narrow gate.

5.8.3.2 Effect Of Processing Conditions

Generally, it has been shown that the pattern of fiber orientation in the molding is quite insensitive to changes in molding conditions [89,92]. In this study, the experimental observations of fiber orientation show the same general orientation profile from skin to core, in agreement with reported results. Figure 5.71 shows the orientation profiles at position 2 for melt temperatures of 200 °C and 280 °C. Both samples show similar trends. It is interesting to note that a layer of near random orientation is at the surface for the 200 °C sample, while it is in the layer below the surface for the 280 °C sample. This observation seems to be more in harmony with the amorphous orientation distribution in the

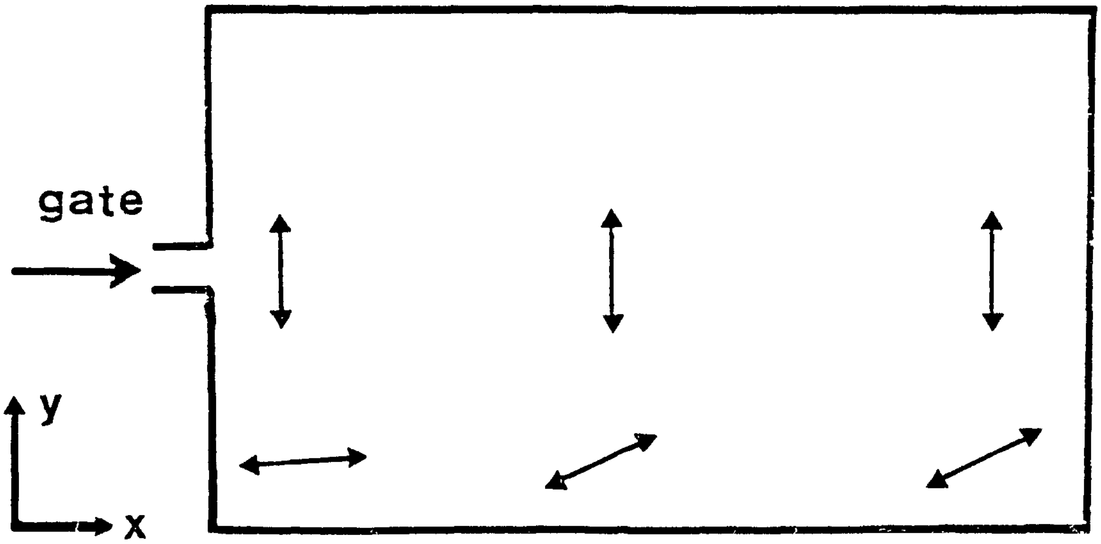

Fiber Orientation in the core

Figure 5.70 Mean fiber angles in the core layer in the injection molded sample (Condition ZCEN).

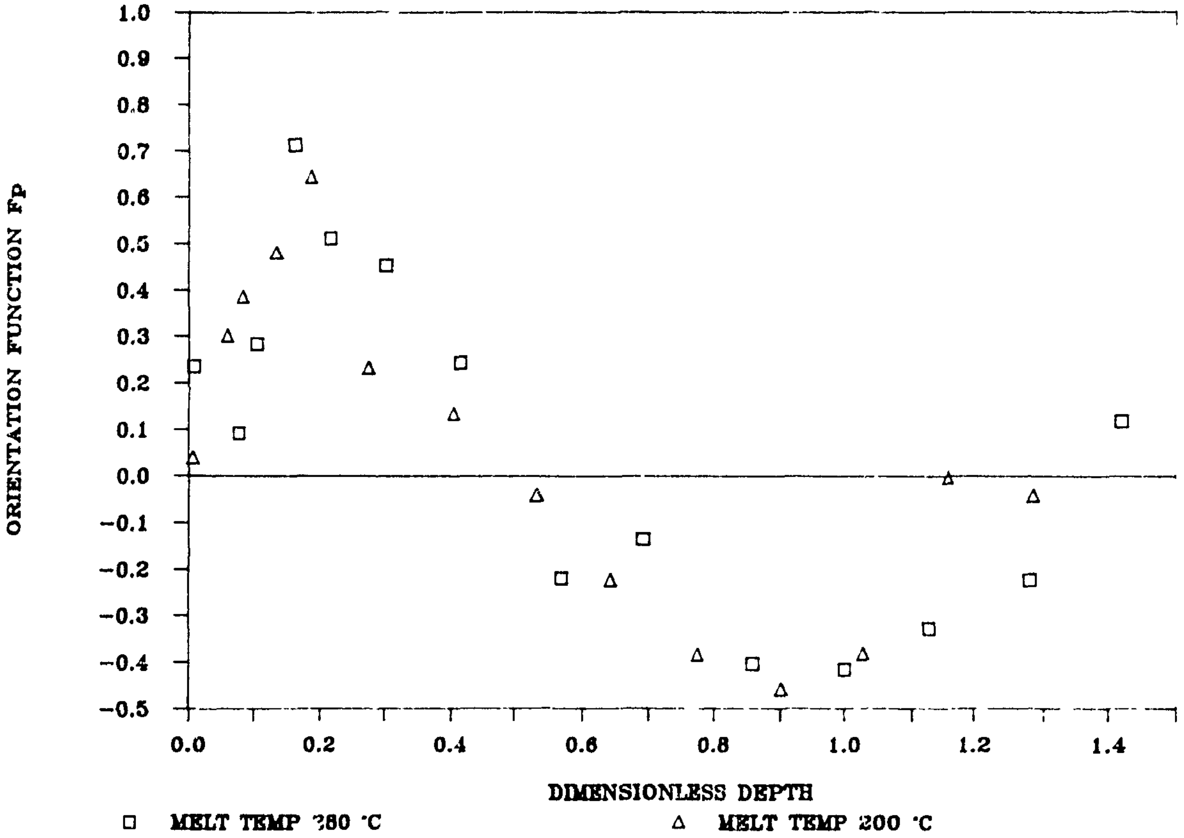

Figure 5.71 Effect of melt temperature on fiber orientation distribution in injection molded samples (Conditions ZHMT, ZLMT).

matrix than with the crystalline orientation distribution (see Figure 5.42).

The fiber orientation profiles for the two filling times are very similar in shape, as can be seen in Figure 5.72. The longer fill time provides a longer time for the frozen layer to grow. The smaller cross-sectional area available for flow, reduces the spreading flow at the gate. Thus the fibers will retain their flow orientation from the sprue. The smaller cross-sectional area also increases the shear stresses, a stronger orienting effect produces a wider region of higher parallel fiber orientation. Other researchers have reported complete parallel fiber orientation in the flow direction with very slow fill rates [87]. The fill times used in the study were very small, in the range of one to two seconds. These would be more typical of commercial injection molding processes.

Figure 5.73 shows the fiber orientation profiles for holding times of 0 and 2 seconds. The thickness of the transverse core is smaller with the higher holding time. With additional holding time, extra material is packed into the mold to compensate for shrinkage.This contributes to producing a thicker layer of parallel oriented fibers.

The effect of holding pressure appears to be small, as shown in Figure 5.74. Pressure has been shown to reduce the transverse fiber orientation in the core [74].

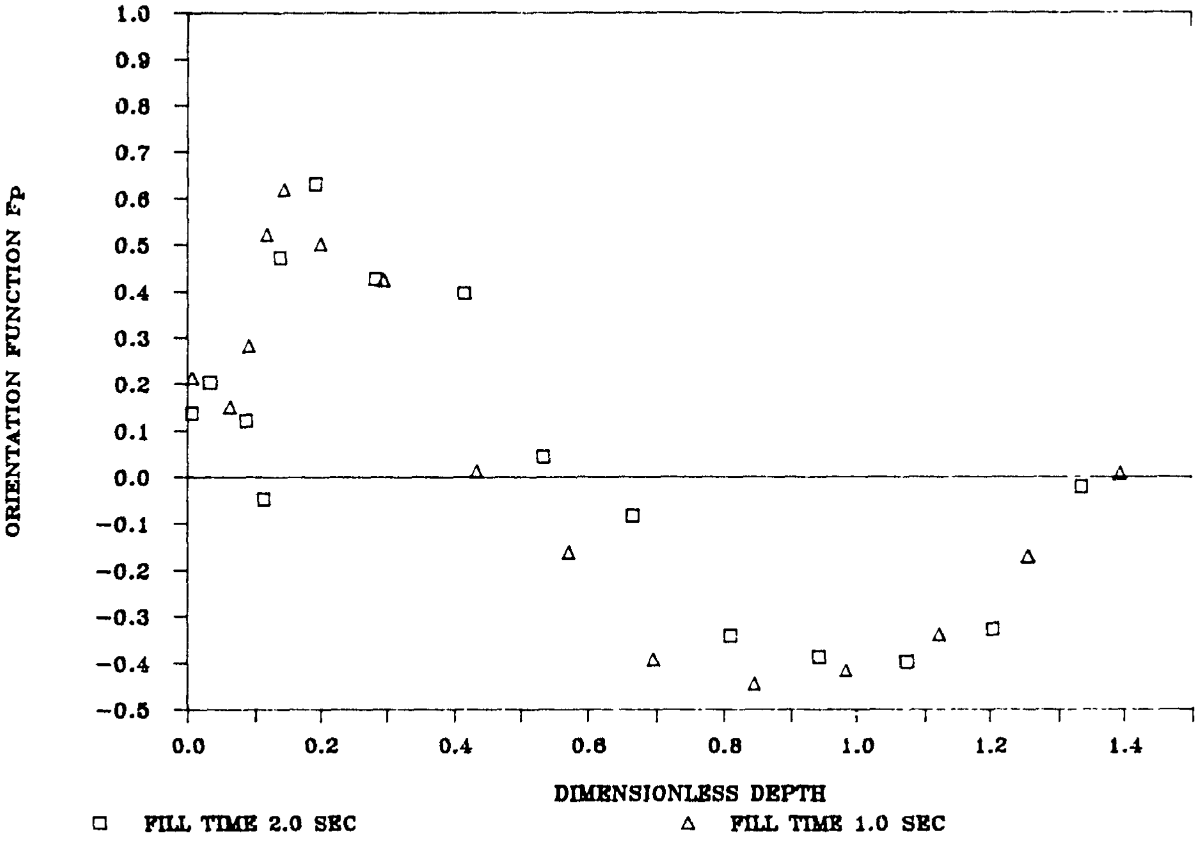

Figure 5.72 Effect of filling time on fiber orientation distribution in injection molded samples (Conditions ZHIT, ZLIT).

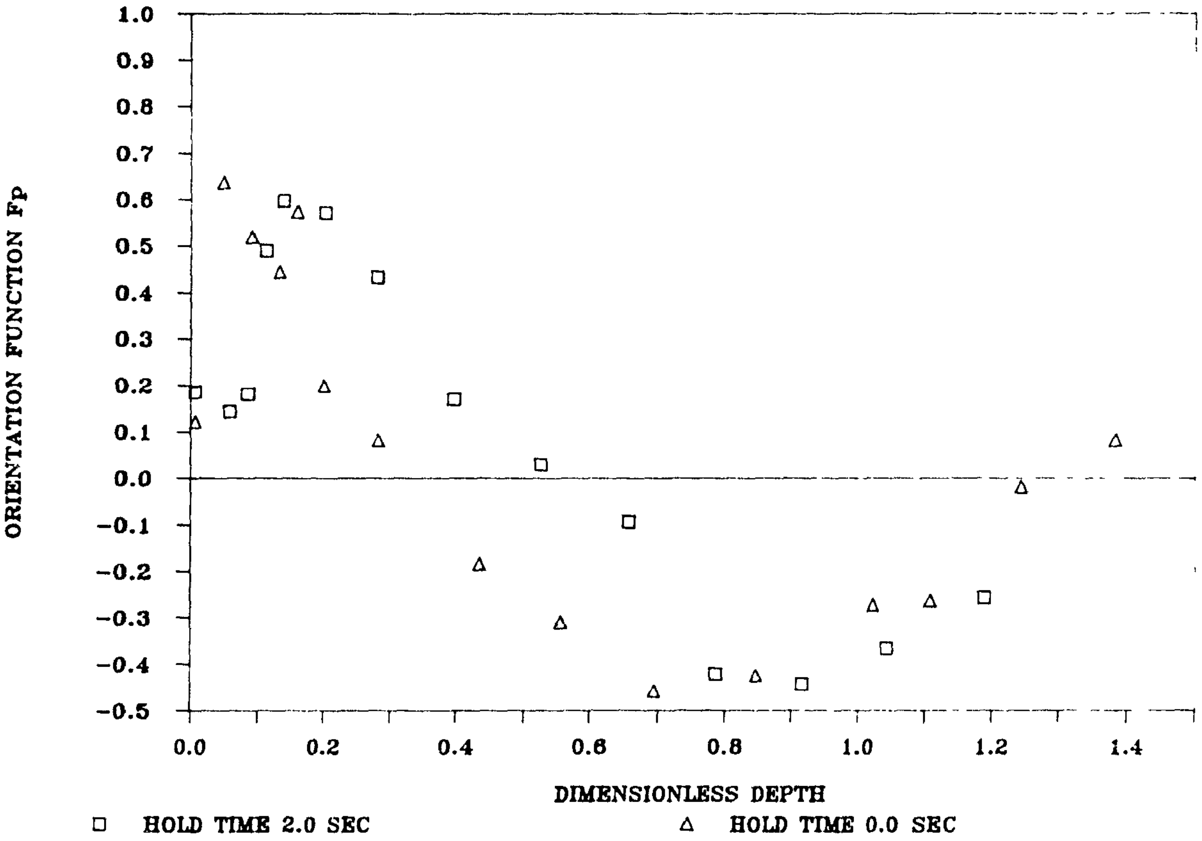

Figure 5.73 Effect of holding time on fiber orientation distribution in injection molded samples (Conditions ZLHT, ZHHT).

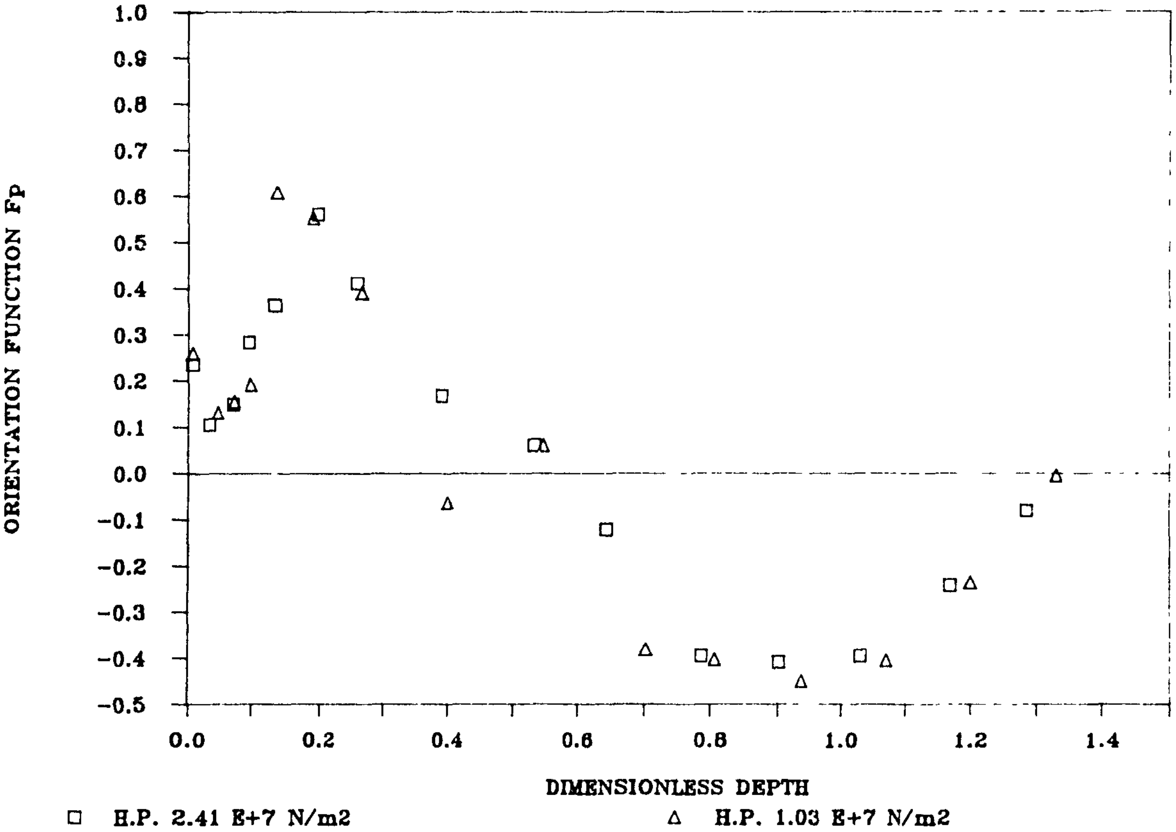

Figure 5.74 Effect of holding pressure on fiber orientation distribution in injection molded samples (Conditions ZHHP, ZLHP).

Overall, the final orientation distribution in the injection molding samples appears to be determined by the effects of several processes.

(1) Elongational flow at the gate.

In the gate region, the expansion flow is in the x-y plane because the change in dimensions from gate to mold is in this plane. The fibers are aligned parallel to the flow front. The fibers will lie parallel to the major surface and in the directions as shown in Figure 5.70. This direction varies at different positions in the mold, e.g. at positions 1, 2 and 3, the direction would be perpendicular to the injection direction, at position 4,5 and 6, the direction would be at varying negative angles to the injection direction. The extensional process should give rise to fiber orientation in the x-y plane with very few if any fibers lying out of this plane. This is the case as seen experimentally.

(2) Fountain flow

At the flow front region, fountain flow effect creates high x-direction orientation in the material that is deposited at the walls. This results in a thin highly oriented skin layer.

(3) Shear flow

The shear flow effect dominates in the region close to the wall of the mold. The shear effect in the x-z plane is much more important than the shear flow in the x-y plane. This is because of the smaller dimension of the z axis relative to that of the y-axis, resulting in higher shear stresses in the x-z plane. The shearing process tends to orient fibers parallel to the flow direction.

(3) Frozen layer

The freezing of the skin layer near the walls leads to a moving interface between the solid polymer and the flowing melt. As the cross-section decreases, shear stresses increase, resulting in higher fiber orientation throughout the flow cross-section.

5.9 Summary of Results

The experimental observations have provided a much better understanding of the microstructural developments in composites during the injection molding cycle. Microstructure varies with spatial position, in the thickness direction, and relative to the gate position. In the cross-section, a skin and core structure, and a shear oriented intermediate layer are quite distinct.

The crystalline structure of the injection molded parts showed significant variation from the skin to the core. The skin structure is that of a quenched material. Shear oriented crystals are seen in the shear zone just below the skin, but only in composite injection molded samples. Although there are significant changes in the crystalline morphology, there is only a gradual increase in total crystallinity from the skin to the centre. The molecular orientation observed in the crystalline phase is relatively low, with a maximum at approximately 300 to 500 μm in depth, which corresponds to the shear zone. The orientation decreases towards the core to become random.

Evidence indicates fiber depletion near the gate of the mold and fiber accumulation at the far end of the mold. Fiber concentration is low at the surface, and it increases towards the core. Fiber length distribution is substantially reduced by processing. There is also significant variation in the average lengths of fibers in layers between the skin and the core. Fiber orientation distribution is more complex than previously thought. The fibers are oriented in the direction of flow at the surface and transverse at the core. A maximum of fiber orientation is observed at approximately 200 to 400 μm depth. At or near the surface, especially in the samples taken along the central axis of the molding, two layers coexists: one with high x-axis orientation, the other with random fiber orientation.

CHAPTER 6

6 THEORETICAL ANALYSIS

The analysis of fiber orientation during the filling of the mold cavity is attempted in this Chapter. The heat transfer and fluid flow are decoupled and solved separately. The fiber orientation distribution within the flow field in the mold is obtained by solving the fluid mechanics problem in conjunction with a fiber orientation model.

Injection molding is a complex process, involving simultaneous heat transfer and fluid flow. In the case of polypropylene, the material is visco-elastic and crystallizes during processing. The packing and holding stages involve compressible, non-isothermal flow.

The process may be modelled by solving the relevant conservation equations of continuity, motion and energy, in conjunction with appropriate constitutive equations and initial and boundary conditions [188]. The conservation equations are presented below in general tensorial formulation.

Continuity

$$\left\{\frac{D\rho}{Dt}\right\} = -\rho(\nabla \cdot \upsilon) \tag{6.1}$$

Momentum

$$\rho\left\{\frac{D\upsilon}{Dt}\right\} = -\nabla P - (\nabla \cdot \boldsymbol{\tau}) + \rho \mathbf{g} \qquad (6.2)$$

Energy

$$\rho C_v\left\{\frac{DT}{Dt}\right\} = -(\nabla \cdot \mathbf{q}) - T\left\{\frac{\partial P}{\partial T}\right\}_\rho \left\{\nabla \cdot \upsilon\right\} - \left\{\boldsymbol{\tau} : \nabla \upsilon\right\} \qquad (6.3)$$

These equations are exceedingly difficult to solve, even numerically. Thus, many simplifying assumptions have to be made. Mathematical models of injection molding with varying complexity have been developed [189-191].

In order to simplify the analysis, the fluid mechanics and heat transfer problem are solved separately. Since the frozen layer plays an important role in establishing the final orientation distribution and since it experiences the largest thermal gradients, the heat transfer analysis was limited to frozen layer development. The frozen layer reduces the cross-sectional area available to flow, thus increasing the shear stresses.

The analysis consists of three parts:

(i) a flow field section to obtain the velocity profile;

(ii) a frozen layer analysis section to solve for the frozen layer thickness;

(iii) a fiber orientation section to solve for the orientation of the fiber in the flow field.

6.1 Flow Field Analysis

The flow geometry is shown with the coordinate system in Figure 6.1. The x-axis is defined as the length direction with dimension L or 2l. The y-axis is in the width direction with dimension W or 2w. the z-axis is in the thickness direction with dimension H or 2h. Melt flow is in the x-direction.

Several assumptions were made in order to derive the flow field in a rectangular mold. The entrance and mold end region were ignored in the analysis. The fluid was assumed Newtonian with viscosity μ, under isothermal, steady pressure flow. Krueger and Tadmor [146], using Finite Element Analysis, showed that the overall filling pattern and flow front shape are only a mild function of the non-Newtonian nature of the fluid. Thus, the assumption of Newtonian fluid is reasonable, and may be justifiable in a first order analysis. Consideration was not given to the influence of local fiber orientation or concentration on the viscosity of the fluid. The fiber reinforced melt is modelled as homogenous with no changes in properties in any direction. During fluid flow into the mold, there is a change of fiber orientation from the initial state. This fiber orientation in turn influences the rheological behaviour of the fluid in the locality. The orientation effects and rheology of fiber filled polymers have been studied by Laun [185] and Mutel [111]. However, this type of inhomogeneity has been ignored in the present analysis.

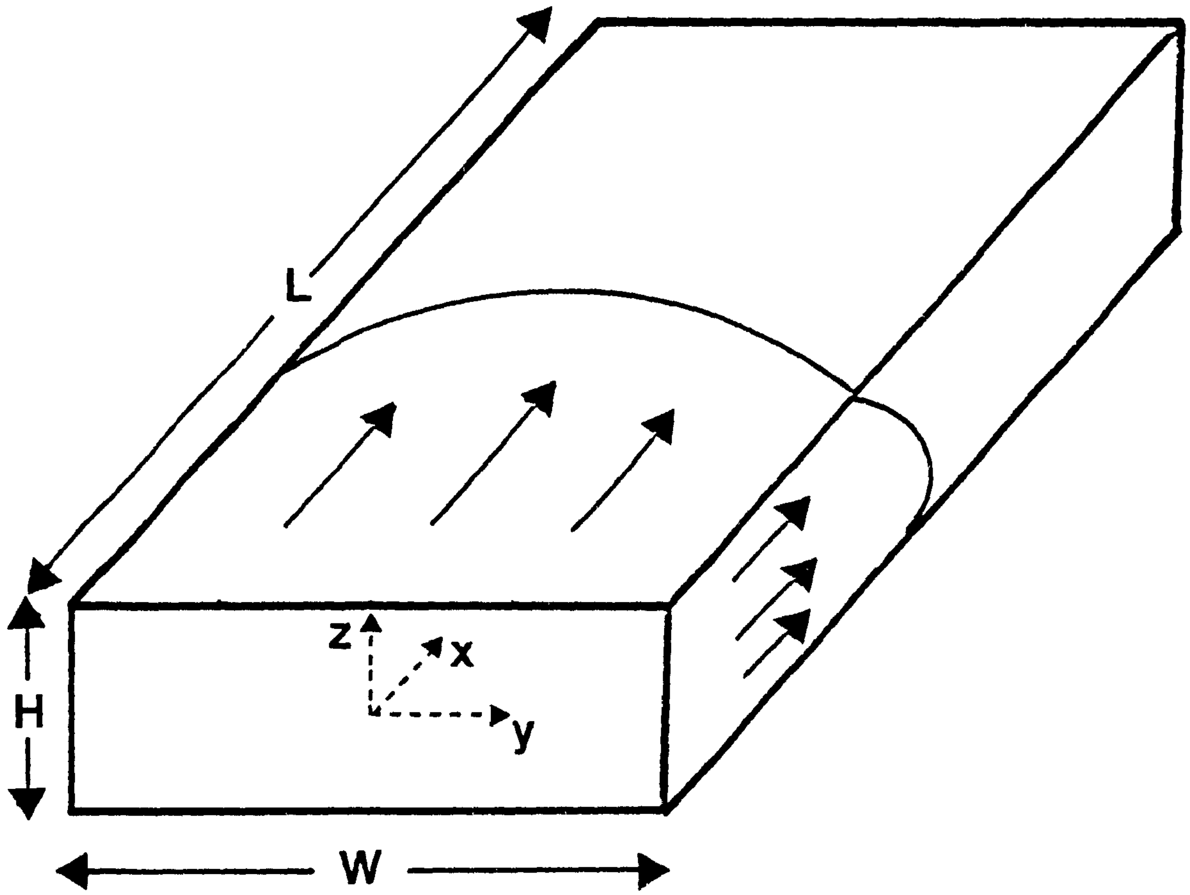

Figure 6.1 Simplified flow geometry used for fiber orientation model.

Under the circumstances, the steady state distribution of velocity in the x-direction, $V_x(y,z)$, and the flow rate, Q, in a rectangular cavity were determined analytically by Boussinesq [192], as follows.

The velocity distribution $V_x(y,z)$ and the flow rate Q are given as:

$$V_x(y,z) = \frac{\Delta P}{\mu L}\left\{ \frac{z^2}{2} - \frac{zH}{2} + \frac{4H^2}{\pi^3} \sum_{i=1,3}^{\infty} \frac{\cosh((i\pi/2H)(2y-W)).\sin(i\pi z/H)}{i^3 \cosh(i\pi W/H)} \right\} \qquad (6.4)$$

$$Q = \frac{WH^3}{12\mu} \frac{\Delta P}{L} \left\{ 1 - \frac{192H}{\pi^5 W} \sum_{i=1,3.}^{\infty} \frac{\tanh(i\pi W/2H)}{i^5} \right\} \qquad (6.5)$$

The velocity is seen to be constant in the x-direction. The velocity gradients in the y- and z-directions are given below:

$$\frac{\partial V_x}{\partial y} = \frac{\Delta P}{\mu L} \frac{4H^2}{\pi^2} \sum_{i=1,3..}^{\infty} \frac{\sinh((i\pi/2H)(2y-W)).\sin(i\pi z/H)}{i^2 \cosh(i\pi W/H)} \qquad (6.6)$$

$$\frac{\partial V_x}{\partial z} = \frac{\Delta P}{\mu L} \left\{ z - \frac{H}{2} + \frac{4H^2}{\pi^3} \sum_{i=1,3..}^{\infty} \frac{\cosh((i\pi/2H)(2y-W)).\cos(i\pi z/H)}{i^2 \cosh(i\pi W/H)} \right\} \qquad (6.7)$$

6.2 Heat Transfer Model

As a result of the high viscosity and low thermal conductivity of polymer melts, the temperature distribution in the melt shows high gradients only in a thin boundary layer close to the solid-melt interface. When the hot, molten material is injected into the cold mold, some material close to the mold wall freezes. The development of the frozen layer has a significant impact on the flow field in the remaining flow cross-section in the mold. Extensive work has been reported regarding efforts to model such a process [193-199].

A heat transfer analysis has been carried out to investigate the growth of the frozen skin layer. The analysis follows the approach proposed by Richardson [193]. The flow of the melt can be divided into two regions:

(i) the thermal entrance region;

(ii) the melt front region, with a short matching region connecting them.

The flow is approximated by flow between parallel plates, for a power law fluid. The thickness of the frozen layer is calculated in both the thermal entrance region and the melt front region subject to the boundary conditions. Figure 6.2 illustrates the problem at the mold entrance and at the flow front region.

The following variables are defined:

$(h-h^*)$ = the thickness of the frozen wall layer

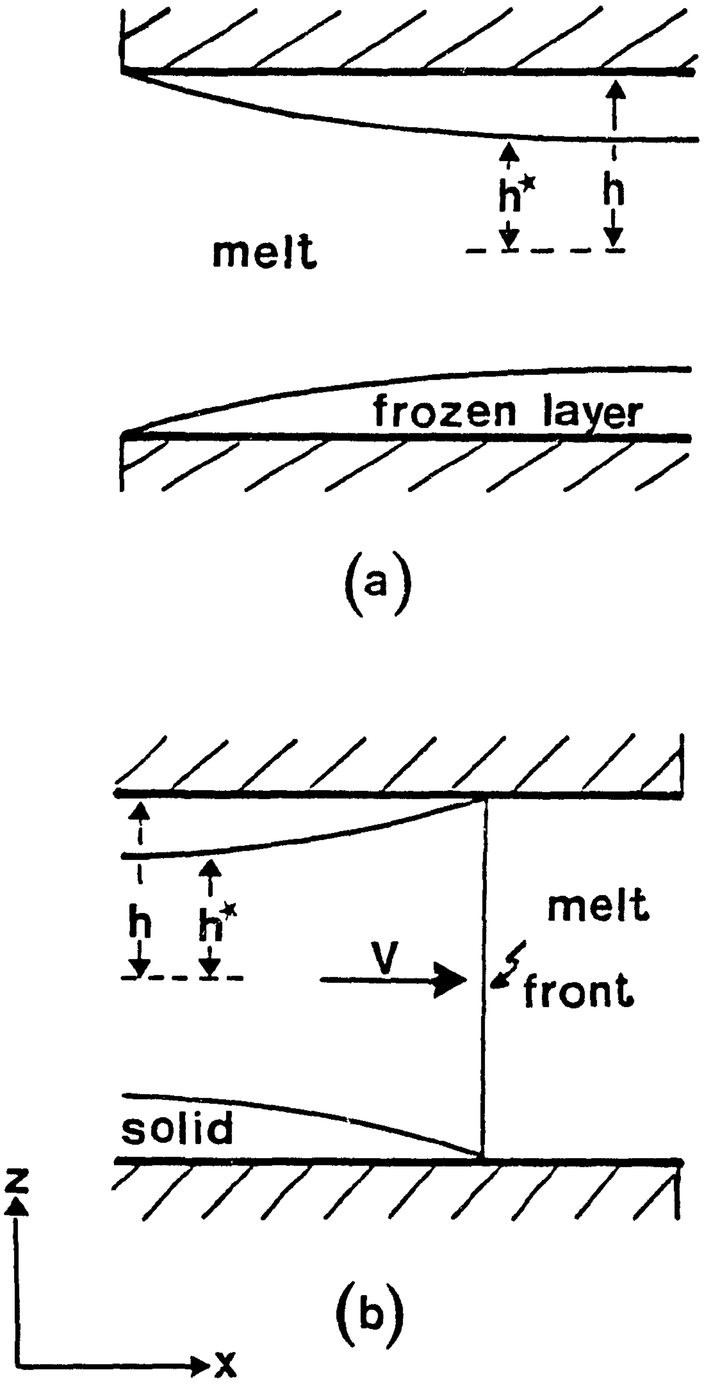

Figure 6.2 Channel flow geometry showing the frozen layer in (a) the mold entrance region and (b) the flow front region.

Q = the volumetric flow rate

p = the pressure

μ = the melt viscosity is described by a power law relationship

c_L = the specific heat capacity of the melt

k_L = the thermal conductivity of the melt

k_s = the thermal conductivity the solid

T = the temperature

ρ_L = Density of the melt

L = Length of the mold

w = Width of the mold

x_f = melt front position in the mold

Λ = latent heat of fusion of polymer.

It is assumed that $2h/L \ll 1$ and that $|dh^*/dx| \ll 1$. Also, $2h/w \ll 1$, so that flow in the channel can be approximated by flow between two parallel plates. The Reynolds number is defined as $Re = \rho_L Q/w\mu^*(Q/4wh^2)^{n-1}$ and is assumed not too large, i.e. $Re2h/L \ll 1$. The Peclet number is defined as $Pe = \rho_L c_L Q/wk_L$ and is assumed large.

The energy equation in the melt has the form:

$$\rho_L c_L \left\{ u_x \frac{\partial T}{\partial x} + u_y \frac{\partial T}{\partial z} \right\} = k_L \frac{\partial^2 T}{\partial z^2} + \left(\frac{\partial u_x}{\partial z} \right)^2 \qquad (6.8)$$

And, in the frozen layer, it reduces to the following form:

$$\left\{ k_s \frac{\partial^2 T}{\partial z^2} \right\} = 0 \qquad (6.9)$$

T_i denotes the inlet melt temperature, T_m the maximum temperature of the polymer at which flow is not possible, and T_w is the mold wall temperature. The following boundary conditions must be obeyed:

$$\left.\begin{aligned} &T = T_i \text{ at } x = 0 \\ &\partial T/\partial z = 0 \text{ at } z = 0 \\ &T = T_m \text{ at } z = h^* \end{aligned}\right\} \qquad (6.10)$$

in the melt,

$$\left.\begin{aligned} &T = T_m \text{ at } z = h^* \\ &T = T_w \text{ at } z = h \end{aligned}\right\} \qquad (6.11)$$

in the frozen layer,

$$-k_L \frac{\partial T}{\partial z}\bigg|_{\text{melt}} = -k_L \frac{\partial T}{\partial z}\bigg|_{\text{frozen layer}} \quad \text{at } z = h^* \qquad (6.12)$$

at the interface between the melt and the frozen layer.

Richardson [193] obtains a power law solution for the energy equation in terms of dimensionless variables. The following dimensionless numbers are defined:

$$\text{Brinkman Number} = Br = \left(\frac{\mu^*(Q/4wh^2)^{n-1}Q^2[2(n+2)/n]^{n+1}}{4w^2h^2k_L(T_i-T_m) \qquad 4}\right] \qquad (6.13)$$

$$\text{Graetz number} = Gz = (2\rho_L c_L Qh/wk_L I_i) \qquad (6.14)$$

$$\text{Modified Graetz number} = Gz^* = (Gz(n+2)/(4(n+1)) \qquad (6.15)$$

The dimensionless variables are defined as follows:

$$\left.\begin{aligned}
\eta &= z/h \\
\eta^* &= h^*/h \\
\xi &= x/L \\
\theta &= (T_m - T_w)/(T_i - T_m) \\
\theta^* &= k_s(T_m - T_w)/k_L(T_i - T_m) \\
\lambda &= [(n+1)/2n]^{1/3} \\
\psi &= (9\xi/2Gz^*)^{1/3} \\
\delta &= 1 - \eta^*
\end{aligned}\right\} \tag{6.16}$$

Γ is the Gamma function

The solution is given in terms of a power series in ψ:

$$\delta(\psi) = \psi\delta_1 + \psi^2\delta_2 + \psi^3\delta_3 + O(\psi^4) \tag{6.17}$$

where

$$\delta_1 = \left[\frac{\theta^*\Gamma(4/3)}{\lambda}\right] \tag{6.18}$$

$$\delta_2 = \left[\frac{\theta^*\Gamma(4/3)}{\lambda}\right]^2 \left\{\frac{m}{10\theta^*} - \frac{3}{4}\right\} \tag{6.19}$$

$$\delta_3 = \left[\frac{\theta^*\Gamma(4/3)}{\lambda}\right]^3 \left\{\frac{(10m - m^2)}{560\theta^{*2}} \frac{[\Gamma(5/3)]^2}{[\Gamma(4/3)]^4} - \frac{\Gamma(5/3)Br}{2\theta^{*2}[\Gamma(4/30]^2} - \frac{3}{40} + \frac{m}{50\theta^*}\left[\frac{m}{10\theta^*} - \frac{3}{4}\right]^2\right\} \tag{6.20}$$

where $\Gamma(4/3) = 0.8930$ and $\Gamma(5/3) = 0.9027$. The terms with ψ with powers of 4 or greater are ignored.

At the melt front region, δ is calculated by the gross assumption that the melt front moves with a uniform velocity V. The problem is analyzed by using a reference frame moving at a velocity V. Thus, the flow becomes quasi-steady relative to the flow front.

The energy conservation equation in the melt becomes:

$$-\rho_L c_L V \left\{ \frac{\partial T}{\partial x} \right\} = k_L \left\{ \frac{\partial^2 T}{\partial z^2} \right\} \qquad (6.21)$$

with boundary conditions

$$\left. \begin{array}{l} T = T_1 \text{ at } z = 0 \text{ and at } x = x_f \\ T = T_m \text{ at } z = h^* \end{array} \right\} \qquad (6.21a)$$

The energy conservation equation in the frozen layer is:

$$-\rho_S c_S V \left\{ \frac{\partial T}{\partial x} \right\} = k_S \left\{ \frac{\partial^2 T}{\partial z^2} \right\} \qquad (6.22)$$

with boundary conditions

$$\left. \begin{array}{l} T = T_m \text{ at } z = h^* \\ T = T_w \text{ at } z = h \text{ and at } x = x_f \end{array} \right\} \qquad (6.22a)$$

The interface boundary condition is:

$$-\rho_S \Lambda V \left\{ \frac{\partial h^*}{\partial x} \right\} - k_S \frac{\partial T}{\partial z} \bigg|_{\text{frozen layer}} = -k_L \frac{\partial T}{\partial z} \bigg|_{\text{melt}} \text{ at } z = h^* \qquad (6.22b)$$

The equations are solved to yield:

$$\delta = 4w^* \left(\frac{\xi_f - \xi}{Gz} \right)^{1/2} \tag{6.23}$$

where $w^* = 0.4769$ and ξ_f is the dimensionless melt front position.

6.2.1 Predicted Frozen Layer Thickness

The model was used to calculate the frozen layer growth during the filling stage of condition ZCEN (Table 4.3). The data presented in Chapter 4.2 were employed. The calculated values of the dimensionless frozen layer thickness (δ/h) for varying melt front positions are presented in Figure 6.3.

The results illustrate how the frozen layer grows with the advancing melt front. The frozen layer near the gate represents the first material to be frozen, while the layer at the end of the mold represents the last material to become frozen. The thickness is low at the gate and the melt front, with a maximum at an intermediate location. The frozen layer thickness grows downstream, and not in the gate region because of the thermal entrance effect. The thickness is of the order of 200 - 300μm, which agrees well with the experimental findings of maximum orientation at this position. Also, the gate and the end regions have thinner frozen layer. This agrees qualitatively with the observation of maximum

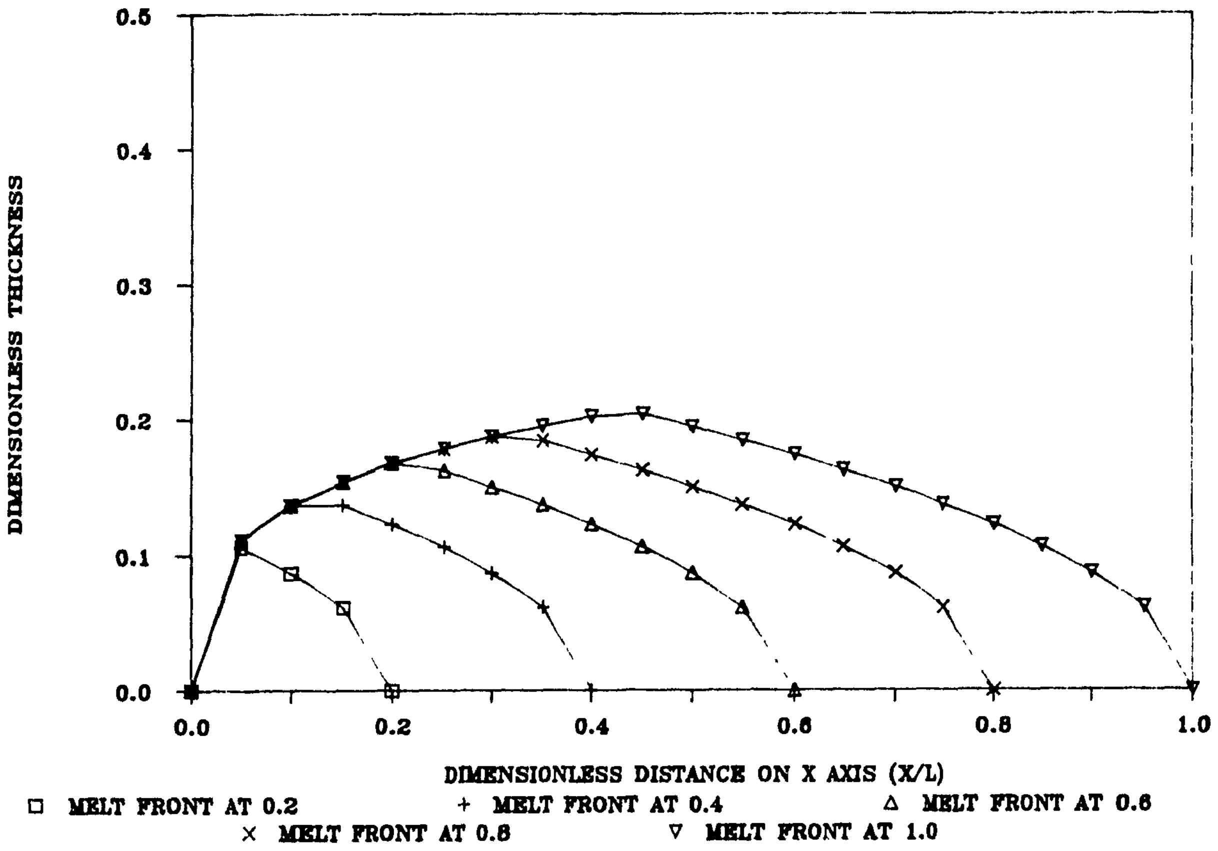

Figure 6.3 Frozen layer thickness profiles with various melt front position (Dimensionless thickness = thickness/half of cavity thickness).

orientation at the surface at positions 1 and 3, while at position 2 the maximum orientation is found at some distance from the surface.

The results were compared using different polymer melt temperatures. The results shown in Figure 6.4 demonstrate substantial differences in the frozen layer thickness profiles. The thermal entrance region is the more seriously affected area. The frozen layer thickness near the gate is greatest for the 200 °C melt temperature case. The maximum thickness for 200 °C melt temperature is 0.36 mm occurring at approximately 3 cm from the gate, while it is 0.26 mm for the 280 °C melt temperature and occurs approximately 5.5 cm from the gate. The thickness profiles in the flow front region show comparatively little variation with melt temperature.

The above results suggest that the effects of different melt temperatures that are associated with the frozen layer should be most clearly manifested at position 1 near the gate, less so at position 2 at the centre and least prominently at position 3, at the end of the mold. These expectations are in good agreement with the DSC findings which show a wider shear zone penetrating into the thickness for the low melt temperature molding. The higher melt temperature showed a much thinner shear zone. The shear zone occurs at the interface of the frozen layer and the melt. The frozen-in orientation in the form of γ-type crystals that occurs in this region, as a result, reveals the growth of the frozen layer. Thus, in the

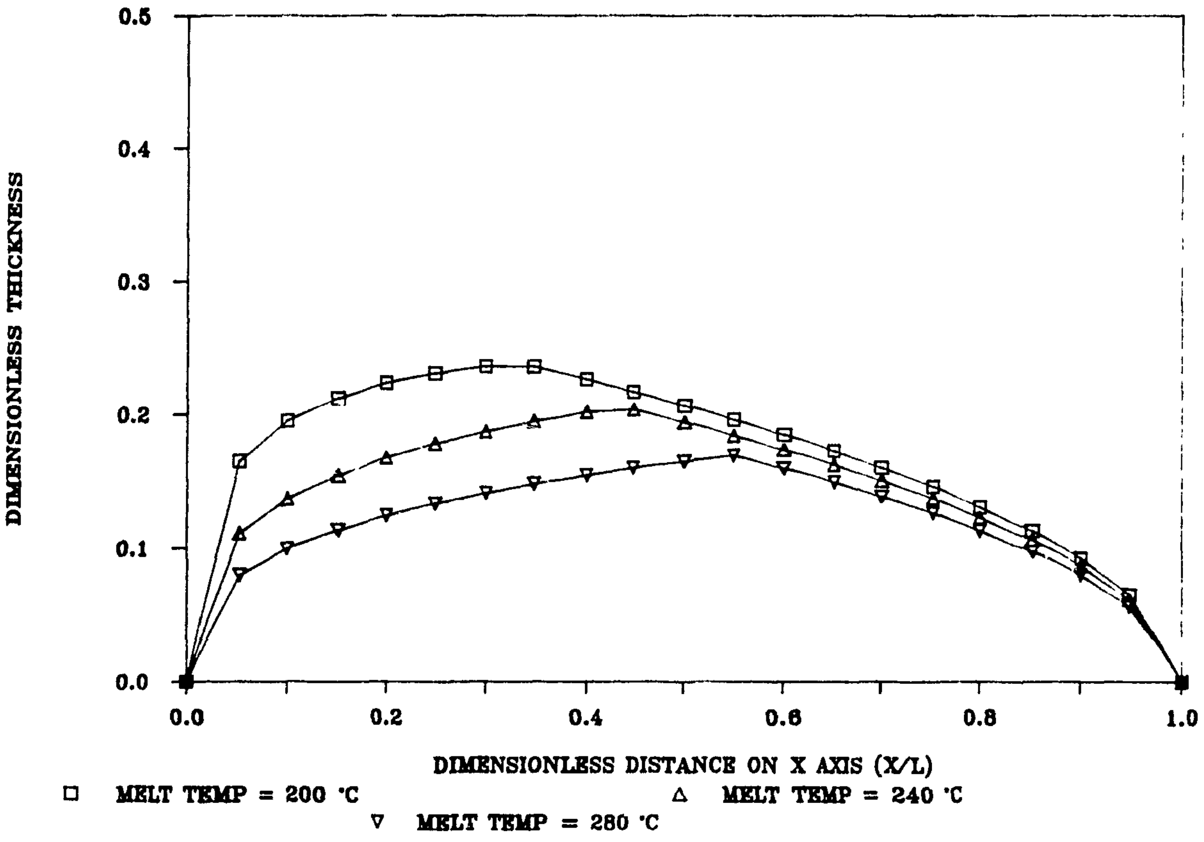

Figure 6.4 Effect of melt temperature on frozen layer thickness profile (Dimensionless thickness = thickness/half of cavity thickness).

low melt temperature molding, the deduction is that the frozen layer grew to a much thicker dimension than in the high melt temperature case. And, this result is in agreement with model predictions.

The effect of different polymer flow rates, or filling times, is evenly distributed in both the thermal entrance region and the flow front region. The lower filling times yield thinner frozen layer thickness profiles as shown in Figure 6.5. The maximum frozen layer thicknesses are 0.34 mm and 0.26 mm for the 1.0 and 2.0 sec filling times, respectively. Both maxima occur at approximately 4.5 cm from the gate. Here, the largest difference in microstructure that is associated with the frozen layer is expected to occur at position 2 in the centre of the mold.

The predictions of the frozen layer thickness during the filling stage compare well with experimental observations. Both temperature and flow rate effects are predicted, however, pressure and crystallization effects are ignored by the model. Thus, the effects of varying pressure or varying material crystallisability on the frozen layer thickness cannot be predicted. These effects are very important in the injection molding process, and thus, modelling of these influences will have to be dealt with in future studies.

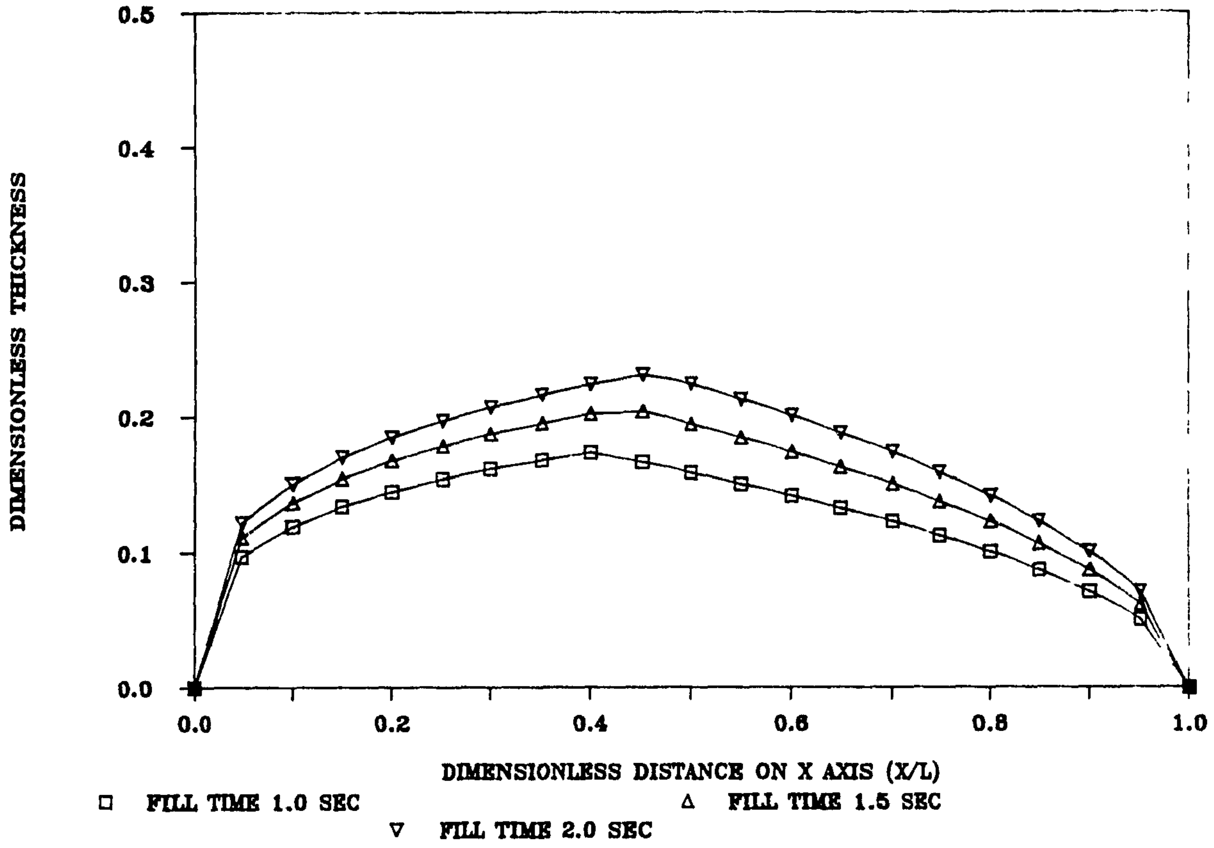

Figure 6.5 Effect of filling time on frozen layer thickness profile (Dimensionless thickness = thickness/half of cavity thickness).

6.3 Fiber Orientation Model

Jeffrey's equations [96] relate the motion of the suspended rigid spheroids to the torque resulting from the hydrodynamic stresses. The equations, in terms of fixed Cartesian coordinates, are given below [97]:

$$\begin{aligned}\frac{d\phi}{dt} = {} & Z_1 - Z_2\cos\phi\cot\theta - Z_3\sin\phi\cot\theta + B\Bigg[-D_{12}\sin\phi\cot\theta \\ & + D_{23}\cos2\phi + D_{31}\cos\phi\cot\theta - \frac{1}{2}(D_{22}-D_{33})\sin2\phi\Bigg]\end{aligned} \tag{6.24}$$

$$\begin{aligned}\frac{d\theta}{dt} = {} & -Z_2\sin\phi + Z_3\sin2\phi + B\Bigg[D_{12}\cos\phi\cos2\theta \\ & + \frac{1}{2}D_{23}\sin2\phi\sin2\theta + D_{31}\sin\phi\cos\theta + \\ & + \frac{1}{4}(D_{22}-D_{33})\cos2\phi\sin2\theta + \frac{3}{4}(D_{22}+D_{33})\sin2\theta\Bigg]\end{aligned} \tag{6.25}$$

The angles ϕ and θ are defined in Figure 6.6. The angle θ is the angle between the fiber and the z-axis, while ϕ is the angle that the projection of the fiber on the xy plane makes with the y-axis. D_{ij} are the components of the rate of deformation tensor D, and Z_i are the components of the vorticity tensor Z.

The local velocity around any single fiber can be separated into two parts, which can be represented as translational and rotational velocity components. The translational velocity acts to transpose the fiber at the

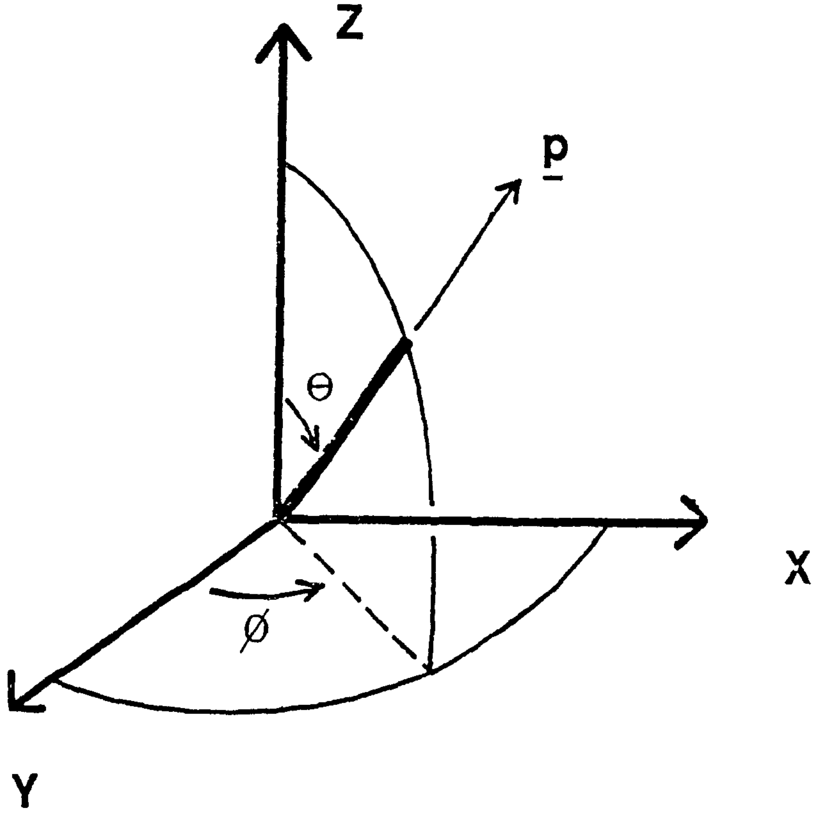

Figure 6.6 Definition of angles used to describe fiber orientation.

mean local velocity. The rate of strain tensor and the vorticity tensor can be obtained by breaking down the velocity gradient tensor ∇V.

In a general flow field, the velocity gradient tensor is defined as follows:

$$\nabla V = \left\{ \begin{array}{ccc} \dfrac{\partial V_1}{\partial x_1} & \dfrac{\partial V_2}{\partial x_1} & \dfrac{\partial V_3}{\partial x_1} \\ \dfrac{\partial V_1}{\partial x_2} & \dfrac{\partial V_2}{\partial x_2} & \dfrac{\partial V_3}{\partial x_2} \\ \dfrac{\partial V_1}{\partial x_3} & \dfrac{\partial V_2}{\partial x_3} & \dfrac{\partial V_3}{\partial x_3} \end{array} \right\} \qquad (6.26)$$

where $\frac{1}{2}\nabla V = -(D+Z)$ (6.27)

$$D = \frac{1}{2} \left\{ \begin{array}{ccc} 2\dfrac{\partial V_1}{\partial x_1} & \dfrac{\partial V_1}{\partial x_2}+\dfrac{\partial V_2}{\partial x_1} & \dfrac{\partial V_1}{\partial x_3}+\dfrac{\partial V_3}{\partial x_1} \\ \dfrac{\partial V_1}{\partial x_2}+\dfrac{\partial V_2}{\partial x_1} & 2\dfrac{\partial V_2}{\partial x_2} & \dfrac{\partial V_2}{\partial x_3}+\dfrac{\partial V_3}{\partial x_2} \\ \dfrac{\partial V_1}{\partial x_3}+\dfrac{\partial V_3}{\partial x_1} & \dfrac{\partial V_2}{\partial x_3}+\dfrac{\partial V_3}{\partial x_2} & 2\dfrac{\partial V_3}{\partial x_3} \end{array} \right\} \qquad (6.28)$$

The components of the vorticity tensor are given by:

$$Z_1 = \frac{1}{2}\left\{ \frac{\partial V_3}{\partial x_2} - \frac{\partial V_2}{\partial x_3} \right\} \qquad (6.29)$$

$$Z_2 = \frac{1}{2}\left\{ \frac{\partial V_1}{\partial x_3} - \frac{\partial V_3}{\partial x_1} \right\} \qquad (6.30)$$

$$Z_3 = \frac{1}{2}\left\{\frac{\partial V_2}{\partial x_1} - \frac{\partial V_1}{\partial x_2}\right\} \tag{6.31}$$

B is the shape parameter that is derived from the particle aspect ratio r_p,

$$B = \left\{\frac{r_p^2 - 1}{r_p^2 + 1}\right\} \tag{6.32}$$

It would be more realistic to use fiber orientation models that would account for visco-elasticity and interactions between fibers. However, as a first order analysis of the problem, the development of orientation in the mold has been analyzed by employing a number of gross simplifying assumptions. Jeffrey's model is used in the absence of another fiber orientation model that is more applicable to the case of a concentrated mixture of glass fibers in a polymer melt.

For the flow field described in section 6.1, Jeffrey's equations for fiber rotation can be simplified to:

$$\frac{d\phi}{dt} = \frac{1}{2}\left\{\frac{\partial V_x}{\partial y}\right\}[1+B\cos 2\phi] + \frac{1}{2}\left\{\frac{\partial V_x}{\partial z}\right\}\cos\phi\cot\theta[1+B] \tag{6.33}$$

$$\frac{d\theta}{dt} = \frac{1}{2}\left\{\frac{\partial V_x}{\partial z}\right\}\sin\phi[1+B\cos 2\theta] + \frac{B}{4}\left\{\frac{\partial V_x}{\partial y}\right\}\sin 2\phi\sin 2\theta \tag{6.34}$$

6.4 Fiber Orientation Predictions

The equations are solved by a fourth order multivariate Runge-Kutta method for initial ϕ and θ. The FORTRAN program is listed in Appendix III. The data used are presented in Chapter 4.2. The effect of the frozen layer was taken into account by decreasing the cross-sectional area of the mold available for flow. The fiber orientation distribution is represented by the numerical simulation of a sequence of single fiber solutions.

The fiber at the entrance of the mold would be expected to be oriented along the y-axis because of the sudden expansion at the gate, with values of approximately 0° for ϕ and 90° for θ. Fiber orientation predictions in expansion flow in the gate region have been studied [103], and the results show fibers aligning in the direction of elongation, i.e. perpendicular to the streamlines. These predictions are in agreement with experimental results [95].

The angle $(\pi/2-\phi)$ and θ are converted to orientation functions f_x and f_z defined as follows:

$$f_x = \frac{1}{2}\left\{ 3\langle\cos^2(\pi/2-\phi)\rangle - 1 \right\} \qquad (6.35)$$

$$f_z = \frac{1}{2}\left\{ 3\langle\cos^2\theta\rangle - 1 \right\} \qquad (6.36)$$

Figure 6.7 and 6.8 show the results of f_x at $x/L = 0$, 0.5 and 1, i.e. at the gate, the centre of the mold and at the

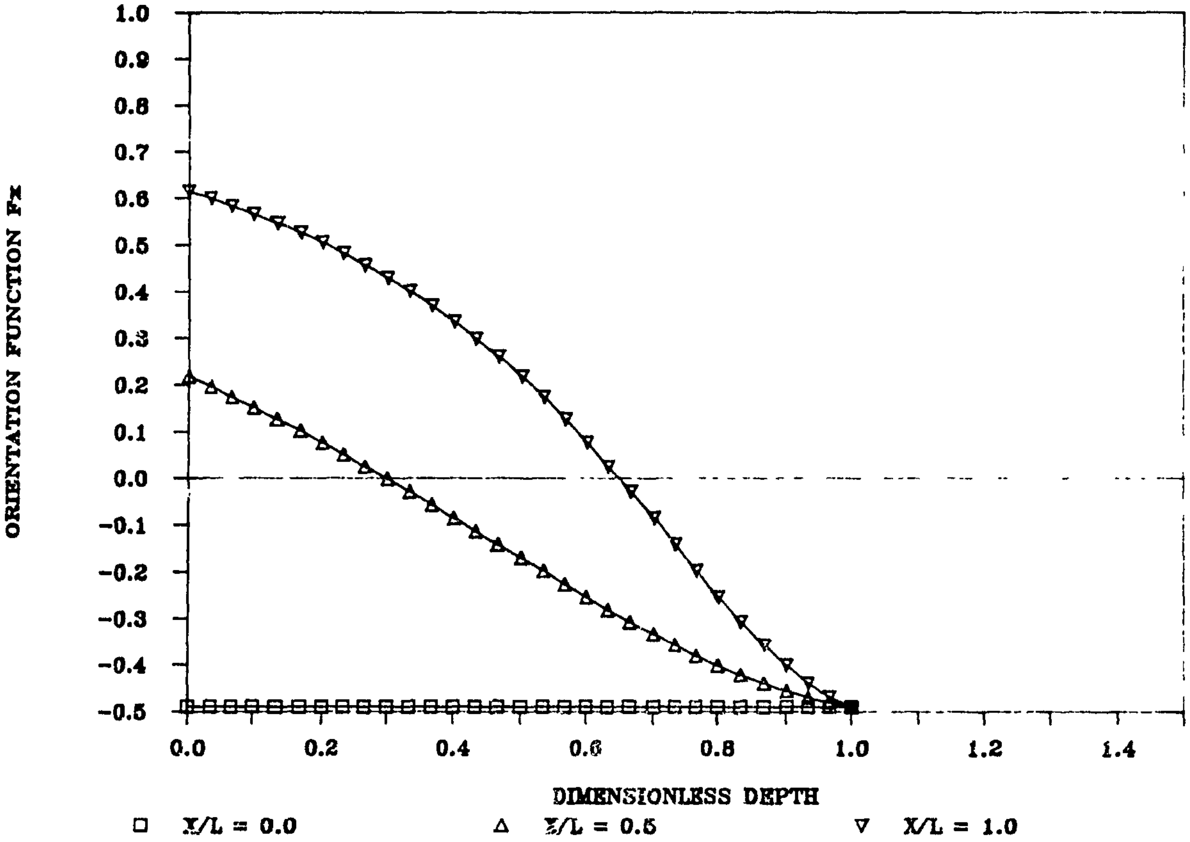

Figure 6.7 Predictions of fiber orientation f_x at positions x/L = 0, 0.5 and 1 (positions 1, 2, and 3 respectively) at initial angles $\theta = 80°$ and $\phi = 10°$.

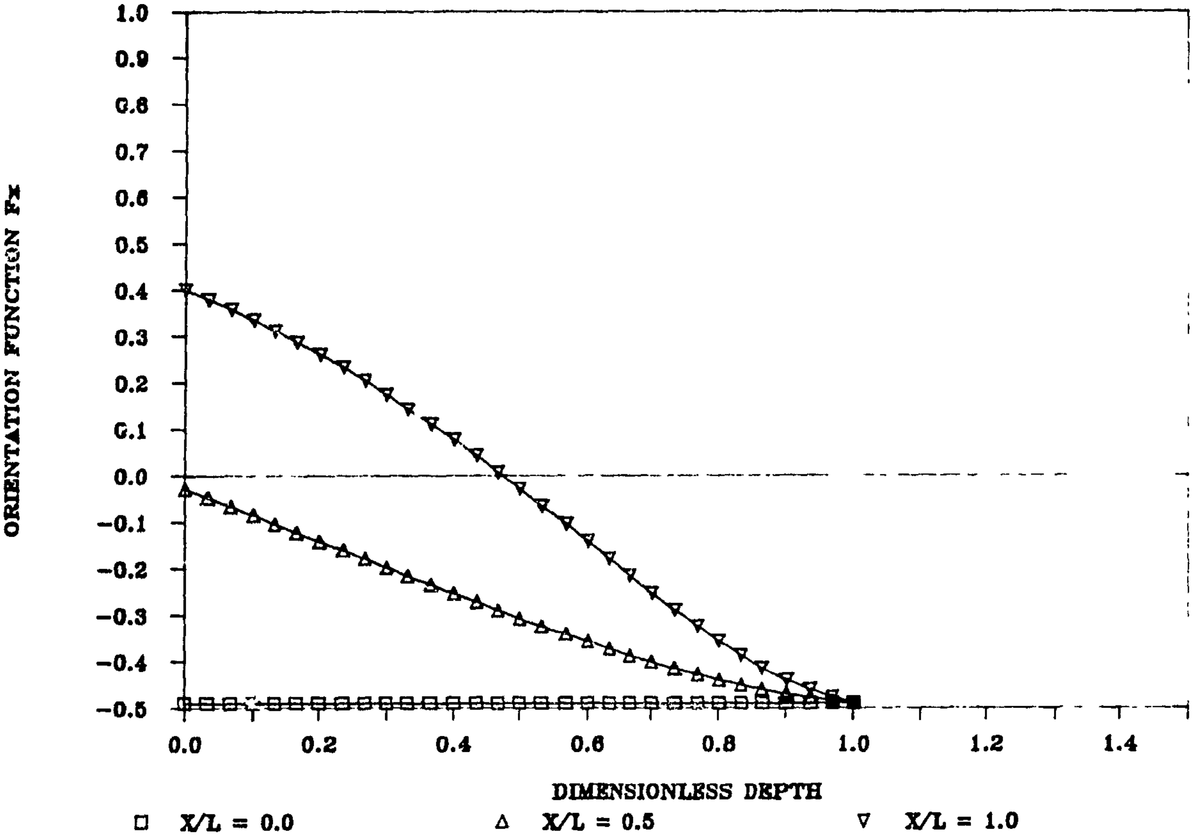

Figure 6.8 Predictions of fiber orientation f_x at positions x/L = 0, 0.5 and 1 (positions 1, 2, and 3, respectively) at initial angles $\theta = 80°$ and $\phi = 0°$.

end of the mold, respectively. The surface and centre are represented by dimensionless depth values of 0 and 1, respectively. It can be seen that the initial transverse orientation changes quickly to longitudinal orientation at the walls. The initial transverse orientation persists in a large region in the core. However, this orientation changes to a large extent to longitudinal orientation towards the surface. With increasing flow distance, the effect is increased. Theoretically, with a very long mold, the transverse orientation would be changed to longitudinal orientation in the entire sample. At position 2, it can be seen that the orientation of the skin layer is random in Figure 6.8, and not in Figure 6.7. The results suggests that the fiber orientation at the surface depends on the initial conditions and the position in the mold.

The case when fibers are initially randomly oriented in relation to both the x and z-axis is considered. The predictions for f_x and f_z are presented in Figures 6.9 and 6.10, respectively. The results indicate that the angle ϕ changes very quickly to roughly 0° from the initial values. The torque on the fiber is greater when the fiber is randomly oriented with respect to the z and x-axes. The result is that the fiber becomes aligned much more quickly. The results are similar for the angle θ which becomes 90°. This indicates that the fibers become oriented perpendicular to the z-axis, i.e. in the xy plane. The results compare favourably with

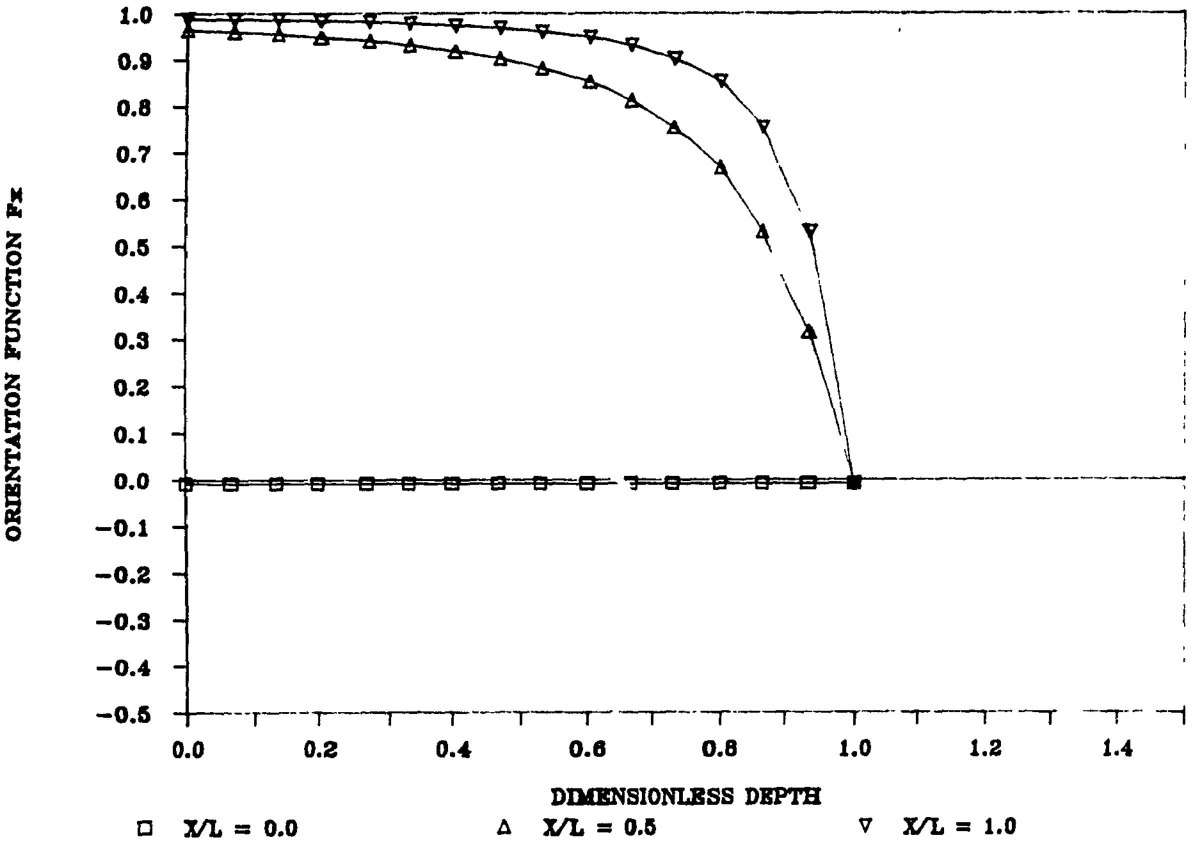

Figure 6.9 Predictions of fiber orientation f_x at X/L = 0, X/L = 0.5, and X/L = 1 (positions 1, 2, and 3, respectively) for initial angles $\theta = 55°$ and $\phi = 35°$.

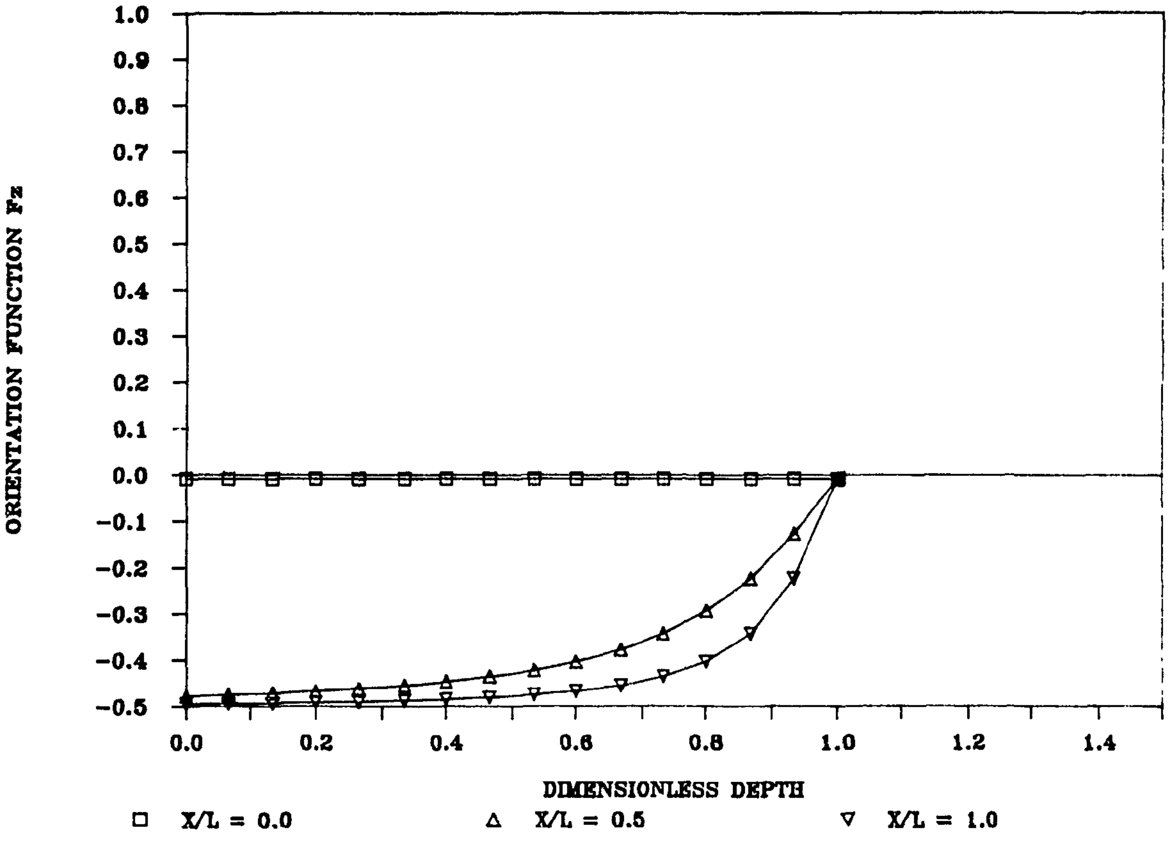

Figure 6.10 Predictions of fiber orientation f_z at X/L = 0, X/L = 0.5, and X/L = 1 (positions 1, 2, and 3, respectively) for initial angles θ = 55° and ϕ = 35°.

experimental results which show transverse orientation in the core and longitudinal orientation in the outer layers, with most fibers lying in the xy plane. Other results not shown, using varying initial angles, indicate that f_z becomes approximately −0.5 almost independently.

In a velocity field, fibers undergo periodic flip-overs, and the orientation does not reach a steady state [103]. The half-wave length of rotation is given as:

$$\lambda = \frac{\pi}{3}(r_p + 1/r_p) \tag{6.37}$$

When the fiber aspect ratio is infinite, the fiber does not flip over, but aligns with the streamline. In this study, the aspect ratio was approximately 28. This was large enough to eliminate the phenomenon of flip-overs within the mold length.

The frozen layer analysis was incorporated into the fiber orientation model to study its effect on fiber orientation. This was done by decreasing the cross-sectional area for melt flow. The initial fiber angles were $\theta = 80^\circ$ and $\phi = 10^\circ$. The predictions, at intermediate stages in filling, shown in Figure 6.11, indicate that the effects of the frozen layer are substantial. The reduction in flow area results in higher shear rates, which produce higher orientation at the melt-solid interface and the surface region. Given that the orientation produced at the interface becomes frozen-in, the final orientation distribution will be described as follows:

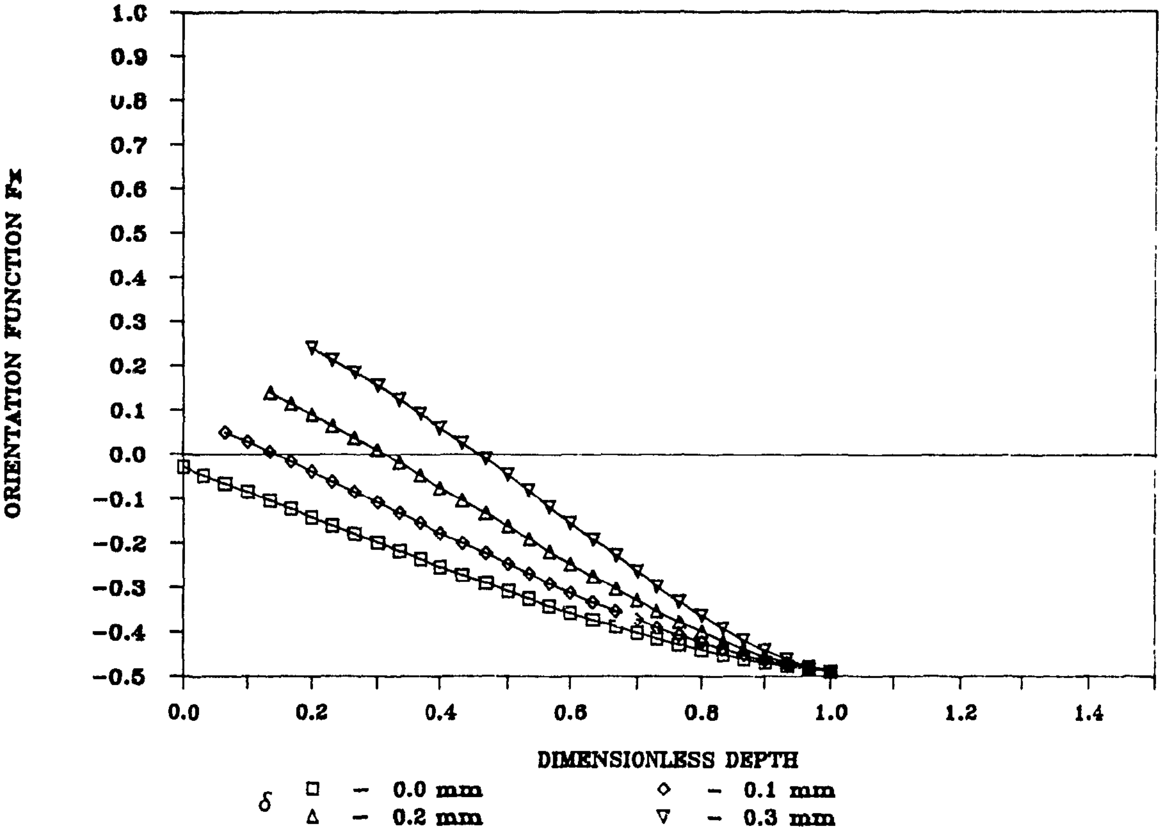

Figure 6.11 Predictions of fiber orientation f_x at position x/L = 0.5 (position 2) with the incorporation of the frozen layer analysis.

- random or near random at the surface; This value depends on the initial conditions and the location in the mold, as shown in Figures 6.7 and 6.8.
- maximum below the surface; The location of the maximum will be the thickness of the frozen layer when mold filling has stopped.
- decreasing orientation towards the initial transverse orientation in the centre. The orientation profile would be the one that remained when the filling stopped.

Figure 6.12 shows the orientation distribution for different melt temperatures at position 2 in the mold (conditions ZLMT, ZCEN, and ZHMT). The different frozen layer thicknesses are taken into account. Only the final orientation profile, i.e at the end of filling, is shown. The results show random orientation at the surface, a maximum flow direction orientation at the intermediate layer, and transverse core orientation. The orientation profiles are the same for each case at the surface. The increase in fiber orientation at the intermediate layer for the lower melt temperature is caused by the thicker frozen layer. Although melt temperature has a great influence on the matrix oriertation profile, it has a much lower influence on fiber orientation. Its influence is demonstrated indirectly through the influence of the frozen layer.

Figure 6.13 shows the predictions for different flow

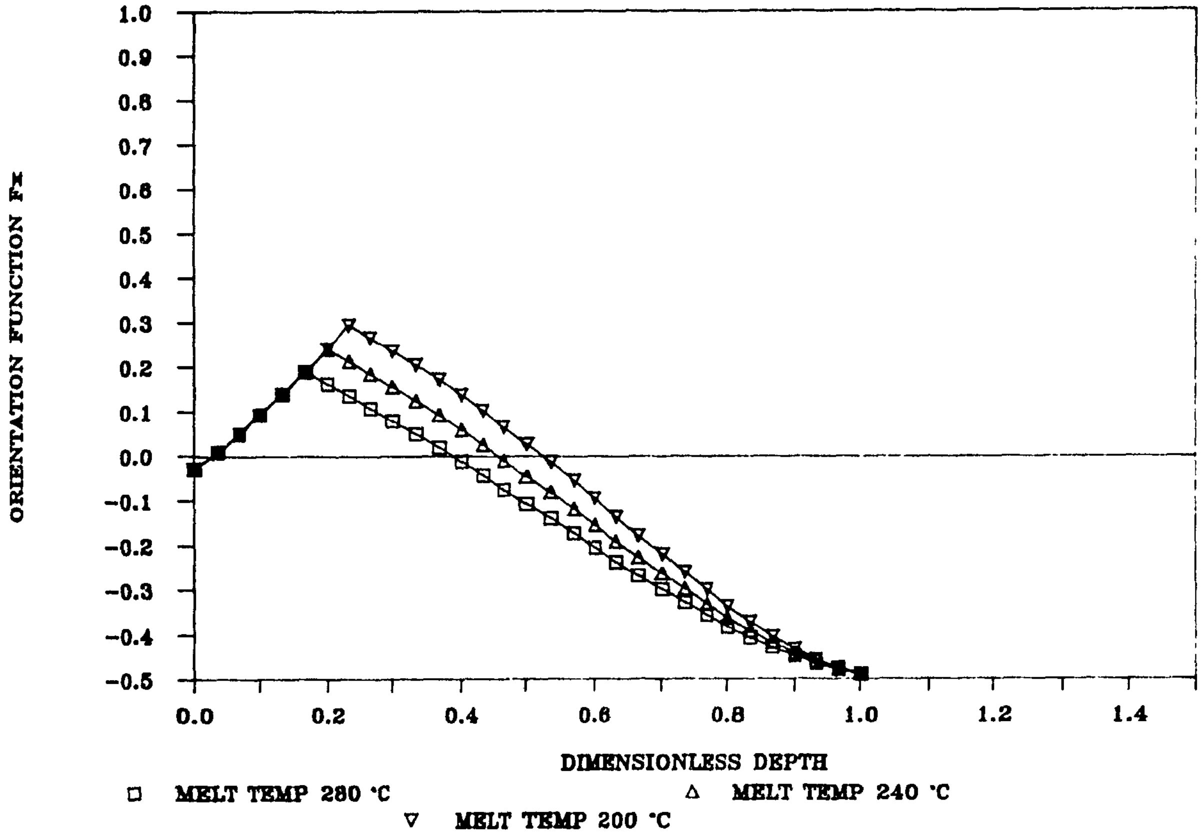

Figure 6.12 Predictions of fiber orientation f_x at position x/L = 0.5 (position 2) with the incorporation of the frozen layer analysis for various melt temperatures.

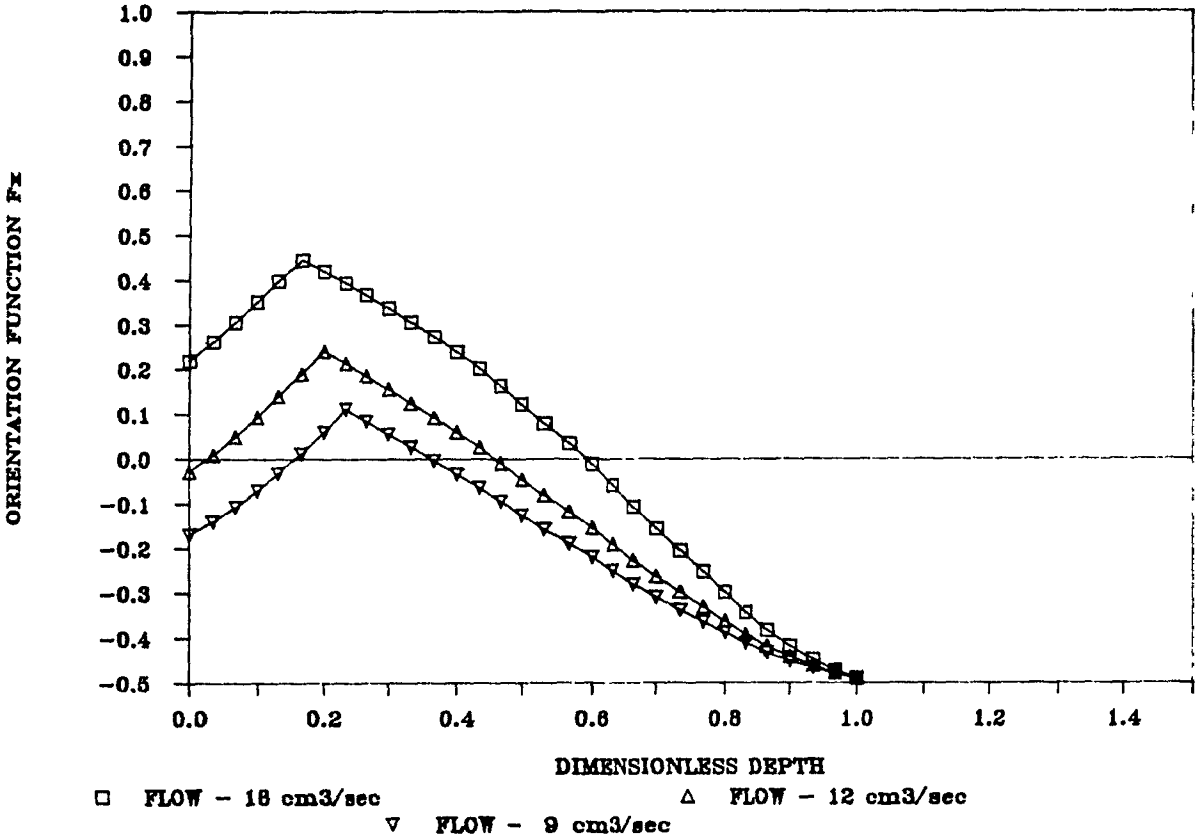

Figure 6.13 Predictions of fiber orientation f_x at position x/L = 0.5 (position 2) with the incorporation of the frozen layer analysis for various flow rates.

rates at the centre of the mold (conditions ZHIT, ZCEN, ZLIT). The different frozen layer thicknesses are taken into account. The orientation in the core region is similar for the various cases. The greatest difference is observed in the outer region. The higher flow rate conditions yield higher surface orientation with the maximum being greater and occurring nearer to the surface. The above results throw some light on the experimental results which yield similar patterns for the changes in fiber orientation at the surface and in the core region.

The model of fiber orientation in flow in a rectangular mold shows good qualitative agreement with the experimental results. It predicts the longitudinal orientation in the outer regions and transverse core orientation as well as the planar xy fiber orientation. When the frozen layer analysis is incorporated, it is possible to predict maximum orientation at the sub-skin region. With this model, a large part of the fiber orientation distribution profile is predicted from the surface to the maximum to the transverse core region. However, the analysis does not predict the details of the orientation in the skin. These limitations are to be expected in view of the many assumptions and simplifications incorporated in the model, and particularly to the absence of detailed analysis of fountain and extensional flow.

The orientation in the skin region is formed, at least in part, as a result of fountain flow at the melt front and is influenced by non-isothermal effects. Thus, it cannot be fully predicted by this model. Fiber orientation predictions in fountain flow [103] show preferred fiber alignment parallel to the free surface. This region, when deposited on the wall, becomes frozen and retains a high flow direction orientation. This is illustrated in Figure 6.14. In the region behind the contact point, it appears that there are many fiber flip-overs. If these are frozen in, this would produce a random fiber orientation layer. However, this is in the x-z plane, and does not account for the experimental observations of random fiber orientation in the x-y plane.

The orientation profiles predicted show smooth transitions from transverse to longitudinal orientation. However, with a Non-Newtonian, non-isothermal, unsteady flow with free surface effects, there would be a distinct change near the surface regions.

The predicted fiber orientation at the surface layer varied depending on the initial fiber orientation and the mold position. It is seen to be also influenced by processing conditions, as observed in Figure 6.13. A conclusive explanation for the formation of the random layer cannot be given, however, it is suggested that the initial fiber orientation, processing conditions, and location in the mold have some influence.

From the analysis presented in this chapter, the simple model for predicting fiber orientation has been shown to

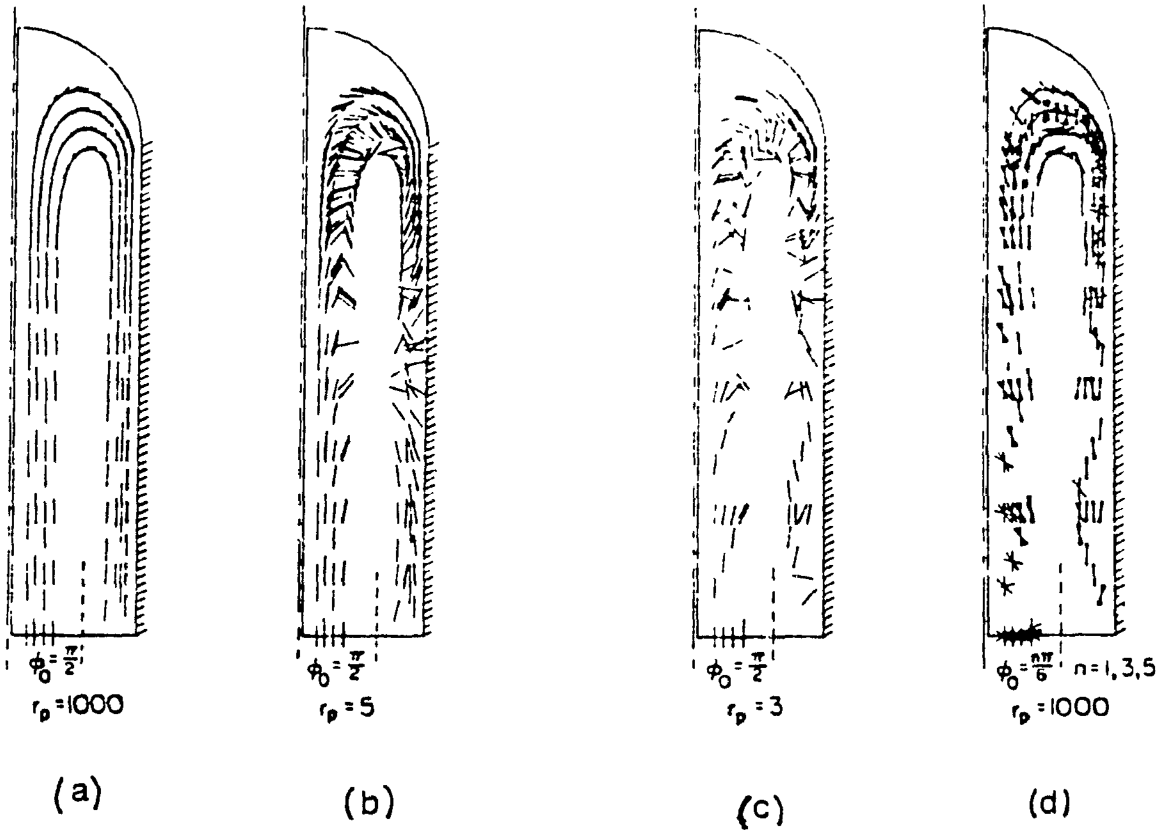

Figure 6.14 Fiber orientation resulting from fountain flow (a) B = 1.0 $\phi_0 = \pi/2$ (b) B = 0.9 $\phi_0 = \pi/2$ (c) B = 0.8 $\phi_0 = \pi/2$ (d) B = 1.0 $\phi_0 = n\pi/6$ n=1,3,5 [103].

predict adequately many of the experimental observations. The strength of the model lies in its ability to account for both x-y and x-z planes. Many elaborate models on fiber orientation have been developed [93,102,103,]. However, these planar models cannot account for both the x-y and x-z planes. For instance, a model for the x-z plane cannot use an initial condition of fiber orientation in the y direction, transverse to both the x and z directions. On the other hand, the model for the x-y plane cannot deal with any z-direction phenomena, such as frozen layer development.

CHAPTER 7

7 CONCLUSIONS

The study undertaken has provided improved understanding of microstructural development in composites during the injection molding cycle. The microstructure of the matrix and fiber phases has been qualitatively investigated in terms of spatial distributions and the effect of processing conditions. A variety of experimental techniques for evaluating microstructure has been developed and used. A summary of the specific conclusions is presented below.

(1) The microstructure of injection molded short glass fiber polypropylene composites has been shown to vary with spatial position in molded parts. The differences were most striking in the thickness direction. At least four layers has been identified in the cross-section. A skin and core structure was quite distinct. The skin layer was apparently formed as a result of a combination of fountain flow and freezing at the walls. The core included the bulk of the molded part and represented the still molten material after the mold cavity was filled. The other layers were formed between the skin and core, and are viewed by some workers as transition zones. One of these layers was distinct and, in fact, did not

involve a transition zone. It was most probably due to the high shear zone occurring adjacent to the frozen surface layer.

(2) The microstructure distribution in the thickness direction changed from one position to the other relative to the gate position. The centre-line regions near the gate showed thinner surface layers and broader cores, while further away, the skin layer assumed larger thicknesses. The differences were less dramatic in the regions that were away from the centre-line.

(3) The characteristic microstructure distribution in the molded parts was a result of several phenomena occurring during the injection molding process. Apart from the regular fluid flow and heat transfer processes, there was fountain flow at the flow front, solidification of the polymer melt at the walls, and shear flow at the interface of the solidified layer and the melt. Fountain flow at the flow front was the process affecting the microstructure at the surface of the molded part. Molten material from the centre of the flow was forced towards the surface where it became frozen on contact with the cold mold walls. At the interface between the frozen surface layer and the molten core, there was a shear zone. The outer layers in this region became frozen while

under shear stress. The centre region remained molten after the cavity has been filled. The cooling was much slower than in the surface regions.

(4) The microstructure of an injection molded composite part varied with the molding conditions. Melt temperature, filling time, holding pressure and holding time had varying effects on microstructural properties. Melt temperature had the most profound influence.

(5) Process variables such as cavity pressures, nozzle pressures, etc., exhibited profiles that were strongly affected by processing conditions. They can be used to provide valuable insight into the characteristic processes taking place during the injection molding cycle.

(6) Mold shrinkage was much higher in the thickness direction than in the length direction. Decreasing melt temperature, increasing holding pressure and holding time led to lower shrinkage. Very large shrinkages were obtained using high melt temperature, fast filling rates and no holding time.

(7) The crystalline structure of the injection molded parts showed variation from the skin to the core. At the skin,

the structure was that of a quenched material. Shear oriented γ-type crystals were seen in the shear zone just below the skin. These shear oriented crystals were not present in the unreinforced injection molded samples. Two types of crystalline structure were present in the core, the growth rates of which were different. In the outer regions, where the cooling rate was fast, the α_1 type crystals were almost nonexistent. In the centre, with slower cooling rates, the amount of α_1 type crystals increased to equal that of the α_2 type crystals.

(8) Although, there were significant changes in the crystalline morphology from the skin to the core, there was only a gradual increase in total crystallinity from the skin to the centre. The exception was with a melt temperature of 200 °C, where there were large increases in the total crystallinity in the shear zone. The shearing was much larger at low temperature, and it covered a broader region, which led to more shear induced crystallization.

(9) The orientation produced in the crystalline phase was low. Crystalline orientation was maximum at approximately 300 to 500 μm in depth depending on molding conditions. This corresponded to the shear zone. The orientation decreased towards the core to become random. Melt

temperature and filling time had the largest influence. The amorphous orientation for the unreinforced polypropylene increased to a maximum just below the surface, then decreased to a minimum at the core. The amorphous orientation was in the x-direction in the entire sample, and did not become random or transverse at the core. In the composite samples, the amorphous orientation became irregular because of localised orientation effects produced by the glass fibers.

(10) There was some evidence of fiber depletion near the gate of the mold and fiber accumulation at the far end of the mold. Fiber concentration was low at the surface, and, it increased towards the core. There was evidence of a fiber free layer near the surface, from both optical and electron microscopy. However, it appeared limited to regions near to the gate where high shear prevailed.

(11) Fiber length distribution was shown to be affected substantially by processing. The average fiber length of the injection molded part was considerably shorter than that of the raw pellet. There was also significant change in the average fiber lengths of layers from skin to core. The average length increased from skin to a maximum corresponding to the shear zone. The length then decreased to a minimum at the core.

(12) Fiber orientation distribution has been shown to be more complex than previously thought. At the surface, the fibers were sometimes oriented in the direction of flow, or random or nearly random. The orientation decreased to random in the case of the oriented skin layer, then, increased to a maximum at approximately 200 to 400 μm depth. After this, there was a decrease towards the core. The fiber orientation in the centre of the thickness direction was oriented transverse to the direction of flow. This direction varied according to the spatial position in reference to the gate. The surface orientation was produced as a result of fountain flow at the front. The flow direction orientation induced in the skin became frozen in as soon as it touched the mold wall. The shearing that occurred in the layer between the frozen skin and the melt tended to orient the fibers in the flow direction also. This orientation was much higher than in the skin layer.

(13) One of the most interesting and somewhat surprising observations in this study relates to the coexistence near the molding surface of two adjacent layers: one with characteristic fiber orientation in the flow direction and the other exhibiting random or near random fiber orientation. In some cases, the layer with nearly random fiber orientation was observed at the surface. It is not possible to give a conclusive explanation of this

observation at this point.

(14) The frozen layer analysis agreed with experimental results on the thickness of the frozen layer. The depth of the sub-skin shear zone, as inferred by observations of orientation and DSC results, agreed well with the model.

(15) The model of fiber orientation in flow in a rectangular mold, when used in conjunction with the frozen layer analysis, showed good qualitative agreement with the experimental results. Although, the model was limited by its assumptions, such as steady isothermal Newtonian flow with no entrance effects, it predicted the trends of longitudinal orientation in the outer regions, a maximum sub-skin orientation, transverse core orientation as well as the planar x-y fiber orientation. The maximum orientation as observed in experimental results was predicted adequately when frozen layer analysis was incorporated into the model.

7.1 Original Contributions

The material presented in this thesis is the result of a comprehensive study of microstructure and its development in injection molded glass fiber reinforced polypropylene composites. The work examined microstructure in terms of both matrix and fiber properties and the effects of processing conditions on microstructure. As part of a more comprehensive effort in progress in this Department, it represents an important and integral step towards achieving a clearer understanding of processing-microstructure-properties relationships in composites and to develop realistic and accurate mathematical models of composite processing.

Some of the original contributions of the present work are listed below:

(1) A comprehensive study was carried out regarding the injection molding of a composite material. The processing characteristics and the microstructure of the samples were evaluated in detail. Although various authors have reported on some aspects of composites injection molding, there has been no unified work linking major aspects of the problem. This work represents the most extensive individual effort to obtain a unified and comprehensive treatment of interactions between microstructure and processing in thermoplastics composite injection molding.

(2) Several methods have been developed to study the microstructure of fiber reinforced composites. These include:

- a semi-automated process to measure fiber orientation distribution in a molded sample. The process covers the steps from microtoming to microscopy to image digitizing and eventual calculations of fiber orientation functions.

- a method to determine molecular orientation in injection molded samples from FTIR spectra. This method is based on work done by Kissin, et al. [7,136].

(3) Microstructural properties such as fiber orientation, matrix orientation, etc., were measured and presented in the thickness direction for layers from the surface to the centre. Unlike bulk properties, these distributions give better understanding of the determining processes and can be used in computer simulation to compare with theoretical results and for prediction of mechanical properties.

(4) This work has documented for the first time to our knowledge, the presence of a layer with random or nearly random fiber orientation at or near the surface of the molding. This layer was observed to coexist with a surface layer with characteristic fiber orientation in the flow direction. In cases where the flow oriented surface layer was not present, the layer of random fiber orientation was observed at the surface.

(5) A fiber orientation model to predict three dimensional fiber orientation in a rectangular mold has been developed and used together with a frozen layer analysis. Although the model was limited in its assumptions, such as steady isothermal Newtonian flow with no entrance

effects, it predicted the trends of fiber orientation at the surface and the core.

7.2 Recommendation for Future Work

In order to enhance and extend the overall usefulness of this study, there are a few areas that are highly recommended for future research.

An area that is directly linked to this work is the study of the mechanical properties of injection molded composites parts. The characterization of the mechanical properties is needed to complement the work done on the processing and microstructure. An understanding of the effect of processing conditions on the microstructure and on the ultimate mechanical properties is extremely useful from manufacturers considerations.

The observation of a layer with random or nearly random fiber orientation at or near the surface of the molding was surprising. It would be useful to pursue this matter, in order to explain the factors that lead to the formation of this layer.

The influence of fiber parameters on microstructure development needs to be studied. Fiber concentration, aspect ratio, shape, and fiber material type, could have significant effects on microstructure. For example, the addition of highly conductive metal or carbon fibers may profoundly affect temperature profiles and crystallization rates with serious implications for the overall microstructure. It is known that plate-like mica particles produce mixtures that have much lower viscosities than fiber composites of the same reinforcement content. High fiber content produces high viscosity mixtures, causing difficulty in filling the mold cavity. An interesting development in industry is the recent trend for injection molded composites with much longer fibers. It would be desirable to study the effects of processing on the microstructure of these systems.

In this study, a simplified mold geometry with a side gate was used. A useful area of research is to evaluate various gate geometries. Injection molded products usually have complex shapes with complicated flow and heat transfer profiles. Some work would be needed to extend the analysis to the study of microstructure development in such parts.

Lastly, the fiber orientation model developed can be expanded to model unsteady, Non-Newtonian flow. Modelling of the entrance region and free surface flow are also important. Flow from the gate into the mold is very important in that it determines the initial orientation. The free surface flow is responsible for the surface orientation.

REFERENCES

1. T. Vu-Khanh, Polymer Composites, 8, 6, 363 (1987)
2. D. Santrach, Polymer Composites, 3, 4, 239 (1982)
3. F. H. Moy, " **Ph. D. Thesis** ", Department of Chemical Engineering, McGill University, Montreal, Canada (1980)
4. S. Kenig, " **Ph. D. Thesis** ", Department of Chemical Engineering, McGill University, Montreal, Canada (1972)
5. D. Kalyon, " **M. Eng. Thesis** ", Department of Chemical Engineering, McGill University, Montreal, Canada (1977)
6. W. Rose, Nature, 191, 242 (1961)
7. Z. Tadmor, J. Appl. Polym. Sci., 18, 1753 (1974)
8. R. L. Schmidt, Polym. Eng. Sci., 14, 797 (1974)
9. M. R. Kamal, S. K. Goyal, and E. Chu, AIChE J., 34, 94 (1988)
10. K. Oda, J. L. White, and E. S. Clark, Polym. Eng. & Sci., 10, 209 (1970)
11. S. S. Katti, and J. M. Schultz, Polym. Eng. & Sci., 22, 16, 1001 (1982)
12. M. R. Kantz, Int. J. Polym. Mat., 3, 245 (1974)
13. M. R. Kantz, H. D. Newman Jr, and F. H. Stigale, J. Appl. Polym. Sci., 16, 1249 (1972)
14. E. S. Clark, SPE J., 23, 7, 46 (1967)
15. E. S. Clark, Appl. Polym. Symp., 20, 325 (1973)
16. E. S. Clark, Plast. Eng., 30, 4, 73 (1974)
17. E. Boehme, Kunststoffe, 60, 273 (1970)
18. E. S. Clark, SPE Tech. Pap. RETEC, Downington, Pa. (1973)
19. E. S. Clark, Appl. Polym. Symp., 24, 45 (1974)
20. G. Menges, A. Wubken, and B. Horn, Colloid. Polym. Sci., 254, 261 (1976)
21. D. R. Fitchum, and Z. Mencik, J. Polym. Sci. Polym. Phys.

Ed., 11, 951 (1974)

22. D. R. Fitchum, and Z. Mencik, J. Polym. Sci. Polym. Phys. Ed., 973 (1973)

23. V. Tan, and M. R. Kamal, J. Appl. Polym. Sci., 22, 2341 (1978)

24. J. Bowman, N. Harris, and M. Bovis, J. Mater. Sci., 10, 63 (1975)

25. W. Y. Chiu, and G. D. Shyu, J. Appl. Polym. Sci., 34, 1493 (1987)

26. F. H. Moy, and M. R. Kamal, Polym. Eng. & Sci., 20, 14, 957 (1980)

27. M. Fleissner, Kolloid-Z., 251, 1006 (1973)

28. G. Menges, and G. Wubken, ANTEC'73, 519 (1973)

29. P. D. Patel, and D. C. Bogue, Polym. Eng. & Sci., 21, 8, 449 (1981)

30. R. S. Spencer, and G. D. Gilmore, Modern Plastics, 28, 97 (1950)

31. G. B. Jackson, and R. L. Ballman, SPE J., 16, 1147 (1960)

32. H. Keskkula, and J. W. Norton, Jr, J. Appl. Polym. Sci. Polym. Phys. Ed., 6, 289 (1959)

33. M. Jensen, and R. R. Whisson, Polymer, 14, 193 (1973)

34. D. E. Scheperel, Plast. Eng. Dec., 46 (1973)

35. R. J. Samuels, Polym. Eng. & Sci., 23, 5, 257 (1983)

36. W. R. Krigbaum, J. Polym. Sci., Part C, 15, 251 (1966)

37. J. Clements, R. Jakeways, I. M. Ward, and G. W. Longman, Polymer, 20, 295 (1979)

38. M. Takayanagi, K. Imada, and T. Kajiyama, J. Polym. Sci., Part C, 15, 263 (1966)

39. R. S. Stein, and F. H. Norris, J. Polym. Sci., 21, 381 (1956)

40. S. Hosino, J. Powers, D. G. Legrand, H. Kawai, and R. S. Stein, J. Polym. Sci., 58, 185 (1962)

41. R. J. Samuels, J. Polym. Sci., Part C, 253 (1967)

42. A. Turner Jones, J. M. Aizlewood, and D. R. Beckett, Macromol. Chem., 75, 134 (1973)

43. G. Natta, and P. Corradini, Nuovo Cimento, Suppl, 15, 40 (1960)

44. J. M. Crissman, J. Polym. Sci., A-2, 7, 289 (1969)

45. A. J. Lovinger, J. O. Chua, and C. C. Gryte, J. Polym. Sci. Polym. Phys. Ed., 15, 641 (1977)

46. H. Dragaum, H. Hubeny, and H. Muschik, J. Polym. Sci. Polym. Phys. Ed., 15, 1779 (1977)

47. F. J. Padden, Jr., and H. D. Keith, J. Appl. Phys., 30, 1479 (1959)

48. J. Kardos, A. W. Christiansen, and E. Baer, J. Polym. Sci. Part A, 2, 4, 777 (1966)

49. H. P. Frank, " **Polypropylene** ", Gorden and Breach Science Publishers Inc., N.Y. (1965)

50. P. H. Geil, Polymer single crystals, Polymer Reviews, Vol 5, Interscience, New York, (1963)

51. R. J. Samuels, J. Polym. Sci., Part A-2, 6, 1101 (1968)

52. J. S. Vrentas, C. M. Vrentas, A. H. Bhompal, and M. S. Lahalih, Polym. Eng. & Sci., 20, 14, 925 (1980)

53. M. R. Kamal, and S. Kenig, Polym. Eng. & Sci., 12, 294 (1972)

54. M. R. Kamal, Y. Kuo, and P. H. Doan, Polym. Eng. Sci., 15, 863 (1975)

55. M. R. Kamal, and S. Kenig, Polym. Eng. Sci., 12, 302 (1972)

56. Y. Kuo, and M. R. Kamal, AIChE J., 22, 661 (1976)

57. J. L. White, and H. B. Dee, Polym. Eng. Sci., 12, 212 (1974)

58. T. Aoba, and H. Odaira, Proceedings of the 14th Japanese Congress on Materials Research, Kyoto, Japan, 124 (1970)

59. A. I. Isayev, Polym. Eng. & Sci., 23, 5, 271 (1983)

60. L. C. E. Struik, Polym. Eng. Sci., 19, 223 (1979)

61. A. Seigmann, A. Buchman, and S. Kenig, Polym. Eng. Sci., 22, 560 (1980)

62. R. G. Treuting, and W. T. Read, Jr, J. Appl. Phys., 22, 130 (1951)

63. L. D. Coxon, and J. R. White, Polym. Eng. & Sci., 20, 3, 230 (1980)

64. J. Kubat, and M. Rigdahl, Int. J. Polym. Mat., 3, 287 (1975)

65. J. R. White, J. Mater. Sci., 20, 2377 (1985)

66. J. L. White, and W. Dietz, Polym. Eng. Sci., 19, 1081 (1979)

67. A. I. Isayev, and C. A. Heiber, Rheol. Acta, 19, 168 (1980)

68. A. Siegmann, M. Narkis, and N. Rozenzweig, Polym. Eng. & Sci., 19, 3, 223 (1979)

69. P. So, and L. J. Broutman, SPE ANTEC Tech. Paper., 26, 114 (1976)

70. Isayev, Cornell report #7, Cornell Injection Molding Project

71. Isayev, Cornell report #8, Cornell Injection Molding Project

72. Z. Bakerdjian, and M. R. Kamal, Polym. Eng. Sci., 17, 96 (1977)

73. L. J. Broutman, and S. M. Krishnakumar, Polym. Eng. & Sci., 16, 2 (1974)

74. M. W. Darlington, and A. C. Smith, Polym. Compos., 8, 16 (1987)

75. S. H. Emerman, Polym. Eng. & Sci., 27, 14, 1105 (1987)

76. S. Wu, Polym. Eng. & Sci., 19, 9, 638 (1979)

77. R. P. Hegler, and G. Mennig, Polym. Eng. & Sci., 25, 7, 395 (1985)

78. S. I. Rubinow, and J. B. Keller, J. Fluid Mech., 11, 447 (1961)

79. F. Gauthier, H. L. Goldsmith, and S. G. Mason, Trans. Soc. Rheol., 15, 297 (1971)

80. J. Karger-Kocsis, and K. Friedrich, Compos. Sci Tech., 32, 293 (1988)

81. R. vonTurkovich, and L. Erwin, Polym. Eng. & Sci., 23, 13, 743 (1983)

82. V. B. Gupta, R. K. Mittal, P. K. Sharma, G. Mennig, and J. Wolters, Polym. Comp., 10, 8 (1989)

83. V. B. Gupta, R. K. Mittal, P. K. Sharma, G. Mennig, and J. Wolters, Polym. Comp., 10, 16 (1989)

84. J. Milewski, Polym. Plas. Technol. Eng., 3, 101 (1974)

85. D. M. Biggs, ANTEC'84, 668 (1984)

86. M. J. Owens, D. H. Thomas, and M. S. Found, Proc. Reinf. Plast. Congr., Paper 18, (1978)

87. P. F. Bright, and R. J. Crowson, M. J. Folkes, J. Mater. Sci., 13, 2497 (1978)

88. M. W. Darlington, and P. L. McGinley, J. Mater. Sci., 10, 906 (1975)

89. M. Vincent, and J. F. Agassant, Polymer Composites, 7, 2, 76 (1986)

90. M. Vincent, and J. F. Agassant, Rheol. Acta, 24, 603 (1985)

91. L. A. Goettler, Polym. Compos., 5, 60 (1984)

92. P. F. Bright, and M. W. Darlington, Plastics & Rubber Processing & Applications, 1, 2, 139 (1981)

93. S. Kenig, Polymer Composites, 7, 1, 50 (1986)

94. G. Menges, and P. Geisbusch, Colloid Polym. Sci., 260, 73 (1982)

95. L. A. Goettler, Modern Plastics, 140, Apr. (1970)

96. G. B. Jeffrey, Proc. Royal Society, A102, 161 (1922)

97. H. L. Goldsmith, and S. G. Mason, " **Rheology** ", E. R. Eirich, Ed., 4, Academic Press, N.Y. (1967)

98. L. G. Leal, and E. J. Hinch, J. Fluid Mech., 46, 685 (1971)

99. C. Cohen, B. Chung, and W. Stasiak, Rheol. Acta, 26, 217 (1987)

100. F. Folger, C. L. Tucker III, J. Reinf. Plast. Comp., 3, 98 (1984)

101. F. J. Lockett, Plast. Rubb. Proc., 6, 85 (1980)

102. J. W. Gillespie Jr., J. A. Vanderchuren, and R. B. Pipes, ANTEC'84, 648 (1984)

103. R. C. Givler, M. J. Crochet, and and R. B. Pipes, J. Comp. Mat., 331 (1983)

104. J. L. Koenig, " **The Role of the Polymeric Matrix in the Processing and Structural Properties of Composite Materials.** " J. C. Seferis, and L. Nicolais, Ed., Plenum Press (1983)

105. H. Ishida, Polym. Reprints, 24, 1, 198 (1983)

106. E. P. Plueddemann, Polym. Reprints, 24, 1, 184 (1983)

107. J. K. Kardos, Polym. Reprints, 24, 1, 185 (1983)

108. W. A. Frazer, F. H. Ancker, A. T. Dibeneditto, and B. Elbirli, Polymer Composites, 4, 238 (1983)

109. P. S. Theocaris, " **The Role of the Polymeric Matrix in the Processing and Structural Properties of Composite Materials.** " J. C. Seferis, and L. Nicolais, Ed., Plenum Press, 481 (1983)

110. M. R. Piggott, Polymer Composites, 3, 4, 179 (1982)

111. T. Mutel, " **Ph.D. Thesis** ", Department of Chemical Engineering, McGill University, Montreal, Canada (1989)

112. A. T. Mutel, and M. R. Kamal, Polymer Comp., 5, 29 (1984)

113. S.Sourour, " **Ph.D. Thesis** ", Department of Chemical Engineering, McGill University, Montreal, Canada (1978)

114. M. R. Kamal, V. Tan, and F. Kashani, Adv. in Polym. Tech., 3, 89 (1983)

115. D. Hansen, and G. A. Bernier, Polym. Eng & Sci., 12, 204 (1972)

116. T. R. Fuller, and A. L. Fricke. J. Appl. Polym. Sci., 15, 1729 (1971)

117. R. C. Progelof, J. L. Throne, and R. R. Ruetsch, Polym. Eng. & Sci., 16, 9, 615 (1976)

118. H. W. Cox, C. C. Mentzer, and R. C. Custer, Polym. Eng. & Sci., 24, 7, 501 (1984)

119. S. C. Cheng, and R. I. Vachon, Int. J. Heat & Mass Transfer, 12, 249 (1969)

120. G. T. Tsao, Ind. Eng. Chem., 53, 395 (1961)

121. H. Fricke, Physics Review, 24, 575 (1924)

122. R. L. Hamilton, and O. K. Crosser, Ind. Eng. Chem. Fund., 1, 187 (1962)

123. J. Ashton, J. Halpin, and P. Petit, " **Primer on Composite Materials; Analysis,"** Technomic Pub. Co., Stamford, Conn. (1969)

124. T. Lewis, and L. Neilsen, J. Appl. Polym. Sci., 14, 1449 (1970)

125. M. R. Kamal, and P. G. Lafleur, Polym. Eng. & Sci., 24, 9, 692 (1984)

126. I. Kirshenbaum, Z. W. Wilchinsky, and B. Groten, J. Applied Polym. Sci., 8, 2723 (1964)

127. F. M. Mirabella, Jr., J. Polym. Sci., Polym. Phys. Ed., 25, 591 (1987)

128. R. W. Wilkinson, and M. Dole, J. Appl. Polym. Sci., 58, 1089 (1962)

129. M. R. Kamal, and E. Chu, Polym. Eng. Sci, 23, 27 (1983)

130. E. F. -H. Chu, " **M.Eng Thesis** ", Department of Chemical Engineering, McGill University, Montreal, Canada (1983)

131. K. Nakamura, T. Watanabe, K. Katayama, and T. Amamo, J. Appl. Polym. Sci., 17, 1031 (1973)

132. R. Burns, and D. Pennington, SPE ANTEC., Tech Papers, 25, 1 (1979)

133. A. S. Malowany, M. D. Levine, M. R. Kamal, R. Kurz, and A. Mansouri, Graphics Interface'86, Vision Interface'86, 300 (1986)

134. C. Y. Liang, " **Newer Methods of Polymer Characterization** ", B.Ke ed., J.Wiley & Sons. N.Y. (1964)

135. R. J. Samuels, " **Structured Polymer Properties** ", J.Wiley & Sons. N.Y. (1974)

136. Y. V. Kissin, I. A. Lekaye, Y. A. Chernova, N. A. Davydova, and N. M. Chirkov, Kysokomol Soyed., A16, 3, 667 (1974)

137. A. Boldizar, and J. Kubat, Polym. Eng. & Sci., 26, 12, 877 (1986)

138. G. Akay, Polym. Eng. & Sci., 22, 16, 1038 (1982)

139. G. D. Gilmore, and A. S. Spencer, Modern Plastics, 27, 4, 143 (1950)

140. P. H. Doan, " **M. Eng. Thesis** ", Department of Chemical Engineering, McGill University, Montreal, Canada (1974)

141. R. B. Staub, SPE J., 16, 4, 429 (1960)

142. H. W. Cox, and C. C. Mentzer, Polym. Eng. & Sci., 26, 7, 488 (1986)

143. G. Menges, Plastverarbeiter, 29, 369 (1978)

144. Y. T. Koita, Polym. Eng. & Sci., 14, 840 (1974)

145. T-S. Chung, Polym. Eng. & Sci., 25, 772 (1985)

146. L. Krueger, and Z. Tadmor, Polym. Eng. & Sci., 20, 426 (1980)

147. J. Greener, Polym. Eng. & Sci., 26, 12, 886 (1986)

148. M. W. Darlington, A. J. Scott, and A. C. Smith, Polym. Eng. & Sci., 26, 18, 1282 (1986)

149. K. K. Wang, Progress Report No. 6, Injection Molding Project, Cornell University, Ithaca, NY, (1979)

150. T. L. Magila, G. G. Vitale, and D. G. LeGrand, GE Tech. Info Ser. June 1977, NO 77 Crd138

151. J. Kubát, and H-E. Stromvall, Plastics & Rubber: Processing, 45, June (1980)

152. D. J. Harry, Plast. Design and Proc., 13, 6, 16 (1973).

153. J. M. Schultz, " **Polymer Materials Science** ", Prentice-Hall, New York (1974)

154. C. C. Carroll, Mod. Plast., Sept, 108 (1984)

155. F. Kumamaru, T. Oona, T. Kajiyama, and M. Takayanagi, Polymer Composites, 4, 2, 141 (1983)

156. K. D. Pae, J. Polym. Sci., A-2, 6, 657 (1968)

157. Y. S. Yadav, and P. C. Jain, Polymer, 27, 721 (1986)

158. H. D. Keith, and F. J. Padden Jr., J. Appl. Phys., 44, 1217 (1973)

159. P. Jacoby, B. H. Bersted, W. J. Kessel, and C. E. Smith, J. Polym. Sci. B, Polym. Phys., 24, 461 (1986)

160. G. Guerra, V. Petraccone, P. Corradini, C. DeRosa, R. Napolitano, B. Pirozzi, and G. Giunchi, J. Polym. Sci. Polym Phys. Ed., 22, 1029 (1984)

161. B. Wunderlich, and T. Davidson, J. Polym. Sci. A-2, 7, 2043 (1969)

162. T. Davidson, and B. Wunderlich, J. Polym. Sci. A-2, 7, 2051 (1969)

163. R. B. Prime, and B. Wunderlich, J. Polym. Sci. A-2, 7, 2061 (1969)

164. R. B. Prime, and B. Wunderlich, J. Polym. Sci. A-2, 7, 2073 (1969)

165. R. B. Prime, and B. Wunderlich, J. Polym. Sci. A-2, 7, 2091 (1969)

166. C. L. Gruner, and B. Wunderlich, R. C. Bopp, J. Polym. Sci. A-2, 7, 2099 (1969)

167. G. Akay, Rheol. Acta., 18, 256, (1979)

168. J. P. Trotignon, J. L. Lebrun, and J. Verdu, Plast. Rubber Appl., 2, 3, 247 (1982)

169. F. M. Mirabella, Jr., J. Polym. Sci. B, Polym. Phys. Ed., 25, 591 (1987)

170. S. G. Turley, and H. Keskkula, J. Appl. Polym. Sci. 9, 2693 (1965)

171. A. Garton, Polymer Composites, 3, 4, 189 (1982)

172. V. Tan, and M. R. Kamal, SPE ANTEC Tech. Paper., 21, 339 (1976)

173. J. Kubát, and J. -A. Månson, Polym. Eng. Sci., 23, 869 (1983)

174. M. Houska, and M. Brummel, Polym. Eng. & Sci., 27, 12, 917 (1987)

175. P. H. Hermans, J. J. Hermans, D. Vermaas, and A. Weidinger, J. Polym. Sci., 3, 1, (1948)

176. E. S. Hsiue, R. E. Robertson, and G. S. Y. Yeh, Polym. Eng. Sci., 23, 74 (1983)

177. M. R. Kamal, and F. Moy, J. Appl. Polym. Sci., 28, 1787 (1983)

178. W. Heckmann, U. Johnsen, Colloid Polym. Sci., 252, 826 (1974)

179. C. G. Gogos, C-F. Huang, and L. R. Schmidt, Polym. Eng. & Sci., 26, 20, 1457 (1986)

180. M. R. Kamal, E. Chu, P. G. Lafleur, and M. E. Ryan, Polym. Eng. & Sci., 26, 3, 190 (1986)

181. J. Kubat, and A. Szalanczi, Polym. Eng. & Sci., 14, 873 (1974)

182. G. Akay, and T. Tincer, Polym. Eng. & Sci., 21, 8 (1981)

183. T. Tincer, and G. Akay, Polym. Eng. & Sci., 22, 410 (1982)

184. S. Jalopin, Advan. Chem. Ser., 134 (1974)

185. H. M. Laun, Colloid & Polymer Sci., 262, 4, 257 (1984)

186. J. C. Malzahn, and J. M. Schultz, Compos. Sci. Tech., 25, 187 (1986)

187. G. R. Smith, M. W. Darlington, and D. McCammond, J. Strain Analy., 13, 221 (1978)

188. Z. Tadmor, and C. G. Gogos, " **Principles of Polymer Processing** ", John Wiley & Sons Inc., N.Y. (1979)

189. M. Grmela, Polym. Eng. & Sci., 24, 9, 673 (1984)

190. H. Mavridis, A. N. Hrymak, and J. Vlachopoulos, Polym.

Eng. & Sci., 26, 7, 449 (1986)

191. M. R. Kamal, and P. G. Lafleur, Polym. Eng. & Sci., 26, 1, 92 (1986)

192. M. J. Boussinesq, J. Math. Pure Appl., Ser 2, 13, 377 (1868)

193. S. M. Richardson, Rheol. Acta, 22, 223 (1983)

194. S. M. Richardson, Rheol. Acta, 24, 509 (1985)

195. S. M. Richardson, Rheol. Acta, 25, 180 (1986)

196. S. M. Richardson, Rheol. Acta, 25, 308 (1986)

197. S. M. Richardson, Rheol. Acta, 25, 372 (1986)

198. H. Janesschitz-Kriegl, Rheol. Acta, 16, 4, 23 (1977)

199. H. Janesschitz-Kriegl, Rheol. Acta, 18, 693 (1979)

200. Y. L. Lee, R. S. Bretzlaff, and R. P. Wool, J. Polym. Sci. Phys. Ed., 22, 681 (1984)

201. J. P. Luongo, J. Appl. Polym. Sci., 3, 9, 302 (1960)

202. W. Heinen, J. Polym Sci., 38, 545 (1959)

203. R. G. Quynn, J. L. Riley, D. A. Young, and H. D. Noether, J. Appl. Polym. Sci., 2, 5, 166 (1959)

204. P. J. Hendra, J. Vile, H. A. Willis, V. Zichy, and M. E. A. Cudby, Polymer, 25, 785 (1984)

205. Y. V. Kissin, J. Polym. Sci. Phys. Ed., 21, 2085 (1983)

206. R. D. B. Frazer, **Analytical Methods of Protein Chemistry**, Vol 2, Pergamon Press, London (1960)

207. R. P. Wool, J. Polym. Sci. Polym. Phys. Ed., 14, 603 (1976)

208. S. G. Advani, and C. L. Tucker III, ANTEC'85, 1113 (1985)

209. M. L. Lovrich, and C. L. Tucker III, ANTEC'85, 1119 (1985)

APPENDIX I

A.1 FTIR Analysis

Infra-red spectroscopy has been utilized by many researchers for the study of crystallinity, molecular orientation and stress in polymeric matrices.

The position of the absorption bands in the spectra of polymers is determined by the normal modes of vibration of the molecules. Infra-red studies of polypropylene have concentrated in the region from 1400 cm^{-1} to 700 cm^{-1} wavenumber, where the infra-red bond assignments are known. This information is given in Table A.1 [200]. Infra-red absorption can arise due to stretching, bending, etc., of molecular bonds.

Commercial polypropylene consists of an isotactic and an atactic phase. The isotactic phase is largely crystalline, whereas, the atactic is mostly amorphous. Fully isotactic and 100% atactic polypropylene give rise to characteristic absorption spectra which differ significantly.

The 100% isotactic spectrum has strong absorption bands at 1366, 1330, 1305, 1295, 1258, 1220, 1168, 1103, 1045, 995, 973, 938, 895, 842, and at 810 cm^{-1}. These become extremely weak or disappear in the spectrum of 100% atactic polypropylene. Figure A.1 [201] illustrates the differences. The peaks at 1380, 1154 and 973 cm^{-1} are the main ones in 100%

TABLE A.1

A.1 Assignments for FTIR absorption bands for polypropylene.

Frequency cm-1	Phase (polarization)	α deg	Band Assignment
1461	A,C	($^\perp$)	
1378	A,C	70	CH_3 symm. bend
1304	C,A	(//)	CH_2 wag, CH_2 twist
1257	A,C	0	CH_2 twist, CH ax. bend, CH eq. bend
1168	C,A	0	C-C ax. stretch, CH_3 ax. rock
998	C	18	CH_3 eq. rock, CH bend, $C-CH_3$ stretch, CH_2 twist
974	A,C	18	CH_3 ax. rock, C-C ax. stretch, C-C eq. stretch
900	C	($^\perp$)	
841	C	(//)	CH_2 rock, CH ax. bend

Reference [174]

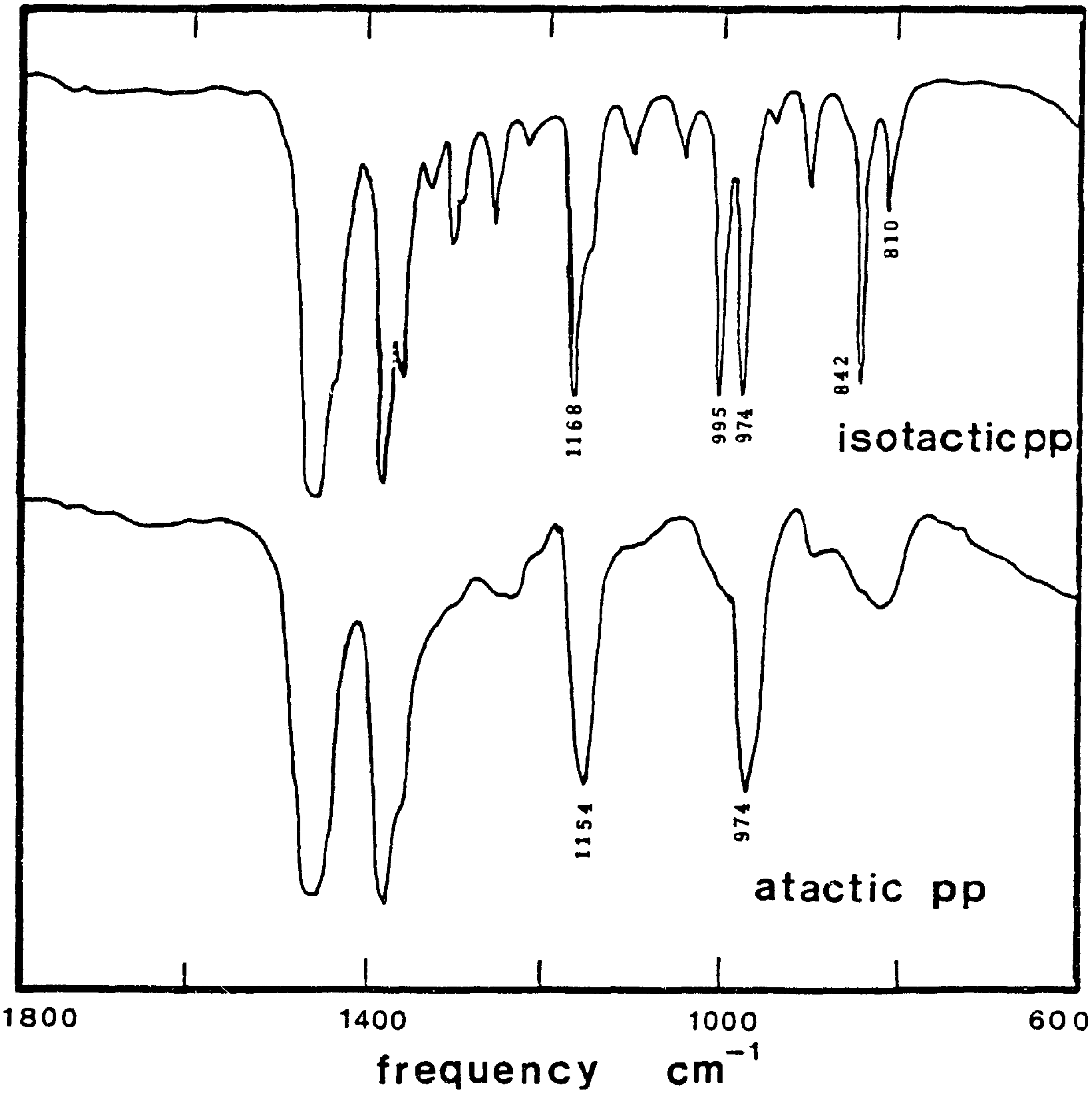

Figure A.1 FTIR spectra for 100% isotactic and 100% atactic (100% amorphous) polypropylene.

atactic polypropylene. The spectrum of molten polypropylene is very similar to that of 100% atactic polypropylene.

Heinen [202] studied the spectra of polypropylene at different temperatures. He showed that the spectra of crystalline and amorphous polypropylene differ considerably. The bands 1450, 1370, 1171, 978 and 890 cm^{-1} were seen to be nearly independent of temperature while 1329, 1305, 1223, 1106, 1048, 1003, 944, 904 and 846 cm^{-1} decreased in intensity at higher temperatures. The sharp drop in intensity of certain peaks in the melting region suggests connection with the degree of crystallinity. The 846 cm^{-1} band seemed to be the most suitable crystalline band. The 800 cm^{-1} band increased in intensity with temperature, which suggests an amorphous band.

Heinen [202] used the 846 cm^{-1} band to calculate the crystallinity of polypropylene samples. The 1171 cm^{-1} band was used as an internal standard to compensate for sample thickness because its intensity was independent of temperature or crystallinity. He plotted crystallinity versus the ratio at the absorbances of the 846 and 1171 cm^{-1} bands, with the resulting equation:

$$X = 0.77(A_{846}cm^{-1}/A_{1171}cm^{-1}) + 0.06 \qquad (A.1)$$

Quynn, <u>et al.</u> [203] showed that the degree of crystallinity is closely related to the isotactic content. The steric regularity of the isotactic product confers a crystallizability not possessed by the atactic material. The differences between the amorphous or atactic polypropylene spectrum and that of the isotactic polypropylene have led to the use of infra-red methods for determining crystallinity and isotacticity. However, with the similarities of the atactic and amorphous polypropylene spectra, there is some confusion with regards as to what is actually being measured.

Hendra, et al. [204] carried out studies on the crystallinity of polypropylene. Some bands have at various times been associated with regularity in structure, such as helices or crystalline zones. Other bands have also been related to molecules in disordered arrays. They used the ratio of the absorbances at the 998 cm^{-1} and the 973 cm^{-1} bands to measure crystallinity. The 998 cm^{-1} arises from the regular 3 helices of 10 monomer units. The 841 cm^{-1} arises from larger sequences. The bands at 120, 900, 809 cm^{-1} originate from extended sequences of regular isotactic polypropylene molecules in helical sequence.

Kissin [205] used the absorbances of the 1220 and 1250 cm^{-1} bands to measure crystallinity. Crystallinity was related to the ratio of ($A°_{1220}cm^{-1}$ / $A°_{1250}cm^{-1}$) where:

$$A°_{1220} = \frac{1}{3}\left\{ A_{1220\,//} + 2A°_{1220\,\perp} \right\} \qquad (A.2)$$

$$A°_{1250} = \frac{1}{3}\left\{ A_{1250\,//} + 2A°_{1250\,\perp} \right\} \qquad (A.3)$$

The ratios were calculated using the absorbances of parallel and perpendicular polarized spectra. Other bands such as the 841 and 1168 cm^{-1} bands had high absorbances and so were not suitable.

The molecular orientation of the matrix phase has to be characterized by measurements of crystalline and amorphous orientations. Measurements of crystalline orientation by Fourier Transform Infra-Red spectroscopy methods have been reported, but none for amorphous orientation. This parameter is usually calculated from birefringence or ultrasonic data and the orientation of the crystalline phase, taking into account the crystallinity. There are many problems with this procedure. The separation of total birefringence into two constituents Δ_{cry} for the crystalline phase and Δ_{am} for the amorphous phase requires precise values for the limiting birefringence values Δ°_{cry} and Δ°_{am} for the completely oriented phases. The reported values can differ significantly, with ranges as follows:

$\Delta^{\circ}_{cry} = 0.067 - 0.0131$

$\Delta^{\circ}_{am} = 0.0618 - 0.0381$

The same is true for the limiting moduli in the ultrasonic method. The range of the limiting modulus E is as follows:

$E = 2.1 \times 10^{10} - 3.9 \times 10^{10}$ dynes/cm^2

Estimation of crystallinity of oriented polypropylene is difficult. Polypropylene has the tendency to change crystalline structure from the usual monoclinic to the smectic form which has different physical properties. The above complications reduce the reliability of such methods for measurement of orientation in the amorphous phase.

When an anisotropic material such as an oriented polymer film is examined with polarized infra-red light, there are two absorption processes.

(i) Structural dependent absorption is the integrated absorption over all the sample configurations. It is dependent only on the number of absorbing species present and their absorption characteristics as long as the Beer-Lambert law is obeyed. This type of treatment is suitable for the study of absorbing units, which change concentration as a result of the physical treatment of the material. As an example, conditions which increase the crystallinity of a material will increase the absorption which is characteristic of the crystalline regions of the polymer.

(ii) Orientation dependent absorption is the absorptions with which measures of anisotropy can be made.

The measurement of orientation in polypropylene films using infra-red spectra, has been evaluated by various researchers [35,136,205]. Theoretical and experimental aspects of infra-red spectroscopy orientation measurements were developed in detail, and the possibility of a quantitative evaluation of the degree of orientation of polymers in three mutually perpendicular axes was pointed out.

Samuels [35] used infra-red dichroic ratios to measure orientation of polymer films. The dichroic ratio $D = A_{//}/A_{\perp}$ is the ratio for the same band calculated in two spectra recorded with the polarization plane of a polarizer parallel and perpendicular to the film stretching or reference direction.

The infra-red dichroic ratio D of a uniaxially oriented polymer is a function of two characteristic orientation angles θ and α. θ is the angle that the polymer chain axis makes with the reference direction (eg. the stretch direction) and α is the angle that the transition moment makes with the polymer chain axis. The angle α is generally not known. Frazer [206] derived general equations relating θ and α to the dichroic ratio of a uniaxially oriented fiber. He showed that if all the molecular chain axes of an oriented fiber were perfectly aligned parallel to the reference direction, the dichroic ratio would be a function of the transition moment angle α only:

$$D_0 = 2 \cot^2 \alpha \tag{A.4}$$

where D_0 is the dichroic ratio of perfectly aligned chains. Under normal conditions, when the molecular chain axis is oriented at an average angle θ to the reference direction, a quantitative definition of orientation is given by Hermans orientation function f_p [35]. :

$$f_p = \left\{ \frac{D-1}{D+2} \right\} \left\{ \frac{D_o+2}{D_o-1} \right\} \qquad (A.5)$$

$$f_p = \frac{1}{2} \left\{ 3 \cos^2\theta - 1 \right\} \qquad (A.6)$$

where

D = the measured dichroic ratio.

subscript

p can be replaced by c or am.

c = crystalline phase.

am = amorphous phase.

when 0 = 0 f_p = 1.0 the orientation of the chain axis is parallel to the direction of deformation.

when 0 = 54.7 f_p = 0 random orientation.

when 0 = 90 f_p = -0.5 perpendicular orientation.

In order to determine f_p from infra-red measurements, the relation between the infra-red frequencies used and the intrinsic molecular response to that frequency (transition moment angle α) must be known.

The dichroic ratio $D = k_l/k_t$ where k_l and k_t are the principal absorption coefficients for radiation polarized parallel and perpendicular to the orientation direction respectively. The quantity actually measured is $D' = e_l/e_t$ where e_l and e_t are the optical densities, $\log I_0/I$, parallel and perpendicular to the orientation axis, respectively. I_0 and I are the incident and transmitted intensities, respectively. The quantity D' is equal to D if there is no scattering or reflective losses, in which case e_l and e_t are equal to k_l and k_t, respectively.

In order to determine Do, a value of α_{av} is assumed for a known frequency band. The value of f_p is then calculated and used as a constant to derive α_{av} for other frequency bands. In this technique, the transition moment angle is assumed to be invariant from compound to compound. Another method involves measuring f_p by x-ray diffraction and using that to calculate α_{av} [35].

Each infra-red frequency is absorbed differently by the polymer. The strongly absorbed frequencies are used for thin films, while the weakly absorbed ones are used for thick samples. For thick samples, the frequency region lies between 350-1000 cm^{-1}. For isotactic polypropylene, the 400 cm^{-1} is due to the crystalline phase absorption and 528 cm^{-1} is due to the absorption of both phases. For thin films, the absorption frequencies are 1220 cm^{-1} and 1256 cm^{-1} for the crystalline and average phases, respectively. The 1220 cm^{-1} band is due to absorption by the crystalline phase only, however, there is no agreement as to the assignment of the vibration modes. The band represents the motion of one, or more of the three bonds CH, CH_2, and $C-CH_3$. Isotactic polypropylene has a helical conformation in the crystalline phase and each bond makes an angle of about 72° with the helical axis. For the 1220 cm^{-1} absorption band, the transition moment angle, α_{av}, is 72°.

The 1256 cm^{-1} absorption band results from both the crystalline and amorphous phases. The orientation measured correlates with the average orientation which can be expressed as:

$$f_{av} = \beta f_c + (1-\beta) f_{am} \tag{A.7}$$

β = fraction crystallinity

f_c, f_{am} = orientation functions of the amorphous and crystalline phases respectively.

For isotactic polypropylene

400 cm^{-1} is due to the crystalline phase absorption with α_{av} - 20

528 cm^{-1} is due to the average phase absorption with $\alpha_{av} = 90$

1220 cm^{-1} crystalline phase with $\alpha_{av} = 72$

1256 cm^{-1} average with $\alpha_{av} = 38.5$

Kissin, et al. [205] showed that the polarization spectra of highly oriented polypropylene had many bands that were characteristic of long isotactic helix sequences in the crystalline phase (both monoclinic and smectic) at 1168, 998, 900, 841 and 809 cm^{-1}. The 841 and 809 cm^{-1} bands were most suitable for orientation measurements because of their strong absorption peaks. The transition moment angles were 0° and 90°, respectively.

Wool, et al. [200,207] used the 998 and 975 cm^{-1}

absorption bands with transition moment angle of 10° and 45°, respectively.

Kissin, et al. [136,205] used infra-red spectroscopy to determine the molecular orientation in three mutually perpendicular axes in the crystalline phase and along one axis in the amorphous phase of polypropylene. Using the stretch direction of the polymer films as the reference x-direction, they used parallel, perpendicular and nonpolarized spectra in their method. They derived the following relationships using the 841 and 809 cm^{-1} bands for the measurement of orientation in the crystalline phase:

$$\left\{\frac{A_{841}}{A_{809}}\right\}_{//} = \left\{\frac{NP_x}{1-P_x}\right\} \tag{A.8}$$

$$\left\{\frac{A_{841}}{A_{809}}\right\}_{\perp} = \left\{\frac{NP_y}{1-P_y}\right\} \tag{A.9}$$

$$\left\{\frac{A_{841}}{A_{809}}\right\}_{o} = \left\{\frac{NP_z}{1-P_z}\right\} \tag{A.10}$$

where the nomenclature represents,

A_n = absorption at the specific peak in cm^{-1}

N = the doubled ratio of the absorption coefficient of these two bands E_{841}/E_{809} (N = 5.80, obtained from the spectra of isotropic films)

P_x, P_y, P_z = orientation parameters which represent apparent fractions of polymer chain segments (in crystalline or amorphous phase) aligned parallel to the corresponding axes. Thus

$P_x + P_y + P_z = 1$

subscript

// = parallel polarized spectra

⊥ = perpendicular polarized spectra

° = nonpolarized spectra

x = axis of stretching direction

y = perpendicular to the stretching direction in the plane of the polymer film

z = axis perpendicular to the stretching direction and to the film plane

$P_x = P_y = P_z = 0.33$ for an unoriented film

$P_x = 1$, $P_y = P_z = 0$ for complete orientation in the x axis.

For uniaxially drawn films, the cylindrical approximation is used, where $P_y = P_z$ and $P_x = 1 - 2P_y$. Thus a single orientation parameter is sufficient for the description of orientation in a particular phase. P_x is related to Hermans orientation parameter f_x as shown:

$$f_p = \frac{1}{2}\left\{ 3P_x - 1 \right\} \qquad (A.11)$$

The infra-red spectrum of molten or amorphous isotactic polypropylene has only a few absorption bands. There are three bands that can be used for orientation measurements. The stretching modes in the 300 - 2800 cm^{-1} range, and, the deformation modes at 1460 and 1380 cm^{-1} which have very high intensities are unsuitable for orientation measurements. The 815 cm^{-1} is a wide absorption band. The 973 cm^{-1} is a narrow band which coincides with the intense band of the crystalline polymer. The polarization characteristic of this band can be used for the estimation of the general orientation in polypropylene samples.

The 1155 cm^{-1} is also a narrow band. It is sufficiently separate from the crystalline 1168 cm^{-1} band and is most suitable for estimation of orientation of the amorphous phase. The absorbance of the 1155 cm^{-1} band is measured in the perpendicular polarized spectrum only. The parallel polarized spectrum is almost completely overlapped by the more intense 1168 cm^{-1} band. Even in the perpendicular polarized spectra, separation of the bands is needed.

The amorphous phase orientation was also derived using a similar method [136,205]. The true absorption of the 1155 cm^{-1} band $(A^{*}_{1155})_{\perp}$ was derived from the experimentally measured values.

$$A^{*}_{1155\,\perp} \approx A_{1155\,\perp} - \frac{0.133}{0.98}\left\{ A_{1168} \right\}_{\perp} \qquad (A.12)$$

The general expression for band absorption in the polarization infra-red spectrum with the polarization plane perpendicular to the film stretching direction is:

$$A^{*}_{1155\perp} = K_{1155}[P_x^{am}(\mu_a E)^2 + P_y^{am}(\mu_c E)^2 + P_z^{am}(\mu_a E)^2]CL \qquad (A.13)$$

P_x^{am}, P_y^{am}, P_z^{am} are the orientation parameters of the amorphous phase

K = absorption coefficient of the 1155 cm^{-1} band
L = film thickness
C = concentration of absorbing units = 1-X,
X = crystallinity
E = electric field vector for incident infra-red radiation
μ_a, μ_b, μ_c = transition moment unit vectors

$$\left\{ \frac{\mu_a}{\mu_c} \right\} = \frac{1}{2} \tan^2\theta \qquad (A.14)$$

For uniaxially drawn film $P_y^{am} = P_z^{am} = 1/2(1-P_x^{am})$, thus:

$$A^{*}_{1155\perp} = \frac{1}{4} K_{1155}\left\{P_x^{am}(\tan^2\theta-2)+2+\tan^2\theta\right\}(\mu_c E)^2(1-X)L \qquad (A.15)$$

To avoid measuring the thickness L, an internal sample thickness method is applied using the absorbance of some other band in the spectrum. The 809 cm^{-1} band was used. The absolute absorbance A° of this band is calculated independent of orientation.

$$A^{\circ}_{809} = \frac{1}{3}\left\{ A_{809\,//} + 2A^{\circ}_{809\perp} \right\} \qquad (A.16)$$

since θ_{809} = 90° and it is a crystalline band, then C = X

$$A^{\circ}_{809} = K_{809}(\mu_c E)^2 XL \qquad (A.17)$$

Substituting yields an equation which can be used in the calculation of P_x^{am}.

$$\left\{\frac{A^{*}_{1155\perp}}{A^{\circ}_{809}}\right\}\left\{\frac{X}{(1-X)}\right\} = \frac{1}{4}\left\{\frac{K_{1155}}{K_{809}}\right\}\left\{P_x^{am}(\tan^2\theta-2)+2+\tan^2\theta\right\} \qquad (A.18)$$

In order to calculate P_x^{am}, the measurements needed are:

$A^{*}_{1155\perp}$ is calculated from the perpendicular spectrum

A°_{809} from both parallel and perpendicular spectrum

X crystallinity

K_{1155}/K_{809} and θ_{1155} should be estimated independently.

APPENDIX II

B.1 Fiber Orientation Parameters

The orientation state of the fibers in the composite plays an important role in the determination of the properties. Thus, the orientation state is a quantity which must be calculated from processing conditions and which must be known to find mechanical properties. In view of this, a quantitative structural characterization of the fiber orientation state is needed.

Advani and Tucker [208] used a tensor description of fiber orientation. They used two sets of even order tensors to describe the distribution of the fiber orientation. The orientation distribution function ψ written as $\psi(\theta,\phi)$ is the most general description of fiber orientation. The angles θ and ϕ are defined such that the probability of finding a fiber between the angles θ_1 and $\theta_1+d\theta$ and ϕ_1 and $\phi_1+d\phi$ is given by:

$$p(\theta_1 \leq \theta \leq \theta_1 + d\theta,\ \phi_1 \leq \phi \leq \phi_1 + d\phi) = \psi(\theta_1,\phi_1)\sin\theta_1 d\theta d\phi \qquad (B.1)$$

It can also be described using a vector p pointing along the fiber to describe its direction. The distribution function (p) with the component p is related to θ and ϕ as shown in Figure 6.6

$$p_1 = \sin\theta\cos\phi \tag{B.2}$$

$$p_2 = \sin\theta\sin\phi \tag{B.3}$$

$$p_3 = \cos\theta \tag{B.4}$$

with

$$\sum_{i=1}^{3} p_i^{\,2} = 1 \tag{B.5}$$

and the normalized distribution function

$$\int_{\theta=0}^{\pi} \int_{\phi=0}^{2\pi} \psi(\theta,\phi)\sin\theta\, d\theta\, d\phi = \oint \psi(p)\, dp = 1 \tag{B.6}$$

and $\psi(p) = \psi(-p)$ since one end is indistinguishable from the other. This distribution does not take into account fiber length, however, it is a complete unambiguous, but rather cumbersome description of orientation. It is not very economical to use in computer modelling of fiber orientation in molded parts.

Fiber orientation can also be described by a set of orientation parameters. These have been used extensively in theories of mechanical properties of short fiber composites. They possesses symmetry:

$$\psi(\theta,\phi) = \psi(-\theta,\phi) = \psi(\theta,-\phi) \tag{B.7}$$

and separation of products ψ_θ and ψ_ϕ.

Only four parameters are needed to calculate mechanical properties.

$$f_p = 2 \left\{ \cos^2\theta - 1 \right\} \tag{B.8}$$

$$g_p = \frac{1}{5} \left\{ 8 \cos^4\theta - 3 \right\} \tag{B.9}$$

$$f_a = \frac{1}{2} \left\{ 3 \cos^2\theta - 1 \right\} \tag{B.10}$$

$$g_a = \frac{1}{4} \left\{ 5 \cos^4\theta - 1 \right\} \tag{B.11}$$

where the angle brackets denote weighted averages over the distribution function defined as:

$$<\cos^n\phi> = \int_0^{2\pi} \psi_\phi \cos^n\phi d\phi \tag{B.12}$$

Physical interpretations of f_p and g_p provides information about alignment in the 1-2 plane. A value of 0 indicates random distribution while a value of 1 indicates total alignment in the 1 axis direction. The parameters f_a and g_a provides information about axial alignment along the 3 axis. f_a ranges from -1/2 to 1 and is the Hermans orientation function for axi-symmetric orientation states. For $f_a = g_a = 0$ corresponds top random distribution in the angle θ. $f_a = -1/2$ and $g_a = -1/4$ corresponds to all fibers aligned perpendicular to the 3 axis and $f_a = g_a = 1$ corresponds to all the fibers aligned along the 3 axis.

Another method of describing fiber orientation is by a set of tensors. These tensors have many advantages. They are concise, unambiguous, and are free from assumptions of the nature of the orientation.

The dyadic product of the vector p is used to form tensors, and then, the product of these tensors with the distribution function over all possible directions. The odd order integrals are zero since the distribution function is even. The second and fourth order orientation tensors are:

$$a_{ij} = \oint p_i p_j \psi(p)\, dp \tag{B.13}$$

$$a_{ijkl} = \oint p_i p_j p_k p_l \psi(p)\, dp \tag{B.14}$$

An infinite number of these tensors are possible, however, up to the fourth order is adequate for most applications of fiber orientations. The tensors are completely symmetric and are normalized such that.

$$\sum_{i=1}^{3} a_{ij} = 1 \tag{B.15}$$

The knowledge of the fourth order tensors can be used to calculate the second order tensors.

$$\sum_{k=1}^{3} a_{ijkl} = a_{ij} \tag{B.16}$$

For planar fiber orientation, Lovrich and Tucker [209] used the set of tensors developed by Advani and Tucker. The second order tensors were used.

$$a_{11} = \int_0^{\pi} \cos^2\phi\psi(\phi)\,d\phi \qquad (B.17)$$

$$a_{12} = \int_0^{\pi} \sin\phi\cos^2\phi\psi(\phi)\,d\phi \qquad (B.18)$$

where

a_{11} is the moment about axis 1

a_{12} is the moment in the plane 1-2

Using Mohr's circle, the maximum principle moment is calculated.

$$A_1 = 0.5 + (a_{11}-0.5)^2 + a^2_{12} \qquad (B.19)$$

A_1's direction with respect to the coordinate axis 1 ϕ_1,

$$\phi_1 = \frac{1}{2}\sin^{-1}\left\{\frac{a_{12}}{0.5 + (a_{11}-0.5)^2 + a^2_{12}}\right\} \qquad (B.20)$$

A_1 is a measure of the degree of alignment which is directly related to the degree of anisotropy in a part.

$A_1 = 0.5$ random

$A_1 = 1.0$ completely aligned

$\phi = 0$ direction along x1

$\phi = 90$ direction along x2

APPENDIX III

C.1 FORTRAN Program Listing for fiber orientation model

```
C*********************************************************
C PROGRAM FIBER ORIENTATION IN RECTANGULAR CHANNEL         *
C                                                          *
C*********************************************************
C THIS PROGRAM WILL SET UP AND SOLVE NUMERICALLY THE       *
C PAIR OF JEFFERY'S EQUATIONS WITH THE INITIAL             *
C CONDITIONS OF PHI - Y1(0) AND THETA - Y2(0)              *
C THE SOLUTION IS OBTAINED AT 25 POINTS OVER THE           *
C INTERVAL (0,B) USING A MULTIVARIATE 4-TH ORDER           *
C RUNGE-KUTTA METHOD                                       *
C                                                          *
C CALLS: MRUKU                                             *
C OUTPUT:                                                  *
C     X(I)=VALUE OF X (DISTANCE) FOR I=1,25                *
C     Y(J,I)=APPROXIMATED VALUE OF Y1 AND Y2 AT X(I)       *
C                                                          *
C*********************************************************

      IMPLICIT REAL*16 (A-H,O-Z)
      CHARACTER*32 FILNAM1
      DIMENSION X(101),Y(2,101),FX(101),FZ(101)
      COMMON VELX,DVDY,DVDZ,FB

      FILNAM1='FIB_ORI.DAT'
      OPEN(UNIT=1,FILE=FILNAM1, DEFAULTFILE='FO.DAT',
     1STATUS='NEW')
      WRITE(1,17)
17    FORMAT(1X,'FIBER ORIENTATION IN A RECTANGULAR MOLD
      1',/,' FLOW RATE =  9 CM**3/SEC',/,' MELT TEMPERATURE
      2=  240 C',//,'      Z     FX(X /L=.1) FZ(X/L=.1)
      3FX(X/L=.5) FZ(X/L=.5) FX(X/L=.9) FZ(X/L=.9)',/)

C CAVITY DIMENSIONS 10CM X 6CM X 3MM IN METRES
      CL=0.10
      CW=0.06
      CCH=0.003

C FLOW RATE IN M**3 PER SECOND
      CQ=0.000009

C VISCOSITY
      VIS=2860

C FIBER ASPECT RATIO
      FR=28.0
C SHAPE FACTOR FOR JEFFREY'S EQUATION
```

```
      FB=(FR**2.0-1.0)/(FR**2.0+1.0)

C NUMBER OF DIFFERENTIAL EQUATIONS DESCRIBING THE
C RELATIONSHIP BETWEEN THETA AND PHI WITH Y AND Z
      M=2

C SET INITIAL AND FINAL FLOW DISTANCE
      X(1)=0.0
      B=CL

C NUMBER OF DATA POINTS TO BE TAKEN IN THE
C FLOW LENGTH INTERVAL
      N=50

C FOR VARYING INITIAL ANGLE PHI
      PI=22.0/7.0
      DO 6000 NPHI=0,2
      Y(1,1)=0.0+(PI/36.0)*NPHI+0.00001

C FOR VARYING INITIAL ANGLE THETA
      DO 7000 NTHETA=1,2
      Y(2,1)=PI/2.0-(PI/36.0)*NTHETA-0.00001

C SET UP COORDINATE SYSTEM
C Y INTERVAL - 0.0100 METRES
C Z INTERVAL - 0.0001 METRES
      YINT=0.030
      ZINT=0.0001

C FOR DECREASING MOLD THICKNESS DUE TO GROWTH OF FROZEN
C LAYER: SET INITIAL THICKNESS OF FLOW AREA
      DO 8000 KFZ=0,4
      CH=CCH-KFZ*ZINT*2.0

C SET UP COORDINATES CY,CZ FOR SOLUTION
      NYINT=CW/(2.0*YINT)
      DO 2000 KY=NYINT,0,-1
      CY=CW/2.0-KY*YINT

      NZINT=CH/(2.0*ZINT)
      DO 1000 KZ=NZINT,0,-1
      CZ=CH/2.0-KZ*ZINT

C VELOCITY PROFILE FUNCTION OF (CY,CZ)
      SUM1=0.0
      DO 19 L=1,25,2
      A1=(QSINH(0.5*L*PI*CW/CH)/QCOSH(0.5*L*PI*CW/CH))
     1/(L**5.0)
      SUM1=SUM1+A1
19    CONTINUE

C PRESSURE DROP
```

```
      DP=-1.0*((12.0*VIS*CQ*CL)/(CW*(CH**3.0)*(1.0-192.0*
     1CH*SUM1/((PI**5.0)*CW))))
      SUM2=0.0
      DO 29 L=1,25,2
      A2=(QCOSH((0.5*L*PI/CH)*(2.0*CY-CW))/QCOSH(L*PI*
     1CW/CH))*QSIN(L*PI*CZ/CH)/(L**3.0)
      SUM2=SUM2+A2
29    CONTINUE
      VELX=(DP/(VIS*CL))*(0.5*(CZ**2.0)-0.5*CZ*CH+4.0*
     1(CH**2.0)*SUM2/(PI**3.0))

C DIFFERENTIAL OF VELOCITY WITH CY
      SUM3=0.0
      DO 39 L=1,25,2
      A3=(QSINH((0.5*L*PI/CH)*(2.0*CY-CW))/QCOSH(L*PI*
     1CW/CH))*QSIN(L*PI*CZ/CH)/(L**2.0)
      SUM3=SUM3+A3
39    CONTINUE
      DVDY=(DP/(VIS*CL))*(4.0*CH*SUM3/(PI**2.0))

C DIFFERENTIAL OF VELOCITY WITH CZ
      SUM4=0.0
      DO 49 L=1,25,2
      A4=(QCOSH((0.5*L*PI/CH)*(2.0*CY-CW))/QCOSH(L*PI*
     1CW/CH))*QCOS(L*PI*CZ/CH)/(L**2.0)
      SUM4=SUM4+A4
49    CONTINUE
      DVDZ=(DP/(VIS*CL))*(CZ-0.5*CH+4.0*CH*SUM4/(PI**2.0))

C SUBROUTINE WILL APPROXIMATE THE SOLUTION
C RETURNING N+1 VALUES IN ARRAYS X AND Y

      CALL MRUKU(X,Y,N,B,M)

C OUTPUT ORIENTATION FUNCTIONS AS A FUNCTION OF DEPTH FOR
C X AT 0CM, 5CM AND 10.0 CM ALONG THE LENGTH OF THE MOLD.
C FX IS ORIENTATION FUNCTON WITH RESPECT TO THE X AXIS
C FZ IS ORIENTATION WITH RESPECT TO THE Z AXIS
      DO 900 I=1,11,5
      IE=(((I-1)*N)/(CL*100.0))+1
      FX(I)=0.5*(3.0*((QCOS(PI/2.0-Y(1,IE)))**2.0)-1.0)
      FZ(I)=0.5*(3.0*((QCOS(Y(2,IE)))**2.0)-1.0)
900   CONTINUE
      WRITE(1,100)CZ,FX(1),FZ(1),FX(6),FZ(6),FX(11),FZ(11)
100   FORMAT(1X,F9.4,6F11.4)
1000  CONTINUE
      WRITE(1,111)CY,CH,(Y(1,1)*180.0/PI),(Y(2,1)*180.0/PI)
111   FORMAT(1X,/,'   Y   POSITION   = ',F10.5,/,' FLOW WIDTH
     1 = ',F10.5,/,' INITIAL ANGLE PHI = 'F10.5,/,'INITIAL
     2ANGLE THETA = ',F10.5 ,//,'     Z   FX(X/L= 0) FZ(X/L=
     30) FX(X/L=.5) FZ(X/L=.5) FX(X/L= 1) FZ(X/L=1)',/)
2000  CONTINUE
```

```
8000  CONTINUE
7000  CONTINUE
6000  CONTINUE
      CLOSE(UNIT=1)
      STOP
      END

C**********************************************************

       SUBROUTINE MRUKU(X,Y,N,B,M)

C**********************************************************
C THIS SUBROUTINE COMPUTES THE SOLUTION TO A SET OF       *
C SIMULTANEOUS DIFFERENTIAL EQUATIONS OVER THE            *
C INTERVAL [X(1),B] GIVEN THE J-TH COORDINATE OF THE      *
C DEFINING FUNCTION F(U,V,J) AND USING THE 4-TH           *
C ORDER RUNGE-KUTTA METHOD                                *
C                                                         *
C USAGE:                                                  *
C  CALL SEQUENCE: CALL MRUKU(X,Y,N,B,M)                   *
C  EXTERNAL FUNCTIONS/SUBROUTINES: FUNCTION F(U,V,J)      *
C                                                         *
C PARAMETERS:                                             *
C  INPUT:                                                 *
C   M   =NUMBER OF DIFFERENTIAL EQUATIONS                 *
C        (MAXIMUM OF 100)                                 *
C   X(1)=INDEPENDENT VARIABLE INITIAL VALUE               *
C   Y(1,1),Y(2,1),......Y(M,1)                            *
C       =DEPENDENT VARIABLE INITIAL VALUES                *
C   B   =SOLUTION INTERVAL ENDPOINT (LAST X, VALUE)       *
C  OUTPUT:                                                *
C   X=N+1 BY 1 ARRAY OF INDEPENDENT VARIABLE VALUES       *
C   Y=M BY N+1 ARRAY OF DEPENDENT VARIABLES SOLUTION      *
C     VALUES (EACH ARRAY ROW IS THE SOLUTION FOR ONE      *
C     OF THE M DIFFERENTIAL EQUATIONS                     *
C**********************************************************

      DIMENSION X(N+1),Y(M,N+1),V(100),T(100,4)
      COMMON VELX,DVDY,DVDZ,FB
      REAL*16 B,F,X,Y,V,T,H,U,VELX,DVDY,DVDZ,FB

      H=(B-X(1))/N
      DO 1 I=2,N+1
         X(I)=X(I-1)+H
         U=X(I-1)
         DO 2 J=1,M
            V(J)=Y(J,I-1)
2        CONTINUE
         DO 3 J=1,M
            T(J,1)=F(U,V,J)
3        CONTINUE
         U=U+0.5*H
```

```
         DO 4 J=1,M
            V(J)=V(J)+0.5*H*T(J,1)
4        CONTINUE
         DO 5 J=1,M
            T(J,2)=F(U,V,J)
5        CONTINUE
         DO 6 J=1,M
            V(J)=Y(J,I-1)+0.5*H*T(J,2)
6        CONTINUE
         DO 7 J=1,M
            T(J,3)=F(U,V,J)
7        CONTINUE
         U=U+0.5*H
         DO 8 J=1,M
            V(J)=Y(J,I-1)+H*T(J,3)
8        CONTINUE
         DO 9 J=1,M
            T(J,4)=F(U,V,J)
9        CONTINUE
         DO 10 J=1,M
           Y(J,I)=Y(J,I-1)+H*(T(J,1)+2.0*T(J,2)+2.0*T(J,3)+
     1T(J,4))/6.0
10       CONTINUE
1     CONTINUE
      RETURN
      END
C***********************************************************

C***********************************************************
C                                                          *
C FUNCTION F SPECIFIES THE DIFFERENTIAL EQUATIONS          *
C IT IS CALLED BY SUBROUTINE MRUKU                         *
C DVDY = DIFFERENTIAL OF VELOCITY WITH Y                   *
C DVDZ = DIFFERENTIAL OF VELOCITY WITH Z                   *
C FB = SHAPE PARAMETER                                     *
C***********************************************************

      FUNCTION F(U,V,J)
      COMMON VELX,DVDY,DVDZ,FB
      DIMENSION V(2)
      REAL*16 F,VELX,DVDY,DVDZ,FB,U,V

      IF (J.EQ.1) THEN

C FIRST OF JEFFERY'S EQUATION RELATING PHI TO THE
C FLOW LENGTH DOWN THE MOLD (SINCE THE VELOCITY IS CONSTANT
C WITH Z

      F=(0.5*DVDY*(1.0+FB*QCOS(2.0*V(1))))+(0.5*DVDZ*
     1QCOS(V(1))*(QCOS(V(2))/QSIN(V(2)))*(1.0+FB))

      ELSE
```

```
C SECOND OF JEFFERY'S EQUATION RELATING THETA TO THE
C FLOW LENGTH DOWN THE MOLD

      F=(0.25*FB*DVDY*QSIN(2.0*V(1))*QSIN(2.0*V(2)))+(0.5*
     1DVDZ*QSIN(V(1))*(1.0+FB*QCOS(2.0*V(2))))

      ENDIF
      RETURN
      END

C************************************************************
```

APPENDIX IV

C.1 BASIC Program Listing for frozen layer model

```
************************************************************
* PROGRAM FROZEN LAYER PREDICTION IN RECTANGULAR CHANNEL   *
*                                                          *
************************************************************
10 OPEN "FRL200.DAT" FOR OUTPUT AS #1
40 REM   DIMENSIONS IN SI UNITS (METRES,ETC)
41 REM   H = THICKNESS OF RECTANGULAR PROFILE
42 REM   W = WIDTH OF RECTANGULAR PROFILE
43 REM   L = LENGTH OF RECTANGULAR PROFILE
44 REM   RL = DENSITY OF MELT, CL = HEAT CAPACITY OF MELT
45 REM   Q = FLOW RATE, KL = THERMAL CONDUCTIVITY OF MELT
46 REM   VIS1 = VISCOSITY, M = POWER LAW INDEX
47 REM   KS = THERMAL CONDUCTIVITY OF SOLID
48 REM   TI = MELT TEMPERATURE, TM = CRYSTALLIZATION
          TEMPERATURE, TW = MOLD TEMPERATURE
50 H=.0015
51 W=.06
52 L=.1
53 RL=738!
54 CL=2465!
55 Q=.000012
56 KL=.257
57 M=1.88
58 KS=.215
59 TM=121.7
60 TW=30!
61 TI=200!
62 VIS1=7847!
600 PRINT#1 ,"MELT TEMPERATURE = ",TI
800 FOR J=0 TO 20
810 XF=J/200!
815 EF=XF/L
820 PRINT#1, " "
830 PRINT#1, "MELT FRONT AT " XF, "    METRES"
840 PRINT#1, "    Z     ; TH EN REG; FL FR REG; MINIMUM"
850 PRINT#1, " "
997 REM
998 REM**************************************************
999 REM
1000 FOR I=0 TO J
1001 REM
1002 REM
1010 X=I/200!
1100 GZ=2!*RL*CL*Q*H/(W*KL*L)
1110 GZ1=GZ*(M+2!)/(4!*(M+1!))
1120 EX=X/L
```

```
1500 PSI=((9!*EX)/(2!*GZ1))^(1!/3!)
1994 REM
1995 REM*********************************************
1996 REM
1997 REM CALCULATE D1,D2,D3 : DIMENSIONLESS FROZEN LAYER
     THICKNESS
1998 REM
1999 REM
2500 THETA1=KS*(TM-TW)/(KL*(TI-TM))
2600 LAM=((M+1!)/2!)^(1!/3!)
2800 BR=VIS1*(Q/(4!*W*H^2!))^((1!/M)-1)*Q^2!*(2!*
     (M+2!))^((1!/M)+1)/(4!*W^2!*H^2!*KL*(TI-TM)*4!)
3000 D1=THETA1*.893/LAM
3100 D2=((THETA1*.893/LAM)^2!)*((M/(10!*THETA1))-(3!/4!))
3200 D3=((THETA1*.893/LAM)^3!)*((10!*M-M^2!)*
     0.9027^2!/(560!*THETA1^2!*.893^4!)-.9027
     *BR/(2!*THETA1^2!*.893^2!)-3!/40!
     +M/(50!*THETA1)+(M/(10!*THETA1)-3!/4!)^2!)
4000 DEL=PSI*D1+(PSI^2!)*D2+(PSI^3!)*D3
5000 THICK=DEL*H
5810 DEL2=((EF-EX)/GZ)^.5*.4769*4!
5880 DEL3=DEL
5890 IF(DEL>DEL2) THEN DEL3=DEL2
5900 PRINT#1, USING "###.####";X,DEL,DEL2,DEL3
6000 NEXT I
6500 NEXT J
6800 CLOSE #1
7000 END
```